UNIVERSITY OF CALIFORNIA

Santa Barbara

Material Science for High-Efficiency Photovoltaics: From Advanced Optical Coatings to Cell Design for High-Temperature Applications

A dissertation submitted in partial satisfaction of the requirements for the degree of

Doctor of Philosophy

in

Electrical and Computer Engineering

by

Emmett Edward Perl

Committee in charge:

Professor John E. Bowers, Chair

Professor Steven P. DenBaars

Professor Jon A. Schuller

Dr. Myles A. Steiner

September 2016

The dissertation of Emmett Edward Perl is approved.

_____
Professor Steven P. DenBaars

_____
Professor Jon A. Schuller

_____
Dr. Myles A. Steiner

_____
Professor John E. Bowers, Chair

July 2016

Material Science for High-Efficiency Photovoltaics: From Advanced Optical Coatings to

Cell Design for High-Temperature Applications

To my family

To my mom, KK DuVivier, for your unquestioning love & support throughout my life

To my sister, Alice DuVivier, for lighting the path in front of me as I follow in your footsteps

To my dad, Jim Perl, for encouraging my curiosity in the world from a young age

ACKNOWLEDGEMENTS

I am grateful to many people who have helped immensely during my graduate career. First and foremost, I would like to thank my advisor, John Bowers, for the many opportunities he has given me over the past five years. John is the primary reason why I came to UC Santa Barbara and has provided excellent support and guidance throughout my time in his group. I am grateful for the flexibility that he gave me in conducting research, which allowed me to do work that would have been difficult to pursue with anyone else. There is no question that my life would be very different today if not for John.

I would like to thank my other UC Santa Barbara committee members, Professors Jon Schuller & Steven DenBaars, who have been great mentors. I was lucky enough to share an office suite with Jon and his group, and he has been a good resource. I have great respect for Steve, who has taught me a lot both through classes and discussions.

I am very grateful to everyone in the III-V group at NREL, it has been a dream of mine to join the group for many years. I would like to especially thank Myles Steiner for mentoring me for the past two years and agreeing to be a part of my committee. Even before coming to NREL I had a deep respect for Myles and his work, and he has since taught me much and helped me grow as a researcher. William McMahon also deserves a special thank you. Bill was the first person I knew from NREL and patiently taught me about the workings of solar cells when I was first at UC Santa Barbara. Bill has asked many insightful questions that helped shape my early research, and has been a great example of what a good scientist should be.

I owe a lot to Dan Friedman, who had enough confidence in me to bring me into the III-V group at NREL. I have learned a lot and had many great discussions with John Geisz, Scott Ward, John Simon, Iván García, Ryan France, Kevin Schulte, & Nikhil Jain. I would also like to thank Alan Kibbler, Waldo Olavarria, Anna Duda, Carolyn Beall, & Michelle Young for all their help with getting my research off the ground. This truly is a world-class group at NREL and I am thankful for the opportunity to be a part of it.

This work would not have been possible without all the other solar cell researchers from UCSB who helped me along the way. In particular, I would like to thank Tony Lin for mentoring me at the beginning of my graduate school career. I learned a lot from Tony and we had many great discussions about our research. I am grateful to Robert Farrell for his guidance. Bob helped develop many of the optical coating ideas and initiated various collaborations with the researchers working on InGaN/GaN photovoltaics. I'm thankful to Nathan Young and Nik Toledo for being a part of these collaborations with me.

I would like to thank everyone in the Bowers group, including Jared Bauters, Jock Bovington, Ben Curtin, Mike Davenport, Jared Hulme, Tin Komljenovic, Geza Kurczveil, Sid Jain, Alan Liu, Jon Peters, Molly Piels, Ashok Ramu, Daryl Spencer, Alex Spott, Sudha Srinivasan, Eric Stanton, and Chong Zhang. I had three good interns, Carl Bycraft, Jason Farkas, and Sen Jiang who helped build our testing setups at UC Santa Barbara and challenged me to pass my knowledge along. I am thankful to Ceanna Bowman, Alyssa Canada, Val de Veyra, Lisa King, and Shannon Gann for being great assistants and helping me through the logistical maze of getting a Ph.D.

I would also like to thank those from the outstanding UC Santa Barbara research community that made my experience much more enriching. I would like to thank the entire

Curriculum Vitae

Emmett Edward Perl

EDUCATION

Doctor of Philosophy in Electrical and Computer Engineering, 2016
University of California, Santa Barbara
Advisor: Professor John E. Bowers

Master of Science in Electrical and Computer Engineering, 2013
University of California, Santa Barbara
Advisor: Professor John E. Bowers

Bachelor of Science in Electrical Engineering, 2007
University of San Diego
Summa Cum Laude

WORK EXPERIENCE

Graduate Student Intern, 2014 - 2016
National Renewable Energy Laboratory, Golden, CO
Advisor: Dr. Myles A. Steiner

Graduate Student Researcher, 2011 - 2014
University of California, Santa Barbara, CA
Advisor: Professor John E. Bowers

Hollings Program Scholar, 2010
National Oceanic and Atmospheric Administration, Boulder, CO
Advisor: James H. Churnside

SURF Scholar, 2009 & 2010
National Institute of Standards and Technology, Gaithersburg, MD
Advisors: Dr. Richard Steiner & John Jendzurski

AWARDS

Best Student Paper Award at the PVSC Conference, 2016
Peter J. Frenkel Foundation Fellowship, 2015
NSF Graduate Research Fellowship, 2011
Eta Kappa Nu Honor Society, 2011
Hollings Scholarship, 2010
Tau Beta Pi, 2010
NSF STEM Scholarship, 2007
Trustee Scholarship, 2007

JOURNAL PUBLICATIONS

[1] **E. E. Perl**, J. Simon, J. F. Geisz, M. L. Lee, D. J. Friedman, and M. A. Steiner, "Measurements and modeling of III-V solar cells at high temperatures up to 400 °C," *Journal of Photovoltaics*, DOI: 10.1109/JPHOTOV.2016.2582398, 2016.

[2] **E. E. Perl**, J. Simon, J. F. Geisz, W. Olavarria, M. Young, A. Duda, D. J. Friedman, and M. A. Steiner, "Development of high-bandgap AlGaInP solar cells grown by organometallic vapor-phase epitaxy," *Journal of Photovoltaics*, vol. 6, no. 3, pp. 770-776, 2016.

[3] A. C. Tamboli, M. F. van Hest, M. A. Steiner, S. Essig, **E. E. Perl**, A. G. Norman, N. Bosco, and P. Stradins, "III-V/Si wafer bonding using transparent, conductive oxide interlayers," *Applied Physics Letters*, vol. 106, no. 26, pp. 263904, 2015.

[4] **E. E. Perl**, W. E. McMahon, R. M. Farrell, S. P. DenBaars, J. S. Speck, and J. E. Bowers, "Surface structured optical coatings with near-perfect broadband and wide-angle antireflective properties," *Nano Letters*, vol. 14, no. 10, pp. 5960-5964, 2014.

[5] **E. E. Perl**, W. E. McMahon, D. J. Friedman, and J. E. Bowers, "Design of antireflective nanostructures and optical coatings for next-generation multijunction photovoltaic devices," *Optics Express*, vol. 22, no. S5, pp. A1243-A1256, 2014.

[6] **E. E. Perl**, C.-T. Lin, W. E. McMahon, D. J. Friedman, and J. E. Bowers, "Ultrabroadband & wide-angle hybrid antireflection coatings with nanostructures," *Journal of Photovoltaics,* vol. 4, no. 3, pp. 962-967, 2014.

[7] N. G. Young, **E. E. Perl,** R. M. Farrell, M. Iza, S. Keller, J. E. Bowers, S. Nakamura, S. P. DenBaars, and J. S Speck, "High-performance broadband optical coatings on InGaN/GaN solar cells for multijunction device integration," *Applied Physics Letters*, vol. 104, pp. 163902, 2014.

[8] C.-T. Lin, W. E. McMahon, J. S. Ward, J. F. Geisz, M. W. Wanlass, J. J. Carapella, W. Olavarria, **E. E. Perl**, M. Young, M. A. Steiner, R. M. France, A. E. Kibbler, A. Duda, T. E. Moriarty, D. J. Friedman, and J. E. Bowers, "Two-terminal metal-interconnected multijunction III-V solar cells," *Progress in Photovoltaics: Research and Applications,* vol. 23, no. 5, pp. 593-599, 2014.

[9] W. E. McMahon, C.-T. Lin, J. S. Ward, J. F. Geisz, M. W. Wanlass, J. J. Carapella, W. Olavarria, M. Young, M. A. Steiner, R. M. France, A. E. Kibbler, A. Duda, J. M. Olson, **E. E. Perl**, D. J. Friedman, and J. E. Bowers, "Metal pillar interconnection topology for bonded two-terminal multijunction III–V solar cells," *Journal of Photovoltaics*, vol. 3, no. 2, pp. 868-872, 2013.

[10] N. G. Toledo, D. J. Friedman, R. M. Farrell, **E. E. Perl**, C.-T. Lin, J. E. Bowers, J. S. Speck, and U. K. Mishra, "Design of integrated III-nitride/non-III-nitride tandem photovoltaic devices," *Journal of Applied Physics*, vol. 111, no. 5, pp. 054503-054503, 2012.

CONFERENCE PUBLICATIONS

[1] **E. E. Perl**, J. Simon, J. F. Geisz, W. Olavarria, M. Young, A. Duda, P. Dippo, D. J. Friedman, and M. A. Steiner, "Development of a 2.0 eV AlGaInP solar cell grown by OMVPE," in *Proc 42nd IEEE Photovoltaic Spec. Conf.*, 2015, pp. 1-6.

[2] **E. E. Perl**, W. E. McMahon, J. E. Bowers, and D. J. Friedman, "Material selection and fabrication parameters for antireflective nanostructures integrated with multijunction photovoltaics," in *Proc 40th IEEE Photovoltaic Spec. Conf.,* 2014, pp. 1174-1179.

[3] **E. E. Perl**, C.-T. Lin, W. E. McMahon, D. J. Friedman, and J. E. Bowers, "Design of ultra-broadband antireflection coatings utilizing integrated moth-eye structures for multi-junction device applications," in *Proc 39th IEEE Photovoltaic Spec. Conf.,* 2013, pp. 1902-1906.

[4] R. M. Farrell, D. J. Friedman, N. G. Young, **E. E. Perl**, N. Singh, J. R. Lang, C. J. Neufeld, M. Iza, S. C. Cruz, S. Keller, W. E. McMahon, S. Nakamura, S. P. DenBaars, U. K. Mishra, J. E. Bowers, and J. S. Speck, "InGaN-based solar cells and high-performance broadband optical coatings for ultrahigh efficiency hybrid multijunction device designs," in *CLEO: Applications and Technology,* Optical Society of America, 2013.

[5] C.-T. Lin, W. E. McMahon, J. S. Ward, J. F. Geisz, M. W. Wanlass, J. J. Carapella, W. Olavarria, M. Young, M. A. Steiner, R. M. France, A. E. Kibbler, A. Duda, J. M. Olson, **E. E. Perl**, D. J. Friedman, and J. E. Bowers, "Fabrication of two-terminal metal-interconnected multijunction III-V solar cells," in *Proc 38th IEEE Photovoltaic Spec. Conf.*, vol. 1, pp. 944-948, 2012.

[6] W. E. McMahon, C.-T. Lin, J. S. Ward, J. F. Geisz, M. W. Wanlass, J. J. Carapella, W. Olavarria, M. Young, M. A. Steiner, R. M. France, A. E. Kibbler, A. Duda, J. M. Olson, **E. E. Perl**, D. J. Friedman, and J. E. Bowers, "Metal pillar interconnection topology for bonded two-terminal multijunction III–V solar cells," in *Proc 38th IEEE Photovoltaic Spec. Conf.*, vol. 2, pp. 1-6, 2012.

[7] M. Rios, M. Riiny, **E. E. Perl**, E. Rayon, "Engineering a Brighter Sudan: bringing sustainable energy to the Theou Village School," in *2011 IEEE Global Humanitarian Technology Conference,* pp. 160-163, 2011.

[8] R. Steiner, D. Haddad, R. Liu, and **E. E. Perl**, "Upgrading the NIST electronic kilogram system," in *2010 IEEE Conference on Precision Electromagnetic Measurements (CPEM),* pp. 32-33, 2010.

Abstract

Material Science for High-Efficiency Photovoltaics: From Advanced Optical Coatings to

Cell Design for High-Temperature Applications

by

Emmett E. Perl

Solar cells based on III-V compound semiconductors are ideally suited to convert solar energy into electricity. The highest efficiency single-junction solar cells are made of gallium arsenide, and have attained an efficiency of 28.8%. Multiple III-V materials can be combined to construct multijunction solar cells, which have reached record efficiencies greater than 45% under concentration. III-V solar cells are also well suited to operate efficiently at elevated temperatures, due in large part to their high material quality. These properties make III-V solar cells an excellent choice for use in concentrator systems. Concentrator photovoltaic systems have attained module efficiencies that exceed 40%, and have the potential to reach the lowest levelized cost of electricity in sunny places like the desert southwest. Hybrid photovoltaic-thermal solar energy systems can utilize high-temperature III-V solar cells to simultaneously achieve dispatchability and a high sunlight-to-electricity efficiency. This dissertation explores material science to advance the state of III-V multijunction solar cells for use in concentrator photovoltaic and hybrid photovoltaic-thermal solar energy systems.

The first half of this dissertation describes work on advanced optical designs to improve the efficiency of multijunction solar cells. As multijunction solar cells move to configurations with four or more subcells, they utilize a larger portion of the solar spectrum.

Broadband antireflection coatings are essential to realizing efficiency gains for these state-of-the-art cells. A hybrid design consisting of antireflective nanostructures placed on top of multilayer interference-based optical coatings is developed. Antireflection coatings that utilize this hybrid approach yield unparalleled performance, minimizing reflection losses to just 0.2% on sapphire and 0.6% on gallium nitride for 300-1800nm light. Dichroic mirrors are developed for bonded 5-junction solar cells that utilize InGaN as a top junction. These designs maximize reflection of high-energy light for an InGaN top junction while minimizing reflection of low-energy light that would be absorbed by the lower four junctions. Increasing the reflectivity of high-energy photons enables a second pass of light through the InGaN cell, leading to increased absorption and a higher photocurrent. These optical designs enhanced the efficiency of a 2.65eV InGaN solar cell to a value of 3.3% under the AM0 spectrum, the highest reported efficiency for a standalone InGaN solar cell.

The second half of the dissertation describes the development of III-V solar cells for high-temperature applications. As the operating temperature of a solar cell is increased, the ideal bandgap of the top junction increases. AlGaInP solar cells with bandgaps ranging from 1.9eV to 2.2eV are developed. A 2.03eV AlGaInP solar cell is demonstrated with a bandgap-voltage offset of 440mV, the lowest of any AlGaInP solar cell reported to date. Single-junction AlGaInP, GaInP, and GaAs solar cells designed for high-temperature operation are characterized up to a temperature of 400°C. The cell properties are compared to an analytical drift-diffusion model, and we find that a fundamental increase in the intrinsic carrier concentration, n_i, dominates the temperature dependence of the dark currents, open-circuit voltage, and cell efficiency. These findings provide a valuable guide to the design of any system that requires high-temperature solar cell operation.

Contents

Chapter 1: Introduction

The transition to renewable energy will be one of the defining challenges of the 21st century. Today, more than 80% of the world's energy is supplied by three fossil fuels: oil, coal, and natural gas [1]. While easy access to these fuels has driven considerable economic growth over the last century, there is a growing urgency to move away from this paradigm as we become aware of the dangers posed by human-related climate change and the inevitable depletion of non-renewable fossil fuels. In response to these concerns, research and development into renewable energy has blossomed. Some of the most promising renewable energy resources include solar, wind, biomass, and geothermal [2]. Of these, solar is by far the most plentiful energy resource available to us. There are ~3.85 yottajoules (3.85×10^{24}) of solar energy incident on the earth each year, enough to supply our global energy needs thousands of times over [3]. The solar energy resource is stable and will not be depleted for billions of years. Simply put, the sun has the potential to provide humanity all the energy it will ever need.

Despite its potential, solar energy represents only a very small fraction of the total energy picture today. The main challenge lies in developing technologies that can convert solar energy into electricity in an efficient and cost-competitive way. While early solar technologies were far too expensive to compete with fossil fuels, the solar energy landscape has experienced a dramatic evolution over the past few decades. Cost reductions and advances in technology have helped spur significant growth, with the United States seeing a ~1500x increase in net electricity generation from solar energy between 2007 and 2015 [4]. While exponential growth has been sustained for more than two decades, there are a number of challenges that must be overcome to continue along this trajectory.

This chapter will provide a brief overview of solar energy to familiarize the reader with the field. It will start with a summary of the different types of solar energy and solar cells, describing the performance and potential of the different technologies. It will then discuss the physics behind the operation of p-n junction solar cells, and explore pathways to attaining higher efficiency. Finally, the design of high-efficiency III-V multijunction solar cells will be discussed and a preview of the dissertation will be described.

1.1 An Overview of Solar Energy Technology

Solar energy today comes in two main forms: photovoltaics and concentrated solar power (CSP). Photovoltaics use semiconducting materials to convert photons to electricity, making it the only mainstream energy source that does not operate by powering a generator. Cell prices have fallen considerably to about 30¢ per watt in 2016, enabling photovoltaics to achieve grid parity in many locations [5-7]. Lowering costs have driven exponential growth for more than two decades, with the cumulative capacity of photovoltaics increasing from 77 megawatts in 1996 to over 200 gigawatts in 2016, more than a 1500x increase [8]. While photovoltaics have realized tremendous growth over the past few decades, they are fundamentally intermittent and without cost-effective energy storage this will lead to a significant reduction in their marginal value at high penetrations [6,9,10]. CSP systems operate very differently. These systems use mirrors to concentrate sunlight onto a central receiver where photons are converted to thermal energy. This thermal energy is used to heat a working fluid that then powers a conventional generator [11,12]. These systems have the ability to cost-effectively store thermal energy, allowing them to continue producing power when the sun is not shining. The main disadvantage to CSP systems is that they are more

expensive than photovoltaics [6]. Today, CSP has an installed capacity of just over four gigawatts [11].

Photovoltaics

Photovoltaics can be classified into four main categories: traditional silicon photovoltaics, low-cost thin-film photovoltaics, high-efficiency multijunction photovoltaics, and emerging technologies. Figure 1.1 shows a plot of the best research-cell efficiencies for each of these categories from 1974 to 2016. While this plot gives an excellent snapshot for how the efficiency of each technology has progressed over the years, it is important to note that it does not show other factors that can impact the potential marketability of each technology. Some important considerations that are not shown in this plot include cell stability, manufacturing costs, and material abundance [13,14].
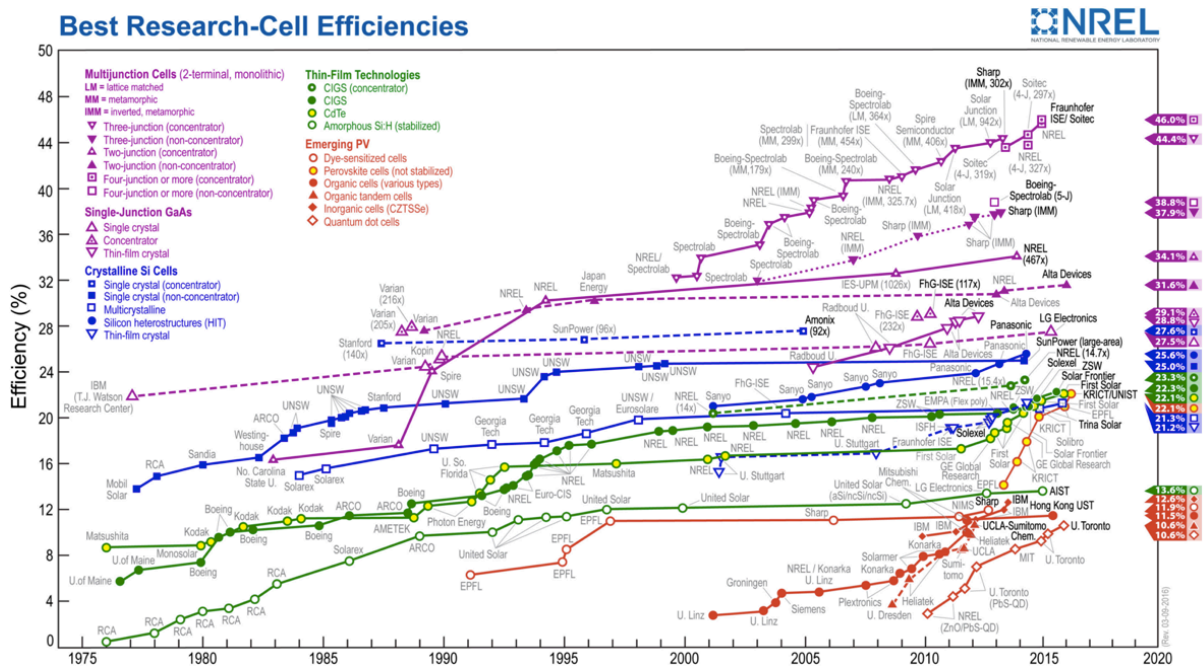
Figure 1.1: Best research-cell efficiencies for the four classes of photovoltaic technologies: multijunction cells (purple), crystalline silicon cells (blue), thin-film technologies (green), and emerging photovoltaics (red) [13].[1]

---

[1] This plot is courtesy of the National Renewable Energy Laboratory, Golden, CO.

Silicon is the most established technology and accounts for over 90% of the photovoltaics market today [15]. The best single-crystal silicon solar cells have achieved efficiencies higher than 25% and the best multicrystalline solar cells have achieved efficiencies above 21% [13,14]. Silicon solar cells are extremely stable and can last for 30 years or longer [16]. While the cost of silicon solar cells has historically been too high to compete with fossil fuels, their price has declined dramatically over the last decade. Figure 1.2 tracks the cost of silicon modules since the late 1970s when the technology was first commercialized.
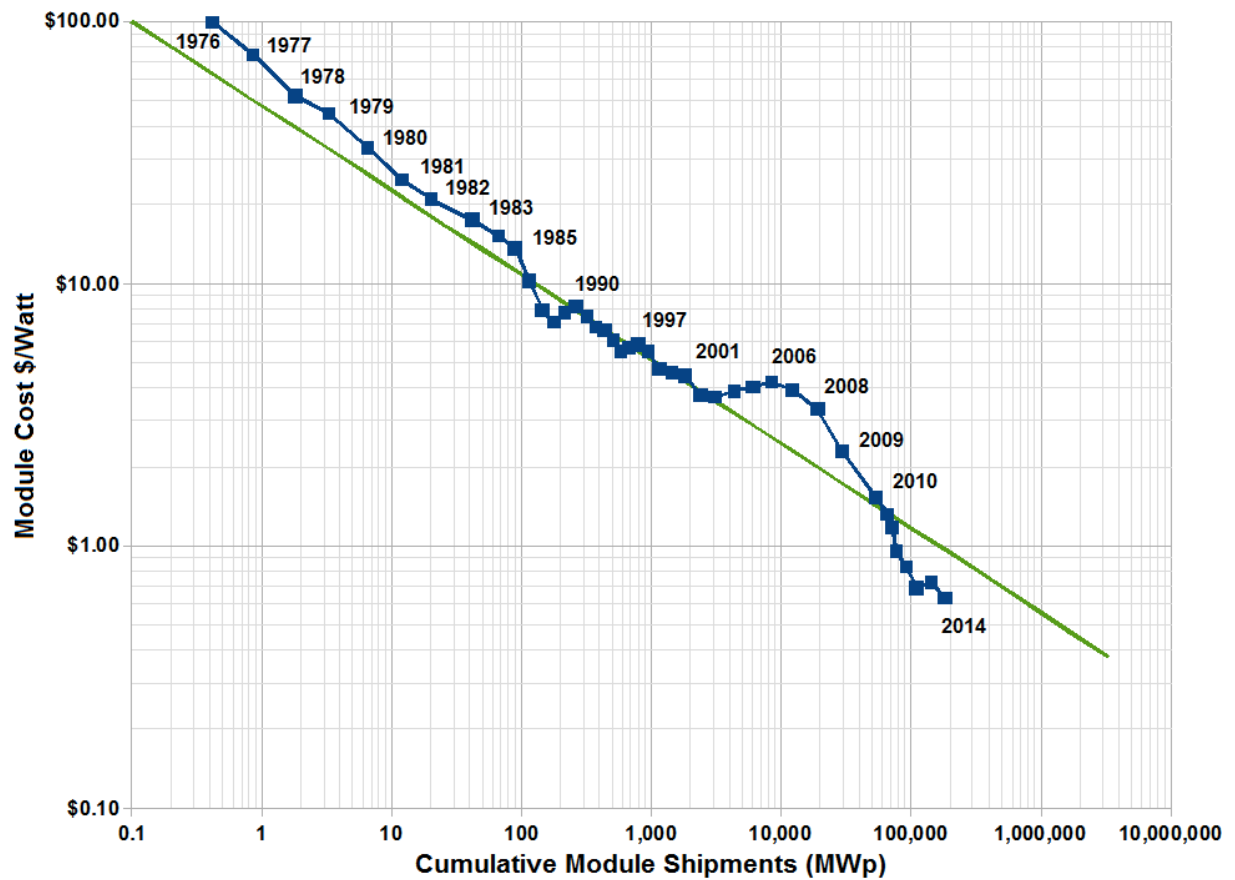
Figure 1.2: Price history of silicon photovoltaic cells showing a 100x reduction in cost since the late 1970s. Silicon module costs are now well below the dollar/watt threshold, enabling grid parity in many locations [8].[2]

---

[2] Plotted using data from [8]

Over the past 40 years, the price of silicon solar cells has dropped more than a hundredfold. Another dramatic price reduction occurred from 2008 to 2014, bringing module prices to well under a dollar per watt. These low costs have driven tremendous growth and today there are more than 200 gigawatts of silicon photovoltaics deployed worldwide. Silicon is also an earth-abundant element, suggesting that there are no fundamental barriers to continued growth [16].

Thin-film photovoltaics are the second most established photovoltaic technology and account for roughly 7% of the photovoltaics market today [15]. Thin-film technologies include solar cells made from cadmium telluride (CdTe), copper indium gallium selenide (CIGS), and amorphous silicon. Traditionally, these technologies have been categorized as having a lower cost than silicon, however, at a lower efficiency. While CIGS and CdTe have typically trailed silicon efficiencies by 5-10% absolute, the past five years have seen rapid advances. Today, both of these technologies have reached efficiencies greater than 22%, only slightly lower than the best silicon solar cells [13,14]. One major downside to CIGS is that it requires indium, an element that is too rare to sustain significant growth [17]. One major downside to CdTe is that both cadmium and tellurium are toxic. Nonetheless, First Solar has grown into one of the world's biggest photovoltaic companies with their CdTe solar cells [18].

Multijunction solar cells based on III-V compound semiconductors have had the highest efficiency of any photovoltaic technology for more than two decades [13,14]. The efficiency of multijunction solar cells have been improving at a rate of roughly 1% per year for more than 15 years and today the world record efficiency is 46.0% under concentrated sunlight. III-V solar cells are the only technology that outperforms silicon, giving them a significant

advantage where high-efficiency and high-performance is required. Most notably, III-V multijunction solar cells comprise 100% of the market for space solar cells today [19]. Unfortunately, their high-cost prevents them from being competitive for one-sun applications in the terrestrial market. For this reason, concentrator systems are required to offset the material cost of multijunction solar cells. Concentrator photovoltaic systems use concentrating optics to focus sunlight onto highly efficient solar cells and require significantly less semiconductor material since the cell area scales inversely with the concentration factor. Today, there are more than 300 megawatts of concentrator photovoltaic systems deployed. Concentrator photovoltaics have attained module efficiencies that exceed 40% and have the potential to reach the lowest levelized cost of electricity in sunny places like the desert southwest [20-23].

Emerging technologies are classified as photovoltaic devices that use new materials that are still in an early stage of research and development [24,25]. Some of these technologies include organic photovoltaics, perovskites, and quantum dot solar cells [13]. One of the key attractions to these materials is that they can be produced at a very low cost, in principle. For example, organic photovoltaics are solution processable and could be manufactured using high-throughput roll-to-roll printing methods [26]. However, one of the major disadvantages to organic photovoltaics and other emerging technologies is that they have low efficiencies, typically converting less than 15% of incoming sunlight into electrical power. The one exception is perovskites, which have already achieved a power conversion efficiency of 22.1% less than three years after they were first used as a solar material [13,14]. For this reason, they have received tremendous attention from the public and from the scientific community. While perovskites deteriorate far too quickly to be commercialized today [27],

substantial improvements to their long-term reliability could enable perovskites to significantly disrupt the solar energy landscape [14].

Challenges with Integrating Photovoltaics into the Grid

While nearly every photovoltaic technology has seen tremendous progress over the past few decades, the common weakness is that photovoltaics are inherently intermittent. This manifests itself in two ways. First, there can be short-term interruptions in electricity on a time-scale of seconds to minutes. For example, on a cloudy day the power output of a photovoltaic array would dip each time a cloud blocks out the sun. Second, the sun only shines during the day. The electrical grid, on the other hand, requires a stable and on-demand source of electricity [6,9].

Figure 1.3 shows the simulated dispatch of electricity for California on a spring and summer day as the penetration of photovoltaics increases from 0% to 10% [9,10]. This is a manifestation of the famous "duck chart" and illustrates one of the major difficulties of integrating a large quantity of photovoltaics into the grid.

(a) Summer Day   **(b) Spring Day**
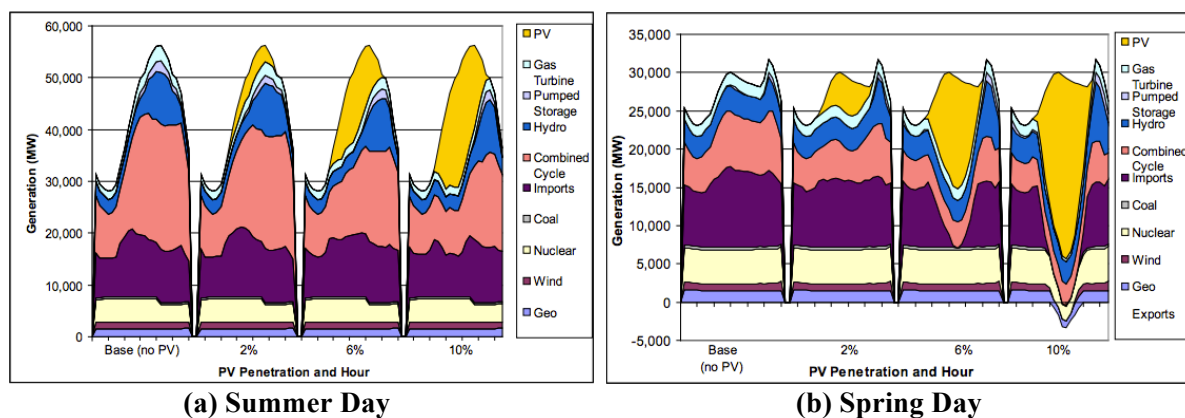
Figure 1.3: Plot showing the simulated dispatch of electricity for California on a (a) summer day and (b) spring day [10].

The first thing to note is that at low penetrations, photovoltaics generate power during peak demand. This means that photovoltaics will have a premium value at low penetrations

7

because they can "shave the peak". Notice in Figure 1.3(a) how the peak demand for non-photovoltaic energy shifts downward and to the right as the penetration of photovoltaics is increased from 0% to 10%. This peak shaving can reduce the need for expensive peaker power plants, thereby giving photovoltaics a premium value at low penetrations. However, as the penetration of photovoltaics increases, its value starts to decline. This is particularly evident at high penetrations, where photovoltaics can provide more electricity than the grid can handle. One example of this is shown in Figure 1.3(b). When photovoltaic penetration reaches 10% on a spring day, as is shown on the far right curve, supply can outpace demand and a significant portion of the generated photovoltaic energy must be thrown away. In this scenario, the value of adding photovoltaic capacity is clearly diminished [10]. Figure 1.4 shows the results from a study on how the marginal economic value of adding photovoltaic generation decreases as the penetration of photovoltaics is increased [9,28].
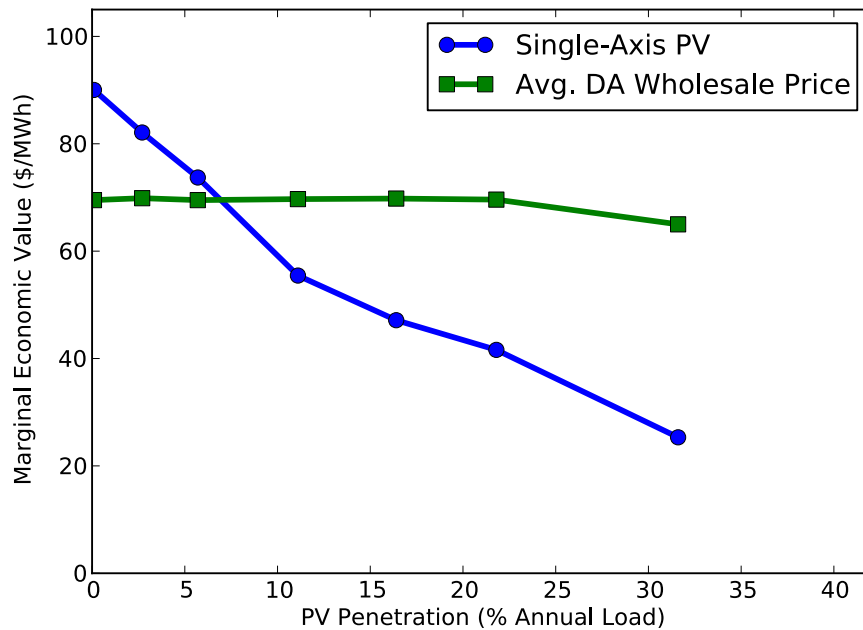
Figure 1.4: Plot showing the marginal economic value of photovoltaic energy as a function of the penetration of photovoltaics [28].[3]

[3] Reproduced with permission from [28]. Copyright © 2013, IEEE.

Note that at low penetrations photovoltaic energy has a value that is higher than the wholesale price of electricity. As penetration increases, however, the marginal economic value of photovoltaic energy drops rapidly. This particular study shows that the marginal economic value of photovoltaic energy will go down by ~4x as the penetration increases from 0% to 30%. Adding energy storage capacity to the grid could significantly change these numbers; and while energy storage technologies exist, they are not cost effective today and would significantly raise the system cost of a photovoltaic installation [6]. The main takeaway from this discussion is that the penetration of photovoltaics will ultimately be limited without breakthroughs in energy storage technology.

Concentrated Solar Power (CSP)

CSP systems operate by using mirrors or lenses to focus sunlight onto an absorber where photons are converted into thermal energy. This thermal energy is transferred to a working fluid, which is used to drive a conventional generator that can supply electricity to the grid on demand [6,12,20]. The big advantage of CSP over photovoltaics is that CSP has the ability to cost-effectively store thermal energy that can be dispatched when the sun is not shining. This enables CSP systems to be a much more steady source of electricity than photovoltaics and even makes it possible for them to generate power in the evening or at night. The primary disadvantage of CSP is that system complexity makes it more expensive than photovoltaics. In sunny areas, CSP plants produce power at a rate of 15-20¢/kWh, which is not yet cost-competitive with other energy sources. CSP has a global installed capacity of less than 5 gigawatts, which is 2-3% of the capacity of photovoltaics today.

Figure 1.5 shows the most common types of CSP technologies. Trough systems are by far the most common technology, accounting for more than 90% of installed CSP systems.

In recent years, however, solar power towers have seen significant growth. The world's largest CSP plant, Ivanpah, is a 392-megawatt power tower plant that was commissioned in 2014 [12].
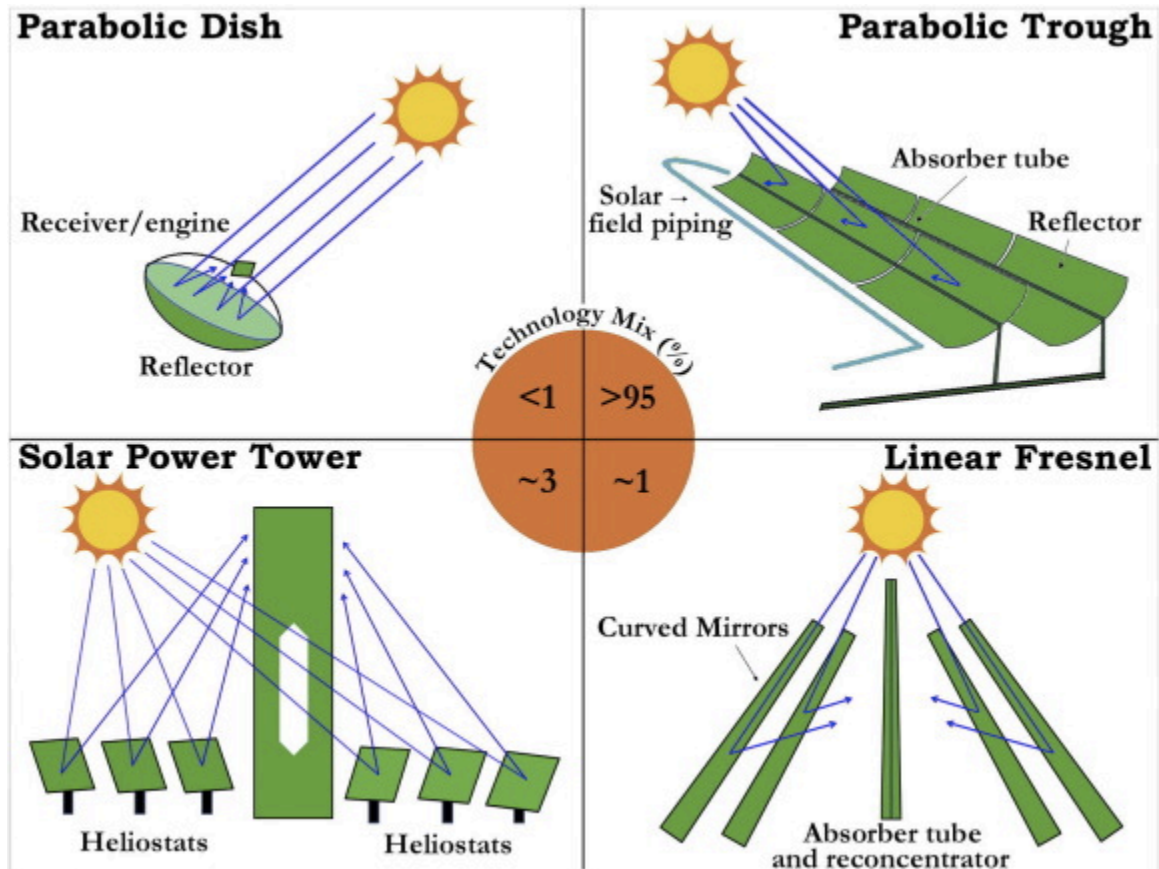
Figure 1.5: Diagram showing various concentrating solar power technologies along with their installed ratios as of 2015 [12].[4]

Hybrid Photovoltaic-Thermal (PV-T) Solar Collectors

Hybrid systems have been proposed that combine photovoltaics with CSP to realize the benefits of both technologies [6,29,30]. While sunlight remains the only input for a hybrid design, these systems will have two outputs. First, the photovoltaic device will produce electricity at a lower cost than what is currently possible with a CSP system alone. However,

---

[4] Reproduced with permission from [12].

this electricity will be intermittent and will have a low dispatchability. Second, the CSP system will generate thermal energy that can be converted into highly dispatchable electricity. While this electricity can be dispatched to the grid on demand, it will come at a higher cost than what is currently possible with photovoltaics [6]. Figure 1.6 shows a schematic comparing the cost and dispatchability of photovoltaics and CSP, and envisions a hybrid photovoltaic-thermal (PV-T) system that can provide electricity to the grid at a low cost and a high dispatchability.
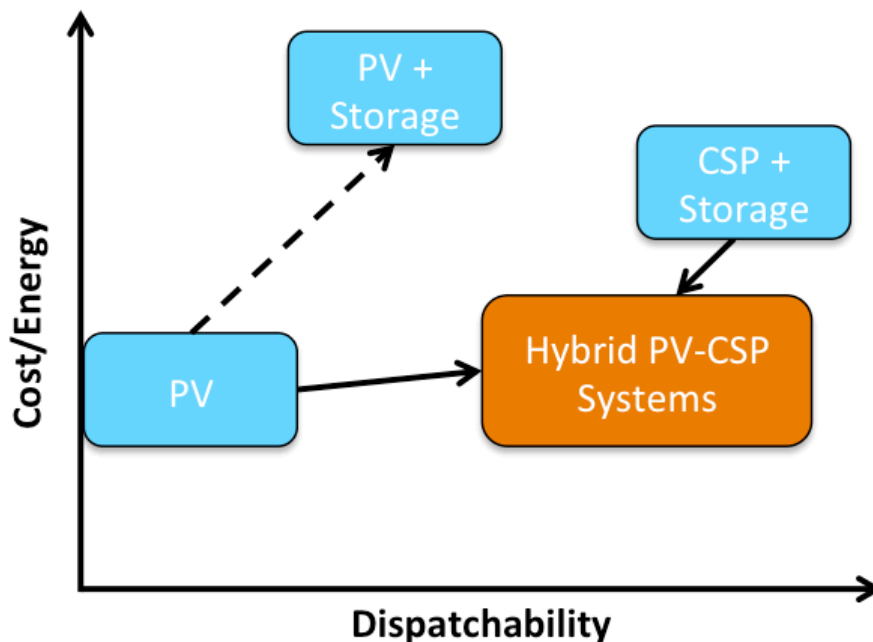
Figure 1.6: Schematic showing the cost and dispatchability of photovoltaic (PV) and CSP systems. The aim of a hybrid photovoltaic-thermal (PV-T) solar collector would be to simultaneously achieve high dispatchability and a low cost.

One family of proposed designs, shown on the left in Figure 1.7, uses advanced optical filters to laterally split the solar spectrum, guiding high-energy light to a photovoltaic cell while sending low-energy light to a thermal receiver. This type of system exploits the strengths of each part of the spectrum: photovoltaics can convert high-energy photons to

electricity at very high efficiencies while CSP systems are better suited to convert low-energy photons to useable energy. One potential disadvantage to a spectrum splitting design is that the use of advanced optics can add complexity and increase the cost of the system [6].
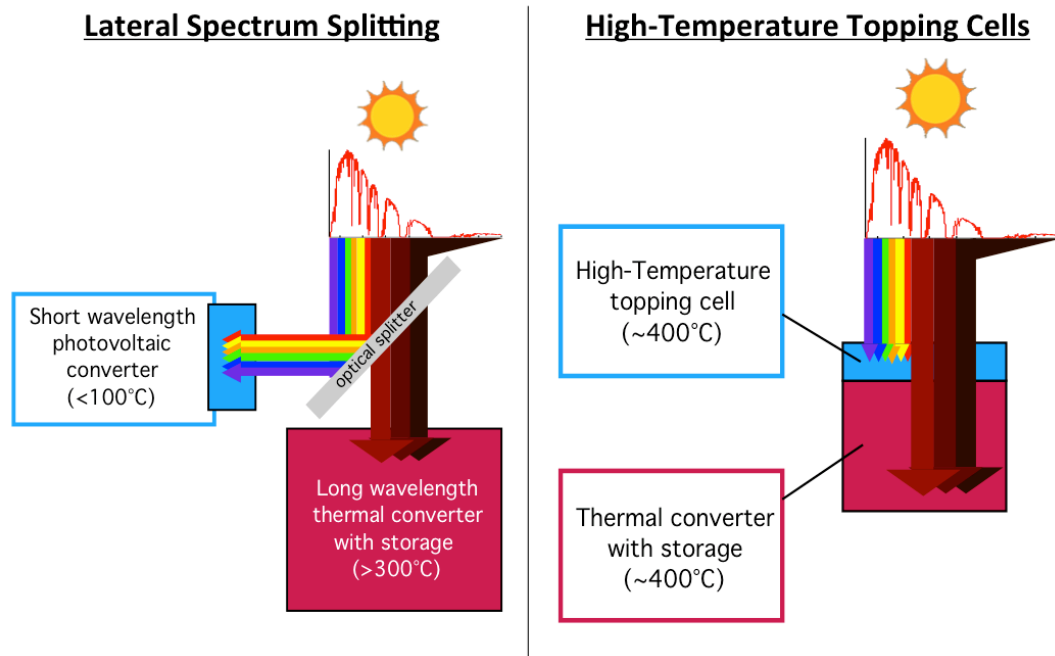
Figure 1.7: Two potential manifestations of a hybrid photovoltaic-thermal (PV-T) solar collector. The design on the left uses optical elements to laterally split the solar spectrum while the design on the right utilizes a high-temperature topping cell that is operated at temperatures around 400°C.[5]

Another concept, shown on the right of Figure 1.7, utilizes a photovoltaic topping device that is operated at high temperatures. While increasing the operating temperature of a photovoltaic device will lead to a fundamental drop in its efficiency, the associated energy losses are primarily converted into heat within the cell. A hybrid solar converter could transfer this heat to a thermal collector that could then provide storage and dispatchable energy to the electrical grid using a conventional generator. One of the main challenges for realizing this proposed design is related to the development of a photovoltaic cell that can operate efficiently and reliably at high temperatures up to ~400°C [6].

---

[5] Courtesy of M. A. Steiner.

1.2 The Solar Spectrum

It is important to understand the solar spectrum in order to appreciate the challenges inherent to designing photovoltaic cells and improving their efficiencies. The sun is a broadband emitter that acts as a nearly ideal blackbody source with a temperature of ~5800K. This corresponds to a spectrum that peaks in the visible range between 400nm and 700nm and falls off rapidly at shorter and longer wavelengths. At the top of the atmosphere, the power density is 1366W/m^2, but as light travels through earth's atmosphere various absorption and scattering mechanisms act to attenuate the solar spectrum [31]. This attenuation is quantified using the Air Mass (AM) coefficient, which is defined by:

$$AM = \frac{L}{L_0} = \frac{1}{\cos(\theta)}$$ (1.1)

Where L is the distance that light travels through the atmosphere at the location of interest, L_o is the distance light travels through the atmosphere at the equator, and θ is the angle of the sun in the sky. AM0 corresponds to the solar spectrum in space, AM1 corresponds to the solar spectrum at the equator, and AM1.5 corresponds to the solar spectrum at a latitude of 48.2°. The increasing Air Mass for high values of θ suggests that the attenuation of sunlight in the atmosphere will vary significantly depending on the latitude. The spectrum will also change with location if the makeup of the atmosphere is different in the two places. For example, a humid climate will have more water vapor in the atmosphere than a dry climate, and thus the atmosphere in a humid location will transmit less light [32].

While there is a significant temporal and spatial variation in the composition of the atmosphere and solar spectrum, it is important to maintain a standard spectrum for testing purposes so that an apples to apples comparison can be made between different solar

13

technologies. The ASTM G173 standard is currently used to define cell efficiencies [33,34].

Figure 1.8 shows the three standard reference spectra.
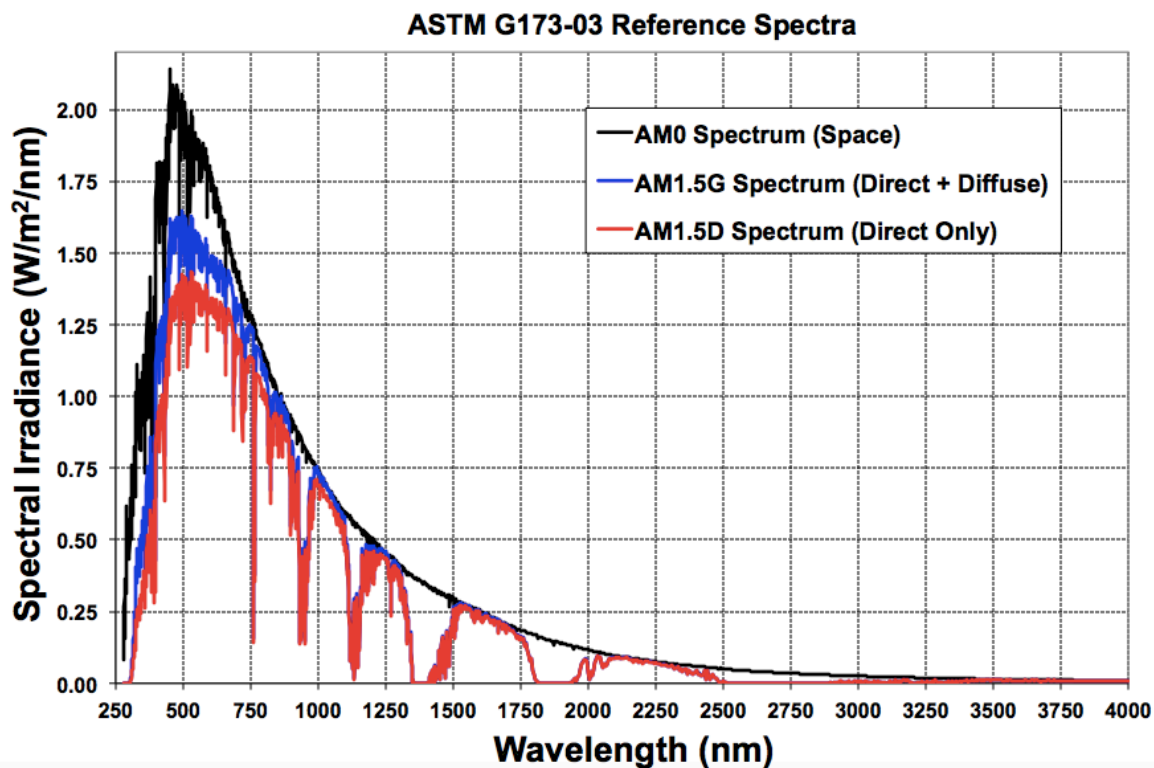
Figure 1.8: The ASTM G173 Standard Reference Spectra for (black) the AM0 spectrum, (blue) the AM1.5G spectrum, and (red) the AM1.5D spectrum.[6]

For standardized measurements, a power density of $1000 W/m^2$ is used for both the AM1.5G and AM1.5D spectra. The AM1.5G spectrum includes both direct and diffuse sunlight while the AM1.5D spectrum includes direct sunlight only. The higher intensity of short-wavelength light in the AM1.5G spectrum is a result of Rayleigh scattering, which acts to diffuse high-energy sunlight (also the reason why the sky is blue). The dips in the terrestrial spectra can be attributed to absorption of sunlight by various atmospheric gases. Figure 1.9 shows the wavelength dependent contributions to absorption and scattering in the atmosphere for both downgoing solar radiation and upgoing thermal radiation.

---

[6] Plotted using data from [29]

Radiation Transmitted by the Atmosphere
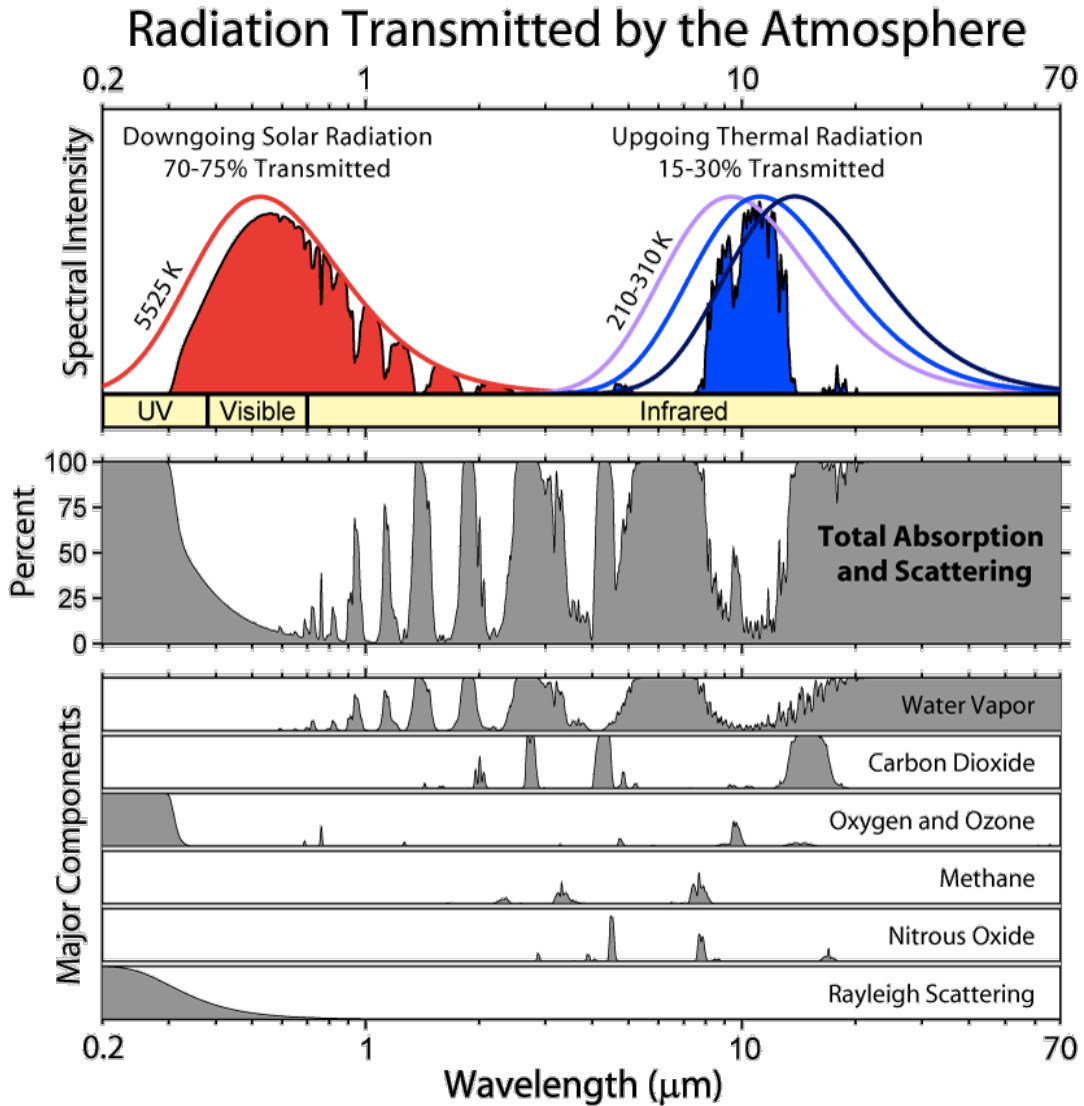
Figure 1.9: Downgoing (red) and upgoing (blue) radiation transmitted by the atmosphere. Spectra for various greenhouse gases as well as Rayleigh scattering are also shown in grey [35].[7]

This shows that the absorption bands in the terrestrial spectra can be largely attributed to water vapor, and that the attenuation of short-wavelength light is primarily a result of Rayleigh scattering and ozone absorption (illustrating the importance of the Ozone layer for blocking out damaging UV radiation).

---

[7] Reproduced with permission from Robert A. Rohde from the Global Warming Art project. https://commons.wikimedia.org/wiki/File:Atmospheric_Transmission.png

While this figure helps illustrate why the solar spectrum looks like it does, it also helps explain the link between global warming and carbon dioxide. Like the sun, the earth also acts as a blackbody radiator. However, the temperature of the earth's surface is much lower than the sun and thus it emits light at much longer wavelengths, as is shown in the purple, blue, and black curves in Figure 1.9. While carbon dioxide absorbs very little downgoing solar radiation, it will absorb a significant fraction of upgoing thermal radiation from the earth. As more carbon dioxide is added to the atmosphere, the transmission of upgoing thermal radiation will decrease while the transmission of downgoing solar radiation will remain largely unchanged [36]. This will create a new equilibrium that necessitates higher temperatures on earth in order to equalize the energy of upgoing and downgoing radiation.

1.3 The Physics of Solar Cells

In its most basic form, a solar cell is a device that converts solar energy into electrical energy [37]. This process is also known as the photovoltaic effect, and requires three things. First, it requires a material that absorbs photons from the sun and converts them into electron-hole pairs. Second, it requires a mechanism to spatially separate the negatively charged electrons and the positively charged holes. This charge separation necessitates an electric field in the material, which can be set up using either a heterojunction (this is the configuration used by organic photovoltaics and quantum dot photovoltaics) or a p-n junction (this is the configuration used by most other photovoltaic technologies). Finally, charge carriers must be extracted to an external circuit where a combination of current and voltage can generate electrical power [11,24,25,37]. Since the vast majority of solar cells use p-n junctions as the mechanism for charge separation, I will focus on the operation of these solar cells.

Electrical Properties of a P-N Junction

A semiconductor is characterized as a material that has a bandgap (E_G), which is an energy range where no electronic states exist. A p-n junction is formed when a p-type semiconductor (doped with electron acceptors causing the Fermi level to be near the valence band) and an n-type semiconductor (doped with electron donors causing the Fermi level to be near the conduction band) are placed in contact. In open-circuit conditions, where there is no outside current, the Fermi level (E_F) is flat and the conduction band (E_C) and valence band (E_V) must align accordingly. This causes a curvature in the band diagram as is shown in Figure 1.10 [38].
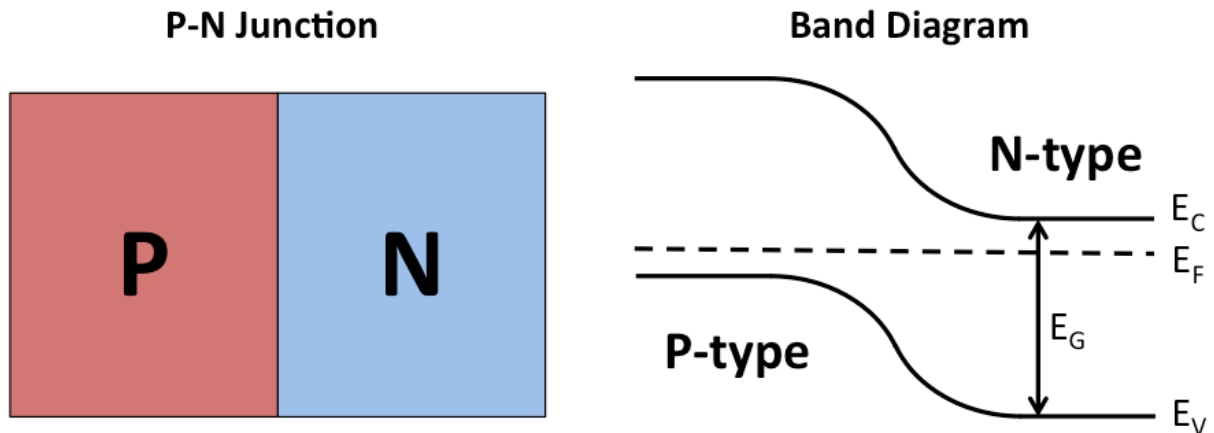
Figure 1.10: Band diagram of a p-n junction in equilibrium with no applied voltage bias.

The slope in the band diagram in this figure corresponds to an electric field pointing from right to left. This electric field will cause negatively charged electrons to move from left to right (downhill) and positively charged holes to move from right to left (uphill). Herein lies the mechanism for charge separation [38].

If a forward voltage (positive voltage applied to the p-type side) is applied, the energy barrier between the n-type and p-type materials will get smaller. This makes it possible for

many majority electrons from the n-type side to thermally surmount the barrier and inject themselves into the p-type side. Similarly, many majority holes from the p-type side will be able to thermally surmount the barrier and inject themselves into the n-type side. This injection of charge amounts to a current from the p-type side to the n-type side [38].

If, on the other hand, a negative voltage is applied, the barrier will get larger and the injection current can be essentially eliminated. When this is the case, a small negative current will remain that is created by thermally excited minority carriers from each side diffusing to the junction. The current-voltage characteristics of a p-n junction can often be described by a two-diode equation:

$$I = I_{01}\left(e^{qV/kT} - 1\right) + I_{02}\left(e^{qV/2kT} - 1\right) \tag{1.2}$$

Where I is the current, I_{01} is the n=1 dark current, I_{02} is the n=2 dark current, q is elementary charge, V is the applied voltage, k is the Boltzmann constant, and T is the temperature in degrees Kelvin. This equation does not take into account series or shunt resistances, however it is straightforward to add terms to this equation to account for these. A more detailed introduction to p-n junctions and a more complete derivation of the diode equation can be found in many textbooks [38-40].

The I-V characteristics from one of the III-V solar cells detailed later in this thesis are shown with both a log and linear scale in Figure 1.11. The dashed lines on the log plot indicate the slopes of ideal diodes with ideality factors of 1 and 2, where the y-intercepts are equal to J_{01} for the n=1 line and J_{02} for the n=2 line. Here, J refers to the current density, which is equal to the current divided by the cell area. Also note that the curves deviate from the n=1 line at high currents due to series resistance. Dark I-V curves like these are one invaluable method to characterize the performance of solar cells.
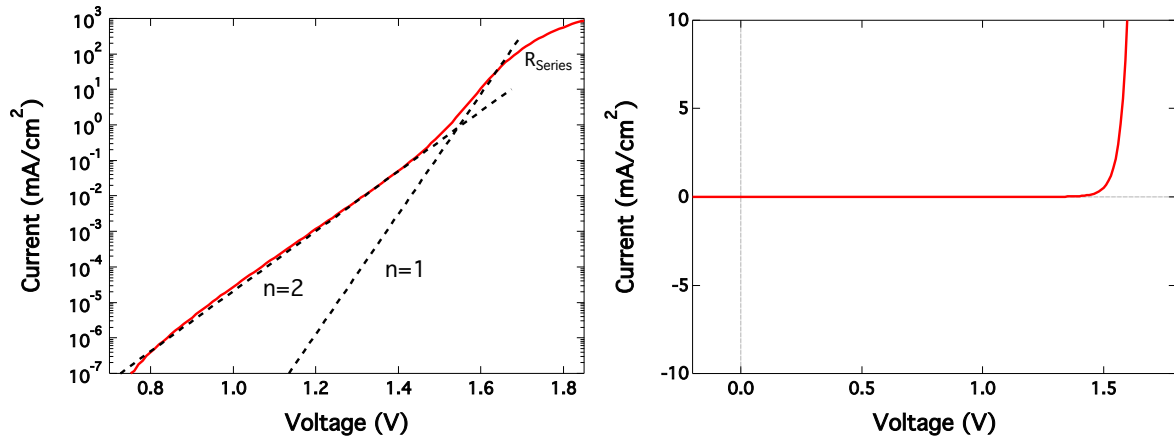
Figure 1.11: Example of the dark I-V curve for a 2.0eV AlGaInP solar cell in the dark shown in both a linear and a log scale.

Properties of an Illuminated P-N Junction

Photons with an energy that is higher than the bandgap can be absorbed in the semiconductor, and when this happens, an electron-hole pair is created. If the photon gets absorbed on the n-type side, a majority electron and minority hole will be created. If, on the other hand, a photon is absorbed on the p-type side, a majority hole and minority electron will be created. The generated majority carrier will be unable to diffuse to the other side of the junction because there is a large energy barrier preventing it from doing so. However, if the generated minority carrier diffuses to the junction it can be swept to the other side by the electric field. This leads to a separation of charge that can be translated to a current and voltage [24,25,37,38].

When sunlight is absorbed, there is typically a large change in the minority carrier concentration but only a small change in the majority carrier concentration. This has the effect of splitting the quasi-Fermi levels, E_{FN} and E_{FP}. This splitting results in a gradient in the quasi-Fermi levels at short-circuit conditions, indicating that current is flowing in the device. Figure 1.12 shows the band diagram of an illuminated p-n junction with no applied

19

voltage bias. If the minority carrier, in this case an electron, can diffuse to the junction before recombining, it will contribute to photocurrent [24,25,37,38].
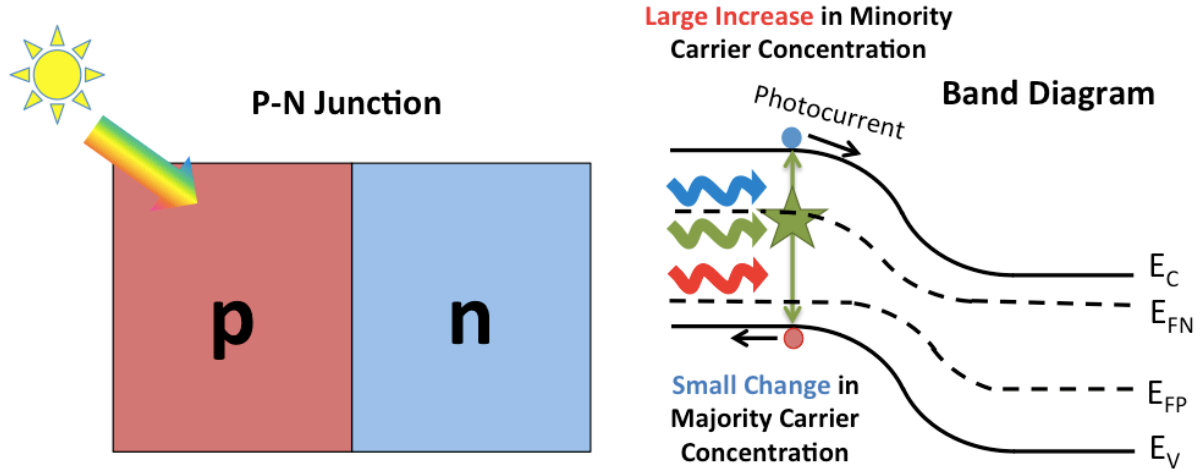
Figure 1.12: Band diagram of an illuminated p-n junction with no applied voltage bias. If the photogenerated electron (blue circle) can diffuse to the junction before recombining then it will contribute to photocurrent.

The wavelength-dependent quantum efficiency is an important metric to evaluate the likelihood of a photogenerated minority carrier being collected by the junction before recombining. The external quantum efficiency (EQE) is defined as: [41]

$$EQE = \frac{N_e}{N_v} \tag{1.3}$$

Where N_e is the number of minority carriers collected and N_v is the number of photons incident on the solar cell. Another important quantity is the internal quantum efficiency (IQE), which is the number of minority carriers collected divided by the number of photons that make it into the semiconductor (i.e. the number of photons that are not reflected at the front surface). The IQE can be related to the EQE using the following equation: [41]

$$IQE = \frac{EQE}{1-R} \tag{1.4}$$

A high-quality material can have an IQE close to 1. However, if the minority carrier diffusion length is short, then a significant number of these minority carriers will recombine before reaching the junction, and thus will not be collected. Figure 1.13 shows an example of the IQE of one of the III-V solar cells detailed later in this thesis.
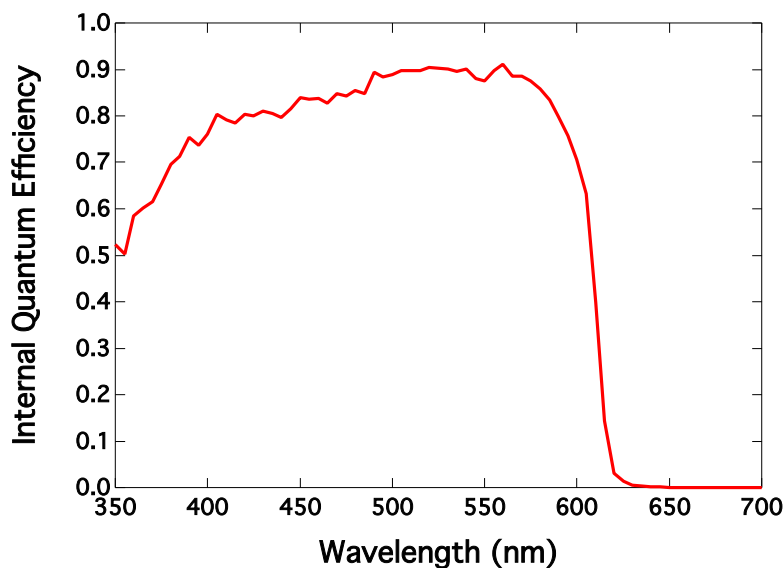
Figure 1.13: Example of the IQE curve for a 2.0eV AlGaInP solar cell.

In this figure, the reduced IQE at short wavelengths can be largely attributed to absorption in the $AlInP_2$ window layer, which is used to passivate the front surface of the solar cell. It is very difficult to reduce these short-wavelength IQE losses for real-world solar cells. The IQE also drops to zero at long wavelengths because sub-bandgap photons will not be absorbed by the solar cell.

When a p-n junction is illuminated, the diode equation must be modified to include a photogenerated current, I_L:

$$I = I_{01}\left(e^{qV/kT} - 1\right) + I_{02}\left(e^{qV/2kT} - 1\right) - I_L \qquad (1.5)$$

The added I_L term has the effect of shifting the I-V curve downwards by the photocurrent, moving a significant part of the I-V curve into the power generating 4th quadrant of the

21

graph. Figure 1.14 shows an example light I-V curve of one of the III-V solar cells detailed later in this thesis.
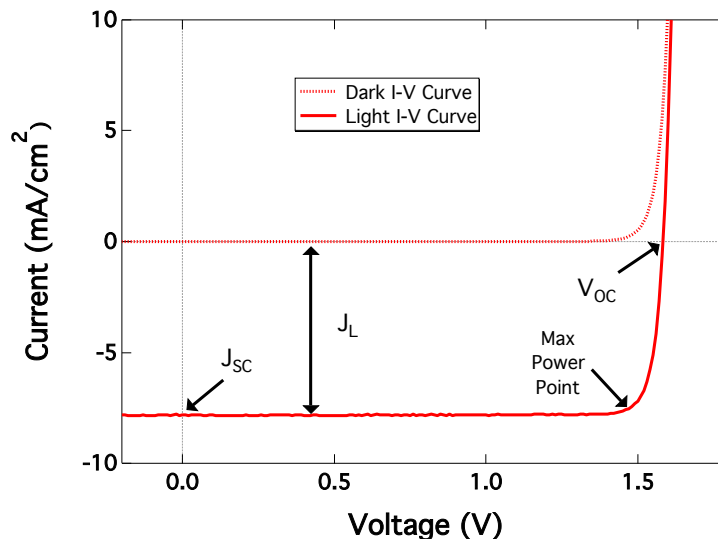
Figure 1.14: Example of the light (solid line) and dark (dashed line) I-V curve for a 2.0eV AlGaInP solar cell shown on a linear scale.

There are a few important quantities that can be extracted from the light I-V curve. The first is the open-circuit voltage, or V_{OC}. This is the voltage that will be measured across the solar cell when there is no current flowing. The diode equation showed earlier can be used to solve for V_{OC} by setting the current to zero. If the solar cell is in the n=1 region of the I-V curve, the V_{OC} can be approximated with the following equation:

$$V_{OC} = \frac{kT}{q} \ln\left(\frac{I_L}{I_{01}} + 1\right) \tag{1.6}$$

If the solar cell is in the n=2 region of the I-V curve, the V_{OC} can be approximated using this equation:

$$V_{OC} = \frac{2kT}{q} \ln\left(\frac{I_L}{I_{02}} + 1\right) \tag{1.7}$$

A second important quantity is the short circuit current, I_{SC}. This is the current that will flow through a zero-resistance external circuit when connected to the solar cell. Note that no

22

power is generated at V_{OC} and I_{SC} since power requires there to be both a voltage and a current. The max power point is the point on the I-V curve corresponding to maximum power generation, which occurs when the product of current and voltage is maximized. In the real world, it is important to operate a solar cell at or near its max power point. For this reason, it is common for solar arrays to include electronics that can track the maximum power point [42].

The fill factor (*FF*) is defined by the following equation, where I_{MP} and V_{MP} are the current and voltage at the max power point:

$$FF = \frac{V_{MP}I_{MP}}{V_{OC}I_{SC}}$$
(1.8)

A good solar cell can have a *FF* of 80-90% at 1 sun. A low *FF* is often indicative of either a high series resistance or a low shunt resistance in the cell, and will often get worse at high concentrations when series resistance is more problematic. The efficiency of a solar cell can be calculated by dividing the maximum electrical output power, $V_{MP}*I_{MP}$, by the incoming light power. The maximum electrical power can also be quantified as the product of $V_{OC}*I_{SC}*FF$ [24,25,37-40].

Fundamental Efficiency Losses in Photovoltaics

In 1961, Shockley and Queisser calculated the fundamental conversion efficiency limit of a single-junction solar cell in what is considered one of the most important papers in the field of photovoltaics [43,44]. The Shockley-Queisser limit is highly dependent on the bandgap of the solar cell, and peaks at an efficiency of ~31% for a device with a bandgap around 1.3eV. The derivation for the Shockley-Queisser limit explores and quantifies the fundamental loss mechanisms for a p-n junction photovoltaic device. Some important assumptions in the model include (1) only a single electron-hole pair can be generated for

each photon with an energy higher than the semiconductor bandgap, (2) carriers can only be extracted at the bandgap energy, and (3) no carriers can be generated from low-energy photons with an energy less than the bandgap of the material.

The two most dominant losses are sub-bandgap loss and thermalization loss. Sub-bandgap loss occurs when photons with energy below the semiconductor bandgap are transmitted, and thus their energy is not used. This leads to a drop in the photocurrent of the solar cell. Thermalization loss occurs when photons with energy higher than the bandgap of the semiconductor are absorbed. When this happens, an electron-hole pair is created with an energy separation equal to the energy of the incident photon. However, almost instantaneously, the carriers relax down to the band edge and the energy losses are converted into heat within the semiconductor [37]. This leads to a drop in the voltage of the solar cell [43,44]. Figure 1.15 illustrates these two losses, where the red arrow represents low-energy light and the blue arrow represents high-energy light.
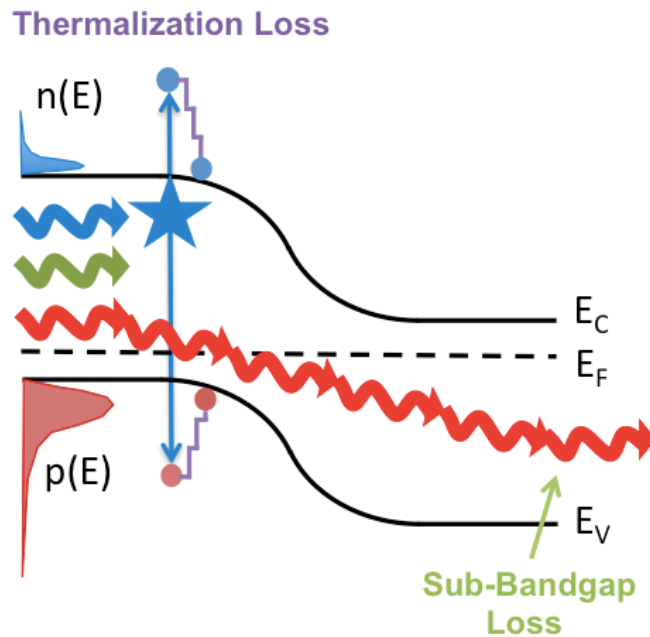
Figure 1.15: Illustration showing the mechanism for sub-bandgap loss and thermalization loss in a single-junction solar cell.

Another major source of loss is the etendue loss, which can be thought of as the expansion of photon modes in a solar cell that lead to an increase in entropy [43,44]. Etendue loss occurs because the solid angle subtended by the sun is very small (only 6.87×10^{-5} steradians or 0.00055% of the celestial sphere), whereas a solar cell can in theory emit light in all directions. Concentrating sunlight can reduce etendue loss by effectively increasing the solid angle of the sun, and will increase in the Shockley-Queisser limit to ~44% [37].

There are a number of smaller efficiency losses, including fill factor loss, Fermi level loss, and electron kinetic loss that are described in more detail elsewhere. Figure 1.16 shows the maximum achievable efficiency and the effect of different loss processes as a function of the cell bandgap.
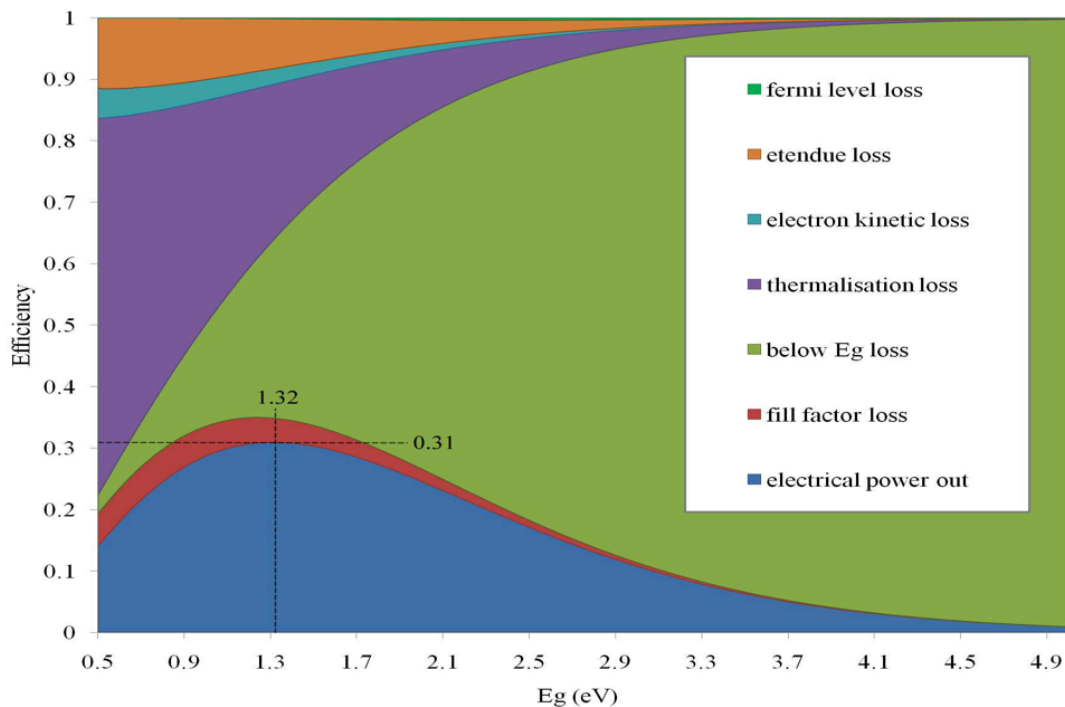
Figure 1.16: Plot illustrating the bandgap dependence of the fundamental loss mechanisms for a single-junction solar cell as a function of bandgap [44].[8]

This plot shows that the maximum achievable efficiency for a single-junction photovoltaic device is ~31% for a cell with a bandgap of 1.32eV. This plot also illustrates how sub-bandgap and thermalization loss will represent the two dominant mechanisms that fundamentally limit the cell efficiency.

1.4 Multijunction Photovoltaic Devices

For more than two decades, multijunction solar cells have achieved the highest efficiencies of any photovoltaic technology. Today, the world-record stands at 38.8% for a five-junction solar cell at a concentration of one-sun and 46.0% for a four-junction solar cell at a concentration of 508 suns [13,14]. These higher efficiencies come about by reducing the three largest fundamental efficiency losses for a photovoltaic device: thermalization loss, sub-bandgap loss, and etendue loss. This section will discuss current state-of-the-art multijunction photovoltaic devices and the prospects for future efficiency gains.

Improved Efficiencies using High-Concentration and Multiple-Junctions

Multiple p-n junctions can be stacked on top of each other to reduce sub-bandgap and thermalization losses in a solar cell. Devices that utilize more than one p-n junction are called tandem solar cells or multijunction solar cells. In these configurations, the material with the largest bandgap is placed on top of the stack where it can more efficiently (with lower thermalization loss) convert high-energy photons into electrical energy than a lower-bandgap material would. Sub-bandgap photons that are not absorbed pass through the top junction and can be absorbed in the underlying lower-bandgap junctions [45].

The Shockley-Queisser limit can be modified to take into account more than one p-n junction and predictably the limiting efficiency increases. As the number of junctions increases from one to three junctions, the Shockley-Queisser limit increases from 31% to

42% to 49% at a concentration of one-sun. For the limiting case of a solar cell with infinite junctions, the Shockley-Queisser limit increases to 68% [37].

Figure 1.17 shows a schematic comparing a single-junction solar cell with an ideal bandgap of 1.32eV to a five-junction solar cell proposed and developed at UCSB. In this particular example, the combined thermalization and sub-bandgap losses can be reduced from 53.2% for an ideal single-junction solar cell to 19.3% for a five-junction solar cell.
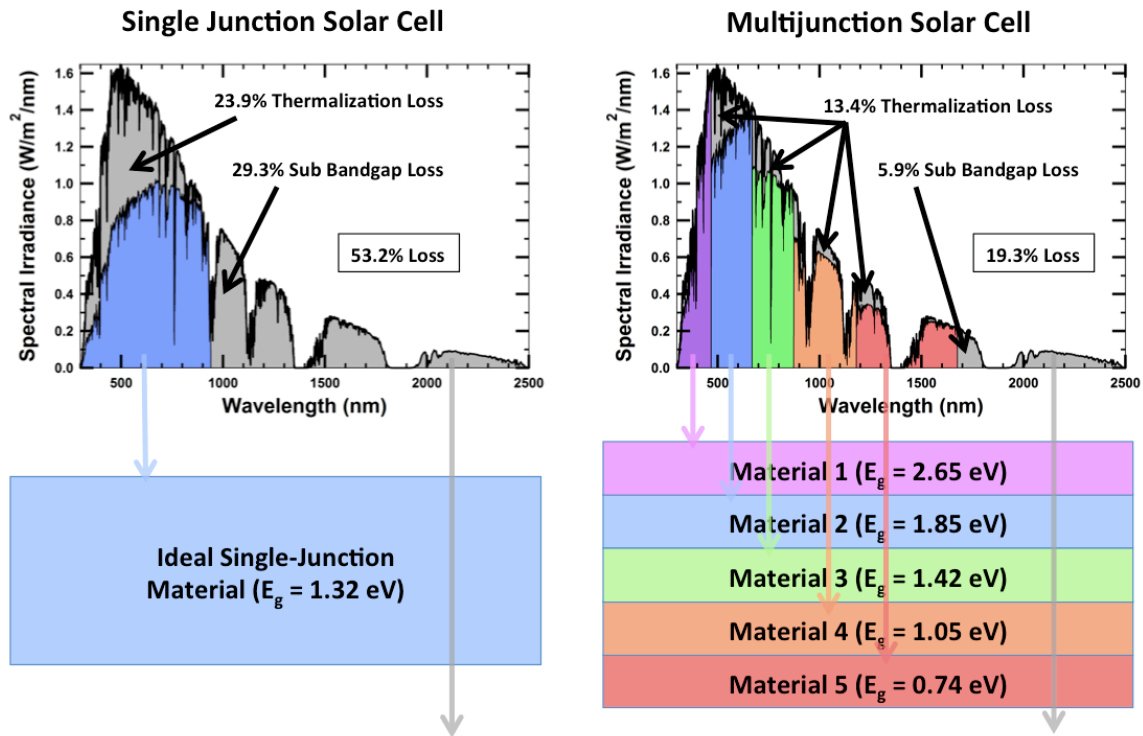
Figure 1.17: Schematic comparing thermalization and sub bandgap losses for (left) a single-junction solar cell with an ideal bandgap of 1.32eV and (right) the five-junction solar cell proposed and developed at UCSB.

It is clear from this schematic that increasing the number of junctions can lead to a significant improvement in cell efficiency by reducing losses due to thermalization and transmission. Another important way that efficiency can be improved is to increase the concentration of sunlight. Concentrating sunlight can reduce etendue loss by effectively increasing the solid angle of the sun, leading to an increase in the Shockley-Queisser limit to

~44% for a single-junction solar cell. For a solar cell with infinite junctions and a maximum concentration of ~46,000, the Shockley-Queisser limit increases to 86.8%, only slightly lower than the Carnot limit of 95% [37].

Bandgap Engineering of Multijunction Solar Cells

In order to achieve optimal efficiencies for a multijunction solar cell, it is important to carefully select the bandgaps of each junction in order to minimize the fundamental loss mechanisms discussed previously. To reduce the combined thermalization and sub-bandgap loss in the structure, the bandgap for each junction will tend to increase as the number of junctions increased. Figure 1.18 shows the ideal bandgaps for multijunction cells for designs with one to six junctions [46].
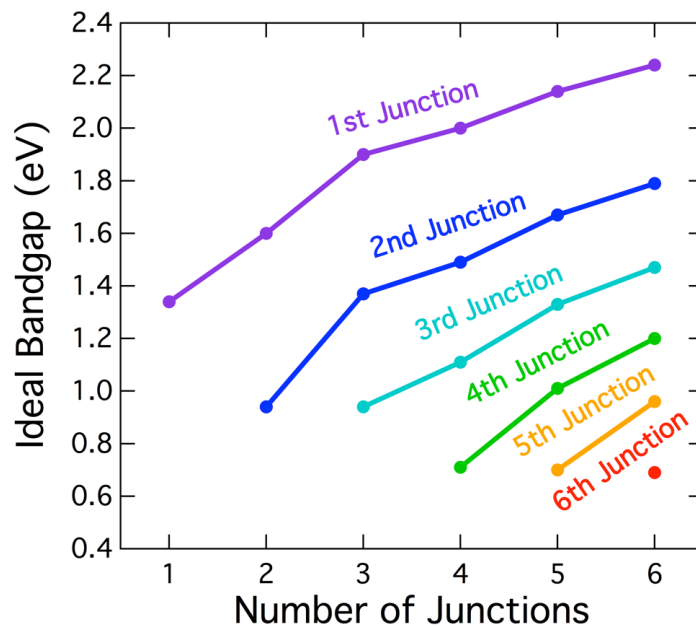
Figure 1.18: Ideal bandgap energy for each junction in a multijunction solar cell as the number of junctions is increased from one to six [46].[9]

While any set of materials with the correct bandgap combination could in theory be used in a multijunction stack, it is also important that each subcell has high material quality.

---

[9] Plotted using data from [46].

Additionally, it is important that there is a feasible method to integrate the different subcells. This is especially challenging for series-connected cells, where failing to current-match the component subcells can cause a significant drop in efficiency if the wrong bandgaps are used. Unfortunately, it is not easy to achieve an arbitrary bandgap combination for a multijunction solar cell in practice [45]. Figure 1.19 shows a plot of bandgap vs. lattice constant for common III-V materials.
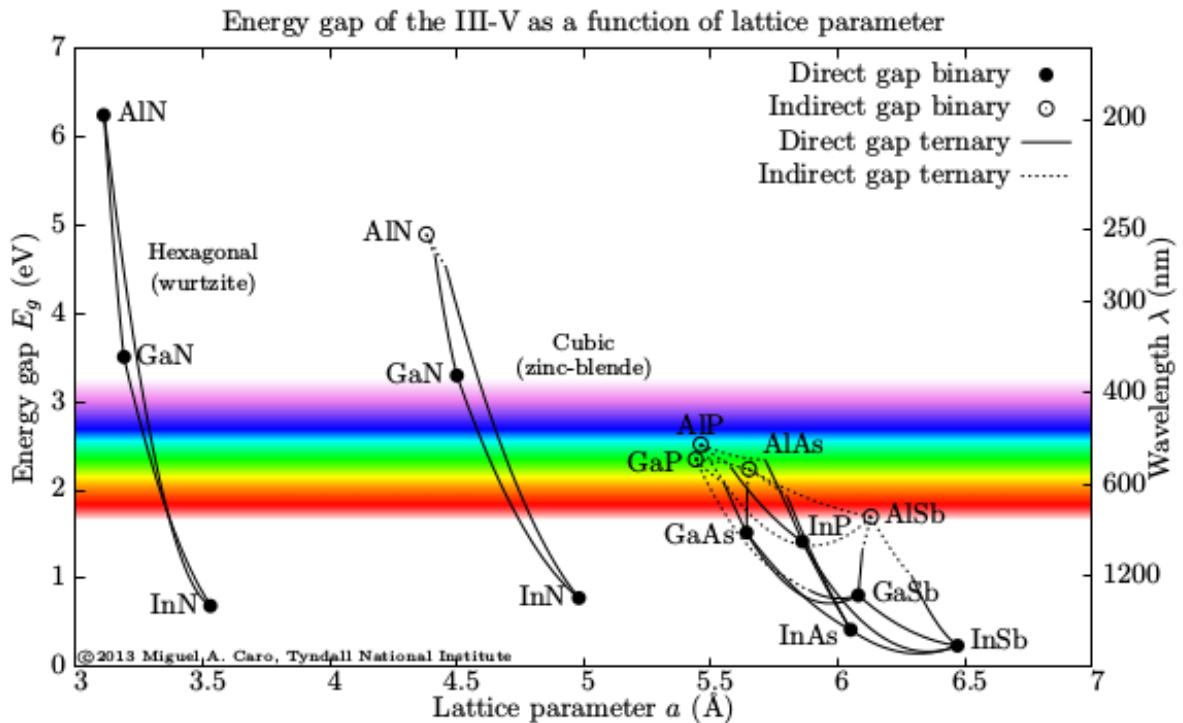
Figure 1.19: Plot showing bandgap vs. lattice constant for common III-V materials [35].[10]

This plot offers a significant amount of insight into how to achieve the correct bandgap combination when constructing a multijunction solar cell. The most common method to integrate materials with different bandgaps is through epitaxial growth. The highest material quality is achievable for materials that are grown lattice matched to a native substrate, where some of the most common substrates include silicon (Si), germanium (Ge), gallium arsenide

[10] Reproduced with permission from Miguel Caro.
http://mcaroba.dyndns.org/wiki/index.php/File:III-V_bandgap.png

(GaAs), indium phosphide (InP), and gallium phosphide (GaP). Today, the majority of commercial multijunction solar cells are triple-junction devices grown on Ge, and combine gallium indium phosphide (GaInP$_2$, E_g = 1.8eV), GaAs (E_g = 1.4eV), and Ge (E_g = 0.7eV) junctions [19]. Currently, Spectrolab holds the record efficiency for a germanium-based triple-junction cell at 41.6% [47]. Unfortunately, this does not use the ideal bandgap combination as the bottom Ge junction is significantly oversupplied with current [22,45].

One common approach to achieve a more ideal bandgap combination and improve cell efficiency is to use metamorphic growth techniques to integrate materials with different lattice constants [48,49]. In particular, the inverted metamorphic (IMM) design has seen a lot of success in recent years. In this design, the solar cell is grown in an inverted configuration, with lattice-matched GaInP$_2$ (E_g = 1.8eV) and GaAs (E_g = 1.4eV) subcells grown first and lattice-mismatched indium gallium arsenide (InGaAs, with E_g = 1.0eV & 0.7eV) subcells grown last. A transparent GaInP metamorphic buffer is used to grade the lattice constant from that of GaAs to the lattice constant of the lower subcells. The cell is then flipped over, bonded to a carrier wafer, and its native substrate removed to put it in the standard configuration with the highest bandgaps on top and the lowest bandgaps on the bottom. Today, the world record IMM cell, developed at NREL, has an efficiency of 45.7% under concentration [49]. While this design has realized a notable efficiency improvement compared to the best Ge-based triple-junction cells, the approach requires increased growth time to accommodate the metamorphic buffer layers, which can lead to a lower throughput and a higher material cost.

Finally, bonding can provide a pathway to combining dissimilar materials into a multijunction stack. In recent years, semiconductor bonding has seen great success in

combining subcells grown on GaAs with subcells grown on InP [50,51]. One big advantage of this approach is that the lower subcells can be grown lattice-matched on an InP substrate, and can thus achieve higher material quality than the lower junctions of an IMM design. The total growth time could also be reduced since a thick metamorphic buffer layer is not necessary. Today, the world-record one-sun device is a semiconductor bonded five-junction design developed by Spectrolab with an efficiency of 38.8% [50] and the world-record concentrator device is a semiconductor bonded four-junction design developed by Fraunhofer ISE with an efficiency of 46.0% [51]. Two significant disadvantages of the bonding approach are that it requires growth on more expensive InP substrates and that it necessitates the addition of a bonding process step, both of which can significantly increase the cell cost.

1.5 Synopsis of the Dissertation

This dissertation explores material science to advance the state of III-V multijunction solar cells for use in concentrator photovoltaic and hybrid photovoltaic-thermal (PV-T) solar energy systems. The dissertation focuses on two main topics. The first topic corresponds to research conducted at UCSB on advanced optical designs for multijunction solar cells. The second topic corresponds to research conducted at NREL on the development of multijunction solar cells for high-temperature applications. Both of these subjects have the overarching theme of improving the efficiency of systems that utilize high-performance multijunction solar cells.

Chapter 1 gave an overview of solar energy: comparing different solar technologies, discussing the physics of solar cells, and providing a background on the design of high-efficiency multijunction solar cells. Chapter 2 will focus on broadband optical coating

design, which is crucial to improving the efficiency of next-generation multijunction solar cells that absorb more of the solar spectrum than today's designs. The development of high-performance broadband optical coatings for InGaN/GaN solar cells will be discussed in detail. The addition of a broadband antireflection coating and dichroic mirror led to the highest reported efficiency for a standalone InGaN solar cell. Chapter 3 will explore antireflective nanostructures as a way to improve upon the performance of conventional interference-based multilayer coatings. While we conclude that standalone nanostructures cannot exceed the broadband performance of conventional antireflection coatings for multijunction photovoltaic devices, we find that a hybrid design that combines nanostructures with interference multilayers can enable significantly improved performance. This hybrid design is developed, leading to near-perfect broadband antireflection for both gallium nitride and sapphire. Chapter 4 will talk about the development of III-V solar cells for high-temperature applications. One of the key challenges was the design of high-bandgap (~2.0eV) aluminum gallium indium phosphide (AlGaInP) solar cells that are desired for high-temperature operation. In this work, we developed an AlGaInP solar cell with the world's lowest bandgap-voltage offset. This chapter will also discuss the robust cell components required for high-temperature operation. Chapter 5 will talk about measurements and modeling of single-junction GaAs and AlGaInP solar cells up to a temperature of 400°C. We find that the high-temperature performance of our solar cells is well predicted by the Hovel model and the Varshni equations, and at 400°C we expect to be able to achieve an efficiency of 18% by combining the top and bottom subcells already developed in the project. Finally, Chapter 6 will summarize the dissertation and present ideas for future work.

Chapter 2: Broadband Optical Coatings

Optical design is essential to the development of high-efficiency solar cells. Without antireflection coatings (ARCs), a photovoltaic device would lose more than a quarter of its efficiency due to reflection losses. To minimize reflection in a cost-effective manner, silicon solar cells typically use a ~75nm thick single-layer ARC composed of silicon nitride (SiN_x) [52]. Multijunction solar cells absorb a larger fraction of the solar spectrum and consequently require ARCs with better broadband performance. Commercial triple-junction GaInP/GaAs/Ge solar cells commonly use two-layer TiO_2/Al_2O_3 ARCs to achieve better broadband performance than what is possible with a single-layer ARC [53]. As multijunction solar cells move to designs with four or more subcells, they utilize an even larger portion of the solar spectrum and better broadband ARCs become necessary. Two approaches to improve ARC performance include adding layers to the thin-film stack [53] and utilizing antireflective nanostructures [54,55]. Both approaches will be discussed in this dissertation.

High-reflectivity optical coatings are also important to solar cell design. Single-junction GaAs solar cells developed by Alta devices achieved a world-record efficiency that was enabled by a high-reflectivity mirror deposited on the backside of the solar cell [56]. Other optical coatings can be designed to selectively reflect some wavelengths of light while transmitting others [57]. These dichroic mirror designs are important for lateral spectrum splitting CPV systems [58] and can also be used in bonded solar cells to improve the efficiency of the upper subcells [57].

In this chapter, we will discuss the design of broadband optical coatings and talk about how they can be applied to multijunction solar cells. The chapter will begin with a short

introduction to thin-film optical coatings and will show examples of idealized ARC and distributed Bragg reflector (DBR) designs. While these idealized examples can be instructive, we will always be constrained by material availability when designing optical coatings for real-world applications. This chapter will examine some of the practical considerations for real-world optical coating designs, and a procedure for optimizing the layer thicknesses in the thin-film stack will be presented. We will then describe the design of optical coatings for multijunction solar cells. Finally, high-performance broadband optical coatings will be applied to an InGaN/GaN solar cell. The application of an ARC and dichroic mirror to a 2.65eV InGaN/GaN device enhanced its efficiency to a value of 3.3% under the AM0 spectrum [57], which is the highest reported efficiency for a standalone InGaN solar cell to date.

2.1 An Introduction to Thin-Film Optical Coatings

The field of thin-film optics is built upon the principle of interference, whereby light waves reflected from different layers in a thin-film coating constructively or destructively interfere with each other to selectively reflect or transmit light. This paradigm has enabled the development of a variety of optical elements, including high-reflectivity coatings, long-pass and short-pass filters, beam splitters, and antireflection filters. Due to their ability to manipulate the passage of light, thin-film optical coatings are commonly used to enhance the performance of semiconductor devices such as solar cells, light-emitting diodes, and lasers [59-61].

To understand how a thin-film optical coating works, consider first the behavior of normally incident light at the interface between air, which has a refractive index (n) of 1, and a hypothetical substrate with a refractive index of four (n=4). When a ray of light

encounters this interface, a fraction of its power will be reflected and a fraction will be transmitted into the substrate. The Fresnel equation for normally incident light, shown below, describes what fraction of light will be reflected and how much will be transmitted [62].

$$R = \left(\frac{n_1 - n_2}{n_1 + n_2}\right)^2 \tag{2.1}$$

Where R is the reflectance, n_1 is the refractive index of the incident medium (air), and n_2 is the refractive index of the substrate. For a substrate with a refractive index of 4, 36% of incoming light will be reflected and 64% will be transmitted.

This reflectance can be significantly reduced using a thin-film ARC. The simplest design, shown in Figure 2.1, utilizes a quarter-wave (QW) layer of a material that has a refractive index between that of the substrate and that of air [59-62].
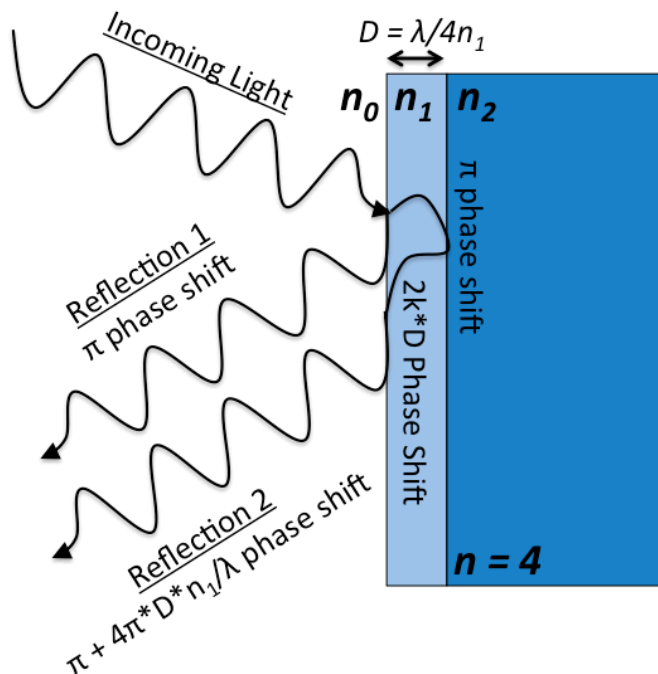
Figure 2.1: Diagram showing the design of a quarter-wave antireflection coating. If the thickness of the intermediate index layer is a quarter-wavelength, then destructive interference will arise between the two partial reflections.

Figure 2.2 shows the reflectance spectrum for a hypothetical single layer optical coating with the ideal refractive index for antireflection, where the transfer-matrix method is used to calculate the reflectance spectrum. Perfect antireflection is achieved when two conditions are met. First, the partial reflections from the front and back interface of the thin-film layer must be 180° out of phase leading to destructive interference between the first reflection and all subsequent partial reflections. For normally incident light, this condition is satisfied when the thin-film layer thickness meets the following criteria:

$$D = \lambda/4n_1 + m\lambda/2n_1, (m = 0,1,2, \dots) \tag{2.2}$$

Where D is the thickness of the thin-film, λ is the wavelength of incoming light, n_1 is the refractive index of the thin-film layer, and m is an integer [59-63].
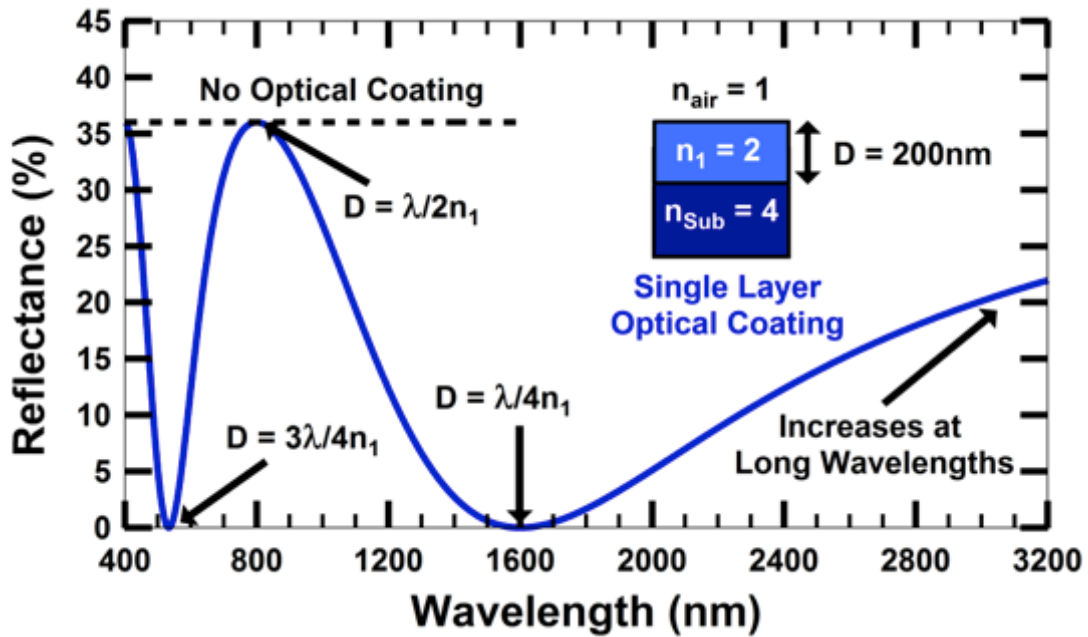
Figure 2.2: Plot showing the reflectance spectrum for a single layer optical coating with visible maxima at $D = \lambda/2n_1$ and minima at $D = \lambda/4n_1$ and $3\lambda/4n_1$ [63].

The second condition is that the magnitude of the front reflection must be equal to the magnitude of the sum of all other partial reflections in the thin-film layer. This condition is

36

met when the refractive index of the thin-film layer is the geometric mean of the refractive indices of its surrounding layers.

$$n_1 = \sqrt{n_0 n_2} \qquad (2.3)$$

Where n_1 is the refractive index of the thin-film layer, n_0 is the refractive index of the incident medium, and n_2 is the refractive index of the hypothetical substrate [59-63]. While perfect antireflection is possible if these two conditions are met, it is important to understand that the region of low reflectivity only occurs across a narrow band of wavelengths. The widest band of low reflection occurs at the $\lambda/4n_1$ minimum. However the region of low reflectivity for a single-layer optical coating cannot adequately cover the entire absorption width of a multi-junction solar cell, which will typically absorb light from ~300-1800nm.
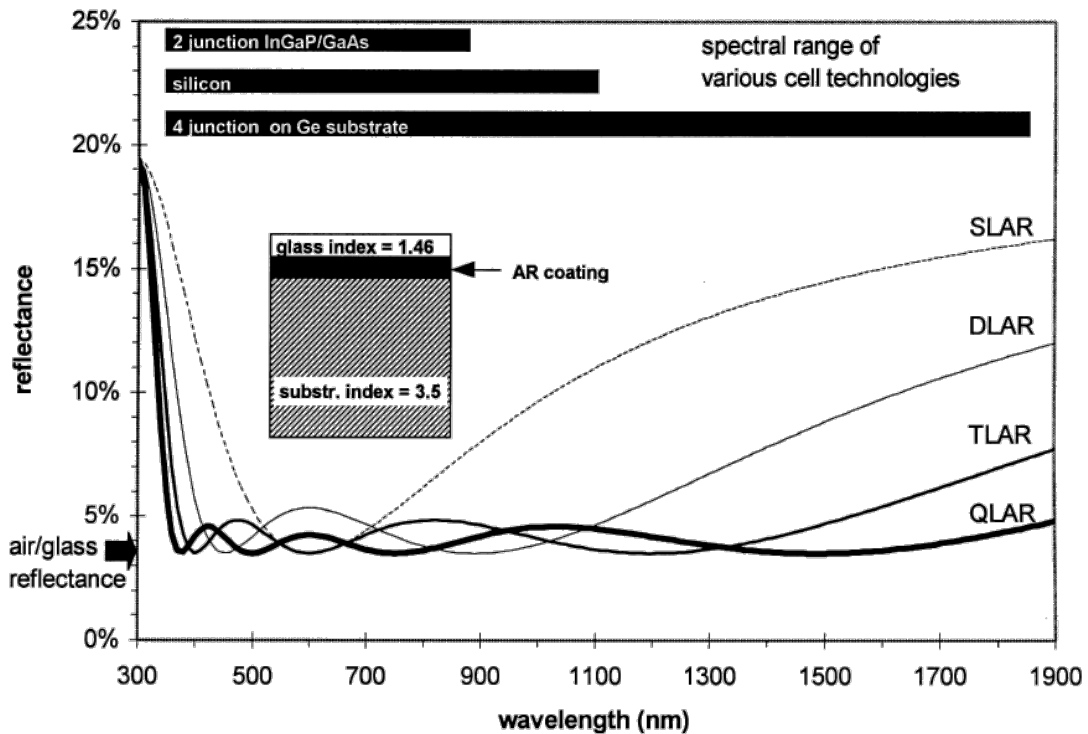
Figure 2.3: The reflectance of several ideal step-down ARCs as compared to the spectral range of several high-efficiency solar cell technologies [53].[11]

---

[11] Reproduced with permission from [53].

To increase the width of the low reflectivity region, additional thin-film layers can be added to the ARC. Similar to a single-layer ARC, optimal performance is obtained when the refractive index of each layer is the geometric mean of the refractive indices of its two neighboring layers. Each layer has the effect of adding a minimum to the reflectance spectrum, which can be used to increase the width of the low reflectivity region. Figure 2.3 shows the simulated reflectance for ideal step-down ARC designs with 1 to 4 layers [53].

Optical coatings can also be designed to have a very high reflectivity if the partial reflections from the thin-film stack constructively interfere with each other [59-61]. The Distributed Bragg Reflector (DBR) is the most well known thin-film mirror, and consists of alternating layers of high and low refractive index materials [64]. Perhaps the most common design is the quarter-wave mirror, where the thickness of each layer in the thin-film stack is one fourth of the desired wavelength of peak reflectivity. Figure 2.4 shows how partial reflections from a quarter-wave DBR stack can constructively interfere with each other.
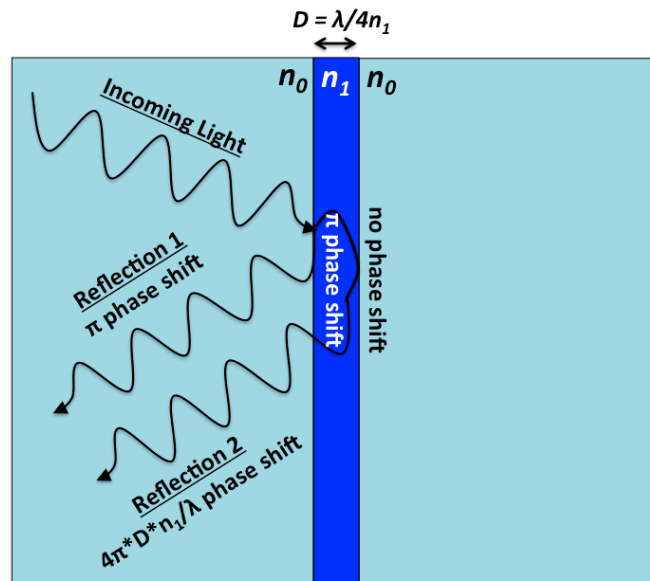
Figure 2.4: Diagram showing part of the design of a quarter-wave Distributed Bragg Reflector. If each layer is a quarter-wavelength thick, then constructive interference will arise between the partial reflections.

Interestingly, both the DBR and the single-layer ARC utilize quarter-wave designs. The reason that a quarter-wave design can yield low-reflectivity in a single-layer ARC and high-reflectivity in a DBR has to do with phase changes at each interface. For the DBR, the phase of the reflected beam will not change at the second interface (from n_1 to n_0), whereas for the single-layer ARC, the phase of the reflected beam at the second interface (from n_1 to n_2) shifts by 180° [62]. These phase shifts are shown in Figure 2.1 and Figure 2.4.

The magnitude and the bandwidth of the DBR peak are determined by the makeup of the quarter-wave layers. The magnitude of the peak reflectivity will increase as the number of alternating layers increases. It will also increase if the index contrast between the two alternating layers is increased. The bandwidth of the reflectivity peak is affected by the index contrast alone, where the width of the reflectivity peak increases when there is a large index contrast between the alternating layers in the thin-film stack [61].

Figure 2.5 shows the reflectance spectra for three DBR designs with a 700nm reflectivity peak. The three colors on this plot show DBR designs with (blue) alternating layers of GaP (n≈3.0) and air (n=1), (green) alternating layers of TiO_2 (n≈2.25) and SiO_2 (n≈1.45), and (red) alternating layers of Al_2O_3 (n≈1.75) and SiO_2 (n≈1.45). The difference between these three designs exemplifies the importance of using thin-film layers with a very high index contrast, as this helps to increase the magnitude of peak reflectivity and also the bandwidth of the mirror. The solid lines on the plot correspond to DBR designs with 20 thin-film layers, while the dashed lines correspond to designs with just 6 thin-film layers. The difference in performance between these curves shows us that as the number of layers in the thin-film stack is increased, a large increase in the magnitude of the reflectivity peak will result. However, we observe no change to the bandwidth of the mirror. When designing a

DBR, it is important to take into account both the index contrast between the thin-film layers and the number of alternating layers in the design.
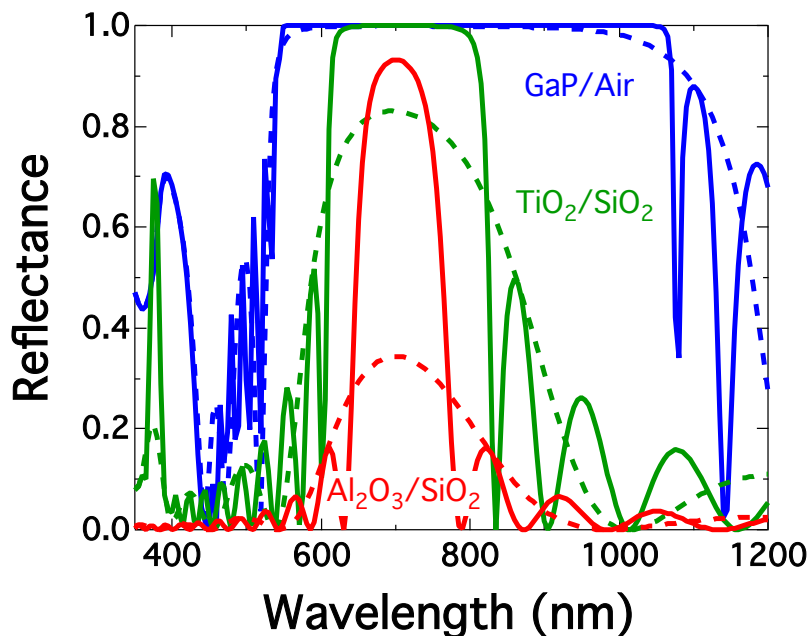
Figure 2.5: Plot showing the reflectance spectrum for DBR stacks composed of (blue) alternating layers of GaP (n≈3.0) and air (n=1), (green) alternating layers of TiO_2 (n≈2.25) and SiO_2 (n≈1.45), and (red) alternating layers of Al_2O_3 (n≈1.75) and SiO_2 (n≈1.45) layers. The solid lines represent DBR stacks composed of 20 thin-film layers and the dashed lines show DBR stacks composed of 6 thin-film layers.

2.2 Real-World Optical Coating Designs

When designing an optical coating for a real-world application, we will always be constrained by material availability. One major limitation is that few solid materials exist with a refractive index lower than magnesium fluoride (n < 1.4) [65]. For an ARC, this constraint will limit both the broadband and wide-angle performance of a multilayer design [63]. It also makes it difficult to design high-performance ARCs for materials with a low refractive index such as a glass lens. For a DBR, this constraint will reduce the attainable index-contrast between the thin-film layers and will limit the bandwidth of the reflectivity peak for many designs [61].

Another major limitation is that there are not many low absorption materials with a refractive index higher than titanium dioxide (n > 2.5) [65]. This will limit the attainable broadband transmittance of an ARC into semiconductors with a high refractive index, and is especially important for optical coatings on gallium arsenide-based multijunction solar cells [63]. For a DBR, this constraint makes it difficult to design a broadband reflector with a high reflectivity at short wavelengths [61]. As an example, it would not be possible to shift the GaP/air DBR, shown in Figure 2.5, to significantly shorter wavelengths because the GaP layers would begin to absorb a significant fraction of this light.
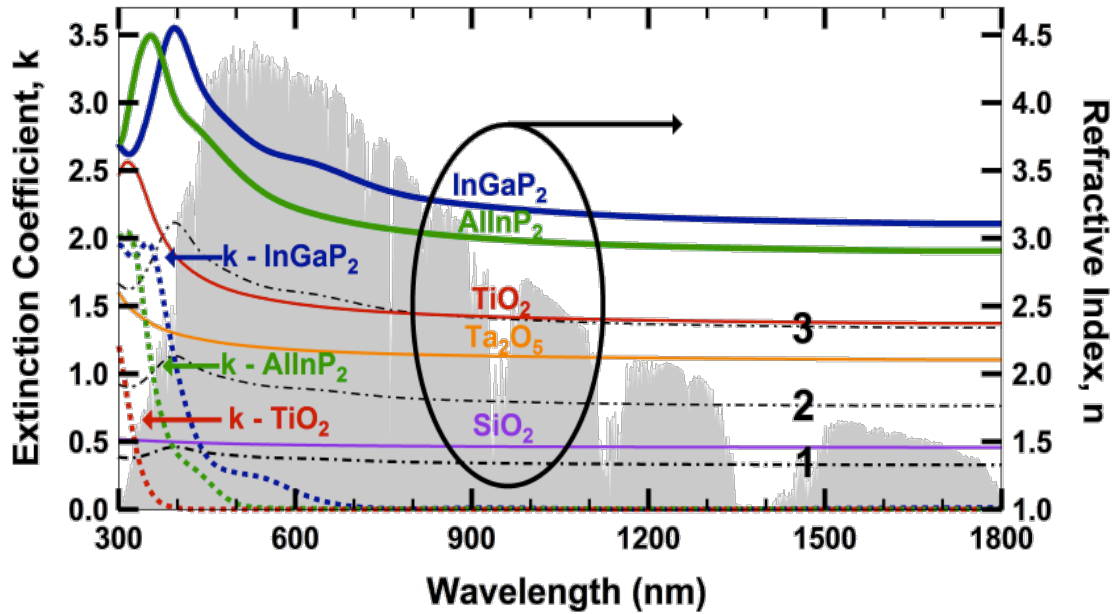
Figure 2.6: Plot showing the refractive index (solid lines) and extinction coefficient (dashed lines) for the top two layers of a typical multijunction cell ($GaInP_2$ and $AlInP_2$) and common materials used for thin-film antireflection coatings (TiO_2, Ta_2O_5, and SiO_2). The dash-dotted black lines show the ideal refractive indices for a 3-layer step-down interference coating [63].

Figure 2.6 shows the refractive index and extinction coefficient for common materials used in the design of ARCs for multijunction solar cells. The top of a multijunction device will commonly consist of a thick (~1 μm) layer of $GaInP_2$ topped with a thin (~20 nm) layer

made of AlInP$_2$. Both of these materials are lattice-matched to GaAs. Titanium dioxide (TiO$_2$), tantalum pentoxide (Ta$_2$O$_5$), and silicon dioxide (SiO$_2$) are regularly used in thin-film coatings. Due to the material constraints discussed previously, these materials are representative of the lower and upper bounds for low-absorption materials that can be used in solar cell ARC design [63].

The dash-dotted black lines represent the ideal indices of refraction for a 3-layer step-down interference coating for GaInP$_2$. In practice, it is often difficult to find intermediate-index materials with refractive indices that are close to ideal. To circumvent this problem, it is possible to obtain the equivalent optical properties of an intermediate-index layer with a Herpin-equivalent stack consisting of alternating layers of high- and low-index materials. William Southwell showed that for non-absorbing films, a combination of many thin high- and low-index layers can achieve the same optical properties as any arbitrary thin-film layer with a refractive index between that of the two layers. Since this alternating layer stack enables us to more closely obtain the desired optical properties of the ideal intermediate-index layers, these designs will often outperform a conventional step-down ARC in the real world [53,63,66].

It is very common for a multilayer optical coating to deviate significantly from the idealized examples discussed in the previous section, and in these cases they quickly become complex and difficult to analyze. To properly design almost any non-ideal optical coating, it is best to optimize the layer thicknesses by minimizing a merit function that describes the quality of the coating. A generalized merit function that can be used to optimize almost any optical coating is shown in Equation 2.4 [67].

$$F = \int_{\lambda_{min}}^{\lambda_{max}} \frac{I(\lambda)D(\lambda)C(\lambda) - T(\lambda)}{N(\lambda)Tol(\lambda)} d\lambda \qquad (2.4)$$

Where λ_{max} and λ_{min} represent the short and long wavelength cutoffs of the design of interest (for a solar cell, λ_{min} ~300nm and λ_{max} ~$E_{g, \text{ bottom junction}}$), $I(\lambda)$ is a weighting function that describes the illuminant (for a solar cell, this could be one of the G173 standard reference spectra), $D(\lambda)$ is the efficiency of the detector (for a solar cell, this would be the EQE), $C(\lambda)$ is the reflectance, absorptance, or transmittance computed using the transfer-matrix method, $T(\lambda)$ is the target value for the product of $I(\lambda)D(\lambda)C(\lambda)$, $N(\lambda)$ is a normalization factor for the target, and $Tol(\lambda)$ is the tolerance of the target. This merit function computes the deviation of the optical coating design from the desired target design, and the best design will minimize the value of the merit function [63,67].

Before attempting to minimize this merit function, it is important to begin with a starting guess for what the optical coating design should look like. As guidance for where to start, we can use the principles that we learned about thin-film optical coatings from the previous section. For example, if we were designing a step-down ARC for a solar cell, we would want to stack four low-loss layers on top of each other with the layers closer to air having a lower refractive index than the layers adjacent to the semiconductor (e.g. Substrate = GaAs, L1 = TiO_2, L2 = Ta_2O_5, L3 = Al_2O_3, L4 = SiO_2). Improved performance can be obtained with a simpler configuration by using a Herpin-equivalent stack, and the starting structure for such a design would consist of alternating layers of high- and low-index materials (e.g. Substrate = GaAs, L1 = TiO_2, L2 = SiO_2, L3 = TiO_2, L4 = SiO_2). As another example, if we were trying to design a DBR to reflect light from 400-800nm, we would again want to use a starting structure with alternating layers of high- and low-index materials (e.g. Substrate = GaAs, L1 = TiO_2, L2 = SiO_2, L3 = TiO_2, L4 = SiO_2, L5 = TiO_2, L6 = SiO_2, L7 = TiO_2, L8 = SiO_2) with quarter-wave optical thicknesses (t_{TiO2} = 67nm, t_{SiO2} = 103nm).

43

Once we have a starting guess, we then need to develop an optimization procedure to minimize the merit function by varying the thicknesses of each layer. In this work, we use TFCalc to optimize the layer thicknesses for our optical coating designs [63,67]. Three optimization methods are used: the gradient method, variable metric method, and simplex method. The gradient and variable metric methods compute the derivative of the merit function, and as the merit function approaches a minimum this derivative goes to zero. The simplex method does not compute the derivative, and is usually more accurate at locating the minimum as the design approaches the optimal. It is important to perform a global search to assure that optimizing from the starting guess will not result in the optimization method getting stuck in a local minimum.

I would also like to stress the importance of using good values for the optical constants for all of the materials that are simulated in this structure. The Sopra database has some optical constants that are very reliable (for example, silicon, gallium arsenide, and other common substrates) [65]. However, there are many materials with optical constants that vary depending on their deposition or growth parameters, and for these materials the optical constants published in the Sopra database should not be used. Instead, it is best to characterize their refractive index and absorption coefficient using ellipsometry or some other method [68]. For non-absorbing materials, the refractive index can be easily and reliably fit using the Cauchy equation.

$$n(\lambda) = A + \frac{B}{\lambda^2} + \frac{C}{\lambda^4} \tag{2.5}$$

For more complicated materials with non-zero absorption coefficients, it becomes more difficult to extract the optical constants. Despite the added complexity, there are a number of techniques that make it possible to extract both the refractive index and extinction

44

coefficient of a material using ellipsometry. Finally, it is important to note that it is best to analyze samples with only a single thin-film layer with unknown optical properties deposited onto a substrate with known optical properties (e.g. a thin layer of TiO_2 on a GaAs substrate), and significant errors are common when trying to analyze a structure with multiple thin-film layers.

2.3 Optical Coating Design for Multijunction Solar Cells

Without an ARC, the reflectance at the air-semiconductor interface would be greater than 30% for most photovoltaic devices. These reflection losses can be reduced to less than 5% by applying a thin-film ARC to the front surface of the semiconductor. This will lead to a substantial improvement in cell efficiency compared to an uncoated device, and for this reason ARCs are deposited onto nearly every commercial solar cell [63].

Silicon solar cells typically use a single-layer of SiN_x (n≈1.95) to minimize this reflection in a cost-sensitive manner [52]. While a dual-layer ARC can be used to further improve performance, the additional cost incurred from the additional layer is usually not worth the added efficiency for solar cells operated at one-sun. Multijunction solar cells are commonly used in space and concentrator systems where efficiency is a much larger driver to reducing system costs than it is for silicon solar cells. Multijunction solar cells also absorb a significantly larger fraction of the solar spectrum than silicon cells and thus require ARCs with better broadband performance.

Two-layer TiO_2/Al_2O_3 ARCs are common for lattice-matched (GaInP/GaAs/Ge) and lattice-mismatched (GaInP/GaAs/InGaAs) triple-junction solar cells, and are quite effective at mitigating reflection losses for these designs. These triple-junction designs incorporate either (lattice-matched design) a Ge bottom junction that is oversupplied with photons and

can tolerate high infrared reflectivity or (lattice-mismatched design) a bottom junction with a bandgap around 1.0eV and a narrower absorption range (~300-1250nm). Figure 2.7 shows a diagram of these triple-junction designs and illustrates why they can tolerate a relatively high infrared reflectivity [53,63,69].
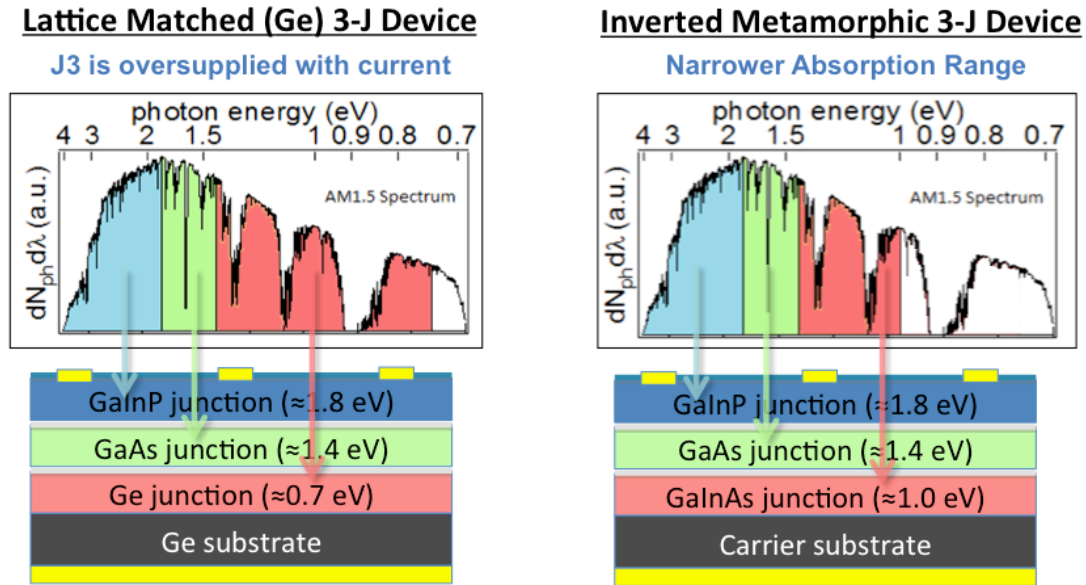
Figure 2.7: Diagram of two common triple-junction solar cells. (Left) The bottom junction of a commercial GaInP/GaAs/Ge triple-junction device is oversupplied with photocurrent, and thus can tolerate a high infrared reflectivity with minimal impact to cell efficiency. (Right) The bottom junction of a GaInP/GaAs/GaInAs triple-junction device has a bandgap around 1.0eV, and thus high-reflectivity at longer wavelengths will not impact cell efficiency.

While dual-layer ARCs are usually adequate for triple-junction photovoltaic devices, the field is rapidly moving toward designs that incorporate additional junctions in order to achieve higher power conversion efficiencies. Recently, world record efficiencies of 46.0% at 508 suns and 38.8% at one-sun have been reported using designs with four and five junctions respectively [13,14]. These four-junction and five-junction designs absorb light across a very broad wavelength range (~300-1800 nm) and have strict current matching requirements for each of the subcells [50,51]. For this reason, the broadband performance of

46

the ARC is more critical for these designs than for today's best triple-junction devices [63,69].

To develop higher-performing ARCs, we use the optimization procedure discussed in the previous section. We found that the amount of power transmitted into the top junction often correlates linearly with the modeled efficiency of a multijunction solar cell, and we will use an optimization procedure that maximizes transmitted power to evaluate the quality of different ARC designs [63,69].

To maximize the amount of power transmitted into the device, we set $I(\lambda)$ from Equation 2.4 to the wavelength-dependent power density from the AM1.5D spectrum. We also set $D(\lambda)=N(\lambda)=Tol(\lambda)=1$ so that we can evaluate the quality of different ARC designs for a generalized multijunction device with unknown EQEs. For $C(\lambda)$, we compute the transmission of light through the window layer and into the top junction. Since the underlying layers are typically composed of other III-V materials with a refractive index that is similar to the top-junction material, we find that there is not a significant difference in the design of an ARC that is optimized using a more complex optical model. Our transmission targets, $T(\lambda)$, are set to one so that minimizing the merit function will equate to maximizing transmitted power into the solar cell [63,69].

For systems that have additional optical elements, such as a CPV module, the merit function can be modified to more accurately describe the optical system. Losses from a primary or secondary concentrating optic can be taken into account by modifying $I(\lambda)$ to describe the attenuated spectrum that will ultimately reach the front end of the photovoltaic device. Additionally, the angular characteristics of a CPV module could be considered by

modifying $I(\lambda)$ to $I(\lambda,\theta)$ and $C(\lambda)$ to $C(\lambda,\theta)$, then integrating across the angular range of the concentrating system [63].

If the EQE is known, we can set $D(\lambda)=EQE(\lambda)$, and minimizing the merit function will then also minimize the solar weighted reflectance (SWR) for a single-junction solar cell.

$$SWR = 1 - \left(\frac{J_{SC}}{J_{SC,R(\lambda)=0}}\right) \tag{2.6}$$

Where J_{SC} is the short circuit current density of the cell and $J_{SC,R(\lambda)=0}$ is the short circuit current density of the cell if the reflectance were zero. By minimizing the SWR, we are maximizing the J_{SC} of the device. For a single-junction solar cell, this will also maximize the cell efficiency. For a multijunction solar cell with known EQEs, a more complicated optimization is required. If the cell is not current-matched then the ARC must maximize transmission into the current-limiting junctions. In this thesis, we focus on the case where $D(\lambda)=N(\lambda)=Tol(\lambda)=1$ so that minimizing the merit function will correspond to an ARC design that maximizes transmitted power into the solar cell. This will enable us to evaluate the relative quality of different ARC designs in a general manner [53,63].

High-reflectivity optical coatings can also be used to enhance the performance of solar cells, as we will discuss in the next section. When designing an optical coating for high reflectivity, we set $I(\lambda)=D(\lambda)=N(\lambda)=Tol(\lambda)$ in Equation 2.4, and instead of computing transmittance with $C(\lambda)$, we compute the reflectance of the stack. All of the target values are set to 1 so that minimizing the merit function will act to maximize reflectance across a given wavelength range. For dichroic mirrors that require high reflectivity for one set of wavelengths and low reflectivity for another, we can still use Equation 2.4 to optimize the layer thicknesses of the design by making $T(\lambda)$ wavelength dependent. For example, we could design an optical coating with a target reflectance of 1 (high reflectance) for

48

wavelengths between 300nm and 700nm and of 0 (low reflectance) for wavelengths between 700nm and 1800nm. If the high reflectivity portion of the design is more critical, then it is possible to add weight the high-reflectivity portion of the design by lowering *Tol(λ)* for those wavelengths [57,61,67].

2.4 High-Performance Optical Coatings on InGaN/GaN Solar Cells

In this section, we will discuss the design of broadband optical coatings that were used to enhance the efficiency of InGaN/GaN solar cells for hybrid InGaN/arsenide-phosphide five-junction solar cells [57]. Bonding provides a feasible pathway to combining lattice-mismatched materials into a multijunction solar cell, and bonded photovoltaic devices have had great success in recent years. Today, the world-record one-sun (38.8%) and concentrator (46.0%) cells use semiconductor bonding to combine very high-quality lattice-mismatched subcells grown on GaAs and InP [50,51]. While it is possible to grow arsenide-phosphides with direct bandgaps between ~0.7-2.2eV, the highest bandgaps require either AlGaInP or lattice-mismatched GaInP, and the general trend is that the material quality decreases as the bandgap is increased from ~1.9eV to 2.2eV. One alternative for a five-junction design is to develop a high-bandgap top cell using InGaN and bond this to an underlying arsenide-phosphide four-junction cell [57,70].

Figure 2.8 shows the modeled efficiency and one proposed design for a hybrid InGaN/arsenide-phosphide solar cell. The plot uses a dark-current model that calculates the efficiency as a function of the bandgap of an overlying single-junction InGaN-based cell and the top junction bandgap of an underlying quadruple-junction inverted metamorphic cell. The bandgaps for the bottom three junctions are unconstrained and were reoptimized at each point on the plot to maximize the efficiency [70].

49
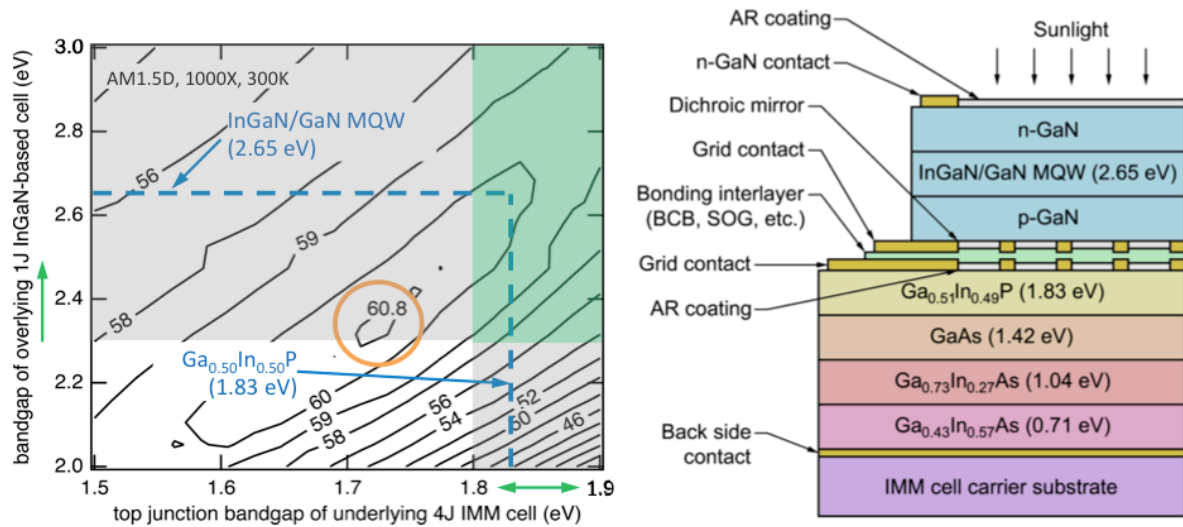
Figure 2.8: (Left) Dependence of modeled efficiency on subcell bandgap for an idealized underlying 4J cell with an overlying electrically independent 1J InGaN-based cell. (Right) Cross-sectional schematic of a hybrid InGaN/arsenide-phosphide five-junction solar cell. This work focuses on the application of an antireflection coating on the front interface of the device and a dichroic mirror for the bonding interface of the solar cell.[12]

The green region on the plot represents the design space where the most technologically feasible bandgaps are attainable. While the global efficiency maximum falls outside of this region, we find that we can attain an efficiency very close to the global maximum using a design that uses a 1.83eV GaInP 2nd junction that is lattice-matched to GaAs, and also raises the bandgap of the InGaN top cell to ~2.65eV, thereby reducing the lattice mismatch between the InGaN and GaN to a more acceptable level.

While a significant amount of work has been done to develop the underlying arsenide-phosphide device [49], the design of the InGaN top cell is less established. A thick 2.65eV InGaN layer cannot be grown directly on GaN due to the significant lattice-mismatch between these two materials. Alternatively, an InGaN/GaN multiple quantum well (MQW) structure can be developed to prevent the formation of relaxation-related defects. For 2.65eV

InGaN, the thickness of the InGaN quantum wells is limited to ~3nm to ensure that the critical thickness is not exceeded and tunneling transport in the MQW region can be enhanced if the thickness of the GaN barriers is limited to ~4nm [57].

Figure 2.9 shows a cross-sectional schematic for the best InGaN/GaN MQW solar cell developed at UCSB. The measured absorption coefficient is shown in the plot on the right.
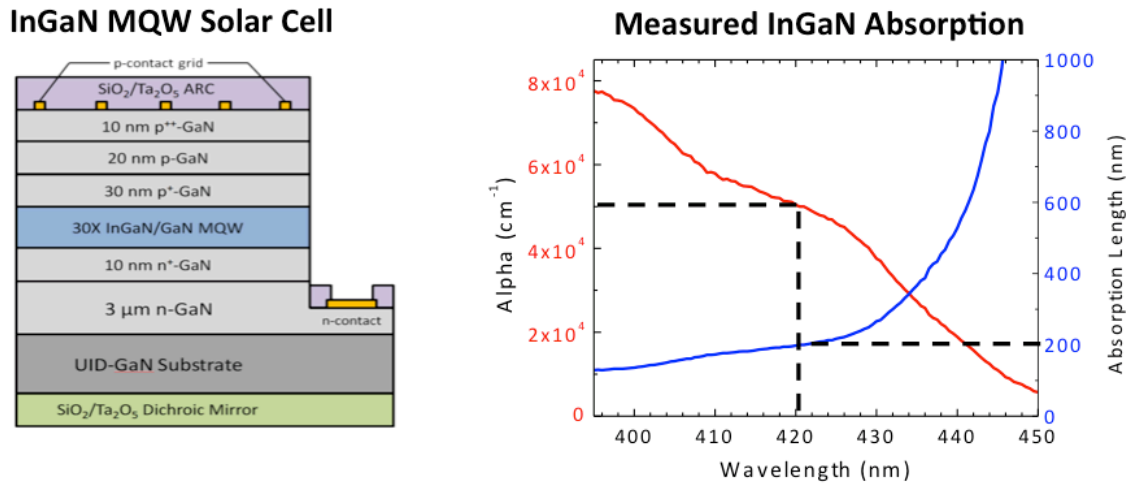
Figure 2.9: (Left) Cross-sectional schematic of the InGaN solar cell structure including contacts and optical coatings. (Right) Plot showing the measured absorption coefficient and absorption length for the InGaN material in the MQW active region [57].[13]

One of the most significant challenges for any MQW solar cell is that it is very difficult to absorb a significant fraction of above-bandgap light incident on the solar cell. To ensure efficient carrier transport, all of the quantum wells must be placed inside the depletion region. However, the thickness of the depletion region (W_D) is limited by the unintentional doping (UID) concentration in the solar cell. For the InGaN/GaN MQW solar cell developed at UCSB, we were able to fit ~30 quantum wells into the depletion region, thereby limiting the total thickness of InGaN in the solar cell to under 100nm. Since this is much shorter than the absorption length of InGaN, a conventional MQW design will not absorb a significant

---

[13] Reproduced with permission from [57]. Data on the right is courtesy of Nathan Young.

fraction of the above-bandgap light and this non-absorption will represent a significant loss to the cell efficiency. The addition of advanced optical coatings can enhance this absorption.

This section focuses on the design and application of an ARC to the front interface of the device and a dichroic mirror (DM) to the bonding interface of the solar cell. All of the dielectric layers were deposited using ion-beam deposition. We found that the optimal ARC consisted of 6 alternating layers of SiO_2 and Ta_2O_5. Figure 2.10 shows the measured and simulated reflectance spectra for the broadband ARC designed for the InGaN/GaN cell.
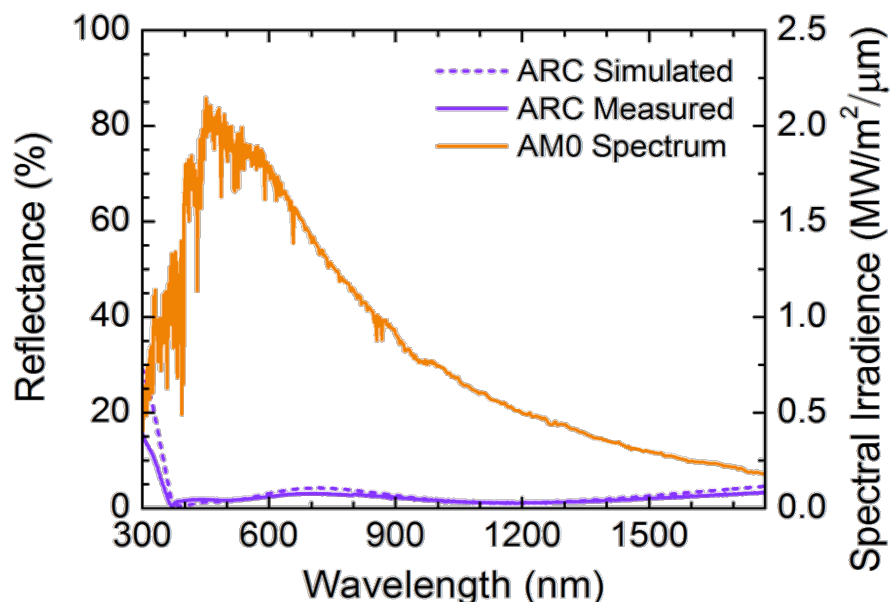
Figure 2.10: Simulated and measured reflectance of the broadband ARC. The AM0 spectrum is shown in orange [57].[14]

There is very good agreement between the simulated and measured reflectance spectra of the ARC, suggesting that the thicknesses of the deposited SiO_2 and Ta_2O_5 layers were very close to the specified design. We measured an average reflectance of just 2.4% for wavelengths between 365-1771nm (3.4-0.7eV). It is also important to highlight that this broadband reflectance is significantly lower than what can be obtained for an ARC designed

---

[14] Reproduced with permission from [57]

for an arsenide-phosphide cell. The reason for this is that the refractive index of GaN (n≈2.4) is lower than the refractive index of typical arsenide-phosphides (n>3.0), and it is thus easier to minimize reflections into this lower index material.

The application of a DM at the bonding interface can help improve the efficiency of the InGaN/GaN MQW cell by reflecting above-bandgap photons back to the front of the device. This gives high-energy light a second pass through the InGaN/GaN solar cell and will increase absorption in the MQW structure. For the DM design, we used Equation 2.4 to maximize the reflectance for 365-470nm light while minimizing the reflectance for 470-1771nm light. We found that adding layers to the thin-film stack will lead to better performance, but chose a DM design that consists of 14 alternating layers of SiO_2 and Ta_2O_5 to balance complexity and performance. Figure 2.11 shows the measured and simulated reflectance spectra for the DM design.
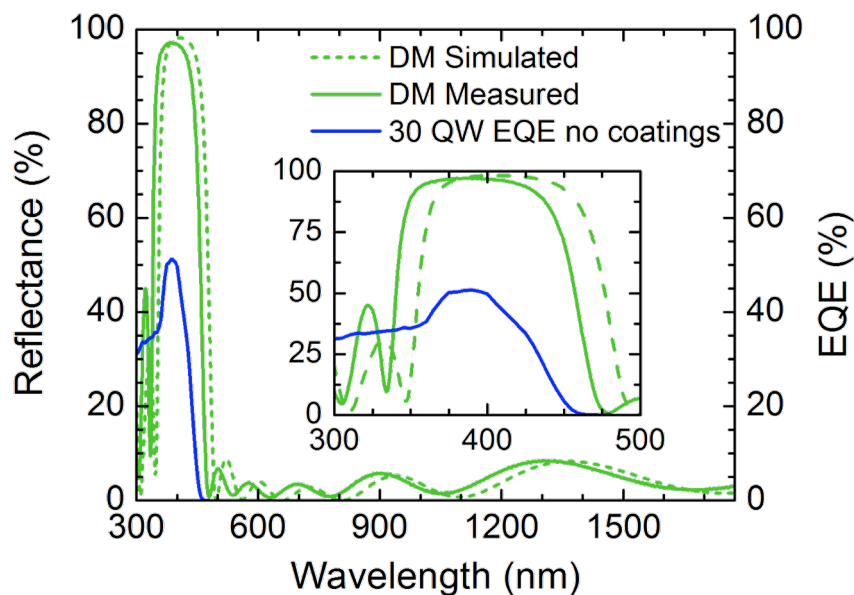
Figure 2.11: Simulated and measured reflectance of the broadband dichroic mirror deposited on the back surface of the InGaN solar cell. The inset clearly shows the overlap between the high reflectivity portion of the dichroic mirror (green) and the InGaN EQE spectrum (blue) [57].[15]

---

[15] Reproduced with permission from [57]

There is again excellent agreement between the measured and modeled reflectance spectra for the DM; we suspect that the ~15nm blue shift in the measured reflectance is caused by a small drift in the deposition rate of the Ta_2O_5. We measure an average reflectance of 89.3% for the high-reflectivity (365-470nm) and 4.0% for the low-reflectivity (470-1771nm) portions of the design. It is important to note that improved designs would be possible by depositing additional layers of SiO_2 and Ta_2O_5 or by using thin-film materials with a larger index contrast than Ta_2O_5/SiO_2.

We expect that the absorption enhancement will lead to a notable increase in the photocurrent, and we can calculate the expected increase to the EQE after deposition of the optical coatings. For the ARC, we expect that the fraction of light that makes it into the solar cell will increase from $(1-R_{GaN})$ to $(1-R_{ARC})$, and the enhancement to the EQE can be approximated by:

$$EQE_{ARC} = EQE_0 \left(\frac{1-R_{ARC}}{1-R_{GaN}}\right) \tag{2.7}$$

To develop an expression that describes the EQE enhancement that we expect after applying the ARC and the DM, we must consider how absorption will change as the reflectance at the front and back surface of the structure is changed. Figure 2.12 is a diagram that illustrates the infinite reflections from the front and back surface of the InGaN/GaN cell.
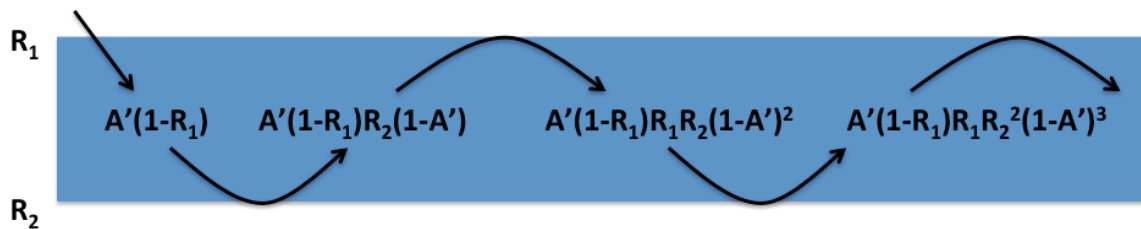
Figure 2.12: Diagram showing the infinite reflections from the front and back surface of the InGaN/GaN solar cell. The EQE enhancement can be calculated by considering the change in absorption as the reflectance at the front interface, R_1, and the back interface, R_2, are varied.

Where A' is the absorption from a single pass of light through the semiconductor, R_1 is the reflectance at the front interface of the solar cell, and R_2 is the reflectance at the back interface of the solar cell. All of these quantities are wavelength dependent.

The total absorption is equal to the sum of all of these terms. After grouping the even and odd terms into infinite summations, we come up with the following expression for the total absorption:

$$A = A'(1 - R_1)\left[1 - R_2\big((1 - A')\big)\right] \sum_{n=0}^{\infty}[R_1 R_2 (1 - A')^2]^n \qquad (2.8)$$

The infinite sums in this equation can be simplified using the following identity, which can be understood using simple algebra:

$$f(x) = \sum_{n=0}^{\infty} x^n = 1 + x + x^2 + \cdots = 1 + x * f(x) = \frac{1}{1-x} \qquad (2.9)$$

Where the final term is found by solving for f(x) in the equation: f(x) = 1 + x*f(x). After combining these two equations, we come up with the following expression for the total absorption in the material:

$$A = \frac{A'(1-R_1)[1+R_2(1-A')]}{1-R_1 R_2(1-A')^2} \qquad (2.10)$$

We expect that the enhancement to the EQE can be calculated by considering the enhancement to the absorption in the material. This assumption can be expressed by the following equation:

$$EQE_{DM+ARC} = EQE_0 \frac{A_{DM+ARC}}{A_0} \qquad (2.11)$$

By combining Equation 2.10 and Equation 2.11, we derived an equation that relates the expected EQE enhancement to just three values: R_{ARC}, R_{DM}, and R_{GaN}.

$$EQE_{DM+ARC} = EQE_0 \frac{(1-R_{ARC})[1+R_{DM}(1-A')][1-R_{GaN}^2(1-A')^2]}{(1-R_{GaN})[1+R_{GaN}(1-A')][1-R_{ARC}R_{DM}(1-A')^2]} \qquad (2.12)$$

55

After deposition of the optical coatings, we measured the wavelength-dependent reflection for the ARC, DM, and air-GaN interface (R_{ARC}, R_{DM}, and R_{GaN}). By plugging these values into Equation 2.7 and Equation 2.12, we can calculate the expected enhancement to the EQE.

Figure 2.13 shows the EQE of the InGaN/GaN solar cell with no optical coatings, after deposition of the ARC, and after deposition of the ARC & DM. The solid lines represent the measured EQE and the dashed lines represent the EQE calculated using Equation 2.7 and Equation 2.12.
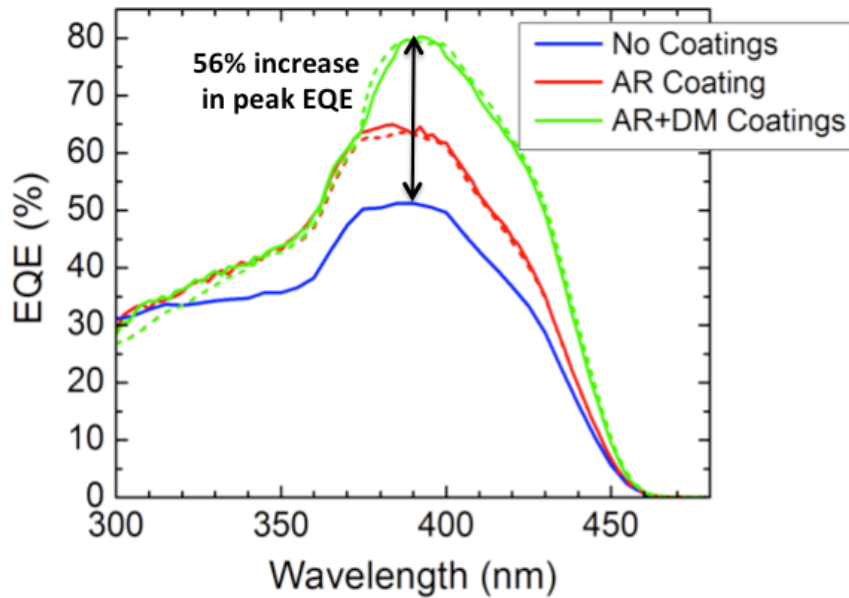
Figure 2.13: EQE measurements of the InGaN solar cell before and after depositing the ARC and DM. The dashed lines show calculations of the expected EQE after deposition of the optical coatings based upon the EQE data of the uncoated device and the measured reflectance data of the ARC and the DM [57].[16]

It is clear from this figure that absorption in the InGaN/GaN solar cell is significantly increased after the deposition of the ARC and the DM. Compared to the EQE of the uncoated device, we measure a 27% relative increase to the peak EQE after deposition of the

---

[16] Reproduced with permission from [57]

ARC and a 56% relative increase to the peak EQE after deposition of the ARC & DM. This increase in the EQE is expected to increase the photocurrent.

Significant improvements to the I-V characteristics of the InGaN/GaN solar cell were observed after deposition of the ARC and DM, and as we would expect the enhanced performance is almost entirely the result of an increase in the J_{SC}. Figure 2.14 shows the 1-sun illuminated current-voltage (LIV) and illuminated power-voltage (LPV), measurements of the InGaN/GaN solar cell before and after deposition of the ARC & DM.
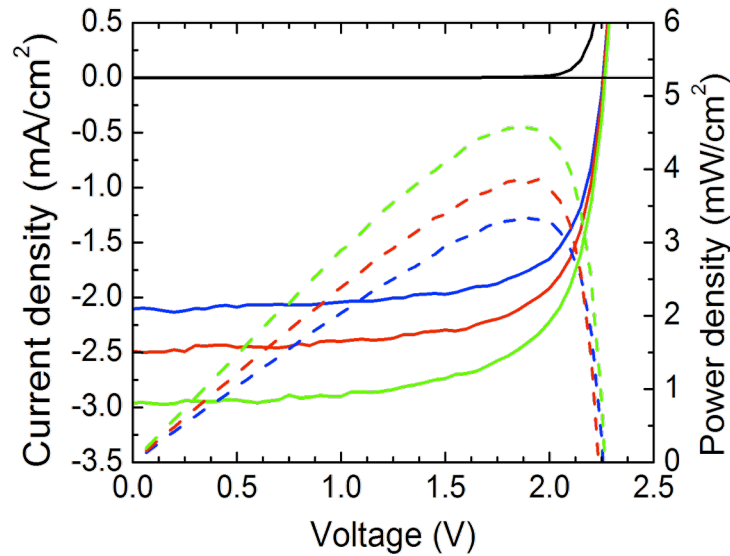
Figure 2.14: LIV and LPV measurements of the InGaN/GaN solar cell before and after depositing the ARC and DM. The blue line corresponds to measurements of the uncoated device, the red line corresponds to measurements after application of the ARC, and the green line corresponds to measurements after the application of the ARC and the DM [57].[17]

The application of an ARC & DM increased the AM0 efficiency of the InGaN/GaN solar cell from ~2.4% without any optical coatings to ~3.3% after the application of the ARC and DM, which corresponds to the highest reported efficiency for a standalone InGaN solar cell. While these results are encouraging, we believe that higher efficiencies are

---

[17] Reproduced with permission from [57]

possible by further improving the performance of the DM, ARC, and InGaN/GaN solar cell. As we show in Chapter 6, we also believe that a well-designed scattering structure could be used to enhance the efficiency of the InGaN/GaN solar cell.

2.5 Chapter Summary

In this chapter, we discussed the design of broadband optical coatings for multijunction solar cells. The chapter started with a brief introduction to thin-film optical coatings and examined the physics of single-layer ARCs and quarter-wave DBR stacks. While these examples are instructive, it is very common for a real-world optical coating to deviate significantly from the idealized case. Since these non-ideal designs quickly become complex and difficult to analyze, it is best to optimize the layer thicknesses by minimizing a merit function that describes the quality of the coating. This chapter described our optimization procedure and examined some of the practical considerations for designing real-world optical coatings. Special consideration was then given to the design of optical coatings for multijunction photovoltaic devices, where it is important to include a weighting function that describes the power in the incoming solar spectrum into the merit function. If the EQE of the device is known, we can optimize an ARC design such that the solar weighted reflectance is minimized. Finally, we discussed the design of broadband optical coatings that were used to enhance the efficiency of InGaN/GaN solar cells for hybrid InGaN/arsenide-phosphide five-junction solar cells. Two optical coatings were developed for a 2.65eV InGaN/GaN solar cell. To maximize transmission of light into the device, we developed a 6-layer ARC for the front surface of the solar cell that reduced the average broadband (365-1771nm) reflectance from 15.7% to 2.4%. To increase the absorption of light in the InGaN/GaN MQW structure, we developed a 14-layer dichroic mirror that achieved an average reflectance of 89.3% for

short-wavelength photons (365-470nm) and 4.0% for long-wavelength photons (470-1771nm). The deposition of these optical coatings improved the peak EQE by 56% relative to the uncoated sample and this led to a notable improvement in the J_{SC} and cell efficiency. An AM0 efficiency of 3.3% was measured for the cell with an ARC and DM, which is the highest reported efficiency for a standalone InGaN solar cell to date.

Chapter 3: Hybrid Optical Coatings with Nanostructures

Antireflective (AR) nanostructures offer an alternative to thin-film ARCs, which are ultimately constrained by the availability of suitable low-index (n < 1.4) and low-loss high-index (n > 2.5) materials. These designs consist of subwavelength protrusions originally discovered on the surface of a moth-eye to minimize visibility to predators. If the nanostructures are tapered, incoming light will see a smooth gradient in the effective index of refraction. With no abrupt interfaces, Fresnel reflections are greatly reduced and near-zero reflectance over a broad range of wavelengths and angles is possible [54,55].

AR nanostructures have been integrated with III-V photovoltaic devices using various approaches [71-75]. However, it is difficult to incorporate these structures without introducing additional loss mechanisms. Direct patterning of the active device is usually coupled with cell damage. This can be avoided by placing the nanostructures into a thickened $AlInP_2$ window layer. However, this will lead to a significant increase in absorption at short wavelengths [71-73]. Etching nanostructures into a low-loss dielectric layer can minimize this absorption, but will introduce a large gap in the refractive index between the dielectric layer and the semiconductor, leading to a significant increase in reflection losses [74,75].

In this chapter, we will discuss a hybrid optical coating design that integrates AR nanostructures with an interference-based ARC [63,69,76]. The AR "moth-eye" layer efficiently transmits light from air into a low-loss dielectric layer such as SiO_2, and the multilayer ARC is designed to maximize transmission into the underlying semiconductor. The chapter will begin by discussing the physics of AR nanostructures and will highlight what is required of these designs in order to achieve good antireflective properties. We will

then describe the benefits of combining thin-film optical coatings with AR nanostructures into a hybrid design and compare its performance to standalone AR nanostructure and conventional multilayer ARC designs for multijunction solar cells. We find that the hybrid approach can increase transmitted power by 2.1% compared to a standalone nanostructure design and 1.3% compared to an optimal multilayer ARC, corresponding to a ~0.5-1% increase in absolute cell efficiency for a multijunction solar cell. We then detail the fabrication process that was used to assemble the hybrid optical coating, and discuss our results. Designs that utilize this hybrid approach yield unparalleled performance, with measured reflection losses of just 0.2% on sapphire and 0.6% on gallium nitride for 300-1800nm light.

3.1 Antireflective Nanostructures

AR nanostructures have been proposed as an alternative to multilayer ARCs, and have demonstrated excellent broadband and wide-angle antireflective properties. These surfaces consist of a regular array of protrusions where the areal fraction of air to the nanostructure material smoothly increases with height [54,55]. Figure 3.1 shows a diagram of an AR nanostructure design along with the effective refractive index of the structure.
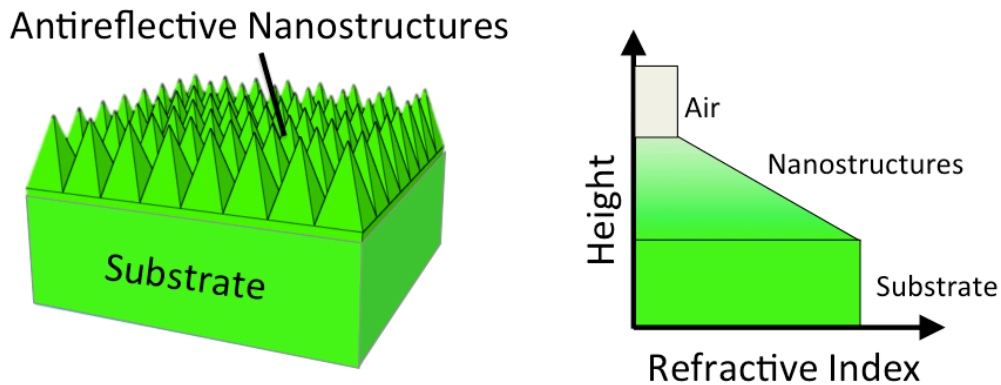
Figure 3.1: (Left) Diagram of an antireflective nanostructures design. (Right) Plot of the effective refractive index versus height for these nanostructures.

The lateral spacing, height, shape, refractive index, and absorption coefficient of the nanostructures are critical to the antireflective properties of the system [77-81]. If the spacing between features is greater than the wavelength of incoming light, the surface will scatter or diffract incident photons and may not have the desired optical properties. For a perfectly periodic array, the nanostructure surface would act as a diffraction grating where transmitted light is diffracted to an angle determined by the following Equation [78].

$$sin(\theta_T) = \frac{m\lambda_0}{nd_{lat}} + sin(\theta_I) \qquad (3.1)$$

Where θ_T is the transmission angle for the diffracted beam, m is the diffraction order ($m = 0,\pm1,\pm2,...$), λ_0 is the wavelength of light in vacuum, n is the refractive index of the nanostructure material, d_{lat} is the lateral spacing between nanostructures, and θ_I is the angle of incidence for incoming light.

For the case where $\lambda_0/(2n^*d_{lat}) > 1$, only zero[th] order diffraction ($m = 0$) is possible for all angles of incidence [63]. In this case, $\theta_T = \theta_I$, and all incoming light will see the nanostructured layer as an effective medium with a smoothly varying refractive index. In order to suppress all higher diffraction orders, it is necessary that the spacing between features be smaller for structures placed into high-index materials than for structures placed into low-index materials. For example, the relative spacing required for nanostructures placed into AlInP$_2$ (n≈3) and SiO$_2$ (n≈1.5) is shown in the following Equation [63].

$$\frac{d_{AlInP_2}}{d_{SiO_2}} = \frac{n_{SiO_2}}{n_{AlInP_2}} \approx \frac{1}{2} \qquad (3.2)$$

In order to calculate the optical properties of the surface, it is necessary to develop a model for the nanostructures. Since the effective index of refraction will change as light moves through the structure, partial reflections will arise at every depth in the surface. The

62

net reflectance can be found by considering the sum of all partial reflections, each having a different phase that is dependent on the distance travelled through the structure. For nanostructure heights greater than $\lambda/2$, all phases are present in the reflected beam and destructive interference will cause the net reflectance to approach zero [55,82,83].

The surface can be approximated by splitting the nanostructures into a large number of evenly-spaced thin-horizontal slices, where the effective index of refraction and extinction coefficient for each layer is calculated using an effective medium approximation. Two common effective medium approximations include the Bruggeman model [84]:

$$0 = F\left(\frac{n_{eff}-n_1}{n_{eff}+n_1}\right) + (1-F)\left(\frac{n_{eff}-n_0}{n_{eff}+n_0}\right) \tag{3.3}$$

And volume averaging theory [85]:

$$n_{eff} = F(n_1) + (1-F)(n_0) \tag{3.4}$$

Where F is the areal fraction of the nanostructure material in each slice, n_0 is the refractive index of air, and n_1 is the refractive index of the nanostructure material. Once a refractive index profile is constructed, the reflectance, absorptance, and transmittance can be calculated using the transfer-matrix method.

The number of layers must be chosen such that the spacing between adjacent slices is much smaller than the wavelength of incoming light. The ratio of the layer spacing to the wavelength of light is shown in Equation 3.5 [63].

$$S/\lambda = \frac{H*n}{\lambda_0*(\# \ of \ slices)} \tag{3.5}$$

Where S is the spacing between slices, λ is the wavelength of light in the layer, H is the height of the nanostructures, n is the effective index of refraction in the slice, and λ_0 is the wavelength of light in vacuum. When modeling tall nanostructures composed of a material

63

with a high index of refraction, a larger number of slices are required to keep this ratio constant. In this dissertation, the tallest nanostructures considered have a height of 1000 nm and the nanostructures with the largest refractive index are composed of $AlInP_2$ [63].

Figure 3.2 shows the calculated reflectance spectrum for 1000 nm tall $AlInP_2$ nanostructures placed on top of an $AlInP_2$ substrate. The different lines show how the calculation varies as the number of slices used to approximate the structures change [63].
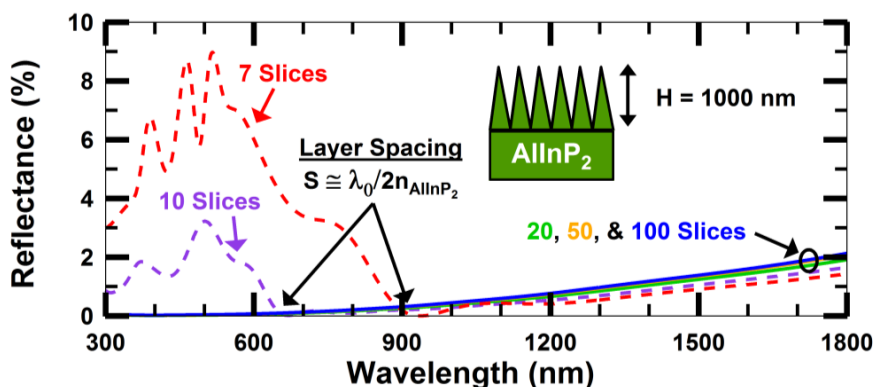
Figure 3.2: Plot showing the reflectance spectrum for 1000 nm tall $AlInP_2$ nanostructures. The calculation begins to converge as the number of slices is 20 or larger [63].

It is evident from Figure 3.2 that the accuracy of the model breaks down when the number of slices used in the model is too small. This is visible at short wavelengths, where a significant deviation in the calculated reflectance occurs when the layer spacing is larger than $\lambda_0/2n_{AlInP2}$. In order to accurately model the nanostructures, it is necessary that the spacing between adjacent slices is less than this for the shortest wavelength considered [63].

As the number of slices used to approximate the nanostructures increases, the calculation begins to converge. For $S < \lambda_0/5n_{AlInP2}$, we find that the deviation in the modeled reflectance becomes linearly dependent on the spacing between slices. For approximations which use 50, 100, and an infinite number of slices, the layer spacing will decrease from 20nm to 10nm to 0nm. This means that the deviation in the calculated reflectance for models using 50 and

100 slices will be equivalent to the deviation for models using 100 and an infinite number of slices. For 300-1800 nm light, we find that the average calculation error is just 0.02% for the 100-slice model. For smaller nanostructure heights and for structures composed of lower index materials, this deviation is expected to be even smaller since the ratio of S/λ will decrease [63].
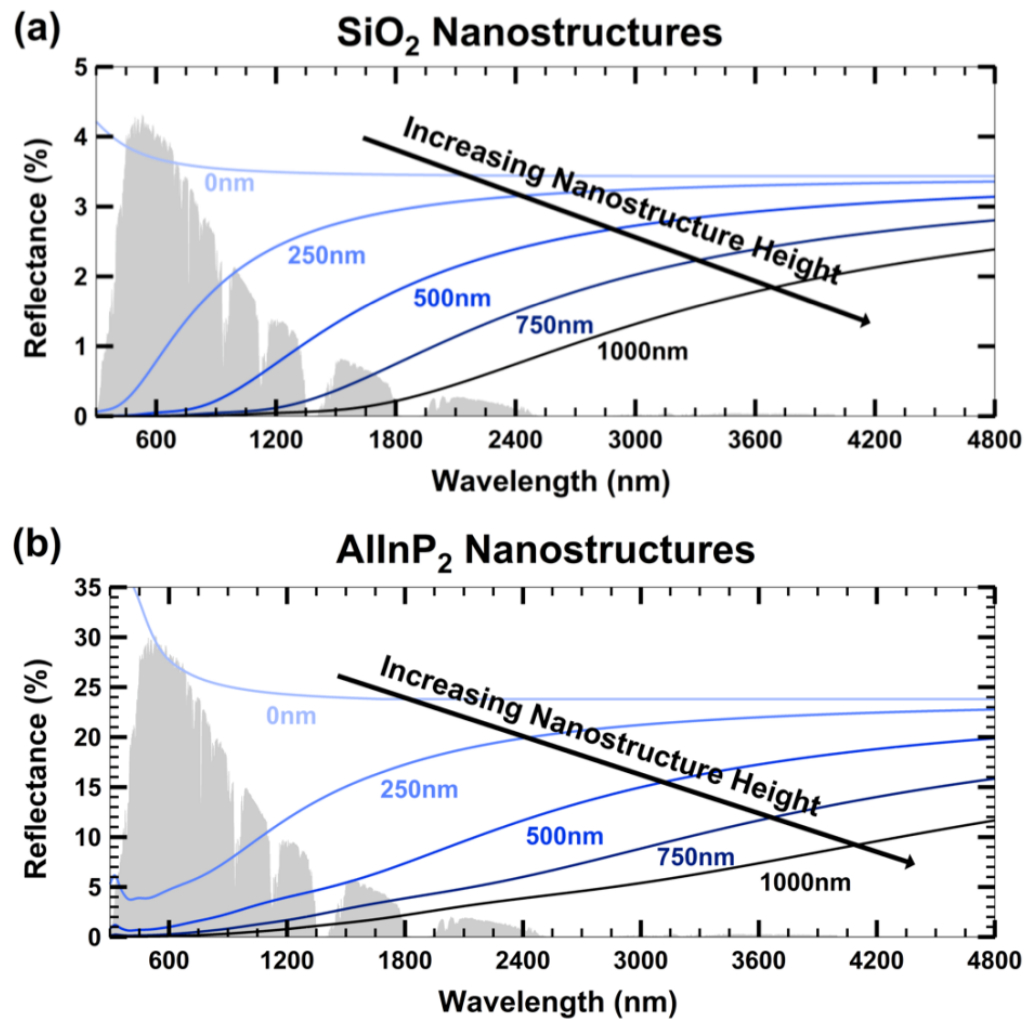
Figure 3.3: Plots showing reflectance as a function of wavelength for (a) SiO_2 nanostructures placed on top of a SiO_2 substrate and (b) $AlInP_2$ nanostructures placed on top of an $AlInP_2$ substrate. The nanostructure height is varied from 0-1000nm [63].

By applying this model, we find that the optical properties of the surface are highly dependent on the nanostructure height. Figure 3.3 shows the effect of nanostructure height

on the reflectance spectrum for SiO_2 nanostructures placed on top of a SiO_2 substrate and $AlInP_2$ nanostructures placed on top of a hypothetical $AlInP_2$ substrate. The lateral dimensions are assumed to be small enough that no diffraction or scattering occurs throughout the entire wavelength range. For the calculations, the nanostructures are assumed to have a quintic index profile, which has been shown to be very close to ideal for a graded-index antireflection coating [63].

In the limit where the wavelength is much larger than the nanostructure height, reflectance approaches that of the Fresnel reflection at a sharp interface. This acts as the upper bound for reflectance in the nanostructured layer. In Figure 3.3, this effect is illustrated at very long wavelengths for the case where the nanostructure height is 250 nm. This upper bound is larger for structures composed of high-index materials such as $AlInP_2$ than for structures composed of low-index materials such as SiO_2, and for this reason a high reflectance is still possible if the nanostructures are not properly designed [63].

When designing for multijunction solar cells with four or more junctions, it is important to maximize transmission for light with wavelengths between 300 and 1800 nm. The height of the nanostructures must be chosen to ensure that the region of low reflectivity matches the absorption range of the device. For $AlInP_2$, which is index matched to the top layer of most arsenide-phosphide multijunction devices, the nanostructure height would need to be around 1000 nm to adequately reduce reflection below that of an optimal multilayer ARC [63].

It is also important to consider absorption in the nanostructured layer. Figure 2.6 (shown again here in Figure 3.4) shows the extinction coefficient of $AlInP_2$, and suggests that absorption will be significant at short wavelengths if the nanostructure height must be around 1000 nm. Similar to $AlInP_2$, all known real-world materials with a refractive index

similar to the uppermost layer of an arsenide-phosphide multijunction solar cell will absorb a significant fraction of the solar spectrum. TiO_2 and ZnS represent the highest index materials that will not absorb significantly for wavelengths longer than ~400nm [63,65].
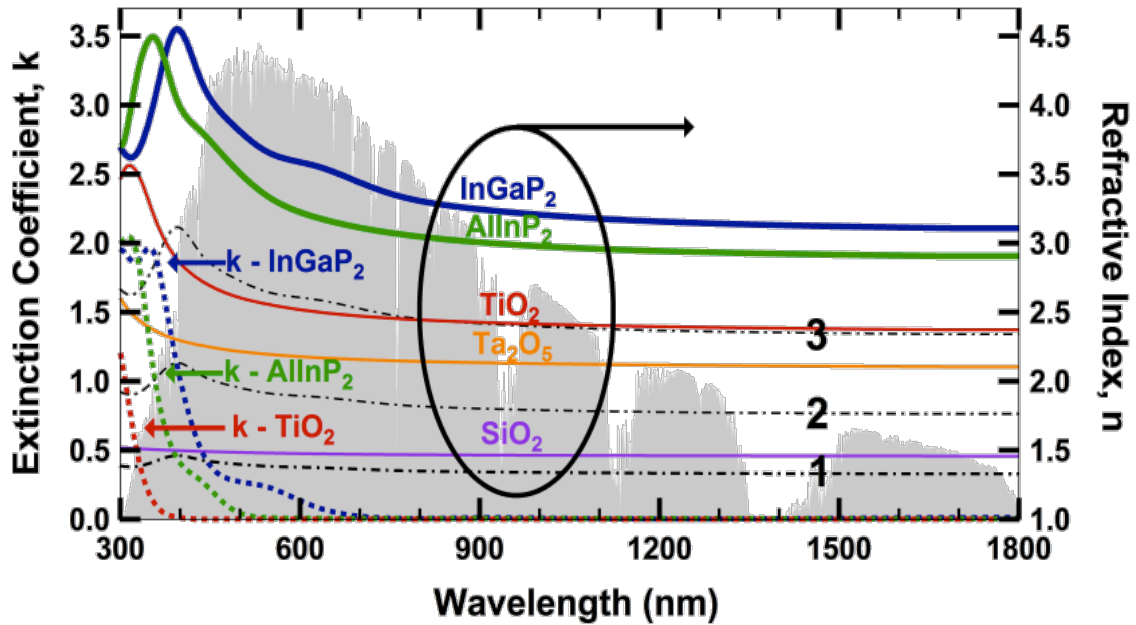
Figure 3.4: Plot showing the refractive index (solid lines) and extinction coefficient (dashed lines) for the top two layers of a typical multijunction cell ($InGaP_2$ and $AlInP_2$) and common materials used for thin-film antireflection coatings (TiO_2, Ta_2O_5, and SiO_2) [63].

To evaluate the performance of various AR nanostructure configurations, we model transmitted, absorbed, and reflected AM1.5D power as the nanostructure height is varied. These calculations help to quantify the tradeoff between material absorption for nanostructures composed of commonly available high-index materials and increased Fresnel reflections at the $AlInP_2$ window layer interface for nanostructures composed of commonly available low-absorption materials [63].

Figure 3.5 shows transmitted AM1.5D power for various standalone AR nanostructure configurations as a function of nanostructure height for a quadruple-junction photovoltaic

device. Absorption is the limiting factor for nanostructures composed of $AlInP_2$ and GaP, which both absorb 400-500 nm light. For nanostructures composed of SiO_2, performance is limited by a large Fresnel reflection at the $SiO_2/AlInP_2$ interface [86].
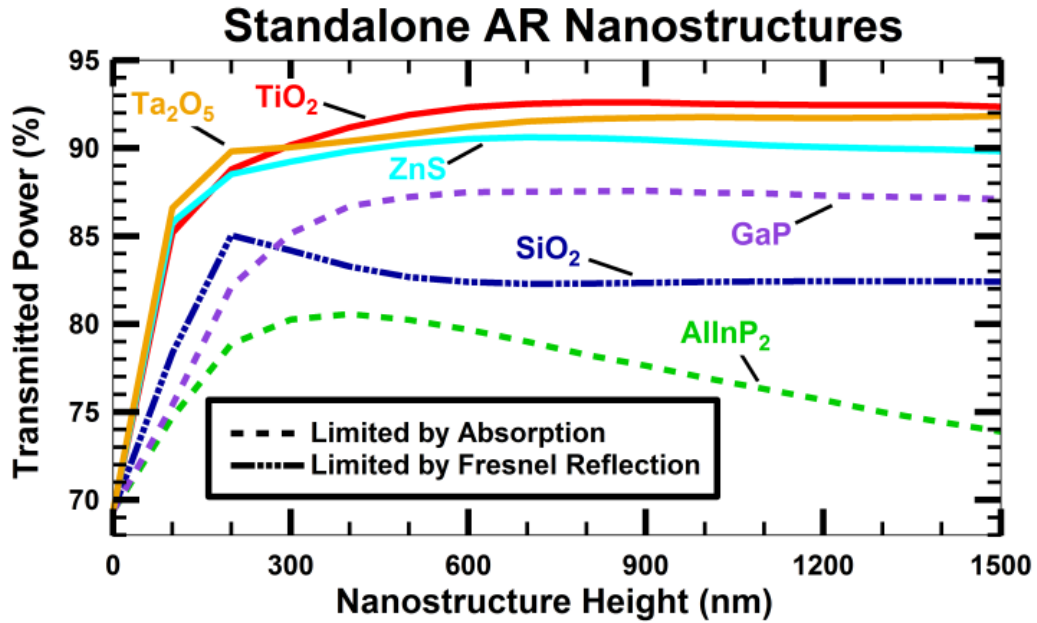
Figure 3.5: Plot showing transmitted power for nanostructures composed of $AlInP_2$, GaP, ZnS, TiO_2, $Ta2O_5$, and SiO_2 [86].

Table 3.1 shows reflected, absorbed, and transmitted power when the nanostructure height is optimal for each material. This table also includes the transmitted power for a 5-layer ARC composed of $TiO_2/Ta_2O_5/SiO_2/Ta_2O_5/SiO_2$, with layer thicknesses optimized using the procedure discussed in the previous chapter [86].

TABLE 3.1
ANTIREFLECTIVE NANOSTRUCTURE COMPARISON

Nanostructure Material	Nanostructure Height	Reflected Power	Absorbed Power	Transmitted Power
$AlInP_2$	400 nm	4.1%	15.3%	80.6%
GaP	900 nm	1.6%	10.8%	87.6%
ZnS	700 nm	3.7%	5.7%	90.6%
TiO_2	800 nm	2.8%	4.6%	92.6%
Ta_2O_5	1500 nm	5.0%	3.2%	91.8%
SiO_2	200 nm	12.3%	2.7%	85.0%
Optimal Thin-Film ARC	No Nanostructures	3.2%	3.4%	93.4%

68

Even though reflected power can be reduced to a value lower than that of an optimal thin-film ARC, absorption loss is very significant for the $AlInP_2$ and GaP nanostructures. Also note that for the SiO_2 nanostructures, the optimal feature height is just 200 nm. In this case, the nanostructured layer acts more like a thin-film ARC with a reflectance minimum between 500-700nm, a wavelength range corresponding to high AM1.5D power [86].

Most importantly though, the optimal thin-film ARC outperforms every nanostructure design considered. These calculations suggest that standalone AR nanostructures composed of real-world materials are not able to outperform a well-designed thin-film ARC, and for this reason they would need to have a significant cost-advantage over conventional optical coatings if they were to be considered a practical alternative for multijunction solar cells [63,86].

3.2 Hybrid Optical Coatings with Nanostructures

By combining the principles of diffractive and thin-film optics, it is possible to attain additional control over propagation of light. In the following sections, we will show that broadband transmission into $AlInP_2$, $GaInP_2$, GaN, and sapphire can be dramatically improved using a hybrid design that combines AR nanostructures with a thin-film ARC [63,69,76,86].

For thin-film coatings to attain high transmission for broadband and wide-angle light, it is necessary that the layers be composed of low-absorption materials that also span the refractive index range from air to the substrate. Unfortunately, this is not always possible due to limitations in material availability. One of the biggest limitations is that few solid materials exist with a refractive index lower than magnesium fluoride (n < 1.4). Importantly, this constraint leads to degradation in both the broadband and wide-angle performance of an

ARC design. This material constraint can be overcome by placing AR nanostructures into the uppermost layer of the thin-film coating [65,87].

This hybrid optical design operates by combining nanostructures, which reduce reflection from air to a low index dielectric (e.g. SiO_2), with a multilayer optical coating, which is optimized to maximize transmission from SiO_2 to the substrate. When this hybrid design is applied to sapphire or GaN, near-perfect broadband and wide-angle antireflection is possible. For higher index materials such as GaAs, silicon, $AlInP_2$, and $GaInP_2$, broadband and wide-angle reflection can be significantly reduced, however if high-transmission is desired then performance will ultimately be limited by the lack of low-absorption materials with a refractive index higher than TiO_2 [63].
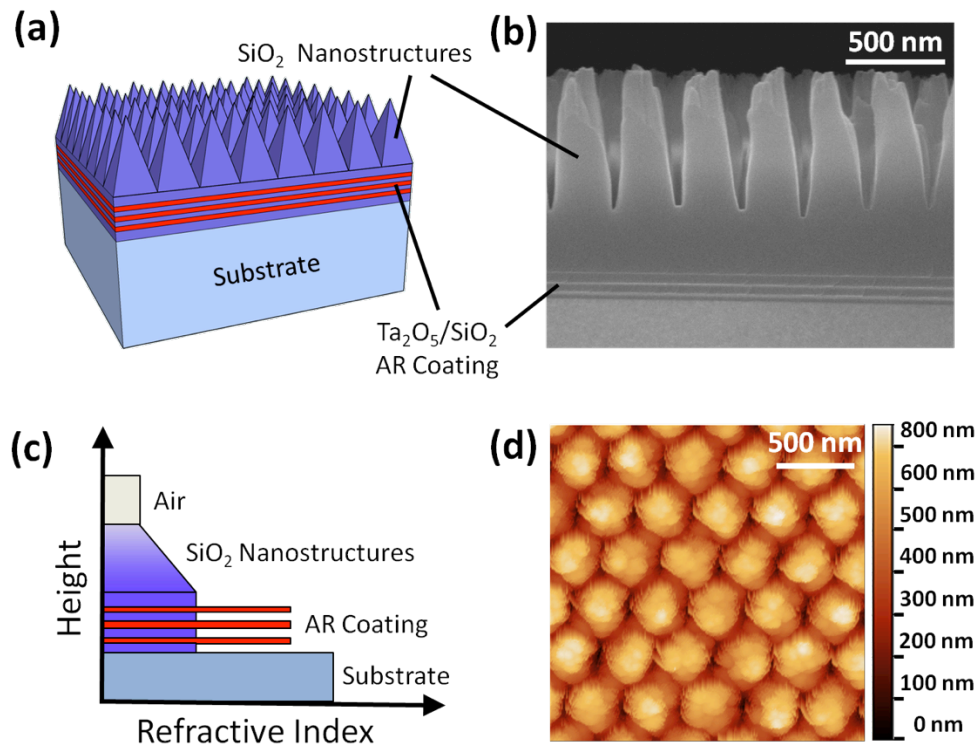
Figure 3.6: Illustration of the hybrid antireflection coating design showing (a) a three dimensional diagram of the hybrid design, (b) a cross section SEM of the hybrid design, (c) the refractive index profile of the design, and (d) a two-dimensional profile of the antireflective nanostructures measured using AFM [76].

Figure 3.6 shows various illustrations of the hybrid design, where the scanning electron micrograph (SEM) and atomic force microscope (AFM) profile are taken for a design placed onto a single side polished (SSP) sapphire substrate. Figure 3.6(a,c) show a three-dimensional diagram of the design and its corresponding refractive index profile. The SEM cross-section and AFM profile from Figure 3.6(b,d) allow us to approximate the nanostructure dimensions and the refractive index profile for the fabricated design [76].

3.3 Modeling the Hybrid Design for Multijunction Solar Cells

In this section, we use our optical model to compare the performance of three proposed nanostructure configurations, shown in Figure 3.7, as the height of the nanostructures is varied from 0-1000 nm.
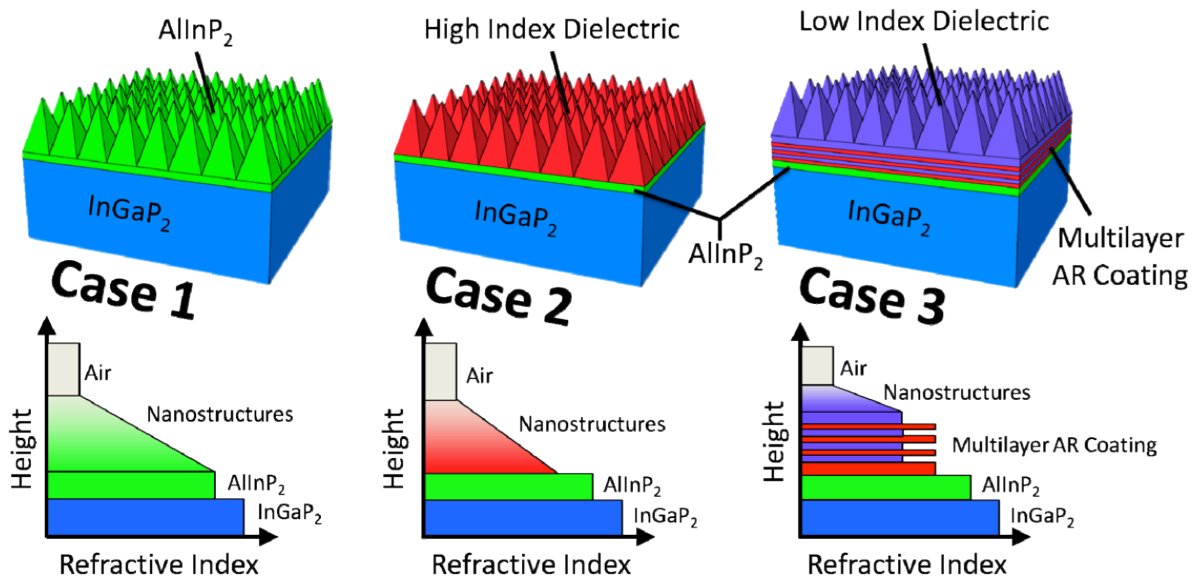
Figure 3.7: Diagram of the antireflective nanostructure designs explored in this section. We compute transmission into the top semiconductor layers of a multijunction solar cell, assuming that the top two layers are composed of a ~1μm thick layer of $InGaP_2$ and a ~20nm thick layer of $AlInP_2$ [63].

For Case 1, the nanostructures are composed of $AlInP_2$, which is index matched to the top layer of the multijunction cell. For Case 2, the nanostructures are composed of low-

71

absorption, high-index dielectric materials; SiO_2, GaP, Ta_2O_5, TiO_2, and ZnS are considered. For Case 3, we consider a hybrid configuration where antireflective nanostructures are placed into SiO_2, a low-index dielectric, which is placed on top of a multilayer ARC designed for maximum transmission into the solar cell. An optimized multilayer ARC and no ARC are also considered as limiting cases for when the nanostructure height is zero [63].

This model assumes a quadruple-junction solar cell with a 0.74 eV indium gallium arsenide (InGaAs) bottom junction lattice-matched to InP ($\lambda_{max}=1676$ nm). The optical stack for these calculations consists of a 20-nm thick $AlInP_2$ layer on top of a semi-infinite $InGaP_2$ junction. The layer thicknesses for the thin-film ARC in Case 3 are found by first performing a global search, then using a simplex optimization to maximize transmitted power into the top $InGaP_2$ layer using Equation 2.4. The optimization accounts for absorption and reflection in the thin $AlInP_2$ layer, which is important when designing an ARC for a real solar cell. The nanostructures are assumed to have a quintic index profile, and the layer thicknesses are reoptimized at each nanostructure height [63].

Designs with a single layer of TiO_2 and 4 alternating pairs of Ta_2O_5/SiO_2 are used as the starting point for the optimization. This design can have similar optical properties to a step-down interference coating with up to 6 layers. TiO_2 is representative of the thin-film material with the highest achievable refractive index, and is thus used as the layer adjacent to $AlInP_2$. The intermediate index layers are built up using alternating pairs of Ta_2O_5 and SiO_2, where a $Ta_2O_5/SiO_2/Ta_2O_5$ combination can approximate the optical properties of an intermediate index layer. Ta_2O_5 is used instead of TiO_2 to help minimize absorption loss in the final structure [63].

It is important to note that the optimization process often reduces the number of layers. We use 9-layers as a starting point to get an upper limit on performance and to gain intuition for how the optimal multilayer design changes as the nanostructure height is varied. However, optimal performance can often be achieved using stacks with 2 or 3 alternating pairs of Ta_2O_5/SiO_2, making it possible to simplify the design and reduce costs [63].

Figure 3.8 shows the optimal designs for the hybrid configuration of Case 3, where the cumulative height of the multilayer coating is plotted as a function of nanostructure height. This plot has a lot of interesting features relevant to the optical design of the ARC. First, note that when the nanostructure height is less than 400 nm, the optimal number of layers collapses from nine to five. This behavior can be linked to the design of an ideal step-down interference coating [63].
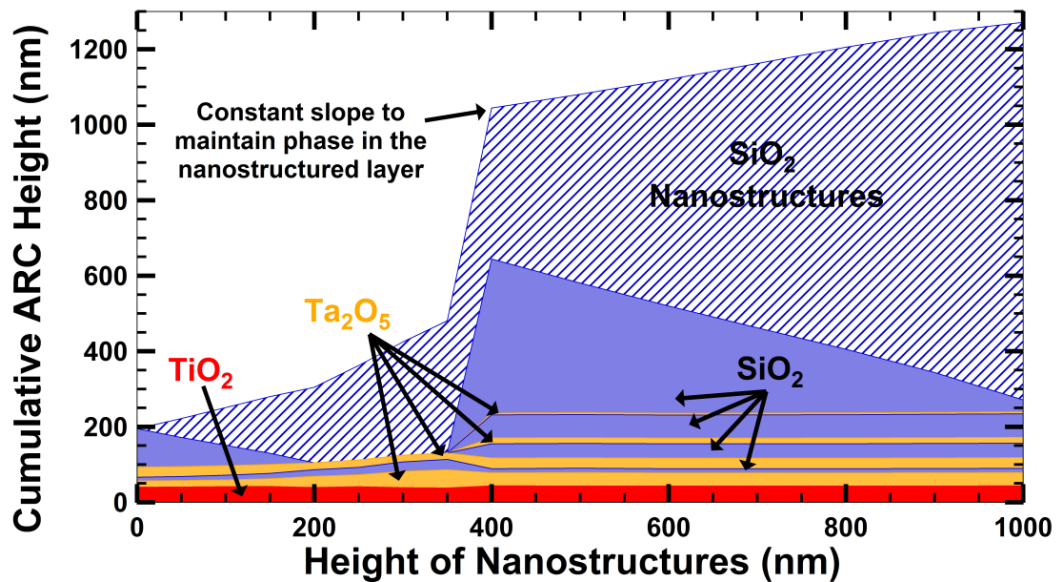
Figure 3.8: Plot showing the cumulative height of the multilayer ARC for the hybrid configuration (Case 3) as a function of nanostructure height [63].

The ideal indices of refraction for a three-layer step-down coating from air-InGaP$_2$ are shown in Figure 3.4. Since the top and bottom layers have refractive indices very close to

SiO_2 and TiO_2, only one intermediate index layer needs to be built up with a Ta_2O_5/SiO_2 equivalent stack. The ideal indices for a four-layer step-down interference coating would require materials with indices lower than SiO_2 and higher than TiO_2, which cannot be achieved using commonly available thin-film materials [63]. For nanostructure heights greater than 400 nm, the design of a step-down interference coating is better approximated by choosing ideal indices that bridge the gap between SiO_2 and $InGaP_2$. All intermediate layers with a refractive index lower than TiO_2 are obtainable, so a design consisting of more than five layers becomes ideal [63].

Another interesting feature from Figure 3.8 is the dependence of the Ta_2O_5 and SiO_2 layer thicknesses on stack position. For designs with a nanostructure height greater than 400 nm, each Ta_2O_5 layer gets thinner and each SiO_2 layer gets thicker near the top of the stack. This translates to higher equivalent indices at the bottom of the stack and lower equivalent indices at the top of the stack. This trend illustrates how the alternating layers of Ta_2O_5 and SiO_2 build up a stack with similar properties to an ideal step-down interference coating [63].

Also note the decreasing thickness of the uppermost SiO_2 layer as the height of the nanostructures increases. This layer has the purpose of maintaining the phase shift for incoming light reflected off the first Ta_2O_5 layer. This results in a nearly constant slope in the cumulative ARC height, and leads to comparable performance for all designs with a nanostructure height greater than 400 nm [63].

The quality of each nanostructure design is evaluated by modeling reflection, absorption, transmission, and cell efficiency for a quadruple-junction photovoltaic device. The model considers reflection and absorption loss in the full optical stack, assuming that absorption in the layers between each junction is negligible. A conventional multijunction cell model is

74

used to calculate the cell efficiency of a quadruple-junction device for each of the antireflective nanostructure designs [63].

Antireflective Design Comparisons

Figure 3.9(a)-3.9(c) show transmitted, absorbed, and reflected power for each configuration as the height of the nanostructures is varied. These values are expressed as percentages summing to 100%. For Case 2, only the results for TiO_2 are plotted. As is shown in Figure 3.5, transmission for SiO_2, GaP, ZnS, and Ta_2O_5 nanostructures was also calculated but was found to be lower than for TiO_2 nanostructures [63].
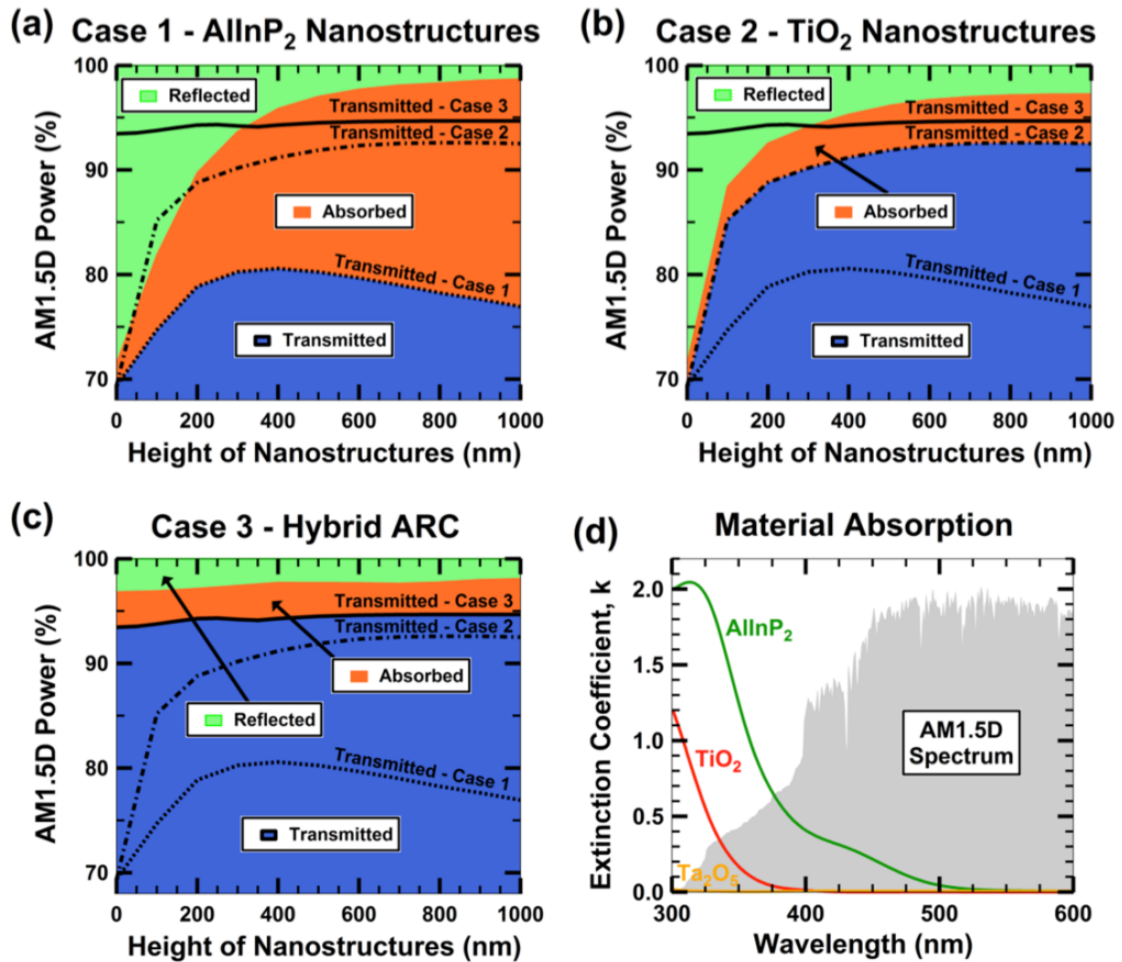
Figure 3.9: Plots showing transmitted, absorbed, and reflected power for (a) Case 1 – $AlInP_2$ nanostructures, (b) Case 2 – TiO_2 nanostructures, (c) Case 3 – The hybrid ARC design. (d) Plot showing absorption for the materials used in these nanostructure designs [63].

75

These plots illustrate the tradeoff between absorption in the nanostructures and increased Fresnel reflection at the $AlInP_2$ window layer interface. Case 1 is limited by absorption, which increases rapidly as the nanostructures become tall due to the high extinction coefficient of $AlInP_2$. Case 2 is limited by reflection due to index mismatch between TiO_2 and $AlInP_2$. Case 3 is the best performing design, achieving low absorption and low reflection [63].

Figure 3.9(d) shows material absorption for $AlInP_2$, TiO_2, and Ta_2O_5. Absorption loss is closely related to the extinction coefficient, k, and can be quantified using Equation 3.6 [63].

$$Absorption\ Loss = 1 - e^{-4\pi kD/\lambda} \qquad (3.6)$$

Where k is the extinction coefficient, D is the distance traveled through the material, and λ is the wavelength of light in vacuum. The optical model includes absorption loss in the 20nm-thick $AlInP_2$ window layer, which accounts for a power loss of 2-3% for all configurations [63].

Table 3.2 shows reflected power, absorbed power, and transmitted power for each case when the nanostructure height is optimal. For comparison, results from the multilayer ARC and no ARC are also shown. The hybrid approach (Case 3) is the most effective antireflective nanostructure design and the only nanostructure design that outperforms an optimal multilayer ARC [63].

Table 3.2. Antireflection Coating Comparison

Configuration	Nanostructure Height	Reflected Power	Absorbed Power	Transmitted Power
No ARC	0 nm	28.4%	2.2%	69.4%
Multilayer ARC	0 nm	3.2%	3.4%	93.4%
Case 1 – $AlInP_2$	400 nm	4.1%	15.3%	80.6%
Case 2 – TiO_2	800 nm	2.8%	4.6%	92.6%
Case 3 – Hybrid	900 nm	1.8%	3.5%	94.7%

The hybrid ARC design increases transmitted power by 25.3% absolute compared to no ARC, 14.1% compared to $AlInP_2$ nanostructures, 2.1% compared to TiO_2 nanostructures, and 1.3% compared to an optimal multilayer ARC. Additionally, scattering loss from the nanostructures is expected be lowest for the hybrid design since the features are placed into a low-index SiO_2 layer. This can be understood from Equation 3.2 [63].

Figure 3.10 shows AM1.5D power loss as a function of wavelength for each of the three cases. The box to the right shows the top subcell power loss for a top junction bandgap of 1.8 eV and 1.9 eV.
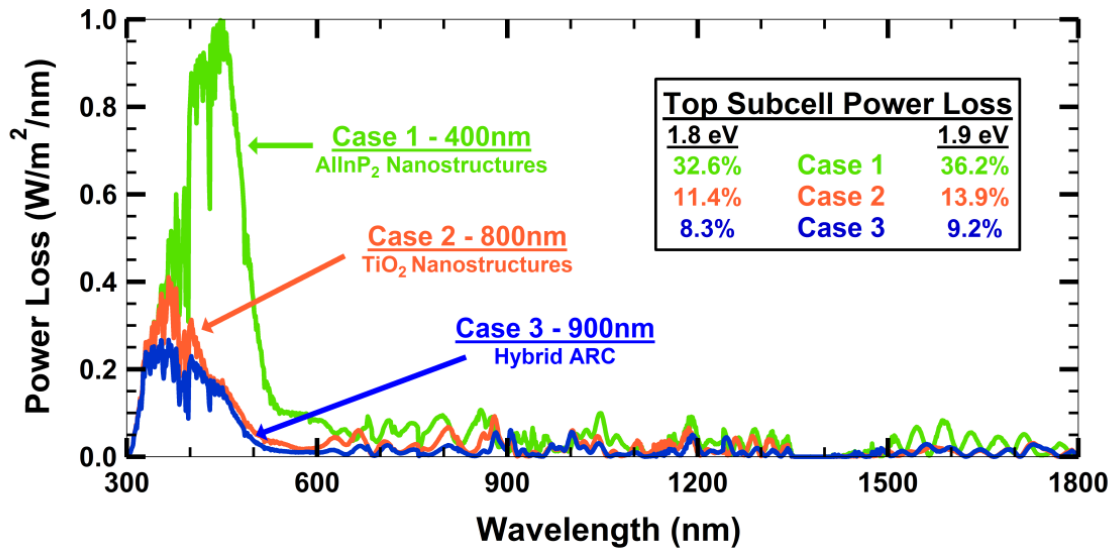
Figure 3.10: Plots showing the sum of reflection and absorption losses as a function of wavelength for the best configuration from Cases 1, 2, and 3. The percentage of power lost in the top subcell is shown in the box on the top right of the plot [63].

The largest optical loss for each case occurs at short wavelengths, leading to a decrease in the power available to the top subcell. Absorption loss is most significant for the $AlInP_2$ nanostructures, which absorb a significant amount of light at wavelengths less than 500 nm. The TiO_2 nanostructures absorb light below 400 nm, and also have a higher reflectance than the hybrid design across most of the solar spectrum [63].

Cell Efficiency Model

Transmittance for each of the three cases is incorporated into a cell efficiency model. Efficiency is calculated for two different top cell bandgaps (1.8 and 1.9 eV). In the model, the bandgaps for the second and third subcell are varied to maximize efficiency, and the bandgap of the bottom subcell is set at 0.74 eV. Some assumptions in the model include the conversion of all absorbed photons into photocurrent, a concentration of 1000 suns, and a temperature of 300K. Junction dark currents are computed by the Shockley-Queisser method, and subcell thinning is allowed when it is beneficial for the design [63].

Figure 3.11 shows the results from the cell efficiency model. We see that there is an excellent correlation between cell efficiency and power loss.
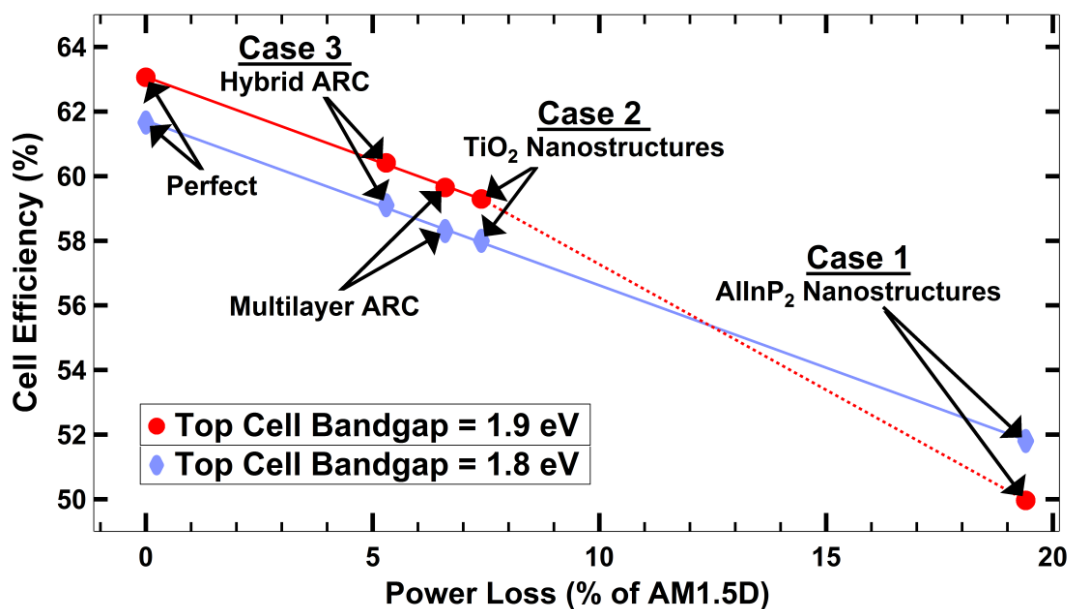
Figure 3.11: Correlation between AM1.5D power loss and modeled cell efficiency at 1000 suns concentration. The two solid lines show linear fits to the data. The dashed line shows where the linear correlation between cell efficiency and power loss breaks down due to undersupply of photons to the top cell [63].

The linear correlation between power loss and modeled cell efficiency can be explained by cell thinning. Typically, a top subcell composed of $InGaP_2$ is oversupplied with photons

78

in a multijunction cell. As long as the top junction is oversupplied, it is possible to distribute light to the other junctions until optimal subcell currents are achieved. With cell thinning allowed, efficiency is linearly correlated with optical loss from the antireflective nanostructures [63].

When the $AlInP_2$ nanostructures are placed onto a cell with a 1.9 eV top junction bandgap, the top subcell becomes undersupplied with photons. The large efficiency drop observed for this case occurs as the top subcell becomes current limited to a value much lower than what is optimal for a quadruple-junction configuration [63].

The absolute efficiencies from Figure 3.11 represent an upper limit. While these efficiencies may not be possible to achieve, their relative values provide a metric to evaluate the quality of the optical design. Furthermore, the linear correlation between cell efficiency and power loss in the antireflective nanostructures indicates that an optical design that maximizes transmission into the solar cell is near ideal when cell thinning can be used as a tool to optimize subcell currents [63].

3.4 Fabrication of Hybrid Optical Coatings

The hybrid design has been placed onto bare GaN and alumina substrates, epilayers of $AlInP_2$ and $GaInP_2$, and on an upright GaAs single-junction active photovoltaic device. In this section, we will detail the fabrication process that we developed for placing the optimized hybrid AR designs onto these samples [69,76,86].

The first step in the fabrication process is to deposit the optimized optical coating onto the front surface of the sample. We used a VEECO ion beam assisted sputter deposition system (IBD), shown in Figure 3.12, to deposit all of the optical coatings in this Chapter

because of the high quality and repeatability of the dielectric films (TiO_2, Ta_2O_5, SiN_x, and SiO_2) that this system can deposit [86,88].
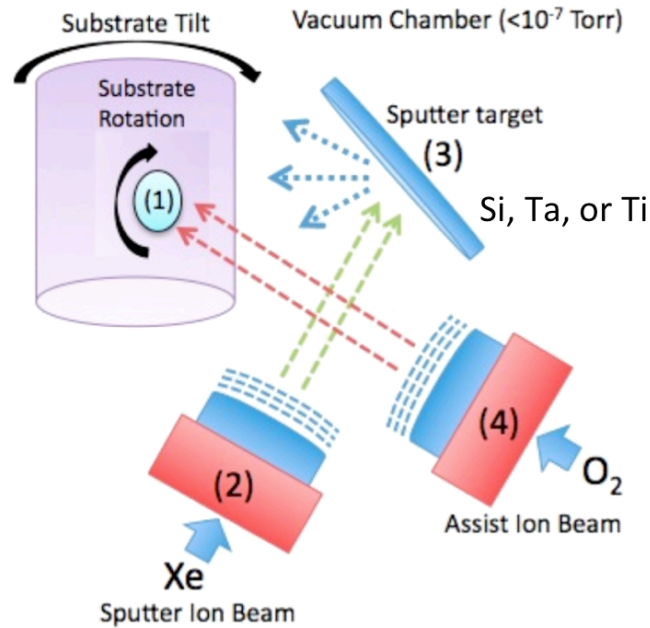
Figure 3.12: Schematic of the Veeco Nexus Ion Beam Assisted Sputter Deposition system that we use to deposit all of the optical coatings in this chapter.

For broadband ARCs, we are able to obtain the highest performance using only three thin-film materials (TiO_2, Ta_2O_5, and SiO_2). On the top surface of the thin-film layers, we deposit an additional 1-2 μm of SiO_2 to accommodate the antireflective nanostructures. For imprinting, it is important that this SiO_2 layer rises above all other features on the sample. This is especially difficult for solar cells with very tall metal grids, which are common for multijunction devices designed for high-concentration. For the single-junction GaAs solar cell, we mask off the metal grids and contact pads during deposition to ensure that the dielectric film will rise above these features [86].

We use nanoimprint lithography (NIL) to transfer the AR nanostructure pattern from a master stamp to our samples, where all of the imprinting was done using a Nanonex

imprinting tool. Our nickel master stamp was fabricated by the company NIL Technology, and the nanostructures were arranged in a hexagonal array with a feature height and pitch of ~350nm. Figure 3.13 shows an atomic force microscope (AFM) profile of the moth-eye pattern on the nickel master showing the geometry of the features [86].
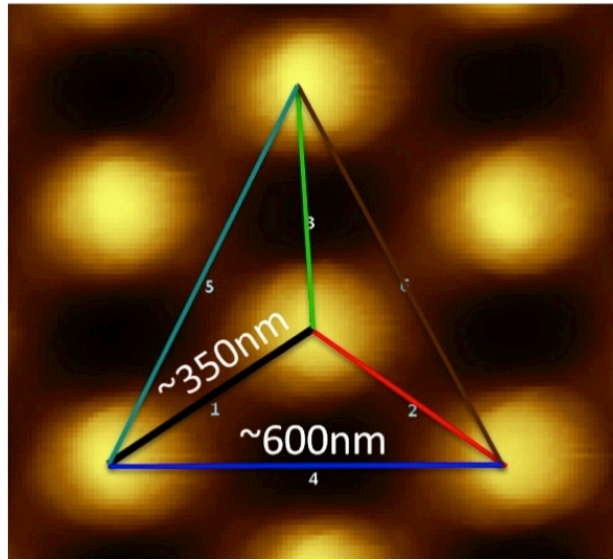
Figure 3.13: AFM profile of the moth-eye pattern on the nickel master stamp showing the hexagonal geometry and the spacing between adjacent features. The height of the peaks that we measured was ~350nm.

At first, we used thermal NIL to transfer the moth-eye pattern from the master stamp to a thin resist layer. This process requires high pressures (400-500 psi), high temperatures (120-140°C), and a rigid stamp. Unfortunately, these high temperatures and pressures have the potential to damage the photovoltaic device, and the rigidity of the stamp makes it difficult to imprint over non-planar features such as the metal grids of a solar cell [89,90].

For this reason, we moved to an alternative process that utilizes ultraviolet (UV) NIL. With UV NIL, the imprinting process can be done at low pressure (2-10 psi), low temperature (20-30°C) and can more readily use a flexible imprinting stamp [91,92]. Figure 3.14 details the UV NIL process [86].
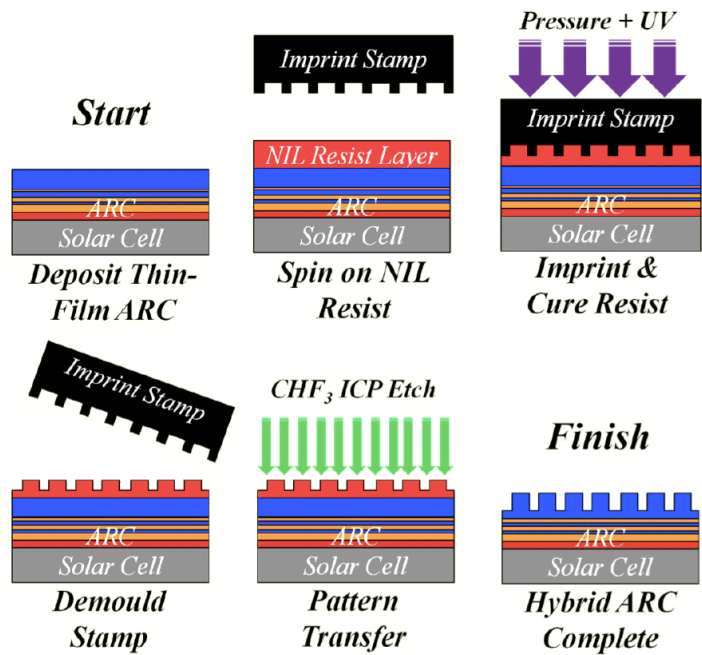
Figure 3.14: Diagram of the UV NIL process used to transfer the AR nanostructures onto our samples [86].

For the UV NIL process, AR nanostructures from the nickel master are first transferred to a flexible and transparent polydimethylsiloxane (PDMS) sample using OrmoStamp, a hybrid polymer developed by Micro Resist Technology. The flexible stamp allows for conformal imprinting even when the surface is not flat, as is the case for most solar cells. A perfluorodecyltrichlorosilane (FDTS) anti-stick treatment is then applied to the PDMS secondary stamp to assist with demoulding [86].

A UV imprint resist (MR-UVCur21) is spin coated onto the sample, and the flexible PDMS stamp is placed pattern down onto the imprint resist. The sample is imprinted at a pressure of 5 psi for 2 minutes so that the UV imprint resist can fill the voids in the PDMS stamp. A UV lamp is then turned on for 20 seconds to cure the resist. After the NIL process is complete, the PDMS stamp is peeled off of the sample, leaving its negative image in the resist layer. After imprinting, the nanostructures have a feature height and pitch of approximately 350 nm [86].

82

An inductively coupled plasma etch is then used to transfer the pattern to the underlying SiO$_2$ layer using a CHF$_3$ etch chemistry. The selectivity of resist:SiO$_2$ is approximately 1:2, allowing the feature height to increase to roughly 700 nm. After pattern transfer, the NIL resist layer is removed [86].
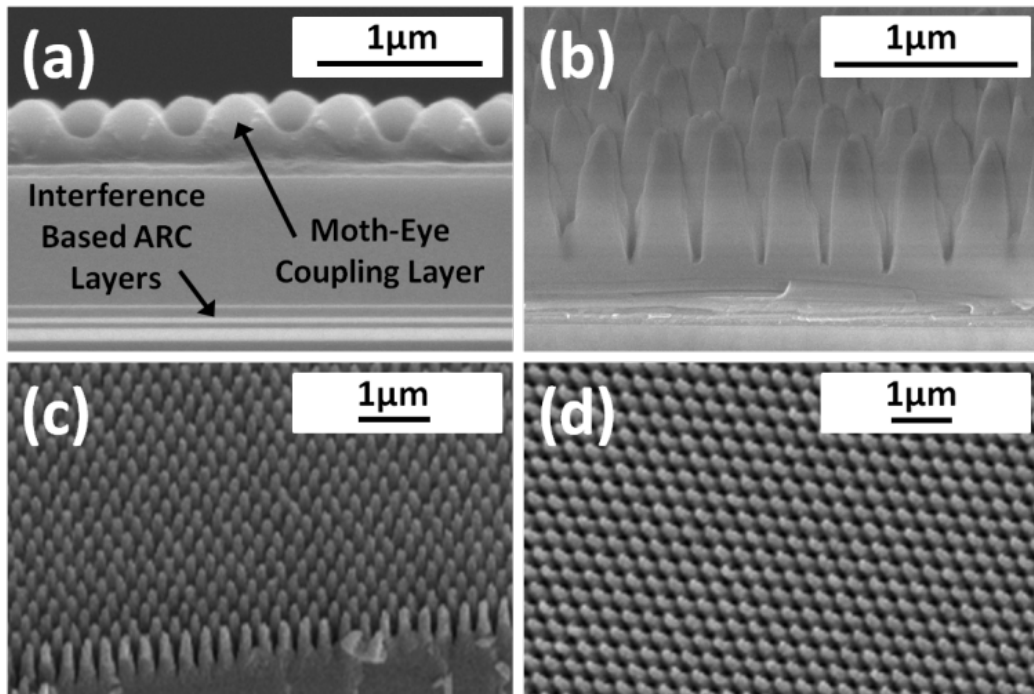
Figure 3.15: SEMs of the hybrid moth-eye design. (a) Cross-sectional SEM showing the multilayer ARC and imprinted moth-eye pattern. (b) SEM of the sample after the ICP etch. (c) SEM of the sample showing excellent replication of the moth-eye pattern. (d) Top view SEM showing the hexagonal geometry of the nanostructures [69].

Figure 3.15(a) shows a cross-sectional SEM of the hybrid ARC after imprinting of the resist layer. The period and height of the moth-eye structure is approximately 350 nm. Figure 3.15(b) shows the sample after the ICP etch and with the resist layer removed. This image allows us to estimate the geometry of the features for modeling their antireflective properties. The measured height of the final moth-eye pattern is approximately 750 nm, and the fill factor appears to increase smoothly from the top of the structure to the bottom without any abrupt jump in the effective index of refraction. Figure 3.15(c-d) shows a larger

section of the pattern after imprinting and etching. These images exhibit the excellent pattern fidelity of the final replicated structure [69,86].

3.5 Results and Discussion

This section will highlight our results for hybrid optical coating designs that have been placed onto bare GaN and alumina substrates, epilayers of $AlInP_2$ and $InGaP_2$, and on an upright GaAs single-junction active photovoltaic device. These results are compared to optimized multilayer thin-film optical coating designs. Specular reflectance and transmittance near normal incidence (8°) are measured using a Cary 500 UV-VIS-NIR Spectrophotometer, and these results are compared to optical models.

Figure 3.16 shows the measured and simulated reflectance for a 2-layer ARC, multilayer ARC, and hybrid ARC with nanostructures for an epilayer of $InGaP_2$ grown on a GaAs substrate. While the measurements do not account for diffuse reflections, close agreement between simulated and measured specular reflectance can provide indirect evidence that the moth-eye layer is not scattering a significant amount of light [69].
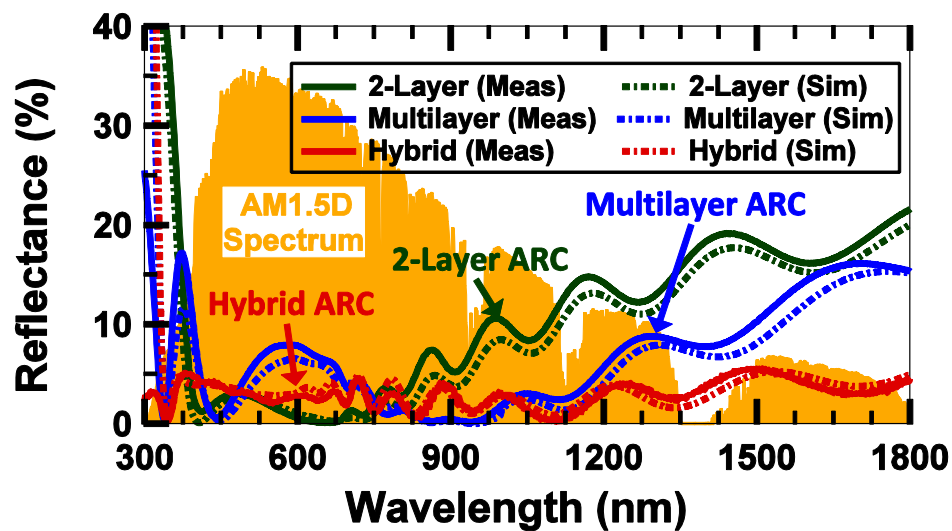
Figure 3.16: Plot showing the measured and simulated reflectance for a 2-layer ARC, multilayer ARC, and hybrid ARC for an epilayer of InGaP grown on GaAs [69].

These simulations take into account the interface between $InGaP_2$ and GaAs. This interface is responsible for the interference fringes that begin around 675nm, corresponding to the bandgap of $InGaP_2$. The period of these fringes is linked to the $InGaP_2$ layer thickness.

Since the merit function is weighted to the direct spectrum, a measure of AM1.5D power loss will provide a good comparison between each design. Using this metric, we find that the hybrid ARC performs much better than the other two designs [69]. The 2-layer ARC specularly reflects 47.4 W/m^2, corresponding to 5.5% of the AM1.5D power in the 4-J wavelength range. The 4-layer ARC reflects 38.6 W/m^2, or 4.5% of the power in the 4-J range. In comparison, the hybrid ARC specularly reflects just 24.0 W/m^2, corresponding to a 2.8% power reflection [69].

Note that the measured reflectance for the hybrid ARC starts to deviate from the simulated value below 350 nm. This occurs because these wavelengths are approaching the lateral dimensions of the nanostructures. Under these conditions, less light will be specularly reflected due to the onset of the 1st diffraction order for the nanostructures. Also note that if the nanostructures were scattering a significant amount of light at longer wavelengths, we could expect to see a similar disagreement between the measurements and the model [69].

Since not all sunlight is normally incident on the surface of the earth, most photovoltaic systems could also benefit from an ARC design with excellent wide-angle performance. A V-VASE Ellipsometer was used to measure reflectance of the hybrid and multilayer ARC as a function of angle. Figure 3.17 compares the measurements to our optical model from 15 to 60 degrees. These values are acquired at a wavelength of 500 nm, and are averaged from s and p polarization data [69]. While Figure 3.17 shows that the hybrid ARC maintains a lower reflectance than the multilayer ARC across the entire measured angular range, it is

important to remember that these measurements are taken at a single wavelength. These data therefore do not show a full comparison between the two designs [69].
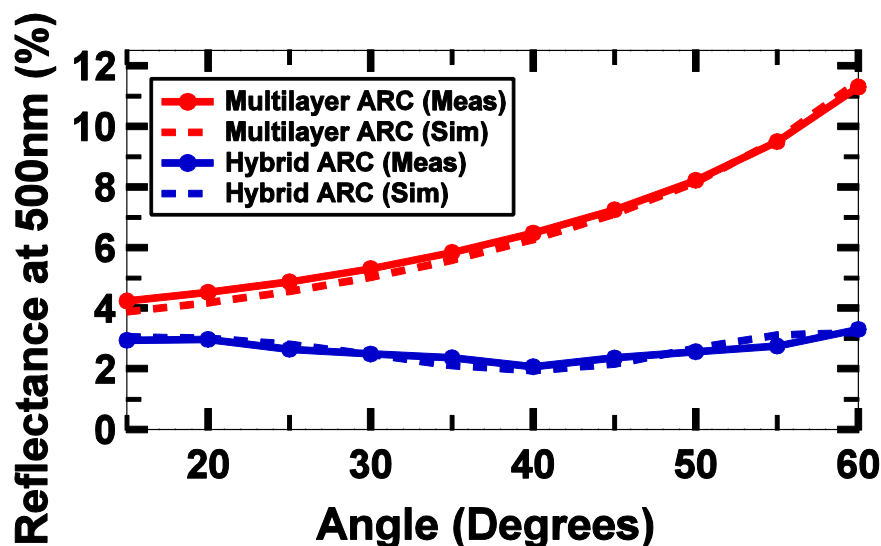
Figure 3.17: Plot showing the measured and simulated reflectance for the hybrid and multilayer ARC at a wavelength of 500nm [69].

The most important result from Figure 3.16 and Figure 3.17 is that they show that the hybrid design is behaving very close to what we would expect from our optical model. These results therefore indicate that the relative efficiency improvements that we discussed in Chapter 3.3 could be realized in practice for multijunction photovoltaics [69].

Figure 3.18 shows the measured and modeled reflectance of a hybrid ARC placed onto a sample consisting of ~500 nm of $AlInP_2$ grown on a GaAs substrate. The reflectance of the uncoated sample is also shown for comparison. The measured AM1.5D reflected power is reduced from 27.5% for the uncoated sample to 2.6% for the sample with a hybrid ARC. There is good agreement between the simulated and measured specular reflectance, which again provides indirect evidence that the nanostructures are not scattering a significant amount of light from the solar spectrum [86].
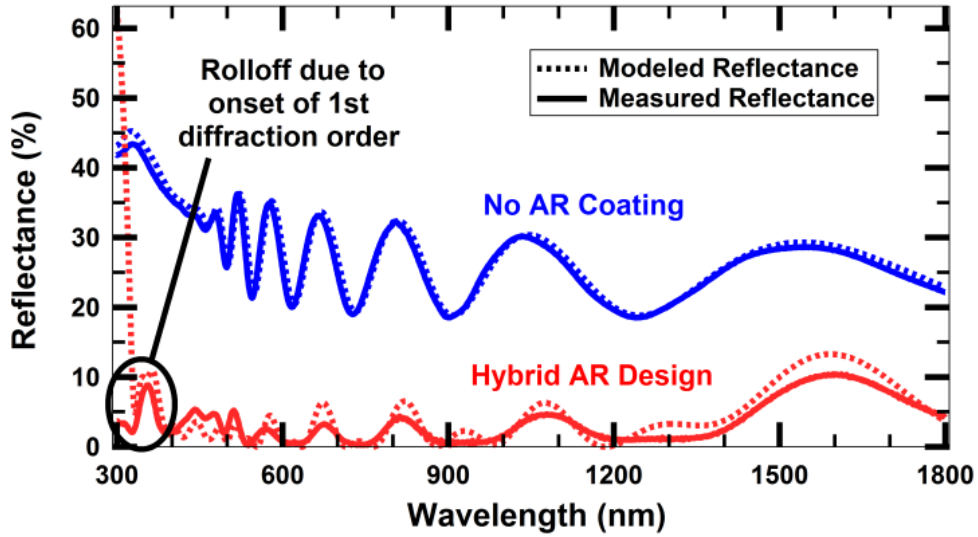
Figure 3.18: Plot showing the measured and modeled reflectance for an AlInP$_2$/GaAs sample with and without a hybrid AR design [86].

For wavelengths shorter than 350 nm, we start to see a big variation between the modeled and measured specular reflectance, similar to what we observed for the hybrid design placed on the InGaP$_2$ epilayer. This occurs because the nanostructures begin to scatter and diffract light with wavelengths shorter than 350 nm, a size corresponding to the lateral dimensions of the features. This results in attenuation for the measured reflectance but not the modeled reflectance. When simulating the reflectance for the hybrid ARC for both of these designs, we assume that the nanostructures are perfect and that the reflection from air-SiO$_2$ is negligible [86].

Figure 3.6(d) showed a two-dimensional profile of the nanostructures from the hybrid design placed onto a sapphire substrate, as measured on a VEECO Dimension 3100 AFM with high aspect ratio AFM tips that are 2 μm tall. With this profile, we were able to extract the areal fraction, F, of SiO$_2$ for a large number of thin-horizontal slices. This data is input into Equation 3.3 and used to calculate the refractive index profile for the fabricated hybrid design. The nanostructures are modeled using a 140-slice approximation, which we

previously showed is a very accurate representation of the optical properties for the nanostructure layer. This method was used to extract the effective index profile for the nanostructures for the hybrid design placed onto both a sapphire and GaN substrate [76].

Figure 3.19 shows the measured and simulated reflectance for single side polished (SSP) sapphire and gallium nitride (GaN) samples with an optimized hybrid ARC, a multilayer ARC, and no optical coating. Specular reflectance is again measured at an incidence angle of 8° using a Cary 500 UV-VIS-NIR spectrophotometer, and black paint is placed onto the roughened backside of the samples to minimize unwanted reflections from the unpolished surface [76].
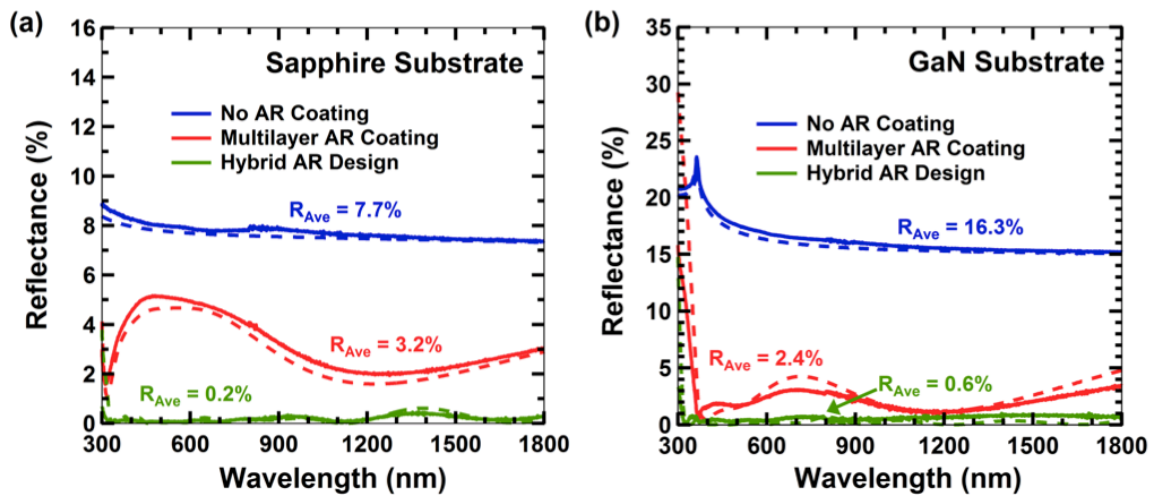
Figure 3.19: Plot of the simulated (dashed lines) and measured (solid lines) reflectance spectrum showing the broadband performance of a hybrid AR design and an optimal multilayer ARC for (a) sapphire and (b) gallium nitride [76].

It is evident that the hybrid design can outperform a conventional multilayer ARC. For 300-1800 nm light, the average measured reflectance is just 0.2% for the design placed on sapphire and 0.6% for the design placed on gallium nitride. This represents a 16x decrease in broadband reflectance for sapphire and 4x decrease for gallium nitride compared to an optimized thin-film ARC [76].

The hybrid design also maintains its quality to very wide incidence angles. Contour plots showing reflectance as a function of both angle and wavelength are shown in Figure 3.20 for the hybrid ARC and multilayer ARC on SSP sapphire. Reflectance is measured using a V-VASE ellipsometer for incidence angles between 15° and 85°. The values shown are averaged from the s- and p-polarization components of light [76].
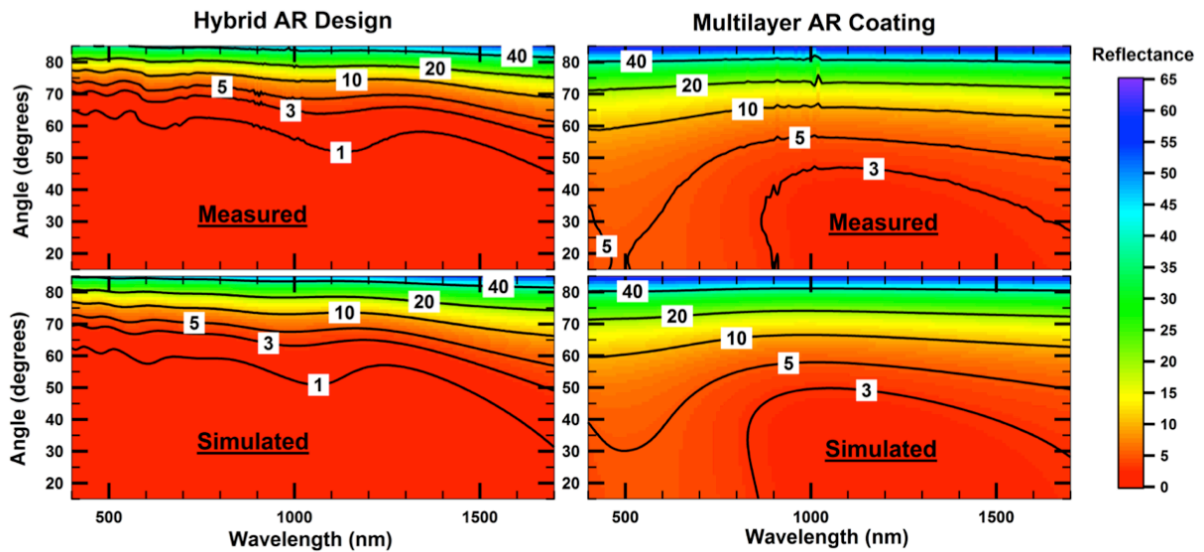
Figure 3.20: Contour plots showing simulated and measured reflectance as a function of both angle and wavelength for (left) the optimal hybrid AR design and (right) the optimal multilayer ARC [76].

We measure less than 1% reflectance at all wavelengths out to an angle of 45° for the hybrid design. In comparison, the reflectance of the multilayer antireflection coating does not drop below 1% for any wavelength or angle measured. The hybrid design achieves much better wide-angle performance than a conventional multilayer ARC for a couple reasons. First, the nanostructure layer has excellent wide-angle antireflective properties due to its smoothly varying refractive index profile. Since light is partially reflected at every point in the structure, destructive interference will be maintained even at wide incidence angles. Second, wide-angle light will be bent closer to normal incidence in SiO_2 due to Snell's law

of refraction, and the magnitude of the partial reflections at the thin-film interfaces will not increase as rapidly as they would for the air-SiO$_2$ interface [76].

We also note that there is excellent agreement between the measured and simulated reflectance for both designs. This suggests that our model accurately describes the optical properties of the nanostructures, and also provides indirect evidence that the nanostructure layer is not scattering or diffracting a significant amount of light [76].

To further investigate scattering and diffraction in the nanostructures, we measure reflectance & transmittance for a double side polished (DSP) sapphire sample with a hybrid design placed on both surfaces. These measurements are shown in Figure 3.21, where loss from absorption, scattering, and diffraction can be quantified as the amount of light that is not specularly reflected or transmitted through the structure (1 - T - R) [76].
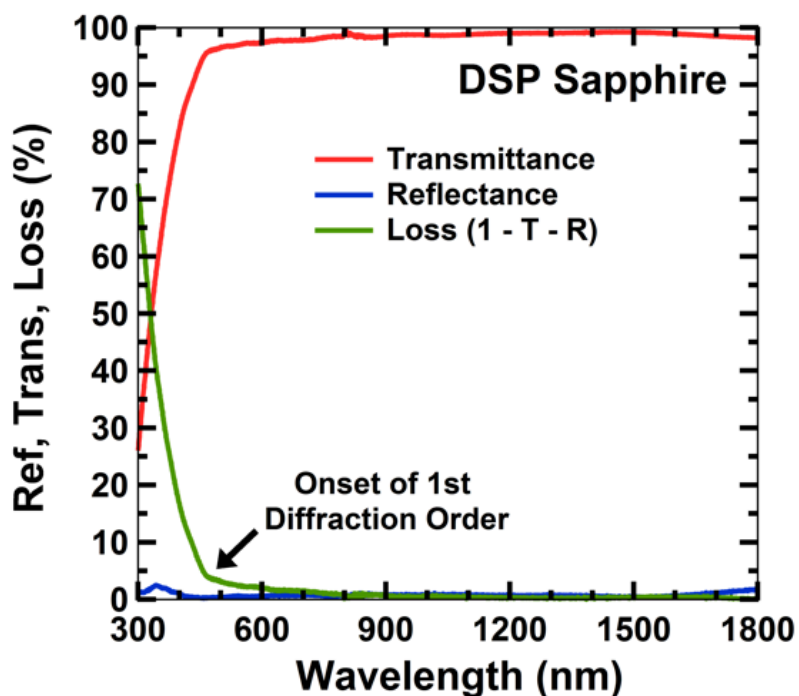
Figure 3.21: Plot showing reflectance, transmittance, and optical loss (1 − T − R) for a hybrid AR design placed on both sides of a DSP sapphire sample. Optical losses can be attributed to absorption, scattering, & diffraction [76].

These optical losses are very small for most of the wavelengths considered, averaging just 0.7% for 500-1800nm light. However, we observe a large increase in optical loss starting around 450-500 nm. This wavelength range corresponds to the onset of the 1st diffraction order. To attain higher transmittance between 300 and 500 nm, it is necessary to further reduce the lateral dimensions of the nanostructures. It is important to emphasize that both scattering and diffraction loss are minimized when the nanostructures are composed of materials with a low refractive index, such as SiO_2. For this reason, we expect that our hybrid design will have lower optical losses than AR nanostructures placed directly into the substrate material [76].

Figure 3.22 shows preliminary I-V characteristics for a single-junction GaAs solar cell before and after the hybrid AR design was placed onto the front surface of the sample [86].
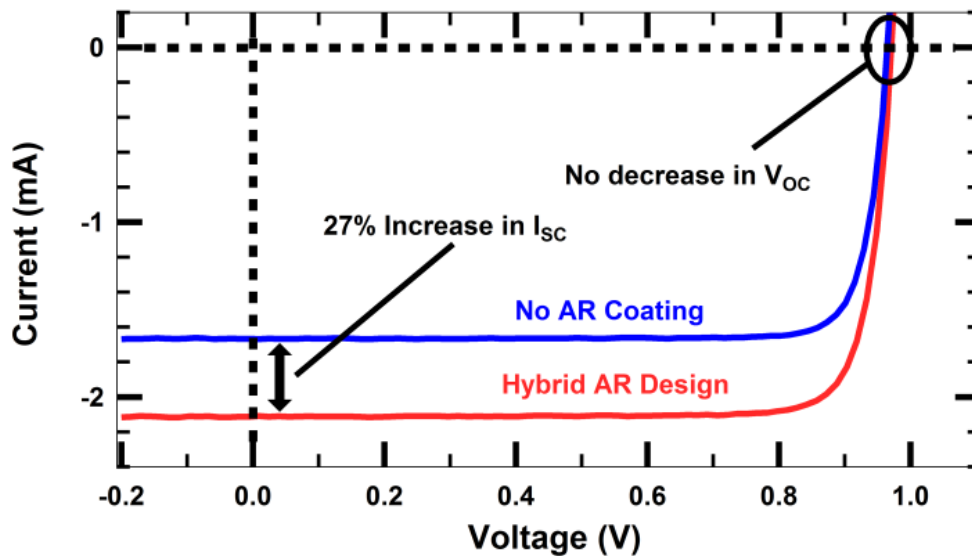
Figure 3.22: Plot showing the I-V characteristics of a single-junction GaAs cell before and after placing a hybrid AR design onto the cell [86].

We measure a 27% increase in the I_{SC} compared to the uncoated device. Further improvements in I_{SC} are expected with a redesigned mask and reoptimized thin-film coating

design. Additionally, note that there is small increase in the cell's open circuit voltage (V_{OC}). This is an indication that the fabrication process is not damaging the photovoltaic device [86].

3.6 Chapter Summary

In this chapter, we discussed the design of a hybrid optical coating that combines nanostructures with a thin-film ARC. The chapter began by examining the physics of AR nanostructures and we developed an optical model to describe the behavior of light incident on the nanostructure surface. To evaluate the performance of various standalone nanostructure configurations for solar cell applications, we modeled transmitted, absorbed, and reflected AM1.5D power as the nanostructure height was varied. We found that maximum transmission is possible for the nanostructures composed of TiO_2, but importantly an optimized thin-film ARC outperforms every standalone nanostructure design considered. The chapter then describes the benefits of combining AR nanostructures with thin-film optical coatings, and with this hybrid design we are able to increase transmitted power by 2.1% compared to a standalone nanostructure design, and 1.3% compared to an optimal multilayer ARC. For a multijunction solar cell, this should correspond to an increase of ~0.5-1% in absolute cell efficiency. The chapter then details our fabrication process for the hybrid design. We use ion-beam assisted sputter deposition to deposit high-quality thin-film optical coatings composed of TiO_2, Ta_2O_5, and SiO_2. To replicate AR nanostructures, we use a UV nanoimprint lithography process. Measurements of the hybrid design for various samples are compared to our optical model, and we find that there is excellent agreement between the two. Designs that utilize this hybrid approach can achieve near-perfect

broadband and wide-angle antireflective properties, minimizing reflection losses to just 0.2% on sapphire and 0.6% on gallium nitride for 300-1800nm light.

Chapter 4: Solar Cells for High-Temperature Operation

There are a number of space and terrestrial applications that would benefit from the development of photovoltaic devices that can operate at high-temperatures. For example, a photovoltaic-thermal (PV-T) hybrid solar collector could utilize a high-temperature photovoltaic topping device to simultaneously achieve dispatchability and a high sunlight-to-electricity efficiency [6,29,30]. For even the most efficient solar cells, a significant fraction of incoming solar energy will be converted into heat within the semiconductor [39,40,43-45,93-96]. A hybrid solar converter could transfer this heat from the photovoltaic cell to a thermal collector that could then provide storage and dispatchable energy to the electrical grid using a conventional generator. A near-sun space mission would also require the development of robust solar cells that remain efficient at elevated temperatures before photovoltaic power generation can be viably considered for these missions. One example is a mission to Mercury, which would require photovoltaic cells to operate at temperatures of about 450°C and light intensities ~10x higher than in earth orbit [97,98].

The development of photovoltaic devices for these applications introduces a number of challenges inherent to high-temperature operation. Raising the operating temperature will increase the J_{01} and J_{02} dark currents exponentially, leading to a significant reduction in the open-circuit voltage of a solar cell [39,40,95]. High-temperature operation could also accelerate material degradation, reduce long-term reliability, and necessitate the development of a stable metallization and cell encapsulant. These challenges need to be carefully explored and understood before any photovoltaic device can be viably integrated into a system that requires high-temperature operation.

In this chapter, we will discuss the development of solar cells for high-temperature operation. The chapter will begin with a brief motivation for why we are investigating the temperature-dependent performance of III-V solar cells. We will then present a model that explores the efficiency of single-junction and dual-junction solar cells as a function of both temperature and the room-temperature bandgap of each subcell. One of the most significant challenges to designing a dual-junction solar cell for high-temperature operation was the development of a high-bandgap (2.0eV) AlGaInP solar cell that is required for high-temperature operation. This chapter will detail the design of a 2.0eV AlGaInP solar cell with the lowest bandgap-voltage offset ($W_{OC} = E_g/q - V_{OC}$) of any AlGaInP solar cell reported to date. Finally, we will discuss some of the critical cell development challenges that we faced, including the development of a stable tunnel junction and front metallization.

4.1 Motivation

The solar energy landscape has experienced a dramatic evolution over the past decade. Cost reductions and advances in technology have helped spur significant growth, with the United States seeing a hundredfold increase in net electricity generation from photovoltaics between 2009 and 2014 [4]. Today, photovoltaics can provide electricity to the grid at or below grid parity in many locations. We should expect that electricity from photovoltaics will continue to get cheaper, with price reductions driven largely by technological advances and economies of scale [6,7,99]. While photovoltaics are poised to become perhaps the most cost-effective form of electricity worldwide [100], the penetration of photovoltaics will ultimately be limited unless photovoltaics can be coupled with cost-effective energy storage technologies [9,10,28].

Germany, which generates approximately 6% of its annual electricity from

photovoltaics, already experiences times when the wholesale price of electricity becomes negative due to an oversupply of electricity from photovoltaics [101-103]. This has led Germany to adopt a generous incentive program that subsidizes the use of energy storage when tied to photovoltaic systems [104]. On the other side of the world in California, modeling of the grid has shown that photovoltaic power will need to be curtailed at times of high solar flux once it supplies approximately 10% of California's annual electricity needs [10]. These examples tell us that as photovoltaic energy is added to the grid, its marginal economic value will decrease due to its fundamental intermittency. Figure 1.4 (shown again here in Figure 4.1) shows the results of one study that explores how the marginal economic value of photovoltaic energy will decrease as its contribution to the electricity supply increases [28].
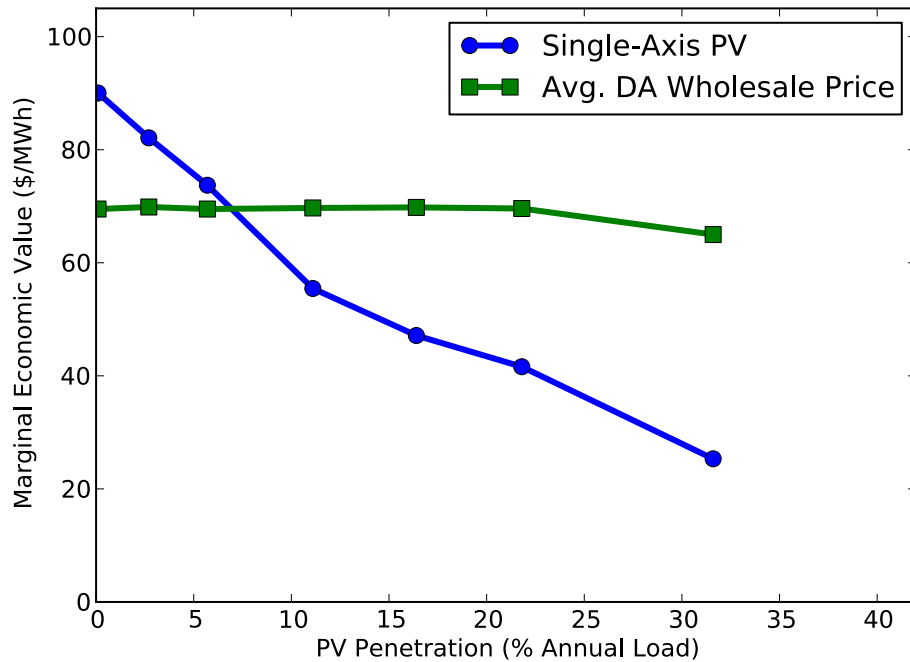
Figure 4.1: Plot showing the marginal economic value of photovoltaic energy as a function of the penetration of photovoltaics [28].[18]

---

[18] Reproduced with permission from [28]. Copyright © 2013, IEEE.

The solution is to develop cost-effective storage technologies that can store excess photovoltaic energy and dispatch electricity to the grid when it is needed. While energy storage technologies exist, they are not cost-effective today and would significantly raise the system cost of a photovoltaic installation [105-107]. One promising approach is to couple photovoltaics with low-cost thermal energy storage. Concentrating Solar Power (CSP) systems already use thermal energy storage to provide electricity to the grid after the sun goes down [108]. While the low marginal cost of adding thermal storage to a CSP plant gives these systems a significant advantage over photovoltaics when dispatchability is required, CSP is currently too expensive to compete with conventional energy sources.
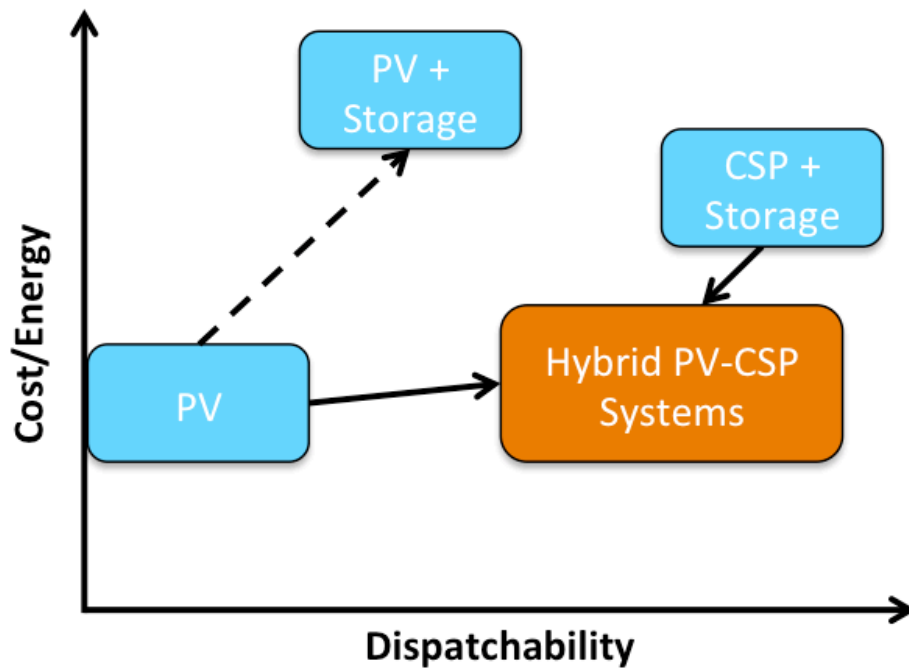
Figure 4.2: Diagram showing the different advantages of PV and CSP and how combining the two can ideally lead to the best of both worlds.

One possible solution is to combine photovoltaics with CSP into a hybrid system that can achieve high dispatchability at a low cost, as was shown in Figure 1.6 (shown again here

97

in Figure 4.2). While photovoltaics have a low-cost today, they provide virtually no dispatchability. Adding storage to photovoltaics can increase their dispatchability, however this would significantly increase the system cost. CSP on the other hand has good dispatchability, but is too costly to compete with conventional energy sources. A hybrid system would combine the two technologies to achieve low cost and high dispatchability.

There are two types of hybrid systems that are being developed. The first uses lateral spectrum splitting to reflect high-energy photons to a photovoltaic cell while transmitting low energy photons to a thermal converter that can then provide dispatchable electricity to the grid. The advantages of this type of system include that it exploits the strengths of each part of the spectrum. That is, photovoltaics are more efficient at converting high-energy light into electricity while CSP is better at converting low-energy light into heat [109].

The second type of system, which we focus on in this dissertation, utilizes high-temperature topping cells [6,29,110]. Figure 4.3 shows a schematic diagram of how a high-temperature photovoltaic device could be integrated into a photovoltaic thermal hybrid solar collector.
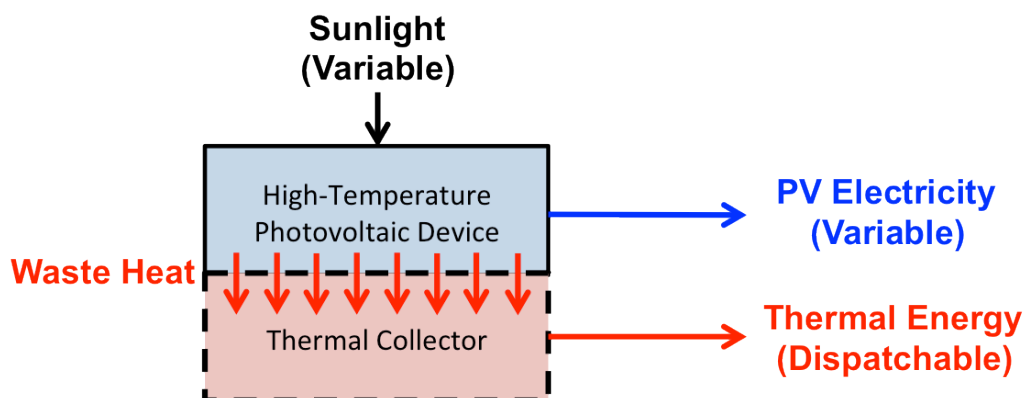
Figure 4.3: Diagram showing how a high-temperature photovoltaic topping device could be integrated into a photovoltaic thermal hybrid solar collector. Energy losses, which are primarily converted into heat, can be transferred to a thermal collector that can drive a conventional generator to provide dispatchable energy to the electrical grid [111].

One of the biggest advantages of this type of system is that it enables the recovery of in-cell thermal losses, which can be stored and converted into usable energy. For even the most efficient solar cells, a significant fraction of incoming solar energy will be converted into heat within the semiconductor [39,40,43-45,93-96]. A hybrid solar converter could transfer this heat from the photovoltaic cell to a thermal collector that could then provide storage and dispatchable energy to the electrical grid using a conventional generator.
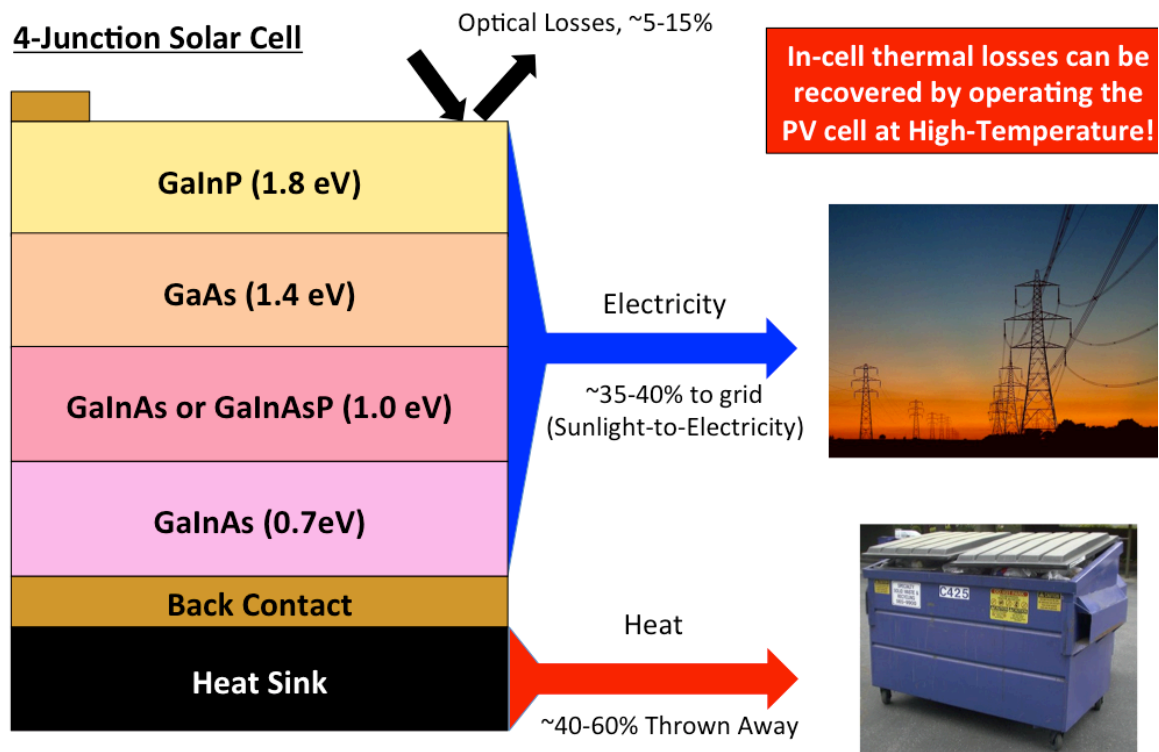
Figure 4.4: Diagram showing where solar energy ends up in a highly efficient CPV system. While module efficiencies of 35-40% have been realized for a number of designs, there are still significant in-cell thermal losses of ~40-60% for these systems. These in-cell thermal losses can be recovered by operating the solar cell at high-temperatures.

To understand this better, consider where solar energy ends up for some of the world's most efficient CPV systems, as is shown in Figure 4.4. All CPV modules will inevitably have some optical losses, on the order of ~5-15%, and this number will be highly dependent

on the system design [112]. For the most efficient CPV systems, ~35-40% of solar energy is converted into electrical energy that can be transferred to the grid [23,113]. While these are very good efficiencies (20% module efficiencies are considered good for most other PV technologies), a significant amount of the original solar energy still ends up being converted into heat in the semiconductor, and for a CPV system this heat is dissipated with a heat sink and is essentially thrown away [45]. However, these thermal losses can be recovered by operating the photovoltaic cell at high temperatures [6].
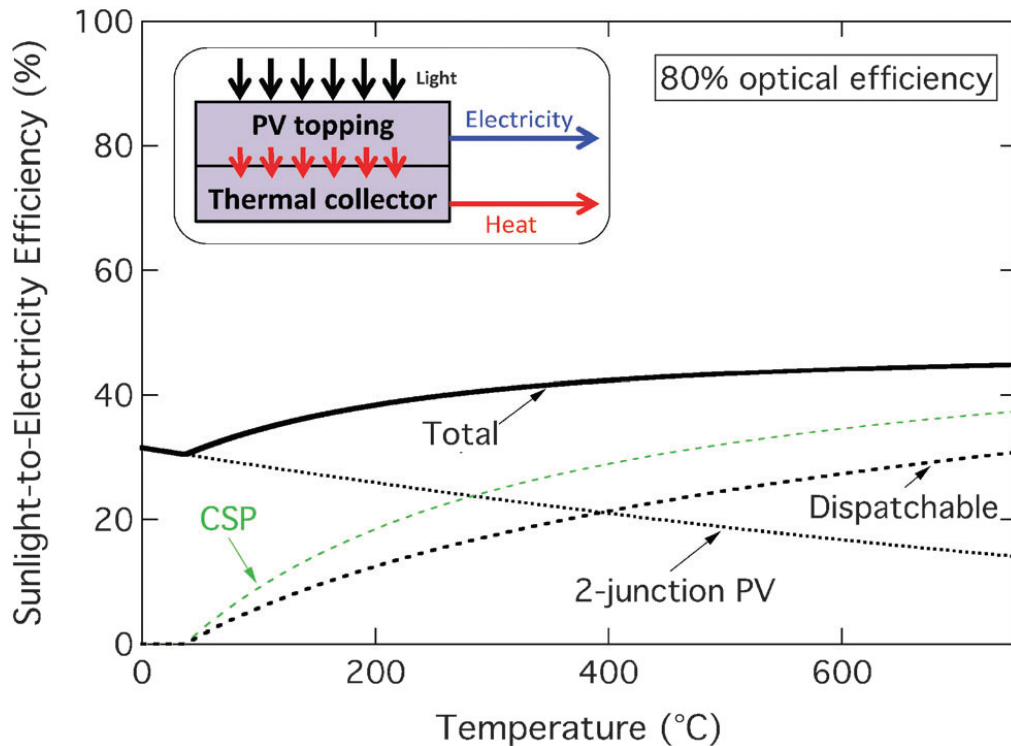
Figure 4.5: Diagram showing the practical sunlight-to-electricity as a function of operating temperature for a PV-topping hybrid system. This shows that while the efficiency of a photovoltaic device will decrease at high-temperatures, the efficiency of a CSP plant and a PV-topping hybrid system will increase [6].[19]

While increasing the operating temperature of a photovoltaic device will lead to a fundamental drop in cell efficiency, it is important to consider the sunlight-to-electricity

---

[19] Reproduced with permission from [6].

efficiency for the hybrid PV-T system. Figure 4.5 shows the results of one study that models the efficiency as a function of temperature for a PV-Topping hybrid system [6]. This shows that although the efficiency of the photovoltaic topping device will decrease at high-temperatures, the efficiency of a thermal converter will increase.

Some of the assumptions in this model include that all the energy that is rejected by the photovoltaic device (heat & infrared photons) will flow to a thermal collector, that the CSP is powered by a practical heat engine limited to 2/3 of the Carnot efficiency, that the ambient temperature is 37°C, the PV concentration is 100x, and the optical efficiency is 80%. This analysis suggests that the system efficiency for a PV-Topping hybrid system can remain high when the operating temperature is increased to several hundred degrees Celsius [6].

It is also important to understand that one of the biggest unknowns in this model is the question: how will a real-world photovoltaic cell behave at these non-standard operating temperatures? While high-temperature operation will lead to a decrease in cell efficiency, it is important to understand how well our models describe the performance of real-world cells. High-temperature operation can also accelerate material degradation, reduce long-term reliability, and necessitate the development of robust cell components that do not damage the cell at high-temperatures. It is very important to understand these challenges before any photovoltaic device can be integrated into a hybrid PV-CSP system [111].

4.2 Efficiency Modeling

The goal of this work is to design, fabricate, and test solar cells that can attain an efficiency of 25% at 400°C. The starting point is to construct a model that predicts the temperature-dependent performance of a solar cell. Regardless of temperature, the efficiency of a solar cell is defined by equation 4.1:

$$Efficiency = \frac{I_{SC}*V_{OC}*FF}{P_{in}}$$ (4.1)

Where P_{in} is the input power, I_{SC} is the short-circuit current, V_{OC} is the open circuit voltage, and *FF* is the fill factor of the solar cell. Our model must predict the temperature dependence of the I_{SC}, V_{OC}, and *FF* [24,37].

The operation of a p-n junction solar cell can be described with a two-diode model, as is shown in Figure 4.6. This model contains a diode with an ideality factor of one (n=1), a diode with an ideality factor of two (n=2), a shunt resistor (R_{Shunt}), and a photocurrent source (J_L) wired in parallel and a resistor (R_S) wired in series [24,37,39].
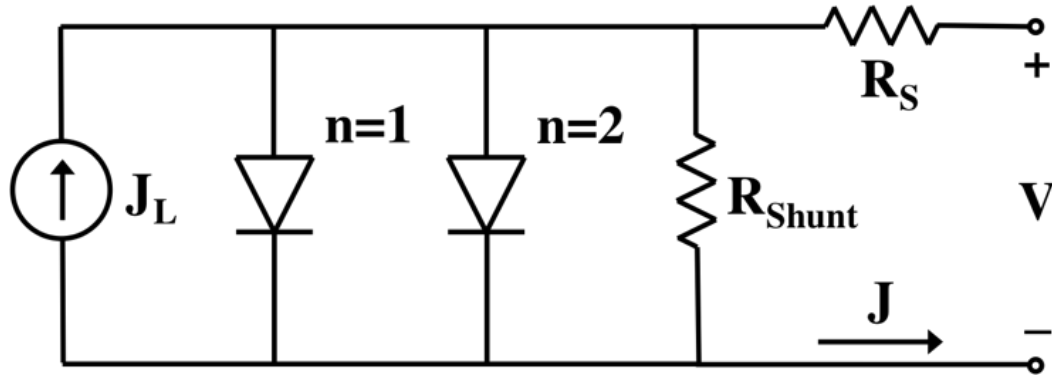
Figure 4.6: Two-diode model of a solar cell that includes a series resistance (R_S), shunt resistance (R_{Shunt}), a photocurrent (J_L), an n=1 diode, and an n=2 diode.

The current density (*J*) of this circuit is given by Equation 4.2, where J_{01} and J_{02} are the dark currents, *q* is elementary charge, *k* is the Boltzmann constant, *T* is the temperature measured in degrees Kelvin, and *V* is the applied voltage. Both resistances use units of $\Omega*cm^2$ [24,37,39].

$$J = J_{01}\left(e^{q(V-JR_S)/kT} - 1\right) + J_{02}\left(e^{q(V-JR_S)/2kT} - 1\right) + \frac{V-JR_S}{R_{Shunt}} - J_L$$ (4.2)

This relationship can be used to determine all the relevant performance characteristics of a solar cell, including the V_{OC}, *FF*, and cell efficiency. For this reason, it is critically important

102

to characterize the temperature dependence of J_L, J_{01}, and J_{02} in order to understand how cell performance will be impacted as the operating temperature is varied.

The analytical drift-diffusion model, also referred to the Hovel model, splits the dark currents into three components corresponding to recombination in the emitter, base, and depletion regions. The J_{01} dark saturation current densities, arising from bulk and interface recombination in the quasi-neutral emitter and base regions, are described by Equation 4.3 & Equation 4.4 [39,40,95]:

$$J_{01,emitter} = q \left[\frac{D_p}{L_p}\right] \left[\frac{n_i^2}{N_D}\right] \left[\frac{\frac{S_p L_p}{D_p}\left(cosh\frac{x_e}{L_p}\right)^2 + sinh\frac{x_e}{L_p}}{\frac{S_p L_p}{D_p}sinh\frac{x_e}{L_p} + cosh\frac{x_e}{L_p}}\right] \tag{4.3}$$

$$J_{01,base} = q \left[\frac{D_n}{L_n}\right] \left[\frac{n_i^2}{N_A}\right] \left[\frac{\frac{S_n L_n}{D_n}\left(cosh\frac{x_b}{L_n}\right)^2 + sinh\frac{x_b}{L_n}}{\frac{S_n L_n}{D_n}sinh\frac{x_b}{L_n} + cosh\frac{x_b}{L_n}}\right] \tag{4.4}$$

Where D_p is the diffusion constant for minority carriers in the n-type emitter, D_n is the diffusion constant for minority carriers in the p-type base, L_p is the minority carrier diffusion length in the emitter, L_n is the minority carrier diffusion length in the base, S_p is the surface recombination velocity at the emitter-window interface, S_n is the surface recombination velocity at the base-back surface field interface, N_A is the acceptor concentration in the base, N_D is the donor concentration in the emitter, x_b is the base thickness, x_e is the emitter thickness, and n_i is the intrinsic carrier concentration.

The J_{02} dark saturation current density, arising from non-radiative recombination in the depletion region, is described by Equation 4.5 [39,40,95].

$$J_{02,depletion} = \frac{q n_i W_D}{2\tau} \tag{4.5}$$

Where W_d is the width of the depletion region and τ is the nonradiative carrier lifetime.

The intrinsic carrier concentration, n_i, is the dominant factor in Equations 4.3-4.5 that will determine the temperature dependence of the dark currents (this assumption will be validated later), and is defined according to Equation 4.6 [38].

$$n_i(T) = 2 \left(\frac{2\pi kT}{h^2}\right)^2 \left(m_n{}^* m_p{}^*\right)^{3/4} e^{-E_g/2kT} \tag{4.6}$$

Where E_g is the bandgap, h is Planck's constant, $m_n{}^*$ is the effective electron mass, and $m_p{}^*$ is the effective hole mass.

Combining Equations 4.3-4.5 with Equation 4.6, we find that the n_i-dominated temperature dependence of the J_{01} and J_{02} dark currents can be described by the following proportionalities [39,111]:

$$J_{01} \; \alpha \; T^3 e^{-E_g/kT} \tag{4.7}$$

$$J_{02} \; \alpha \; T^{3/2} e^{-E_g/2kT} \tag{4.8}$$

These equations indicate that the J_{01} and J_{02} dark currents will increase exponentially with temperature, which will lead to a significant reduction in the V_{OC} at high temperatures.

The J_{SC} is closely linked to the external quantum efficiency (EQE) of the cell, which can also be split into three components corresponding to collection in the emitter, base, and depletion regions [39,40,95]. While these equations can be solved to obtain expressions for the EQE in each region, the solutions are quite complex and there is no single term that will dominate the temperature dependence. While this makes it difficult to accurately model the temperature-dependence of J_{SC}, we do know that the temperature-dependence of the bandgap will play a critical role in determining the photocurrent of the solar cell. As the cell temperature increases, the bandgap of all the semiconductor materials in our solar cell will decrease. This bandgap shift can be described by the Varshni equation [114]:

$$E_g(T) = E_g(0) - \frac{\alpha T^2}{T+\beta} \tag{4.9}$$

Where α and β are material constants and $E_g(0)$ is the bandgap of the material at 0K. For GaAs, Blakemore *et al.* reported an $E_g(0)$ of 1.519 eV, an α of 0.5405 meV/K, and a β of 204K [115]. For GaInP, Lu *et al.* reported an $E_g(0)$ of 1.976 eV, an α of 0.75 meV/K, and a β of 500K [116]. For both materials, increasing the temperature will result in a lowering bandgap. This will increase the number of photons that are absorbed by each of these materials, leading to an increase in the photocurrent as long as the collection probability for a photogenerated carrier is not significantly reduced. For our preliminary efficiency model, we will determine the J_{SC} by assuming that all photons above the bandgap will be converted into photocurrent [111].

In the case where the solar cell is dominated by n=1 recombination, which is often the case for a solar cell that is operated under high-concentration, we can rearrange Equation 4.2 to solve for V_{OC}.

$$V_{OC} = \frac{kT}{q}\left[ln\left(\frac{J_{SC}}{J_{01}}\right) + 1\right] \tag{4.10}$$

Where the temperature dependence of J_{SC} is determined using the procedure described in the previous paragraph, and the temperature dependence of J_{01} is determined with Equation 4.7 and Equation 4.8. We can also determine the *FF* using Equation 4.2 once we know J_{01}, J_{02}, J_{SC}, and R_S. Using the diode equation (Equation 4.2), the Hovel equations (Equations 4.3-4.8), and the Varshni equation (Equation 4.9) we are able to model the temperature dependences of the J_{SC}, V_{OC}, and *FF*. This allows us to construct a temperature-dependent cell efficiency model using Equation 4.1 [111].

To calculate the cell efficiency, we use a semi-empirical model that starts with measured

values for the W_{OC}, and for this reason the voltages calculated with our model are more realistic than the detailed-balance model. Some of the other assumptions in our model include that incoming light is described by the reference AM1.5D spectrum, that the device has W_{OC} of 370mV at room-temperature when $J_{SC} = 16mA/cm^2$, $R_S = R_{Shunt} = 0$, the PV concentration is 1000x, and that the solar cell will be dominated by n=1 recombination at these high light intensities. Figure 4.7 shows the modeled cell efficiency as a function of bandgap and operating temperature for single-junction solar cells at temperatures ranging from 25°C to 500°C.
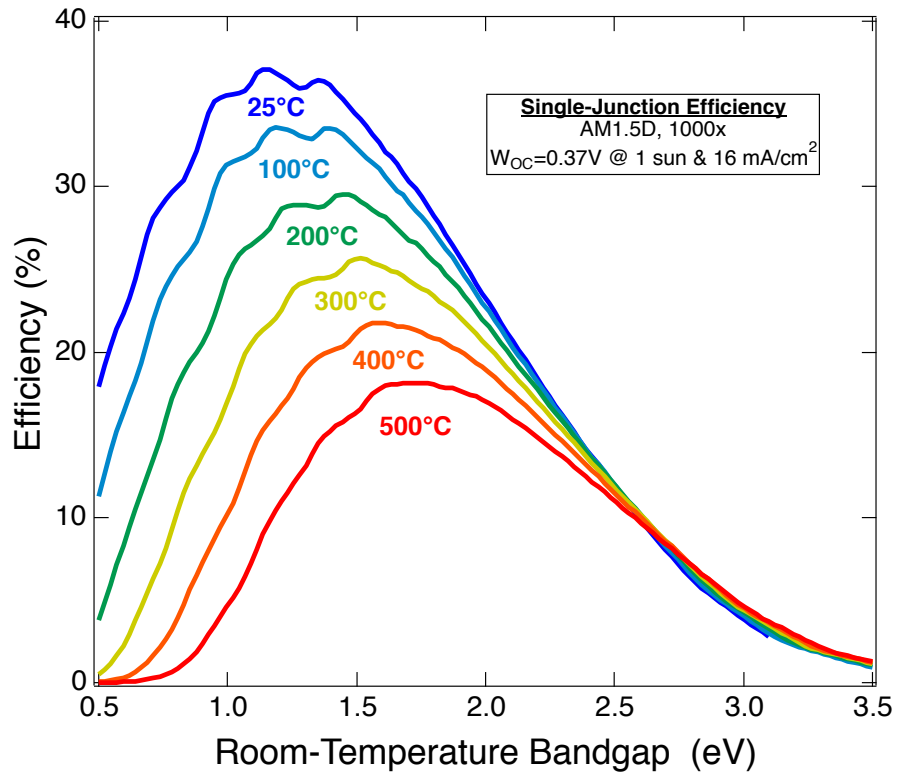
Figure 4.7: Modeled efficiency of a single-junction photovoltaic device as a function of the top-cell room-temperature (300K) bandgap and the operating temperature.

There are two predominant trends in this plot. First, the achievable cell efficiency decreases as the temperature is raised. This is primarily due to the fundamental V_{OC} loss at high-temperatures, which is caused by the exponentially increasing J_{01} and J_{02} dark currents.

Second, the efficiency peak shifts to the right as the temperature is increased, suggesting that higher room-temperature bandgaps are required for high-temperature operation. This can be partially explained from the bandgap reduction that we expect at high-temperatures. If we want to absorb a given portion of the solar spectrum then a cell operated at 400°C will require a higher room-temperature bandgap than a cell operated at 25°C. Note also that the efficiency can increase at high-temperatures for materials with a high-bandgap. The reason for this is that these solar cells are non-ideal, and gain more efficiency at high-temperature from an increased J_{SC} (due to a bandgap decrease) than they lose from the fundamental V_{OC} loss at high-temperatures [111]. Figure 4.7 also shows that our efficiency goal of 25% at 400°C not possible with a single-junction solar cell.
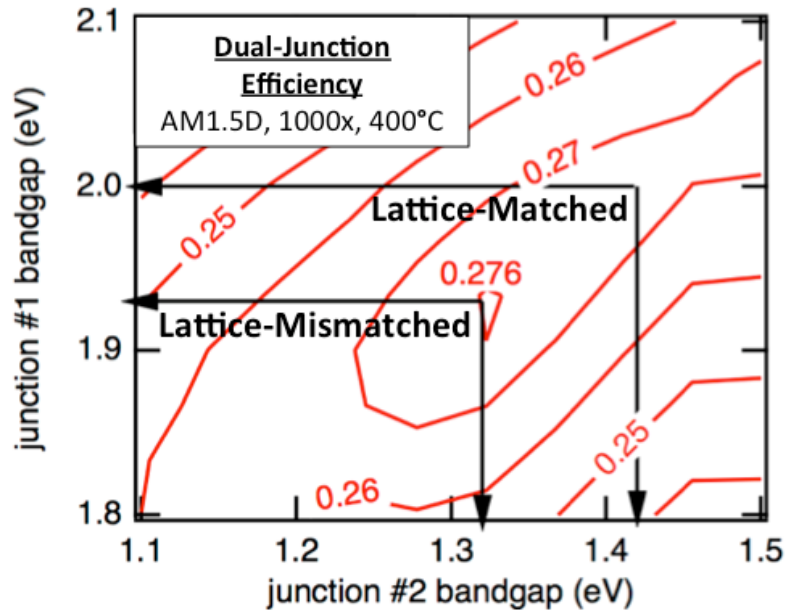
Figure 4.8: Modeled efficiency of a dual-junction photovoltaic device at 400°C as a function of the room-temperature (300K) bandgaps of the top and bottom junction.

One way to improve upon this efficiency is to add junctions, which can help to reduce combined thermalization and non-absorption losses. Figure 4.8 shows a contour plot of the modeled efficiency of a dual-junction solar cell as a function of the room-temperature

bandgaps of the top and bottom junctions. This model uses the same assumptions as the model in Figure 4.7. However, for this model we set the operating temperature to 400°C and allow the top cell to be thinned when necessary to improve current matching [111].

This plot shows that with a dual-junction device, we can attain a modeled efficiency greater than 25% at 400°C. While the global efficiency maximum corresponds to a dual-junction device with a top cell bandgap of ~1.93 eV and a bottom cell bandgap of ~1.32 eV, we find that we can achieve an efficiency very close to the global maximum using a configuration where both subcells are lattice-matched to GaAs. Figure 4.9 shows a chart of bandgap vs. lattice constant for common III-V materials (excluding GaN-based materials).
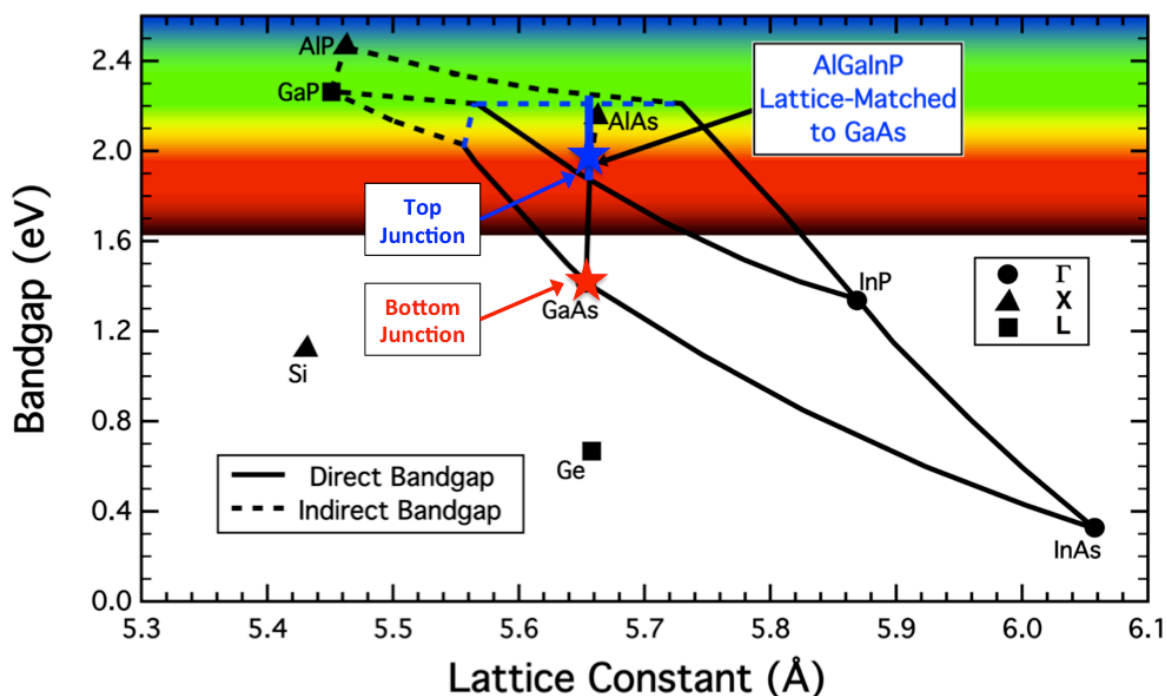
Figure 4.9: Chart showing the bandgap vs. lattice constant for common III-V materials (excluding GaN-based III-V materials).

Our approach, shown in this figure, is to develop a dual-junction solar cell lattice-matched to GaAs with a 1.42eV GaAs bottom junction and a 2.0eV AlGaInP top junction with the same lattice constant as GaAs. Very high-quality GaAs cells have been developed

previously (we typically achieve W$_{OC}$s of ~370mV), so we did not spend a significant amount of time developing this subcell. However, the quality of high-bandgap AlGaInP solar cells significantly lags in performance, and as such we spent a significant amount of time developing this subcell [111].

4.3 AlGaInP Solar Cell Development

Figure 1.18 (shown again here in Figure 4.10) showed the ideal bandgap for multijunction devices with between one and six junctions, illustrating how the ideal bandgap of each junction increases as the number of junctions is increased [46].
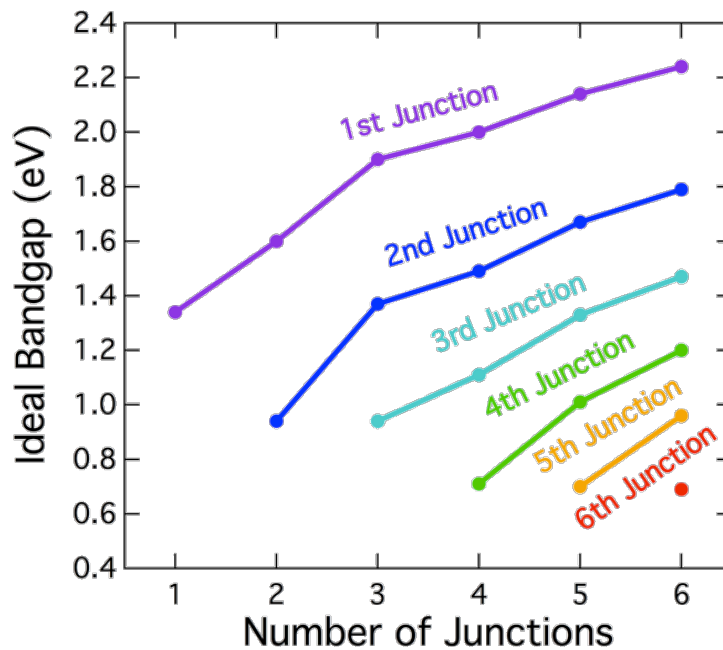
Figure 4.10: Ideal bandgap as a function of the number of junctions for multijunction devices with between one and six junctions. This plot shows how the ideal bandgap of each junction increases as the number of junctions is increased [46].[20]

Today's best four-junction photovoltaic devices have demonstrated a $W_{OC} \leq 400mV$ for each subcell when illuminated at one-sun, which is indicative of the excellent material

---

[20] Plotted using data from [46]

quality of these devices [49,51]. While four-junction photovoltaic devices have attained great success in recent years, the field is moving towards designs with five or six semiconductor junctions to further increase efficiencies [50,117]. While the ternary alloy GaInP can be grown lattice-matched to GaAs with excellent material quality and a near-optimal bandgap for a four-junction device, high-quality top cells with larger bandgap energies are desired for five-junction and six-junction photovoltaic devices [118].

As we discussed previously, higher bandgaps are also preferred for photovoltaic devices that are operated at elevated temperatures. Figure 4.11 shows the modeled efficiency of a dual-junction device as a function of operating temperature and the room-temperature bandgap of the top cell.
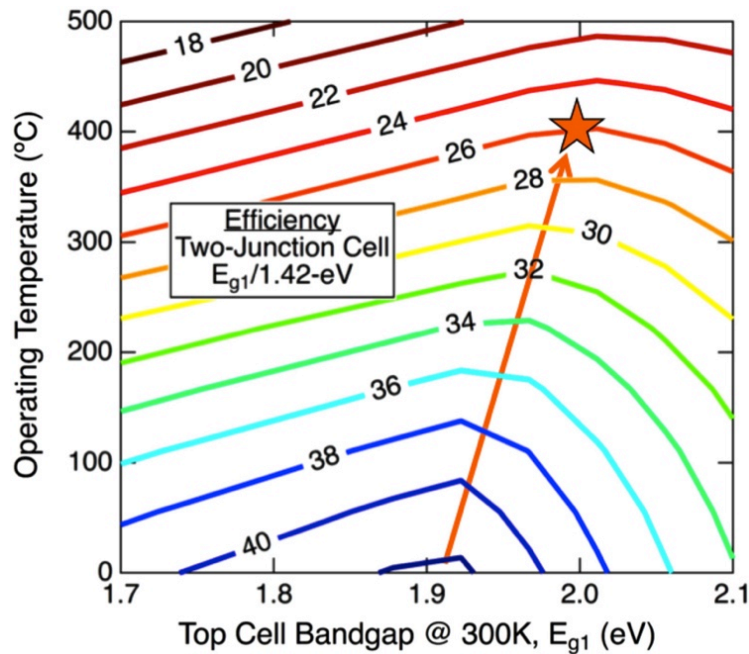

Figure 4.11: Modeled efficiency of a dual-junction photovoltaic device as a function of the room-temperature bandgap of the top cell and the operating temperature [120].

This model constrains the room-temperature bandgap of the bottom subcell to 1.42eV (GaAs) and follows the same assumptions discussed in the previous section. The key

110

takeaway from this plot is that the ideal room-temperature bandgap of the top cell increases and that the cell efficiency decreases as the operating temperature is increased. Again, this model finds that a dual-junction device with subcell bandgaps of 2.0 and 1.42 eV is nearly optimal for a device operated at 400°C and can theoretically reach an efficiency greater than 25% [119,120].

The quaternary alloy AlGaInP offers the highest direct bandgap of any III-V material that is lattice-matched to GaAs. It is, therefore, a promising candidate for use in five-junction and six-junction photovoltaic devices, as well as for solar cells operated at high temperature. By varying the aluminum content of the alloy and controlling the CuPt-ordering in the group III sublattice, direct bandgaps between approximately 1.8 and 2.2 eV are achievable [121-123].

While AlGaInP has great potential for improving the efficiency of the next-generation of multijunction devices, there are several technical challenges that accompany its development. Chief among these is the issue of oxygen contamination, which can be problematic for any aluminum-containing material due to the high dissociation energy of the bond between aluminum and oxygen [121,123-125]. The incorporation of oxygen is often associated with the formation of deep-level traps that can greatly increase the non-radiative recombination rate of a material [126,127].

Despite the growth challenges, a number of groups have worked to develop high-bandgap AlGaInP cells [128-131]. Masuda *et al.* reported an upright 2.0 eV AlGaInP subcell grown by molecular beam epitaxy (MBE) with a W_{OC} of 620mV, but with a significantly lower internal quantum efficiency (IQE) than a GaInP cell [129]. Hongbo *et al.* demonstrated an upright 2.05 eV AlGaInP subcell grown by organometallic vapor phase

epitaxy (OMVPE) with a W_{OC} of 595mV, but also observed degradation in the IQE [130]. Cornfeld *et al.* developed an inverted 2.05 eV AlGaInP solar cell grown by OMVPE that achieved a W_{OC} of 510mV with less degradation in the IQE [131]. Recently, Wanlass *et al.* reported an upright 1.95 eV AlGaInP cell with a W_{OC} of 485mV and minimal IQE loss [128]. Even with these significant advances in cell performance, no AlGaInP cell reported to date has achieved comparable performance to that of the best GaInP subcells of the same configuration. Reducing the W_{OC} while maintaining a high IQE is the key to successfully integrating AlGaInP into a multijunction device. In this section, we demonstrate a ~2.0eV AlGaInP solar cell with a W_{OC} of 440mV and minimal degradation to the IQE compared with upright GaInP solar cells grown under the same conditions [119,120].

All the AlGaInP samples were grown using an atmospheric-pressure OMVPE vertical reactor. The reactor is custom-built and uses trimethylgallium (TMGa), triethylgallium (TEGa), trimethylindium (TMIn), trimethylaluminum (TMAl), arsine (AsH$_3$), and phosphine (PH$_3$) sources. Diethylzinc (DEZn) was added to p-dope the back surface field (BSF) and base layers and dilute hydrogen selenide (H$_2$Se/H$_2$) was added to n-dope the emitter and window layers. All of the solar cell samples were grown on zinc-doped (001) GaAs substrates miscut 6° toward <111>A. Prior to growth, the substrates were etched for one minute in a NH$_4$OH:H$_2$O$_2$:H$_2$O (2:1:10) solution. The graphite susceptor at the center of the reactor was heated to a temperature of 1000°C to drive excess oxygen out of the reactor before the substrate was loaded.

Figure 4.12 shows a schematic of the device that includes the nominal bandgap and thickness of the semiconductor layers. A ~500nm Al$_{0.3}$Ga$_{0.7}$As buffer layer was grown prior to the active device layers in order to getter residual oxygen early in the growth. The

AlGaInP BSF has a nominal aluminum composition of 27% and the AlInP window layer has a nominal aluminum composition of 53%. Unless otherwise noted, the nominal emitter and base thicknesses are 90nm and 900nm respectively, and the nominal aluminum composition in the AlGaInP emitter and base is 12%, corresponding to a bandgap of ~2.0 eV. Unless otherwise noted, the active layers were grown at a temperature of 740°C, a rate of ~6.5μm/hr, and a phosphine flow of ~200 sccm. The 2.0-eV samples grown with varying T_g were AR coated using a bilayer of ZnS/MgF$_2$.
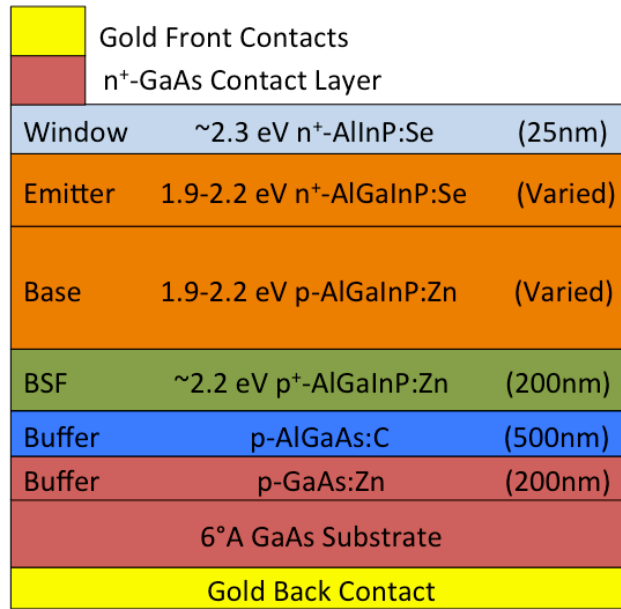
Figure 4.12: Schematic showing the structure of the epitaxially grown layers and metallization of the AlGaInP solar cells studied in this work. The diagram is not to scale [120].

The bandgap of the active layers was determined by subtracting $kT/2$ from the peak emission energy measured by room temperature electroluminescence (EL) [132,133]. It is important to note that this resulted in a bandgap and W_{OC} that is ~20mV higher than what we determined from EQE measurements. The aluminum compositions were estimated by calculating the molar flow rates of the group-III precursors. Room temperature Hall and Capacitance-Voltage (CV) measurements were taken to estimate the concentrations of the n-

type and p-type dopants in the AlGaInP emitter and base. We took illuminated current-voltage (LIV) and dark current-voltage (DIV) measurements using a custom-built solar simulator that uses a Xenon lamp and adjustable, high-brightness LEDs. The spectrum and intensity were adjusted using calibrated reference cells to simulate the AM1.5D spectrum at 1000 W/m^2. These test setups are discussed in more detail elsewhere.

Substrate Miscut

The bandgap of a given AlGaInP alloy has been shown to vary by around 100 meV depending on the degree of CuPt-type ordering in the group III sublattice, where disordered material will have a larger bandgap than ordered material [122,123,134]. To determine the effect of growth temperature (T_g) and substrate miscut angle on ordering, we grew a set of AlGaInP layers on GaAs substrates that were miscut 2° toward the (111)A direction (2°A), 4° toward the (111)B direction (4°B), 6° toward the (111)A direction (6°A), and 6° toward the (111)B direction (6°B) and measured the resulting peak emission wavelength using RT photoluminescence (PL). These results are shown in Figure 4.13.
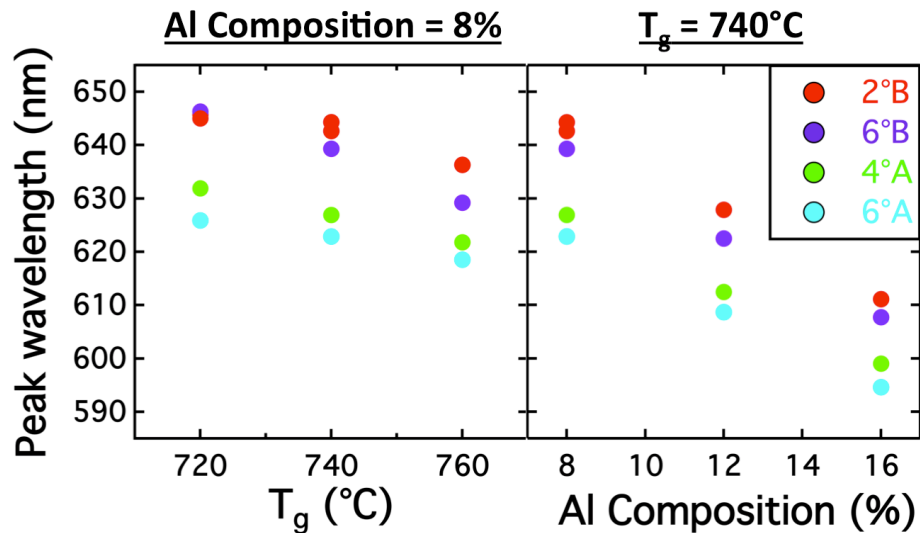
Figure 4.13: Peak wavelength measured with room-temperature photoluminescence as a function of (left) growth temperature and (right) aluminum composition for AlGaInP layers grown on 2°B, 4°A, 6°A, and 6°B GaAs substrates [119].

114

There are a few key takeaways from the PL results. First, increasing the aluminum content clearly raises the bandgap of the AlGaInP layers and therefore lowers the peak emission wavelength, as expected. Second, the 6°A substrates yield the lowest emission wavelengths of all the substrates considered with a peak emission wavelength that is about 20nm lower than for the 2°B substrates. Third, increasing the T_g appears to slightly decrease the peak emission wavelength, although only by about 5-10nm as the T_g is increased from 720°C to 760°C.

These shifts in the peak wavelength are likely caused by a change in the degree of ordering in the AlGaInP layers, due to both temperature and substrate miscut, which is consistent with trends reported in the literature for GaInP. By growing more disordered AlGaInP, it is possible to achieve our target 2.0eV bandgap with a lower aluminum composition than if we were to grow more ordered AlGaInP, helping to minimize oxygen contamination in the AlGaInP layers. All of the solar cells shown below are grown on 6°A GaAs substrates.

Emitter Dopant

The emitter dopant species can have a significant impact on device performance. The first samples that we grew used silicon as the n-type dopant in the AlGaInP emitter. While we were able to obtain a fairly high V_{OC} from these samples, we measured a large decrease in the IQE at short wavelengths compared to GaInP cells grown under similar conditions. This reduction in the IQE of the emitter is similar to what has been seen in previous studies of AlGaInP solar cells [129-131].

We later grew samples using selenium as the n-type dopant, and consistently observed a full recovery in the IQE. Figure 4.14 shows the IQE of AlGaInP solar cells, grown at 740°C,

with silicon-doped and selenium-doped emitters. From RT Hall measurements, we found that the emitter dopant concentration in both of these samples is around 1×10^{18} cm^{-3}.
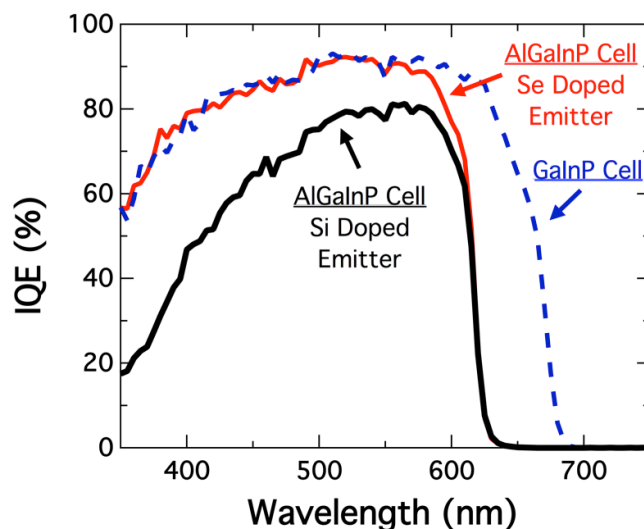
Figure 4.14: IQE for AlGaInP solar cells with a (black) silicon-doped and (red) selenium-doped emitter. The dashed blue line shows the IQE for a GaInP solar cell grown under similar conditions [119].

By replacing silicon with selenium as the n-type dopant, we were able to achieve a comparable IQE to that of an upright GaInP cell for the strongly absorbed light above the bandgap of AlGaInP.
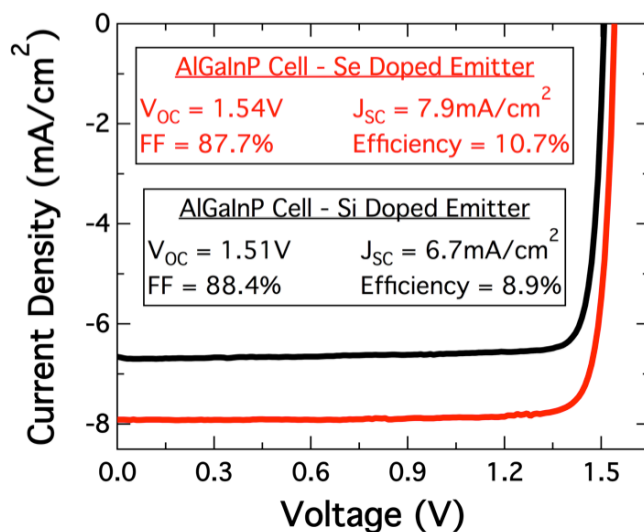
Figure 4.15: One-sun LIV measurements for AlGaInP solar cells with a silicon-doped (black) and selenium-doped (red) emitter [119].

116

These samples also had a notably higher J_{SC} and V_{OC} than the silicon-doped samples. Figure 4.15 shows the LIV characteristics of both AlGaInP samples when illuminated under a simulated AM1.5D spectrum.

Growth Temperature

The material quality of OMVPE-grown AlGaInP is very sensitive to T_g, which affects both oxygen incorporation and CuPt-type ordering [129-131,135]. To study the impact of T_g on cell performance, we grew a set of ~2.0 eV solar cells where we varied the T_g of the AlGaInP layers from 700°C to 800°C while keeping all other growth conditions the same.

TABLE 4.1
SOLAR CELL PARAMETERS FOR SAMPLES GROWN AT DIFFERENT TEMPERATURES

Sample	T_g (°C)	Strain (%)	E_g (eV)	V_{OC} (V)	W_{OC} (mV)	J_{SC} (mA/cm^2)	FF (%)	Efficiency (%)
MN742	700	0.026	1.99	1.49	500	10.9	73.1	11.9
MN746	720	0.028	2.00	1.51	490	10.6	81.7	13.0
MN750	740	0.036	2.01	1.55	460	10.7	87.9	14.6
MN753	760	0.043	2.02	1.56	460	10.7	88.4	14.7
MN775	780	0.076	2.03	1.59	440	10.6	88.0	14.8
MN779	800	0.142	2.05	1.57	480	10.3	88.2	14.2

Table 4.1 shows the measured cell parameters for each of these devices. We found that cell performance improved as the T_g was increased up to 780°C. By increasing T_g from 700°C to 780°C, we were able to decrease the W_{OC} from 500mV to 440mV, increase the fill factor from 73.1% to 88.0%, and increase the efficiency from 11.9% to 14.8%.

Figure 4.16 shows the DIV characteristics for each of these cells. The dashed lines indicate the slopes of ideal diodes with ideality factors of 1 and 2, where the y-intercepts are equal to J_{01} for the n=1 line and J_{02} for the n=2 line. It is clear that both J_{01} and J_{02} decrease as the T_g was increased, up to 780°C. These reduced dark currents correlate to higher V_{OC}s, and are indicative of lower non-radiative recombination rates in the emitter and base.
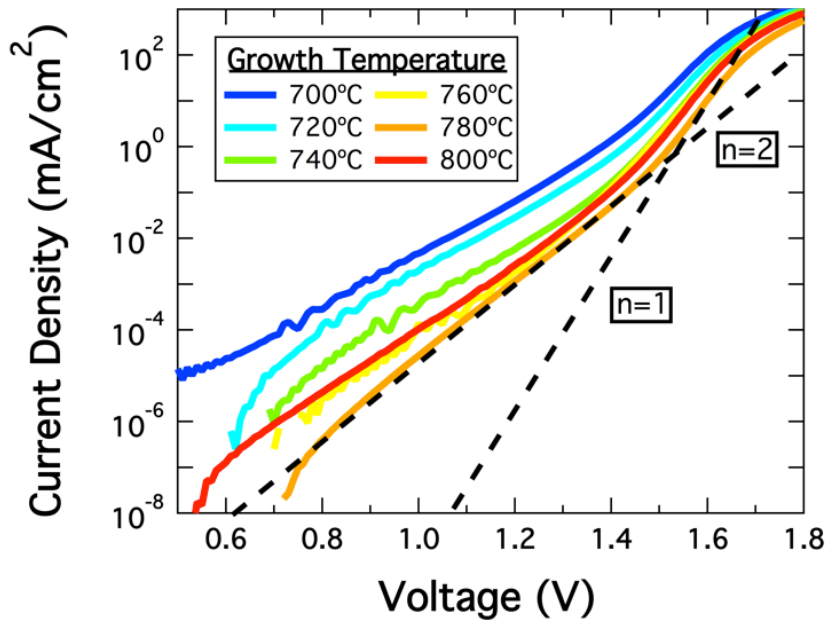
Figure 4.16: DIV characteristics of AlGaInP solar cells grown at temperatures ranging from 700°C to 800°C [120].

We attempted to measure oxygen concentrations by Secondary Ion Mass Spectroscopy (SIMS), but the levels were near the instrument detection limit of $\sim 10^{17}$ cm^{-3} and therefore the measurement did not give a reliable indication of the oxygen variation. However, the improvement in performance at high T_g is consistent with a reduction in oxygen incorporation. It is well known that high growth temperatures can suppress the incorporation of oxygen due to the increased probability of desorption from the surface [124,125]. Minimizing oxygen incorporation can help reduce the non-radiative recombination rate in the AlGaInP layers, which can significantly improve cell performance [122,123,136].

There are a number of other important trends that we observed. First, we found that the bandgap increases with T_g. This can be partially explained by a decrease in CuPt-type ordering with growth temperature [122,123,134]. However, the higher bandgaps could also be a result of lower indium incorporation at high T_g. Using an in-situ wafer curvature measurement technique (MOS) [48], we observed increased tensile strain as the T_g was

118

increased. This is quantified in Table 4.1. The particularly high strain for the sample grown at 800°C could explain why its performance started to degrade.

It is also important to stress that none of the OMVPE flow rates were changed as the T_g was varied. This resulted in lower concentrations of the zinc and selenium dopants for the samples grown at high temperatures because, like oxygen, both zinc and selenium incorporate less efficiently at high T_g. Specifically, as T_g was raised from 740°C to 780°C, we measured a decrease in the emitter doping (N_D) from 1.1×10^{18} cm^{-3} to 8.7×10^{17} cm^{-3} and a decrease in the base doping (N_A) from 1.2×10^{17} cm^{-3} to 5.6×10^{16} cm^{-3}. This change in the doping concentration could also have a significant impact on the cell performance [39,40,95]. For this reason, we ran an experiment where we varied the emitter and base doping flows for six solar cells grown at 780°C. The results of this study are summarized in Table 4.2.

TABLE 4.2

SOLAR CELL PARAMETERS FOR SAMPLES GROWN AT 780°C WITH VARYING EMITTER AND BASE DOPING CONCENTRATIONS

Sample	N_A (cm^{-3})	N_D (cm^{-3})	V_{OC} (V)	Integrated IQE, AM1.5D (mA/cm^2)
MN904	5.5×10^{16}	8.7×10^{17}	1.56	7.7
MN908	6.3×10^{16}	1.8×10^{18}	1.56	7.5
MN912	6.0×10^{16}	3.0×10^{18}	1.55	7.1
MN989	2.9×10^{16}	8.1×10^{17}	1.58	7.8
MN991	5.7×10^{16}	7.9×10^{17}	1.58	7.7
MN993	7.0×10^{16}	8.3×10^{17}	1.57	7.7

The H_2Se/H_2 flow rates for MN904, MN908, and MN912 were 2.5 sccm, 5 sccm, and 10 sccm respectively. The DeZn flow rates for MN989, MN991, and MN993 were 5 sccm, 10 sccm, and 20 sccm respectively. First, note that the measured doping concentrations do not scale in the same proportions as the dopant flow rates, suggesting that the incorporation of zinc and selenium saturate at relatively low concentrations. Second, we observed a decrease

in the IQE as the emitter doping was increased. This is what we would expect since increased doping will lead to an increase in the number of impurities that act as recombination centers for minority carriers, resulting in a reduced minority carrier diffusion length in the n-type emitter [137,138]. Finally, we observed a change of only ~10mV in the V_{OC} as the doping concentrations were varied in these studies. The fact that the V_{OC} is not changing significantly as the doping concentration is varied suggests that the improved performance that we observe at high T_g is not due to the difference in doping concentrations.

Growth Rate and Phosphine Partial Pressure

The growth rate (R_g) and phosphine partial pressure may also have a strong influence on the incorporation of oxygen in aluminum-containing alloys because they affect the surface kinetics during growth. As the R_g is increased, the exposure time of the surface decreases and therefore oxygen atoms have less time to adsorb and accumulate before the surface layer is buried. As the phosphine partial pressure is increased, there will be additional group V elements to compete with oxygen for surface adsorption sites, helping to suppress the incorporation of oxygen [123]. Note that our atmospheric pressure OMVPE reactor allows us to achieve higher partial pressures than a low-pressure reactor.

To study the impact of the R_g and phosphine partial pressure on cell performance, we grew two sets of devices. For the first set, we varied the phosphine flow in the AlGaInP layers from 50 sccm to 200 sccm while keeping the R_g constant at 6μm/hr. For the second set, we varied the R_g of the AlGaInP layers from 2μm/hr to 6μm/hr while keeping the phosphine flow constant at 200 sccm.

The IQEs of these samples are shown in Figure 4.17. As the phosphine flow was increased from 50 sccm to 200 sccm, there was a clear improvement in the short-wavelength

IQE that can be attributed to an increase in the minority carrier diffusion length in the n-type emitter. This is consistent with a lower oxygen concentration in the AlGaInP layers, which has been shown to decrease as the phosphine overpressure is increased [121,123,136]. However, we also observed a reduction in the doping concentration in the emitter from 3.0×10^{18} cm^{-3} to 1.2×10^{18} cm^{-3} as the phosphine flow was increased from 50 sccm to 200 sccm. This lower doping would also result in a longer diffusion length in the emitter, which could lead to a higher IQE. The base doping remained around 10^{17} cm^{-3} and the V_{OC} varied by less than 10mV for all three samples.
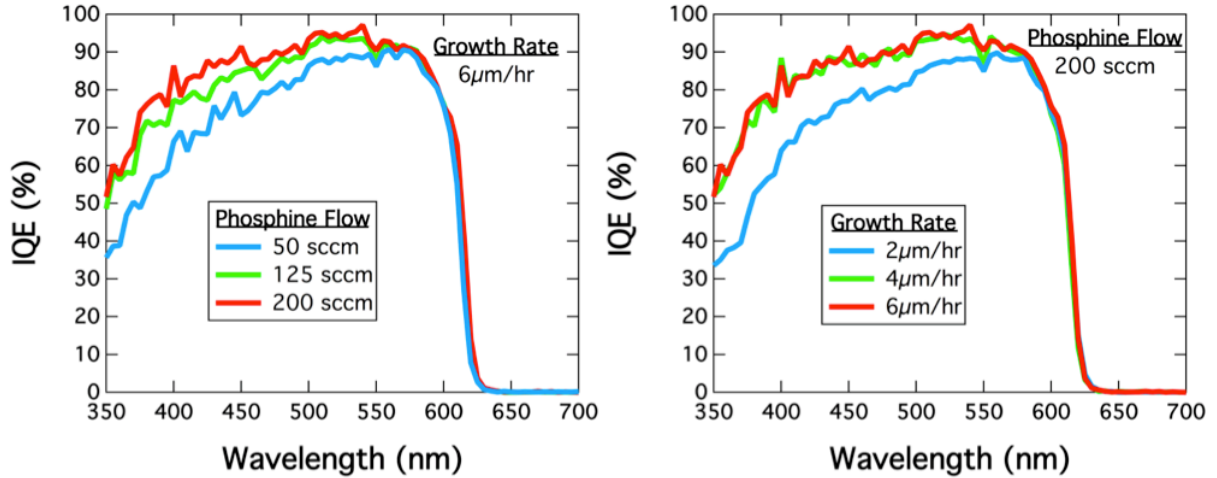
Figure 4.17: Wavelength-dependent IQE of ~2.0eV AlGaInP solar cells with (left) varying phosphine flow and (right) varying growth rate [120].

As the R_g was increased from 2μm/hr to 4μm/hr, there was a notable improvement in the IQE and a ~30mV increase in the V_{OC}. As the R_g was further increased to 6μm/hr we saw almost no change in the IQE, but measured a ~10mV increase in the V_{OC}. There was a negligible difference in the emitter and base doping concentrations for these three samples. These trends are consistent with previous studies on how the R_g and phosphine partial pressure impact oxygen incorporation in aluminum-containing III-V materials [121,123,136].

Thickness of the Emitter and Base

Nearly all investigations of AlGaInP and AlGaAs solar cells have observed a significantly shorter minority carrier diffusion length in the n-type emitter than in the p-type base [50,117,127,129-131,139]. This typically manifests itself in a substantial reduction in the short-wavelength IQE of the device, which leads to a loss of photocurrent and can have a dramatic impact on current matching in a multijunction solar cell. By optimizing the OMVPE growth conditions, we were able to minimize this IQE loss in our ~2.0 eV front-junction AlGaInP solar cells. However, there is still a significant difference between the minority carrier diffusion length of the n-type emitter and the p-type base in these devices.
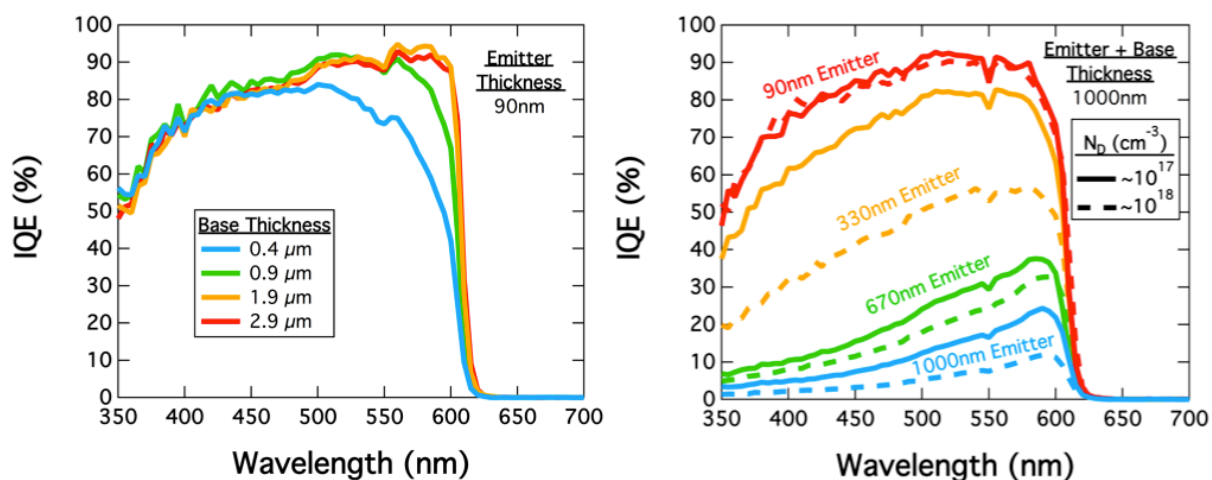
Figure 4.18: Wavelength-dependent IQE of ~2.0eV AlGaInP solar cells with (left) varying base thickness and (right) varying emitter thickness. In the right graph, the doping concentration in the emitter (N_D) was either 10^{17} (solid lines) or 10^{18} (dashed lines) [120].

Figure 4.18 shows how the IQE was impacted as the emitter and base thicknesses were varied. As we increased the base thickness from 0.4 μm to 1.9 μm, there was a clear improvement in the long-wavelength IQE. This is because the cells with a 0.4-μm and 0.9-μm base are not optically thick and absorb only a fraction of the long wavelength light. We observed minimal change in the IQE as the base thickness was further increased from 1.9

μm to 2.9 μm. Both of these devices retained an IQE >90% near the band edge, suggesting that these cells are close to optically thick and are collecting most of the carriers generated far from the junction. This is indicative of the long diffusion length in the p-type base.

As the n-type emitter thickness was increased, we observed a dramatic reduction in the short-wavelength IQE. For this set of samples, we kept the total thickness of the emitter and base constant at 1 μm. For this reason, the reduction in the IQE is not a result of a changing absorption thickness and can instead be attributed to a difference in the minority carrier diffusion length of the n-type emitter and p-type base.

Since the doping concentration can have a notable impact on the diffusion length of a material, we grew an additional set of samples where the doping concentration in the n-type emitter (N_D) was lowered from ~10^{18} cm^{-3} to ~10^{17} cm^{-3}. While this resulted in a consistent improvement in the IQE, we still observed a dramatic reduction in the IQE as the emitter thickness was increased. These results show the significant difference in the collection efficiency between n-type and p-type AlGaInP, and suggest that improvements to the material quality of n-type AlGaInP could be a key driver to attaining high efficiency in a five-junction or six-junction solar cell. Furthermore, these results are in stark contrast to recent reports of rear-heterojunction GaInP solar cells with thick, low-doped n-type emitters, which have maintained a high IQE while achieving the highest V_{OC} and efficiency of any GaInP solar cell reported to date [118].

Aluminum Composition

In order to integrate an AlGaInP subcell into a five-junction or six-junction photovoltaic device, it is important to be able to tune the bandgap of the top cell to attain the highest possible V_{OC} while remaining current matched to the lower subcells. One straightforward

way to raise the bandgap and V_{OC} of an AlGaInP solar cell is to increase the aluminum composition of the alloy. However, it is well documented that alloys with higher aluminum content are more susceptible to oxygen incorporation [121,123,127,136]. To study the impact of aluminum composition on cell performance, we grew a set of samples where we varied the nominal aluminum composition in the emitter and base from 0% to 24%, though no further optimization was done for each sample.
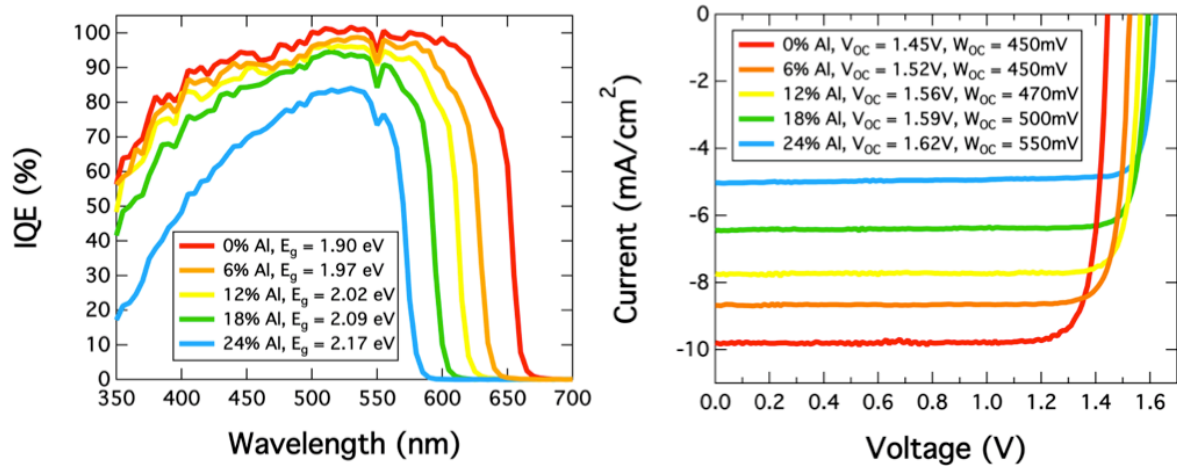
Figure 4.19: (Left) IQE and (right) LIV characteristics of AlGaInP solar cells grown with nominal aluminum compositions ranging from 0% to 24% [120].

Figure 4.19 shows the IQE and LIV characteristics for each of these devices. The bandgaps derived from EL measurements range from 1.90 eV for AlGaInP with a 0% nominal aluminum composition to 2.17 eV for AlGaInP with a 24% nominal aluminum composition. This corresponds to a bandgap increase of ~11meV per 1% increase in the aluminum fraction. We measured <8% reduction in the peak IQE as the nominal aluminum composition was raised from 0% to 18%. However, we observed a much more significant drop in the IQE as the aluminum composition was further increased to 24%. Further analysis is required to understand the precise origin of the degradation, but the trends are consistent

with both an increase in oxygen incorporation as the aluminum fraction is raised and with a less effective passivation as the barrier heights for the window layer and BSF are reduced. The abrupt drop in performance for the 24% aluminum-containing sample could also be related to the direct/indirect crossover for lattice-matched AlGaInP, which occurs at an aluminum composition of ~27%. Similar trends have been observed for AlGaInP LEDs [121,123,127,136]. Figure 4.20 shows pictures of the luminescence from AlGaInP solar cells grown with nominal aluminum compositions of 0% (1.90eV), 12% (2.02eV), 18% (2.09eV), and 24% (2.17eV).
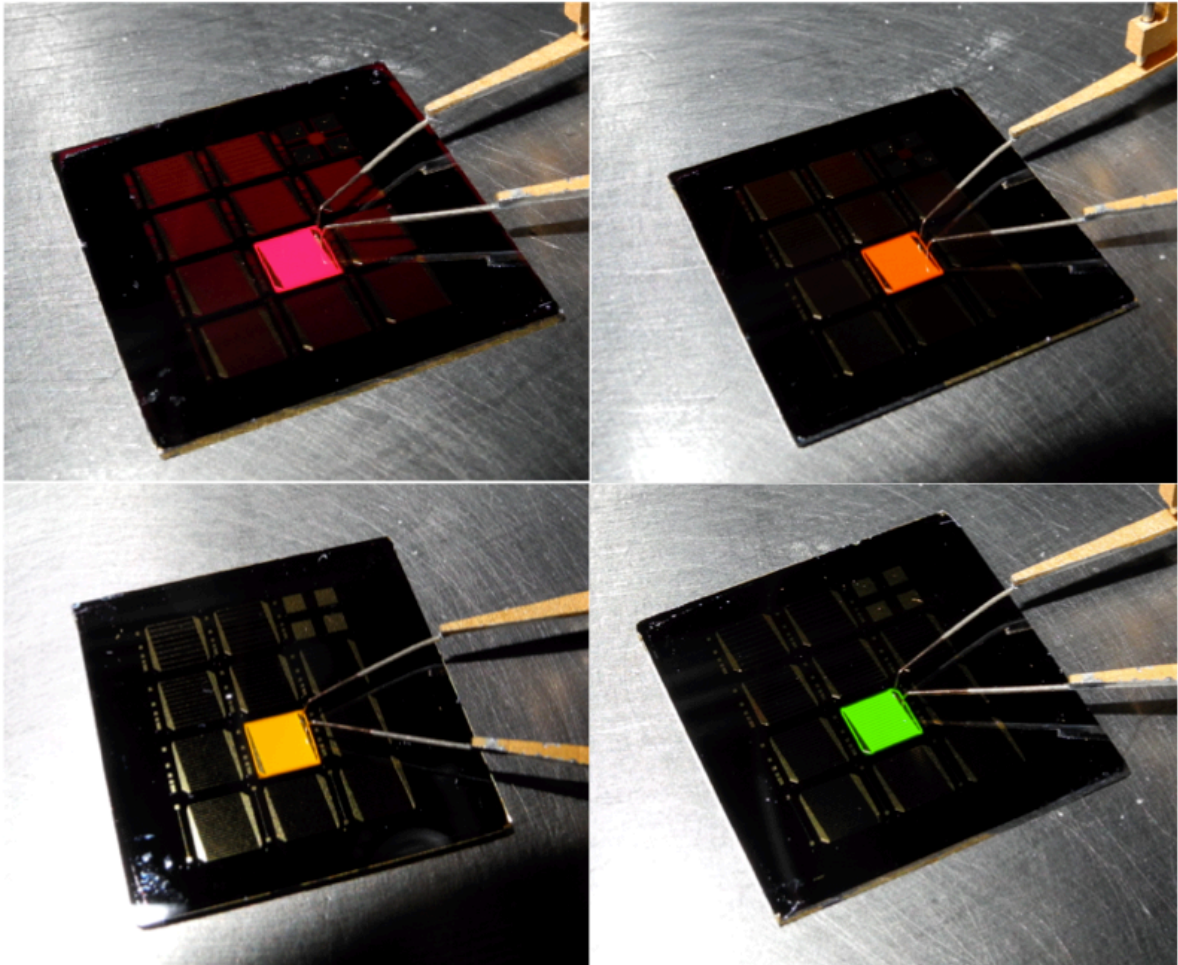
Figure 4.20: Pictures of the luminescence from forward-biased AlGaInP solar cells with nominal aluminum compositions of 0% (top left), 12% (top right), 18% (bottom left), and 24% (bottom right).

The LIV measurements from Figure 4.19 give some indication as to how these cells would perform when integrated into a multijunction device. Increasing the material bandgap means that the active layers are going to absorb less light, which corresponds to a decrease in the J_{SC}. Increasing the bandgap will also lead to a reduction in thermalization loss, resulting in a higher V_{OC}. However, we also saw an increase in the W_{OC} as the aluminum composition was raised, which is what we would expect if oxygen contamination was becoming more problematic as aluminum is added to the alloy. Despite this degradation, the W_{OC} remained at 500mV or less up to a bandgap of ~2.1 eV, which is our target top cell bandgap for future five-junction and six-junction photovoltaic devices. By further optimizing the growth conditions at this bandgap, we expect to demonstrate even better cell performance.

In this work, we have developed high-bandgap AlGaInP solar cells grown by OMVPE for use in the next-generation of multijunction photovoltaic devices. Increasing the growth temperature from 700°C to 780°C for ~2.0 eV AlGaInP devices led to a decrease in the W_{OC} from 500mV to 440mV and increase in the efficiency from 11.9% to 14.8%. We found that growing at a high growth rate and phosphine partial pressure is important to maintaining a high IQE. By varying the junction position and cell thickness, we found that the minority carrier diffusion length in the n-type emitter is significantly shorter than the p-type base, suggesting that the thickness of each of these layers is critical to the cell design. We then grew samples with bandgaps ranging from 1.90 eV to 2.17 eV by varying the aluminum composition in the alloy, and found that the material quality degraded as the aluminum composition was increased. Despite this degradation, we maintained a W_{OC} of 500mV or less up to a bandgap of 2.1 eV. These devices exceed the performance of the best AlGaInP

126

solar cells reported to date, which is an important step toward integrating AlGaInP subcells into multijunction photovoltaic devices with five or more junctions and into dual-junction cells designed for high-temperature operation.

4.4 Challenges for High-Temperature Operation

Even after developing high-quality AlGaInP and GaAs subcells with the correct bandgaps for operation at 400°C, there are a number of additional challenges related to high-temperature operation that must be explored. While solar cells have been studied extensively at or near standard operating temperatures (T < 100°C), there have only been a few studies on solar cell performance and reliability at temperatures that exceed 100°C [140-143]. In particular, there are three challenges that deserve examination since they could have a significant impact on the reliability and performance of a photovoltaic device at elevated temperatures.

Dopant Diffusion

The first is dopant diffusion in the semiconductor, which will be accelerated at high-temperatures due to Fick's laws [144]. While dopant diffusion could impact a number of cell components, it is of particular concern for the tunnel junction. The reason for this is that just a small amount of dopant diffusion could cause the conduction and valence bands to bend in such a way that the tunneling probability would be significantly reduced, and this could eventually lead to a tunnel junction failure [45,145]. While 400°C is significantly higher than standard operating temperature, it is important to remember that solar cells are commonly grown at temperatures in excess of 700°C and are considered stable for a short period of time at these high temperatures [120]. Because of this, we would not expect dopant diffusion to cause a catastrophic tunnel junction failure at a much lower temperature, 400°C,

over a short timespan. However, since these solar cells will have to last for 20 or more years in the field, it is important that we study dopant diffusion over a longer period of time.

To investigate the impact of dopant diffusion on solar cell performance, we have grown a number of tunnel junction structures and have put them through long anneals at temperatures of 400°C or higher. One test involved growing a dual-junction solar cell and annealing it at 400°C for 24 hours. For this sample, we ran a Secondary Ion Mass Spectrometry (SIMS) analysis of the structure before and after annealing [146]. The results of the SIMS study are shown in Figure 4.21.
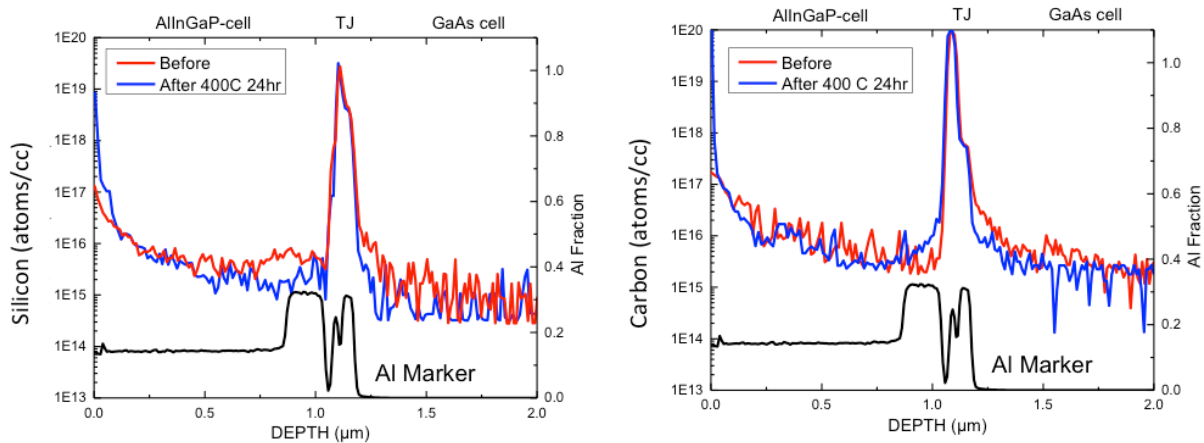
Figure 4.21: SIMS profile of dual-junction cell after being annealed at 24 hours at 400°C. The two elements that are being measured, silicon and carbon, are the dopant materials that we use in the tunnel junction.[21]

The two elements shown in these plots are carbon and silicon, which are respectively the p-type and n-type dopant species in our tunnel junction. We are primarily looking for differences in the two profiles near where they peak (marked TJ at the top of the plot). While the two curves don't overlap exactly, the differences between the curves are very small. This suggests that we are not seeing any appreciable dopant diffusion in the tunnel junction of this sample.

---

[21] Courtesy of Daehwan Jung.

In another test, we took a tunnel junction structure that we grew and annealed it at 450°C for 200 hours. After this anneal, we measured the temperature-dependent IV characteristics of the tunnel junction up to a temperature of 400°C. These IV curves are shown in Figure 4.22.
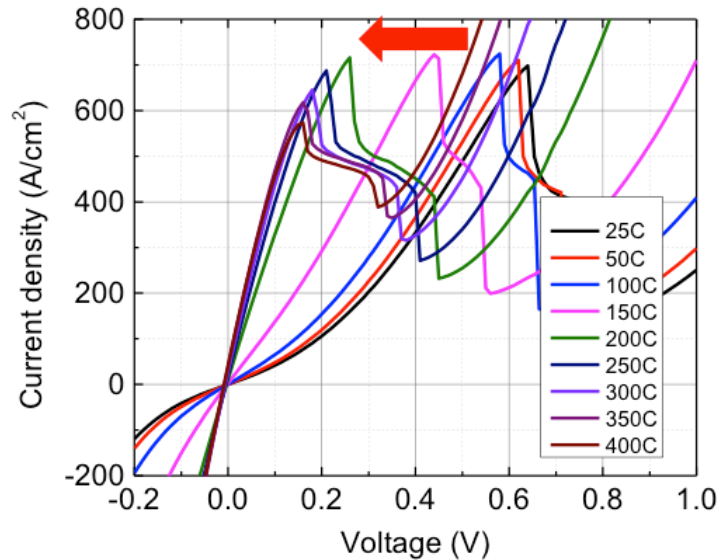
Figure 4.22: Temperature-dependent IV characteristics of a tunnel-junction structure after being annealed at 200 hours at 450°C.[22]

From these curves, we can see that the tunnel-junction still exhibits good tunneling behavior even after a long anneal. At all operating temperatures, we measure a peak tunneling current that corresponds to a light intensity greater than 10,000 suns. Additionally, we observe that the differential resistance of the tunnel junction decreases at high temperatures, suggesting that the series resistance from the tunnel junction will actually be smaller at high operating temperatures. We have not yet seen any hints that dopant diffusion will have a negative impact on cell performance, however it is important to conduct additional degradation studies where we anneal the solar cells at even higher temperatures for longer periods of time.

[22] Courtesy of Daehwan Jung.

Contact Metallization

The second challenge that we investigated was the potential for cell damage arising from the diffusion of metal into the semiconductor. Gold is commonly used as the metal for the front and back contacts of III-V multijunction devices operated at room temperature. However, a glance at the phase diagram for gold and gallium indicates that a eutectic of AuGa will form at temperatures below 400°C, and this will lead to shunting of the solar cell if this metal diffuses through the junction [147]. Even if gold is replaced by a metal that does not form a eutectic with the semiconductor, it is still possible for metal to diffuse into the active device at high-temperatures and damage the cell. Figure 4.23 shows the room-temperature DIV characteristics of AlGaInP solar cells with gold and nickel front contacts after annealing the samples at various temperatures for 30 minutes.
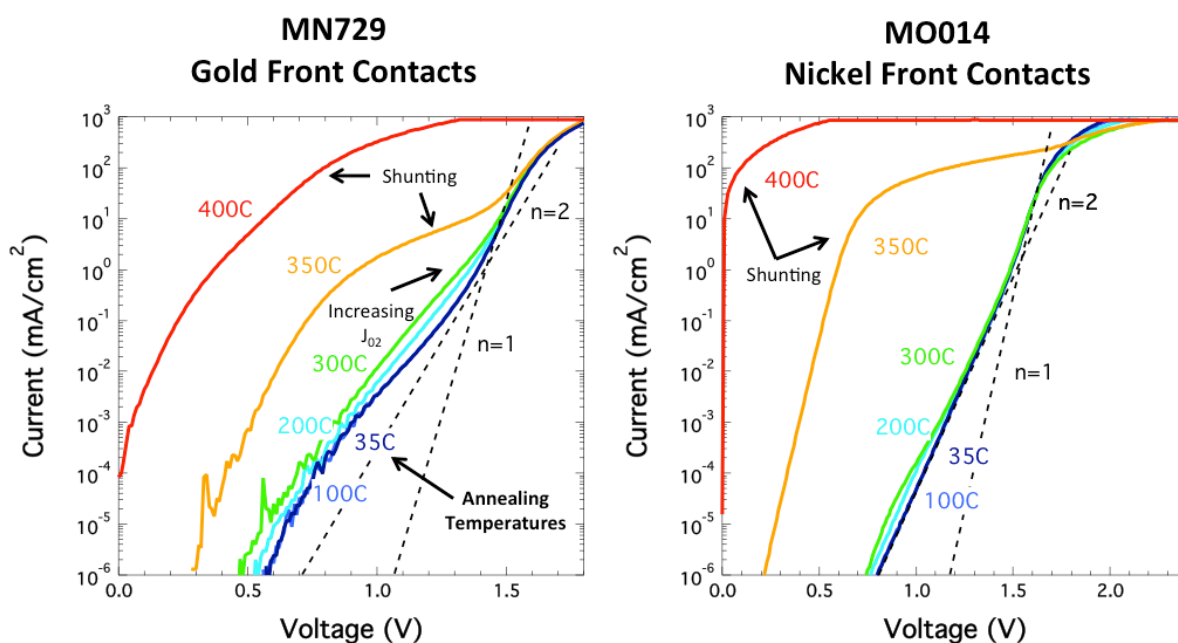
Figure 4.23: DIV characteristics of AlGaInP solar cells with (left) gold and (right) nickel front contacts after annealing the samples at various temperatures for 30 minutes. These measurements indicate that these two metals begin to shunt the solar cell after it is heated up to temperatures above 350°C.

This figure shows two examples of bad metallizations that will damage a solar cell even after very short anneals to temperatures of 400°C. For the sample with a gold metallization, we begin to see a small increase in the J_{02} dark current at annealing temperatures of 200°C and 300°C. After annealing this sample above 350°C, we begin to see a shoulder in the DIV curve, which is indicative of a shunt. For the sample with a nickel metallization, the DIV characteristics remain fairly stable up to annealing temperatures of ~300°C. However, we again see a shunt form in the solar cell once the annealing temperature is increased to 350°C or higher. These shunts are formed because metal is diffusing into the semiconductor and through the junction, opening up a parallel pathway (parallel resistor) for current to flow through the device. Since this diffusion of the metal into the semiconductor will cause a catastrophic failure of the solar cell, it is important that a non-reactive metallization is used.

We have developed a number of promising high-temperature metallizations in this project, all of which follow the same general approach as is shown on the left side of Figure 4.24. We begin by depositing a thin layer of titanium (Ti), which serves the purpose of providing good adhesion between the metal and the semiconductor. This is followed by the deposition of a diffusion barrier that is usually composed of a refractory metal such as tungsten-titanium (WTi, 90%/10%), molybdenum (Mo), palladium (Pd), or platinum (Pt) [148,149]. The purpose of the diffusion barrier is to prevent the upper metals layers from diffusing into the semiconductor and shorting the solar cell. The next layer that we deposit is a thick conductive metal that allows current to flow through the top grid with minimal resistance. This metal must have a high conductivity; we have explored silver (Ag) and aluminum (Al) for this purpose [150]. The final layer is a capping metal, such as Ti, which prevents the conductive metal from tarnishing.

131

Figure 4.24: (Left) A 4-layer approach that we used to develop a stable metallization for high-temperature operation. (Right) Room-temperature DIV characteristics of AlGaInP solar cells with Ti/WTi/Al/Ti front contacts after a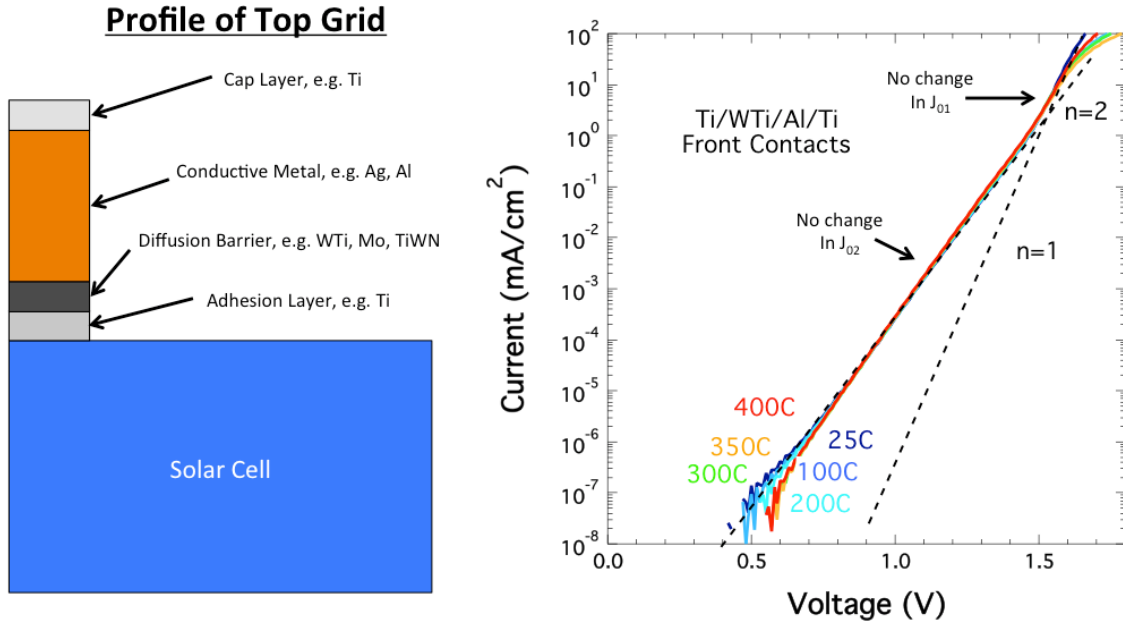nnealing the samples at various temperatures for 30 minutes. This plot is indicative of a stable metallization since we see no change in the J_{01} and J_{02} dark currents and no shunts even after annealing the sample to 400°C.

One of the first metals that we developed was composed of Ti/Pd/Ag/Ti, but unfortunately this metal was not ideal for two reasons. First, we found that Ag is not compatible with our contact layer etchant (NH_4OH:H_2O_2:H_2O, 2:1:10). To mitigate this issue, we attempted to etch our contact layer with a solution of H_3PO_4:H_2O_2:H_2O (3:4:20). While this solution can effectively etch the GaAs contact layer without attacking the metal, we found that it will also damage the solar cell if the window layer is exposed to the solution for too long (~10 seconds or longer). We also found that the Pd did not work well as a diffusion barrier and observed shunting in our solar cells after annealing at temperatures of 400°C.

We then moved to a contact metallization composed of Ti/WTi/Al/Ti. This metal did not react in our standard contact layer etchant (NH_4OH:H_2O_2:H_2O, 2:1:10), and the WTi

appeared to act as a good diffusion barrier at temperatures of 400°C. The plot on the right of Figure 4.24 shows the room-temperature DIV characteristics of an AlGaInP cell with Ti/WTi/Al/Ti front contacts after annealing the samples at various temperatures for 30 minutes.

This plot is indicative of a stable metallization since we see no change in the J_{01} and J_{02} dark currents and no shunts after annealing this sample up to 400°C. It is also important to note that DIV measurements are more sensitive to cell damage than QE measurements, so if any damage were occurring we would likely see it in this plot. While this sample remained stable after annealing, we have observed shunting in a different sample with the same metallization. For this reason, we have moved to a metal stack that consists of Ti/Pt/Al/Ti, where a Pt diffusion barrier is easier to deposit and also acts as an effective diffusion barrier. While these metallizations do not appear to damage our solar cells after anneals of up to 200 hours, it is important that we conduct longer annealing tests to confirm that the metals remain stable over a longer lifetime. Also, we have only explored diffusion barriers with a thickness of 50nm, however we believe that varying the thickness of this layer could have a significant impact on the stability of the metal.

Surface Degradation

The final challenge that we considered was the possibility that the surface would degrade at high-temperatures due to oxidation of the window layer or from the preferential desorption of group-V atoms in III-V semiconductors [151]. The temperature range at which these effects could impact cell performance is unknown, and thus it is important to investigate the potential for surface damage at elevated temperatures. It is also important to note that if damage were occurring at 400°C for an unencapsulated cell, we expect that

depositing an encapsulation layer on the device could protect the semiconductor surface. Two potential encapsulation materials are Al_2O_3 and TiO_2, both of which are commonly used in the ARC of a multijunction solar cell [53].

To date, we have only investigated Al_2O_3 as an encapsulation layer for our solar cells. To test whether Al_2O_3 can prevent surface damage, we have conducted annealing studies at 400°C for an AlGaInP solar cell with a high-temperature Ti/Pt/Al/Ti metallization and a layer of Al_2O_3 deposited on the window of the solar cell. For this test, we measured the one-sun EQE and LIV characteristics of the solar cell before annealing, after a 4-hour anneal, after a 24-hour anneal, and after a 200-hour anneal. The results of this study are shown in Figure 4.25.
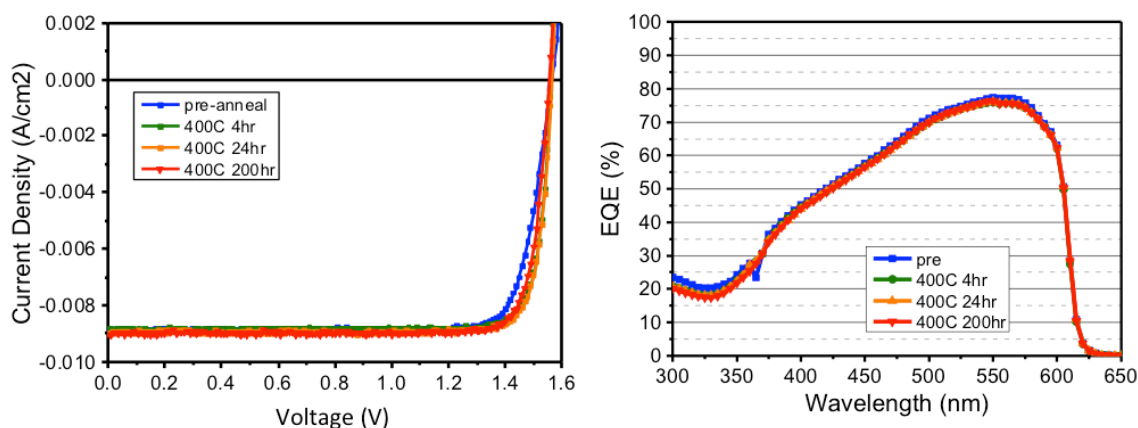
Figure 4.25: (Left) LIV curves and (right) EQE curves of an AlGaInP solar cell after annealing the sample to 400°C for various lengths of time. This sample had a front metal consisting of Ti/Pt/Al/Ti and an encapsulation layer consisting of Al_2O_3.[23]

The most important result from these plots is that we observe very little change in the J_{SC} and V_{OC} of the AlGaInP solar cell after annealing the sample at 400°C for up to 200 hours. This would be the equivalent of about one month of operation in the field, which is less than 1% of the required lifetime of the solar cells if they were to be operated in a PV-T hybrid

---

[23] Courtesy of Yukun Sun.

solar collector. However, it is very encouraging that the cell performance remains stable after being heated to 400°C for this timespan. Also note that the fill factor improves slightly after the sample is first annealed. The reason for this is that the high-temperature contacts have a high series resistance before being annealed, however annealing acts to decrease the contact resistance significantly. Also note that no significant shunts form after the 200-hour anneal for this sample.

The second most important result is that we observe no measurable degradation to the EQE of the AlGaInP solar cell even after it is annealed at 400°C for 200 hours. If the 25-nm thick window layer were damaged during annealing, we would expect an increase in the surface recombination velocity that would lead to a drop in the short-wavelength EQE [95]. Since there is no change in the EQE after annealing, we can deduce that the window layer is not degrading and that the Al_2O_3 encapsulation layer is effectively protecting the surface.

This study addresses all three of the challenges for high-temperature operation that we have investigated in this section. The fact that the AlGaInP cell performance remains stable after annealing at 400°C for 200 hours suggests that dopant diffusion, group-V desorption, window layer oxidation, and metal diffusion are not damaging the subcell. While additional degradation studies are required before any photovoltaic device can be viably considered for a system that requires high-temperature operation, we believe that these annealing studies show that it is possible for III-V solar cells to achieve excellent reliability even when operated at temperatures up to 400°C.

4.5 Chapter Summary

This chapter explored the development of solar cells for high-temperature applications. The chapter started by motivating the development of high-temperature III-V solar cells for

photovoltaic-thermal hybrid solar collectors. We then developed an efficiency model to predict the temperature-dependent performance of single-junction and dual-junction solar cells. While efficiencies greater than 20% at a temperature of 400°C appear to be possible with single-junction III-V solar cells, we determined that we would have to develop dual-junction solar cells in order to reach our efficiency goal of 25% at 400°C. We found that we could nearly attain the global efficiency maximum by developing a lattice-matched dual-junction device with room-temperature bandgaps of 1.42eV (GaAs) and 2.0eV (AlGaInP). While GaAs solar cells have been developed with very good performance (we typically achieve W_{OC}s of ~370mV), one of the most significant challenges involved the development of a high-bandgap (2.0eV) AlGaInP solar cell that is required for high-temperature operation. This chapter detailed the development of 2.0eV AlGaInP solar cells that attained the lowest W_{OC} of any AlGaInP solar cell reported to date. The OMVPE growth conditions were discussed in detail, and we found that the growth temperature and emitter dopant species were among the most important parameters that led to high-performing AlGaInP solar cells. Finally, we discussed some of the critical cell development challenges that we faced in this project, including the investigation of dopant diffusion in our devices, the deposition of an Al_2O_3 encapsulant to protect the semiconductor surface, and the development of a stable Ti/Pt/Al/Ti contact metallization. Even after annealing an AlGaInP solar cell at 400°C for 200 hours, we observed no measurable degradation to the EQE, J_{SC}, and V_{OC} of the device. This result is a testament to the quality of these cell components and shows that it should be possible for III-V solar cells to achieve excellent reliability even when operated at temperatures up to 400°C.

Chapter 5: Solar Cell Properties at High Temperatures

As the operating temperature of a photovoltaic device is varied, its performance is impacted dramatically. An exponential increase in the intrinsic carrier concentration, n_i, at high temperatures will drive an exponential increase in the J_{01} & J_{02} dark currents [39,40,95,152]. This will lead to a notable reduction to the V_{OC}, fill factor, and cell efficiency. High temperatures will also reduce the bandgap of the semiconductor [114], which will result in a small increase to the J_{SC}, provided that the collection efficiency for photogenerated carriers remains high [111].

It is possible to recover some of the lost voltage by operating the solar cell at high light intensities (100-1000 suns), especially since concentration will become more leveraging to cell performance at high temperatures due to the increasing kT/q arguments in the exponents of the diode equation. At 400°C, the V_{OC} will increase by ~133mV per 10x increase in concentration at 400°C, more than twice as fast as the 60mV/decade increase in V_{OC} that occurs at 25°C [111]. Unfortunately, high temperatures will also drive a fundamental increase in both the semiconductor sheet resistance and the metal grid resistance, making it more difficult to achieve a high fill factor under concentrated sunlight [38]. For this reason it is critically important to engineer a metal grid to minimize these resistive losses.

In this chapter, we characterize the temperature-dependent behavior of real-world solar cells. The chapter will begin with a description of our technique for measuring cell performance at elevated temperatures. We will then present and discuss temperature-dependent quantum efficiency, current-voltage, and concentrator measurements for single-junction AlGaInP and GaAs solar cells. These results are compared to the Hovel equations shown in the previous chapter, and we find that there is excellent agreement between our

measurements and the model. Finally, we discuss recent work that has been done to improve the performance of the top cell at 400°C.

5.1 Device Characterization at High-Temperature

To measure the cell performance at elevated temperatures, we used an HFS600E-PB4 temperature controlled stage built by Linkam Scientific Instruments.
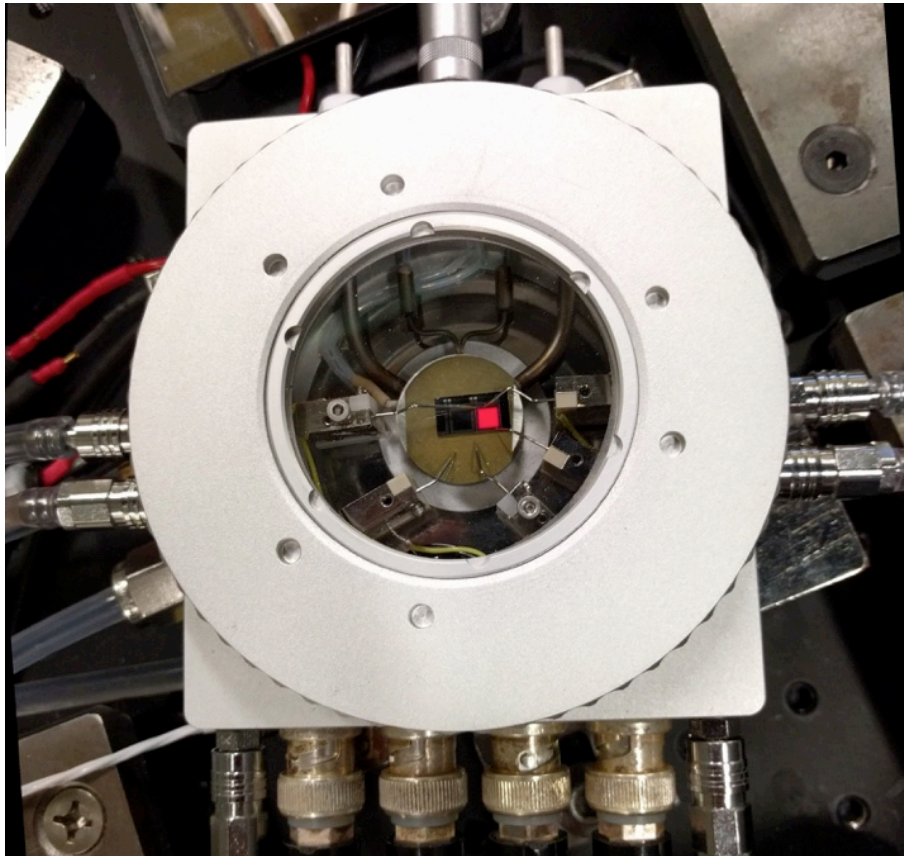
Figure 5.1: Picture of the HFS600E-PB4 Linkam stage used to measure the temperature-dependent characteristics of our solar cells. In this picture, an AlGaInP cell is being forward biased at 400°C, causing a red shift in its electroluminescence spectrum (orange light is emitted at room temperature) [111].

This stage, shown in Figure 5.1, has the ability to control the sample temperature from below room temperature to 600°C and has five sample probes that are used to measure the electrical characteristics of the solar cells. This enables us to make four-probe measurements

of our solar cells. The fifth probe is added to supply current to both busbars, which is important to minimize series resistance measurement artifacts that could arise at high-concentrations. The Linkam stage has a 3-inch diameter glass window that allows for electro-optical measurements of the devices. All of the cells were measured in a nitrogen environment to minimize the risk of oxidizing the window layer, however we have carried out 200 hour anneals at 400°C and observed that the performance of our solar cells remains stable when encapsulated with a layer of Al_2O_3 [111].

This temperature-controlled stage was incorporated into our quantum efficiency, current-voltage, and flash testing setups to enable temperature-dependent measurements of the cell properties. The window of the Linkam stage reflects ~8% of incoming light, which lowers the number of photons incident on the solar cell. Since accurate quantum efficiency measurements require that the intensity of incident light be carefully calibrated, it is necessary for us to characterize the wavelength-dependent reflectance of this window. In order to correct for the window reflectance (R_{window}), we must divide the EQE by ($1-R_{window}$) and the cell reflectance (R_{cell}) by ($1-R_{window}$)^2, where the exponent of 2 comes from the two passes that the monochromatic light makes through the window [111].

To measure the one-sun LIV and DIV characteristics of our cells, we used a custom-built solar simulator with a Xenon lamp and adjustable high-brightness LEDs. The spectrum and intensity are adjusted using calibrated reference cells to simulate the AM1.5D spectrum at 1000W/m^2. When calibrating the one-sun light intensity for cells in the Linkam stage, it is important to take into account the temperature variation of the EQE curves. To do this, we used calibrated GaInP and GaAs reference cells to calculate a spectral mismatch correction factor at each temperature and added LED light until an equivalent one-sun intensity was

139

reached [111].

For concentrator measurements, we used the High Intensity Pulsed Solar Simulator (HIPSS) at NREL. This system uses two low-pressure Xenon arc lamps to deliver millisecond-length pulses of light to the cell, enough time to measure the LIV characteristics of our devices. The light intensity is varied from ~30 suns to ~1500 suns by adjusting the area of an aperture that blocks out a fraction of the light generated by the arc lamps. We assume the photocurrent varies linearly with intensity, and determine the concentration from the ratio of the J_{SC} measured using the HIPSS to the one-sun J_{SC} measured using our solar simulator. At the largest apertures and highest temperatures, the series resistance can prevent the LIV curves from flattening before J_{SC}. When this is the case, the J_{SC} cannot be used as an indicator of the concentration. For those curves, we estimate the concentration by assuming that the variation of photocurrent with temperature is the same at all apertures. Therefore, the relative change in photocurrent from 25–400°C should be the same at the largest aperture (>1000 suns) as it is at the smallest aperture (<40 suns), and the concentrations can be appropriately scaled. This assumption will be validated in the next section [111].

The temperature of the Linkam stage is measured using a thermocouple embedded in the stage. Since our cells are placed on top of the stage, separated from the thermocouple, it is important to verify that the temperature of our devices is close to the thermocouple temperature. To do this, we measured the electroluminescence (EL) spectrum of a GaAs solar cell as the Linkam stage was heated and used the peak emission energy (E_{peak}) as a thermometer for the cell temperature. The bandgap of the GaAs active layers can be calculated by subtracting $kT/2$ from this peak emission energy, where k is the Boltzmann

constant and T is the cell temperature in Kelvin [133]. The temperature dependence of the GaAs bandgap can also be described by the Varshni equation, shown in Equation 5.1 [114]:

$$E_g(T) = E_g(0) - \frac{\alpha T^2}{T+\beta} = E_{peak}(T) - \frac{kT}{2} \tag{5.1}$$

Where α and β are material constants and $E_g(0)$ is the bandgap at 0K. Since the Varshni parameters are well characterized for GaAs (α = *0.5405 meV/K*, β = *204K* [115]), we can use this equation to solve for the cell temperature from the peak emission energy of the cell measured using EL. Figure 5.2 shows a comparison between the cell temperature calculated using Equation 5.1 and the thermocouple temperature.
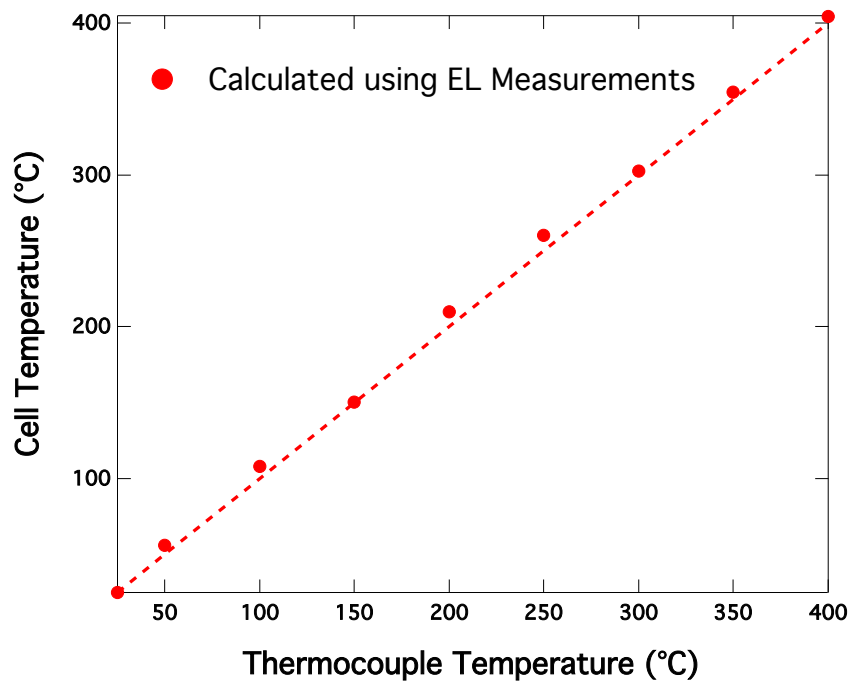
Figure 5.2: Comparison between the cell temperatures calculated using Equation 5.1 and the temperature of the thermocouple embedded in the Linkam stage. The dashed line has a slope of one to indicate how far off the cell temperature is from the thermocouple temperature [111].

The dashed line has a slope of one to indicate how far off the cell temperature is from the thermocouple temperature. This plot gives us a good sense for how the thermocouple temperature and the cell temperature differ. On average, we measure a cell temperature that

is 5.8°C higher than the thermocouple temperature, with a standard deviation of 3.6°C. All temperatures reported in the following sections correspond to the thermocouple temperature.

5.2 Temperature-Dependent Solar Cell Results

Here, we describe quantum efficiency, current-voltage, and concentrator measurements of AlGaInP and GaAs solar cells taken over a temperature range of 25-400°C. Our results are compared to the temperature dependent solar cell model detailed in Chapter 4.

Temperature Dependent Performance of the AlGaInP Solar Cell

The temperature dependent IQE of the AlGaInP cell is shown in Figure 5.3.
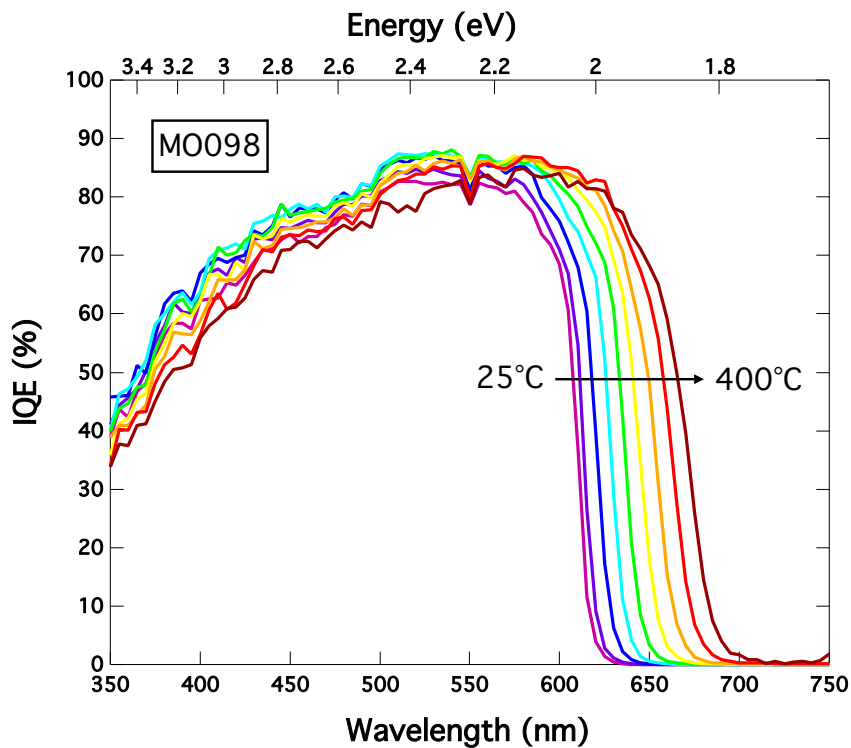
Figure 5.3: Temperature dependent IQE of the AlGaInP solar cell showing no significant degradation to the peak IQE and a reduction in the bandgap of the AlInP window and AlGaInP active layers as the temperature is increased [111].

There are two main takeaways from this plot. First, the IQE does not degrade significantly as the cell temperature is increased, with the magnitude of the peak IQE

remaining at ~86% over the entire temperature range. Second, the bandgap of the cell decreases from ~2.01eV at 25°C to ~1.83eV at 400°C. Note that the bandgap of the AlInP window layer decreases with temperature as well, leading to a drop in the short-wavelength IQE [111].

Figure 5.4 shows temperature dependent LIV measurements of the AlGaInP solar cell taken at 1000 W/m^2 (one-sun) under the AM1.5D spectrum. We observe a small increase in the J_{SC} at high temperatures due to the decreasing bandgap of AlGaInP. We also find that the V_{OC} decreases at a rate of ~2.6mV/°C over this temperature range at a light intensity of one-sun. The dominant factor impacting the cell efficiency is the decreasing V_{OC}, which is a direct result of the exponentially increasing J_{01} and J_{02} dark currents [111].
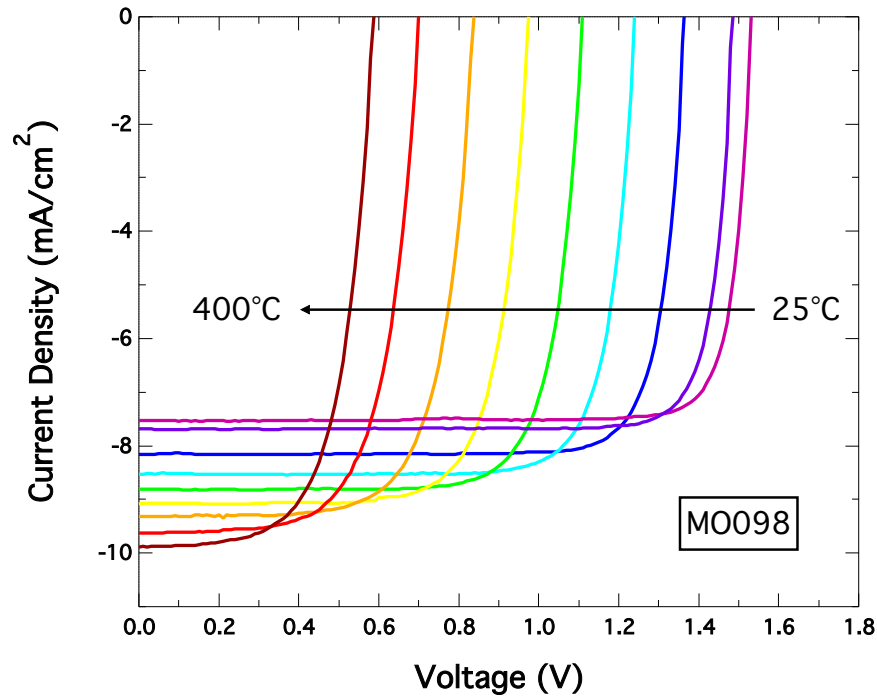
Figure 5.4: Temperature dependent LIV measurements of the AlGaInP solar cell taken at a light intensity of one-sun under the AM1.5D spectrum. As the temperature is increased, we observe an increase in the J_{SC} and decrease in the V_{OC} [111].

Temperature dependent DIV measurements of the AlGaInP solar cell are shown in

Figure 5.5. At low voltages (V < 100mV) the curves bend downwards because of the -1 terms in the diode equations. At high currents (J > 100mA/cm^2), the curves begin to roll over due to series resistance. The dashed lines on this plot indicate the slopes of ideal diodes with ideality factors of 1 and 2, at temperatures of 25°C and 400°C. Note that these slopes change with temperature because of the *kT/q* arguments in the exponents of the diode equation. The y-intercepts of these lines correspond to J_{01} for the n=1 line and J_{02} for the n=2 line. For this AlGaInP cell, there are clear n=1 and n=2 regions at every temperature measured, allowing us to extract the temperature-dependent J_{01} and J_{02} dark currents. In the next section, we will compare these values to the n_i dependence of the dark currents derived in Chapter 4 [111].
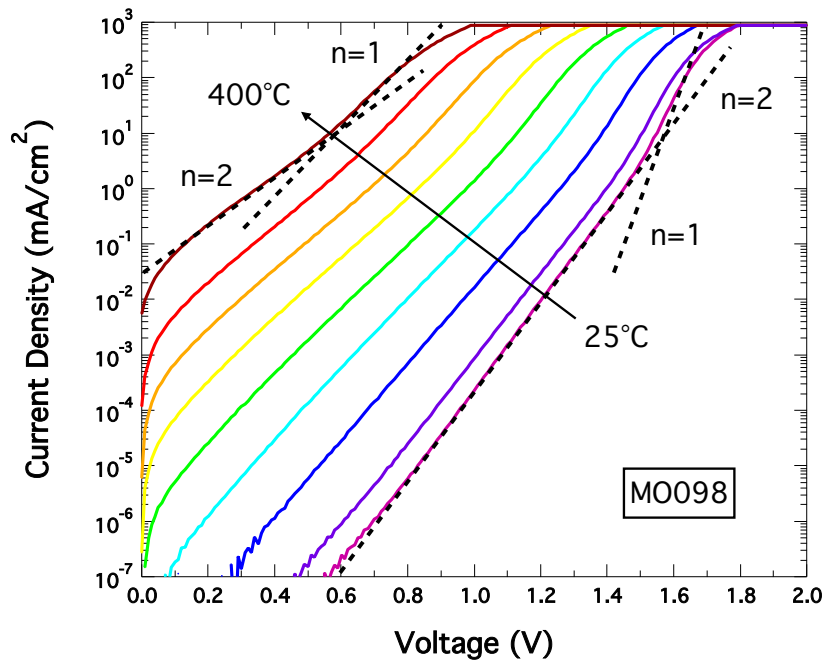
Figure 5.5: Temperature dependent DIV measurements of the AlGaInP solar cell showing an increase in the J_{01} and J_{02} dark currents as the temperature is increased. The dashed lines indicate the slopes of ideal diodes with ideality factors of 1 and 2, at temperatures of 25°C and 400°C [111].

Flash measurements of the AlGaInP cell, taken using the HIPSS, are shown in Figure 5.6. Due to the relatively high R_s of this AlGaInP cell, we observe a drop in the fill factor at

144

all temperatures when the intensity of light is increased above 1000 suns. For the flash measurements taken at 400°C, the fill factor drops from ~71% at 40 suns to ~48% at 1200 suns. We have since been able to achieve a better fill factor at high concentration with an improved grid design and a reduction in the emitter sheet resistance. This will be discussed later in the chapter [111].
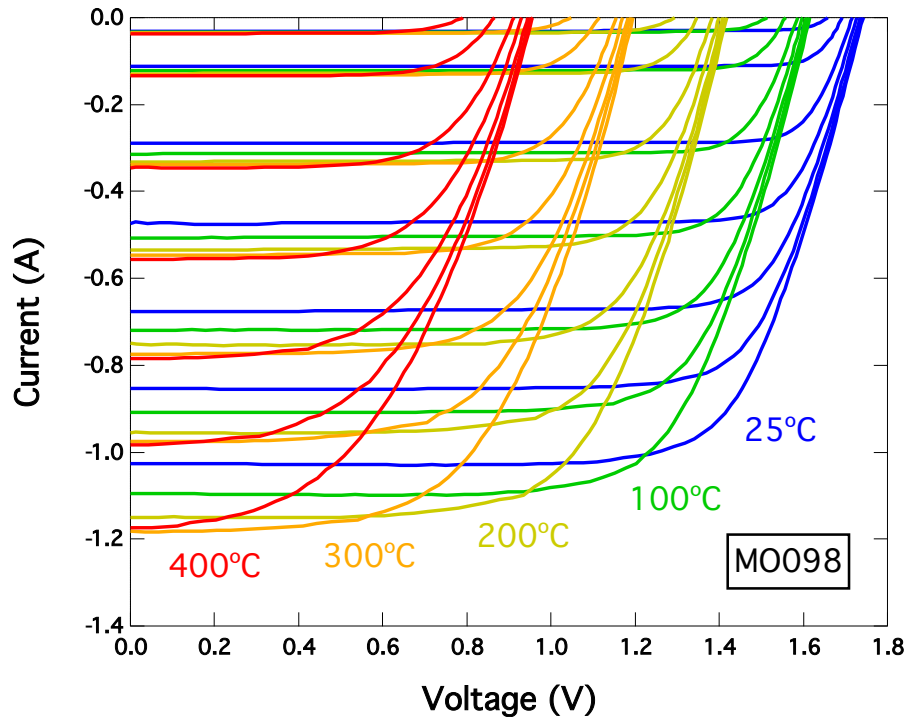
Figure 5.6: Flash measurements of the AlGaInP solar cell taken using the HIPSS at seven different apertures. The light intensities range from less than 40 suns at the smallest aperture to over 1000 suns at the largest aperture [111].

For the measurements taken at 400°C, we cannot determine the concentration from the measured J_{SC} at the four largest apertures (>500 suns) because series resistance prevents the LIV curves from flattening before J_{SC}. For these curves, we estimate the concentration of light using the procedure described earlier in the chapter. To validate this procedure, we compared the ratio of J_{SC} at high temperatures (100°C, 200°C, 300°C, 400°C) to the room temperature J_{SC} at each aperture for the curves that flatten before $J_{SC,}$ and we measure a

145

standard deviation of 0.8% from the average between these ratios. This supports our previous assumption that the linearity of the current vs. light intensity is not changing significantly as we increase the temperature from 25°C to 400°C [111].

Figure 5.7 shows a plot of the V_{OC} of the AlGaInP cell, measured using the HIPSS, as a function of both temperature and concentration. At a temperature of 400°C, the V_{OC} increases from ~600mV at 1 sun to ~950mV at 1000 suns. The dashed lines show the slopes of these curves for an ideal n=1 diode at each temperature. The overlap of this line with our measured data shows that there is a clear n=1 region at lower concentrations; however the V_{OC} starts to roll over at increasing concentrations. We are still investigating the cause of this rolloff. Note also that the slope of the n=1 lines increase with temperature, due to the increasing kT/q arguments in the exponents of the diode equation. This suggests that moving to high concentration is even more leveraging at high temperatures than it is at room temperature [111].
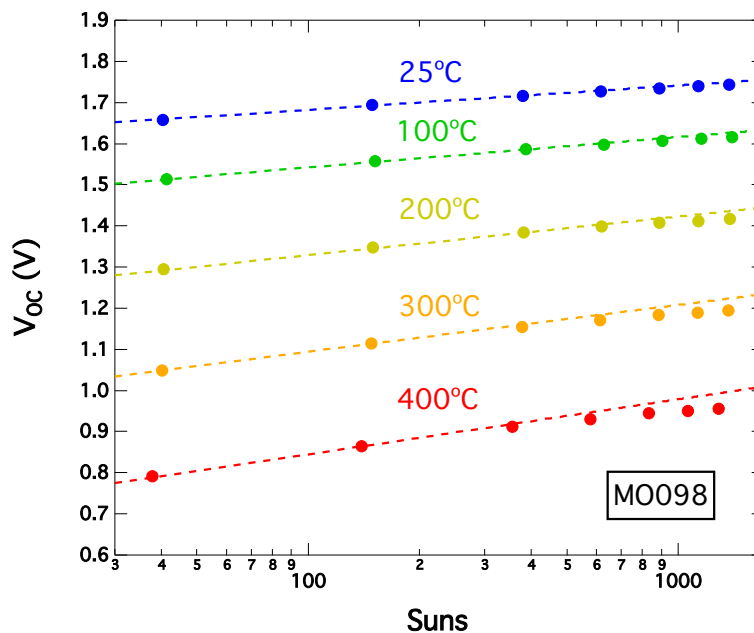
Figure 5.7: V_{OC} as a function of both temperature and concentration for the AlGaInP solar cell. The dashed lines show the slopes of these curves for an ideal n=1 diode at each temperature [111].

Temperature Dependent Performance of the GaAs Solar Cell

The temperature dependent IQE of a filtered GaAs cell is shown in Figure 5.8. Similar to what we observed with the AlGaInP cell, there is no significant degradation to the IQE as the cell temperature is increased, with the magnitude of the peak IQE remaining at ~92% over the entire temperature range. It is also apparent that the bandgap of the GaAs cell and the AlGaInP filter are both decreasing as the temperature is increased, causing the turn-on and turn-off of the IQE curves to shift to longer wavelengths [111].
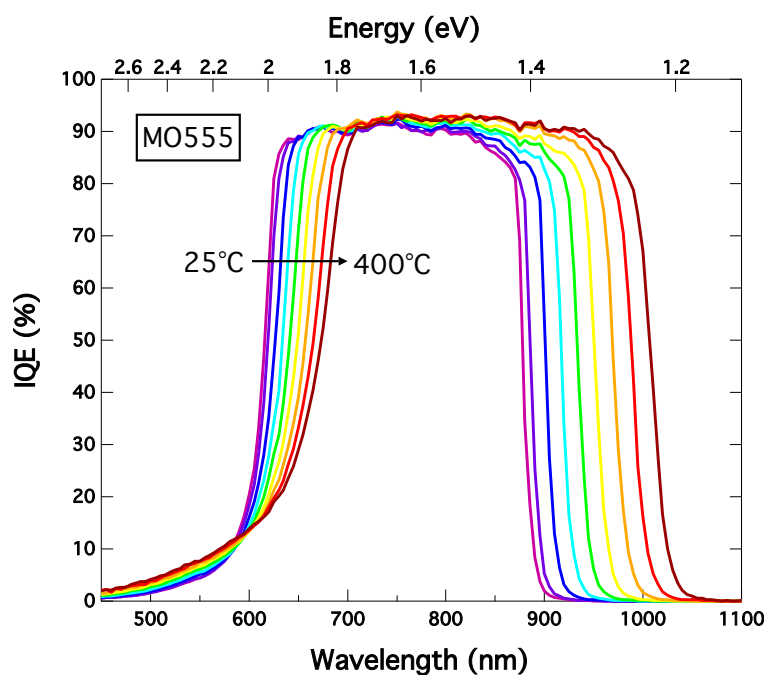
Figure 5.8: Temperature dependent IQE of GaAs solar cells showing no significant degradation to the peak IQE and a reduction in the bandgap of the AlGaInP filter and the GaAs active layers as the temperature is increased [111].

Figure 5.9 shows temperature dependent LIV measurements of the GaAs solar cell taken at one-sun under the AM1.5D spectrum. As the temperature is raised, we observe an increase in J_{SC} due to the decreasing bandgap of GaAs. It is also clear that there is a significant slope at J_{SC} at the highest temperatures, which was not observed for the AlGaInP cell. The reason for this is that the dark currents in the lower bandgap GaAs cell are ~100x

higher than in the AlGaInP cell at 400°C. We find that the V_{OC} is decreasing at a rate of ~2.4mV/°C at a light intensity of one-sun, and again this is the dominant factor impacting cell efficiency. This cell is clearly not suitable for one-sun operation at 400°C due to its low V_{OC} and the large slope at J_{SC}. However, as the concentration is increased the V_{OC} will increase significantly and, provided that the R_S is low, the slope at J_{SC} will become insignificant [111].
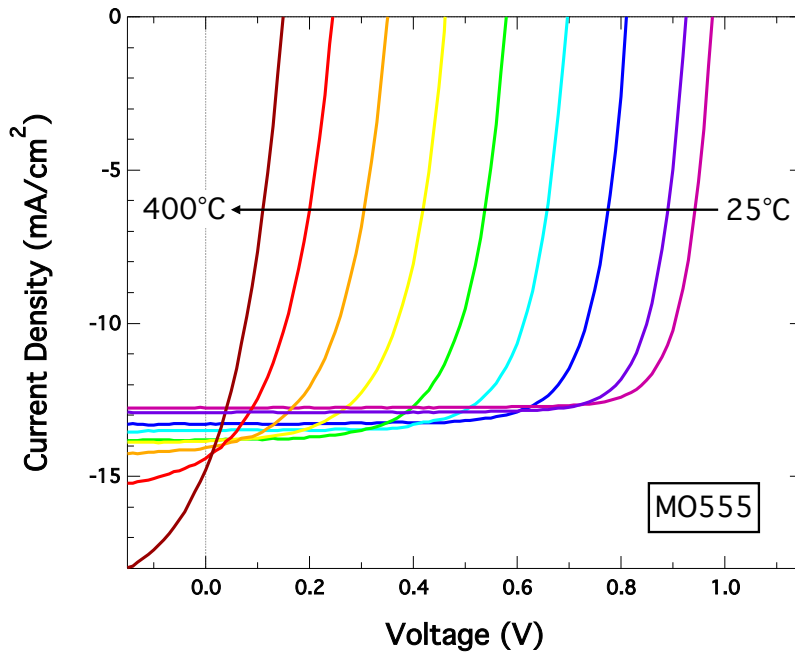
Figure 5.9: Temperature dependent LIV measurements of GaAs solar cells taken at a light intensity of one-sun under the AM1.5D spectrum. As the temperature is increased, we observe an increase in the J_{SC} and decrease in the V_{OC} [111].

Temperature dependent DIV measurements of the GaAs solar cell are shown in Figure 5.10. The dashed lines on this plot indicate the slopes of ideal diodes with ideality factors of 1 and 2 at a temperature of 25°C. As with the AlGaInP cell, there is a clear n=2 region at every temperature measured, allowing us to extract the temperature-dependent J_{02} dark current. However, we were unable to fit to the n=1 line at the highest temperatures so the J_{01} dark currents must instead be extracted using concentrator measurements [111].

148
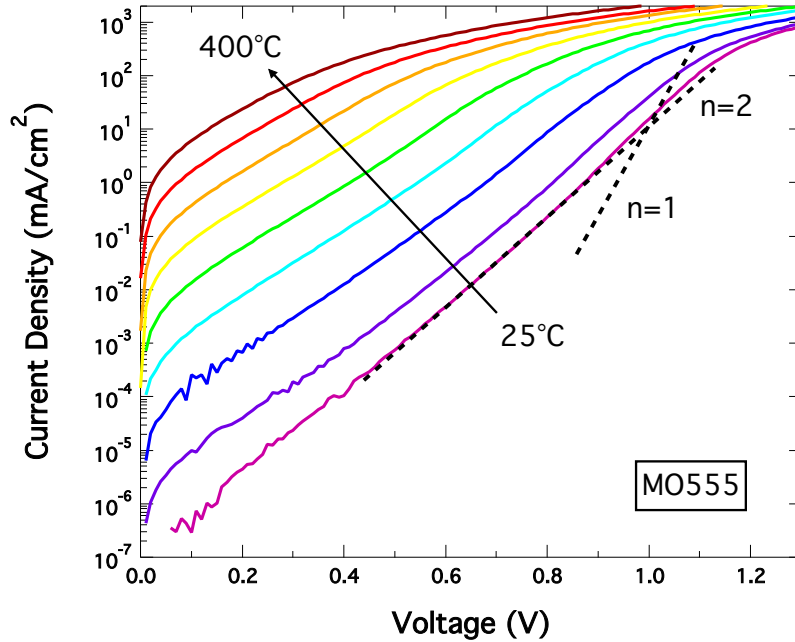
Figure 5.10: Temperature dependent DIV measurements of GaAs solar cells showing an increase in the J_{02} dark currents as the temperature is increased. The dashed lines indicate the slopes of ideal diodes with ideality factors of 1 and 2 at a temperature of 25°C [111].

Temperature-dependent flash measurements of the GaAs cell are shown in Figure 5.11.
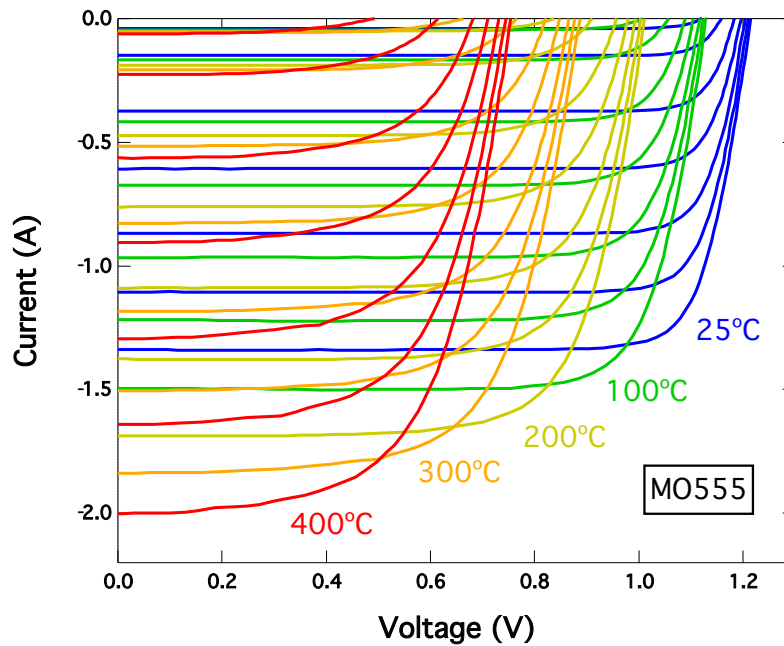
Figure 5.11: Flash measurements of the GaAs solar cell taken using the HIPSS at seven different apertures. The light intensities range from less than 40 suns at the smallest aperture to over 1000 suns at the largest aperture [111].

This sample maintained an excellent fill factor, >60%, at a concentration of 1000 suns and temperature of 400°C. Additionally, the low R_S made it possible for every single LIV curve to flatten before J_{SC}. We again compared the ratio of the high-temperature J_{SC} to the room temperature J_{SC} at each aperture, and the standard deviation between these ratios was 1.0%, further supporting our previous assumption of linearity of the current vs. light intensity [111].

Figure 5.12 shows a plot of the V_{OC} of the GaAs cell as a function of both temperature and concentration, where the dashed lines show the slopes of these curves for an ideal n=1 diode at each temperature.
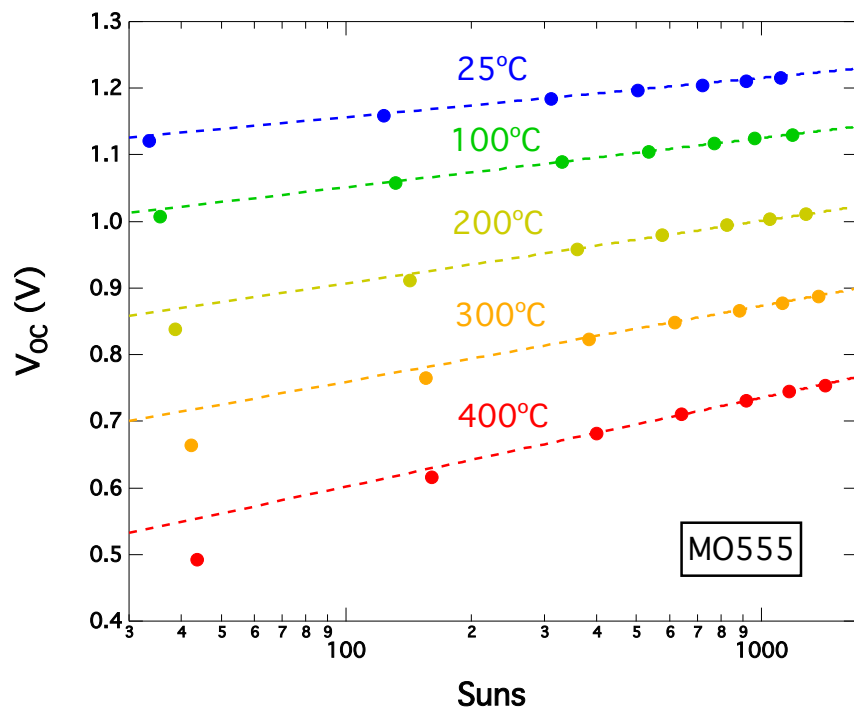

Figure 5.12: V_{OC} as a function of both temperature and concentration for the GaAs cell. The dashed lines show the slopes of these curves for an ideal n=1 diode at each temperature and can be used to extract the temperature dependent J_{01} dark currents [111].

It is clear from these plots that the GaAs cell becomes dominated by n=1 recombination at high light intensities, however this does not occur until a concentration of 200-300 suns is

achieved for the cells measured above 200°C. These plots also illustrate the significant improvement in the V_{OC} at 400°C that occurs when these cells are taken to high concentrations. At a temperature of 400°C, the V_{OC} increases from ~150mV at 1 sun to ~740mV at 1000 suns [111].

5.3 Comparing the Results to the Hovel Model

It is possible to extract the J_{01} and J_{02} dark currents from the temperature-dependent DIV and concentrator measurements of the AlGaInP and GaAs solar cells shown in the previous section. These extracted dark currents can be compared to the n_i-dominated temperature dependence of the J_{01} and J_{02} dark currents that we derived from the Hovel equations in chapter 4 [39,40,95,111]. These temperature dependences are shown again below:

$$J_{01} \; \alpha \; T^3 e^{-E_g/kT} \tag{5.2}$$

$$J_{02} \; \alpha \; T^{3/2} e^{-E_g/2kT} \tag{5.3}$$

When calculating the temperature dependence of the dark currents from these equations, we use values for J_{01} and J_{02} extracted at room temperature as a starting point and extrapolate these values to 400°C with Equation 5.2 and Equation 5.3. The temperature dependence of the bandgap, $E_g(T)$, is derived from EL measurements for the GaAs cell and from EQE measurements for the AlGaInP cell [111].

For the AlGaInP cell, we were able to fit the J_{01} and J_{02} dark currents at every temperature from 25°C to 400°C. Figure 5.13 shows a comparison between the dark currents extracted from the DIV measurements of the AlGaInP solar cell shown in Figure 5.5 and the n_i-dominated temperature dependence of the dark currents calculated using Equation 5.2 and Equation 5.3 [111].

151
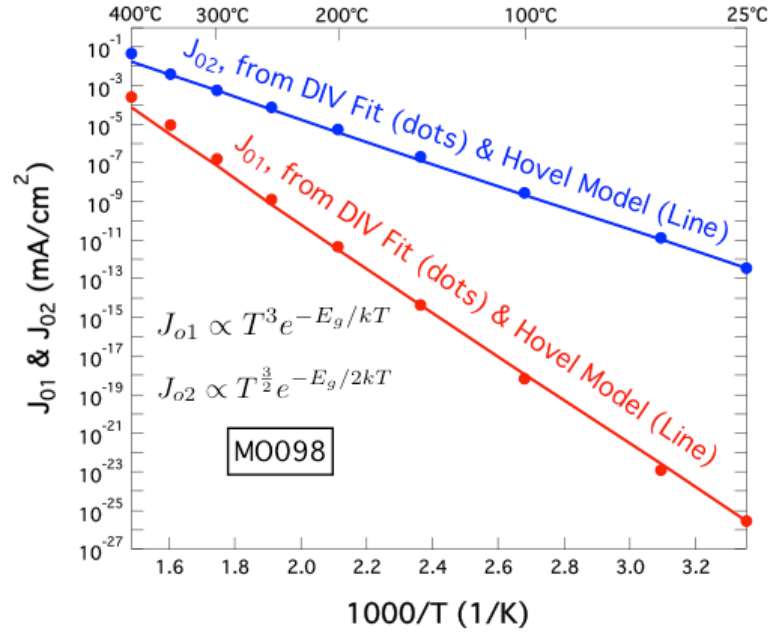
Figure 5.13: Comparison between the dark currents extracted from temperature dependent DIV measurements of AlGaInP solar cells and the n_i-dominated temperature dependence of the dark currents calculated using Eqs. 5.2 & 5.3, which were derived from the Hovel model in Chapter 4 [111].

The excellent agreement between the dark currents extracted from DIV measurements and the dark currents calculated using Equation 5.2 and Equation 5.3 provides evidence that the recombination characteristics that are described by the Hovel model continue to remain valid at temperatures as high as 400°C for the AlGaInP solar cell. This agreement also confirms that the intrinsic carrier concentration, n_i, is the dominant term that impacts the temperature dependence of the dark currents [111].

For the GaAs solar cell, we were able to fit the J_{02} dark currents at every temperature from 25°C to 400°C. However, due to series resistance effects, we were unable to fit the J_{01} dark currents above 100°C. Alternatively, it is possible to extract the J_{01} dark currents as a function of temperature using our concentrator results, since there is a clear n=1 region that can be seen in the V_{OC} vs. suns plot of Figure 5.12. Under the assumption that J_{02} is

negligible at these conditions (which should be the case if we are fitting to the n=1 line), and that $J = R_S = 0$ at V_{OC}, we are able to rearrange the diode equation to solve for J_{01} [111]:

$$J_{01} = \frac{J_L}{e^{qV_{OC}/kT}} \tag{5.4}$$

Using this equation, we are able to extract the temperature dependent J_{01} dark saturation currents of the GaAs solar cell using our flash measurements. Figure 5.14 shows a comparison between the J_{01} dark currents extracted from concentrator measurements, the J_{02} dark currents extracted from DIV measurements, and the J_{01} & J_{02} dark currents calculated using Equation 5.2 and Equation 5.3 [111].
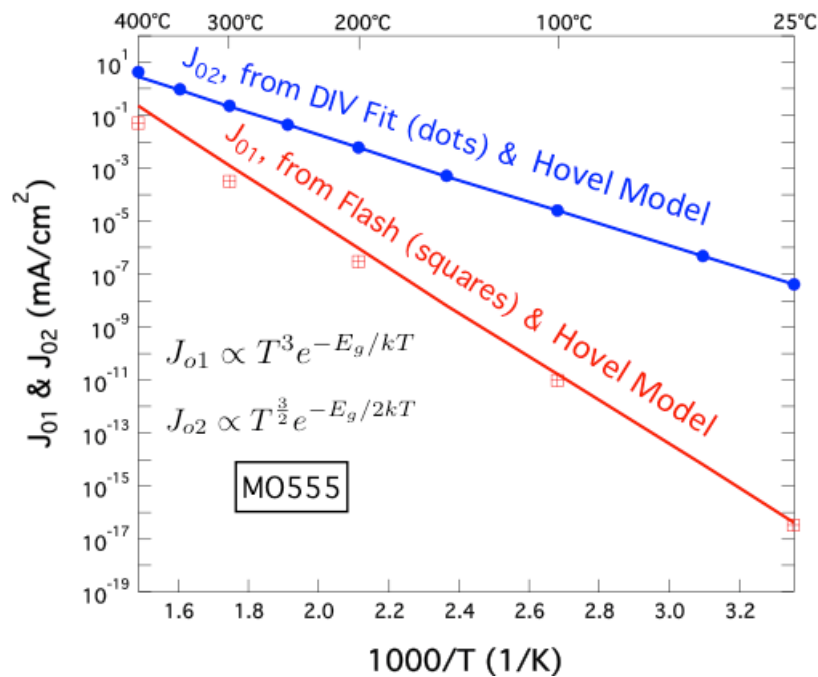
Figure 5.14: Comparison between the J_{01} dark currents extracted from the temperature dependent flash measurements, the J_{02} dark currents extracted from DIV measurements, and the n_i dependence of the dark currents calculated using Equation 5.2 and Equation 5.3 for the GaAs cell [111].

It is clear from this plot that the intrinsic carrier concentration, n_i, dominates the temperature dependence of the dark currents for the GaAs cell, similar to our findings for the AlGaInP cell. The small deviation in the J_{01} curve at high temperatures could arise from

153

the temperature dependence of the other factors in the Hovel equations, and further investigations of these temperature dependences could enable a higher voltage design at elevated temperatures [111].

5.4 Improvements to High-Temperature Performance

In this section, we discuss improvements that have been made to the top subcell to improve the high-temperature performance of the dual-junction device. This work includes the development of a photolithographic process that enables the deposition of 5μm of metal onto the front surface of the solar cell and the design of an improved GaInP top cell that helps to improve current matching, reduce the bandgap-voltage offset, and decrease the emitter sheet resistance.

Process Development to Reduce Series Resistance

In order to achieve a high cell efficiency at 400°C and 1000x concentration, it is critical that the solar cell has a very low series resistance (R_S) in order to minimize Fill Factor losses. The concentrator measurements of the AlGaInP solar cell, shown earlier in Figure 5.6, indicate that this cell is largely limited by a low fill factor, revealing that R_S is significantly impacting the cell efficiency.
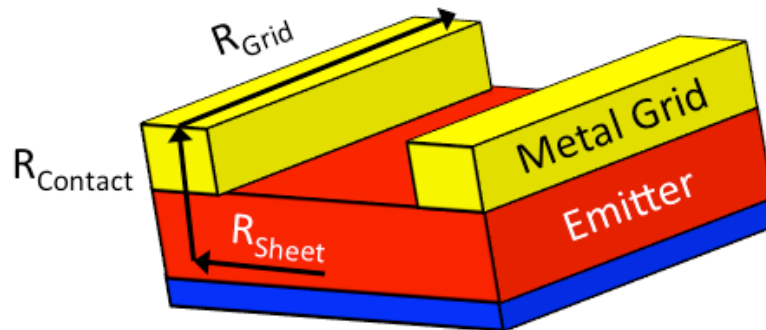
Figure 5.15: Diagram showing the three components that dominate the series resistance of the top cell: the sheet resistance (R_{Sheet}), contact resistance ($R_{Contact}$), and the grid resistance (R_{Grid}).

The R_S of the top cell is typically dominated by three components: a sheet resistance (R_{Sheet}), a contact resistance ($R_{Contact}$), and grid resistance (R_{Grid}) [153]. Figure 5.15 shows a diagram of the top of a solar cell showing where an electron will encounter each of these three resistances. Since R_S appears to be limiting the efficiency of the AlGaInP cell at 400°C and 1000x, it is important to understand the temperature dependence of these three series resistance components.

To this end, we took transmission line measurements (TLMs) of an AlGaInP solar cell with the Linkam stage to determine the temperature dependence of R_{Sheet} and $R_{Contact}$. To determine the temperature dependence of R_{Grid}, we measured the resistance from one busbar to the other (so that current would flow through the solar cell grids) at a number of temperatures. Due to the tremendous difficulty of probing the very small TLM pads using the Linkam probes, we decided to take measurements using the standard probes from the TLM setup and removed the top of the Linkam stage to accommodate these probes. For this reason, we limited the measurements to temperatures of 50°C to 300°C. Figure 5.16 shows the measured temperature dependence of R_{Sheet}, R_{Grid}, and $R_{Contact}$.
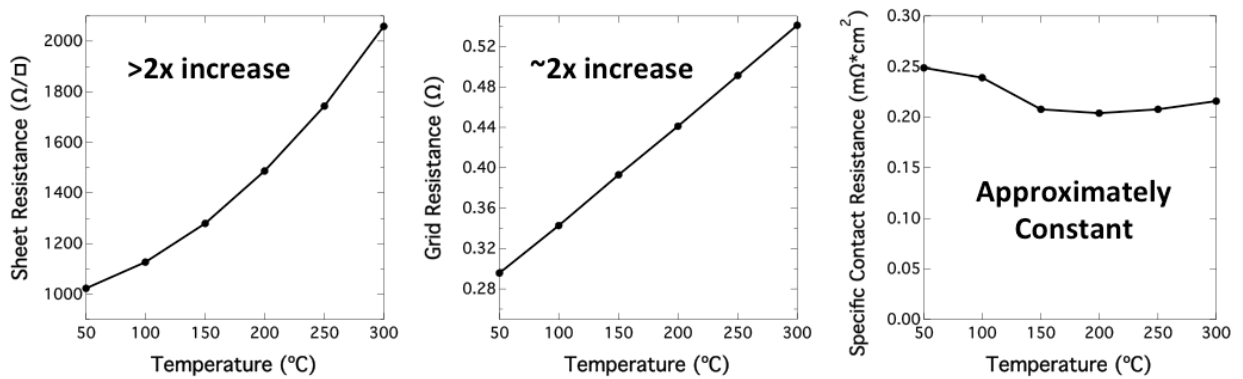
Figure 5.16: Temperature dependence of the (left) the sheet resistance, (middle) the grid resistance, and (right) the contact resistance of an AlGaInP solar cell with gold front contacts. We observe a significant increase (>2x) in the sheet resistance and grid resistance, but little change in the contact resistance as the temperature is increased to 400°C.

The key observation from these plots is that both R_{Sheet} and R_{Grid} increase drastically at high temperatures, increasing by more than a factor of 2 as the temperature is raised from 25°C to 400°C. On the other hand, $R_{Contact}$ remains approximately constant as the temperature is varied. However, the large increase in both R_{Grid} and R_{Sheet} show the importance of working to minimize these resistances.

To reduce R_{Grid}, we have developed a metal liftoff process that utilizes nLof2070 to enable the deposition of very tall metal grids with thicknesses of 5μm or greater. This process involved spin coating the nLof2070 at 2500 RPM, soft baking the sample at 110°C for 1 minute, exposing the grid pattern for 3 seconds, post-exposure baking the sample at 110°C for 1 minute, and developing the sample in AZ300MIF for 90 seconds [35]. Figure 5.17 shows a cross-sectional SEM of the nLof2070 photoresist profile with ~1μm of metal.
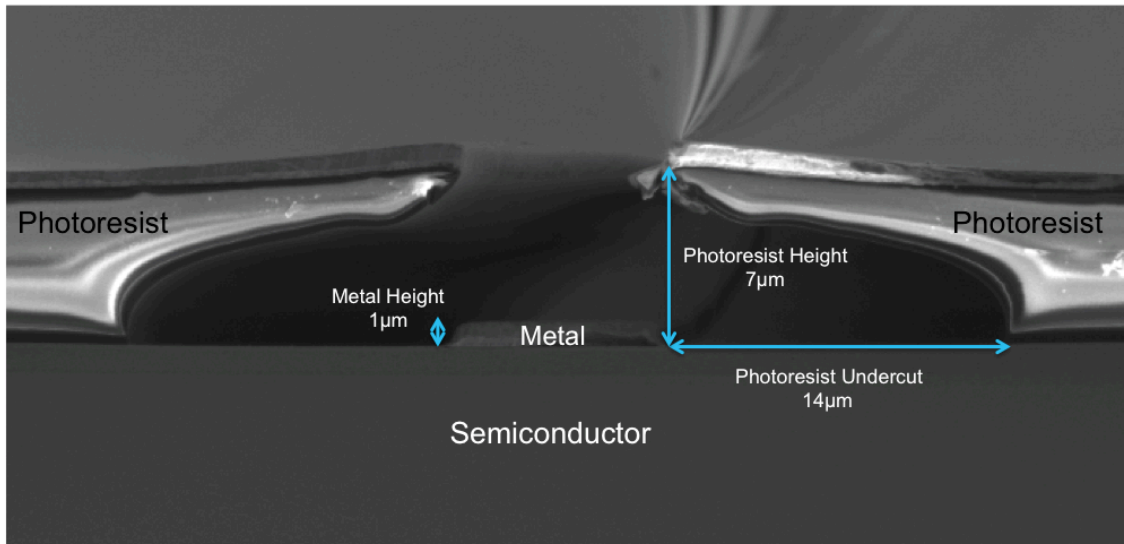
Figure 5.17: Cross-sectional SEM showing the photoresist profile for nLof2070 for the contact metallization. This shows that it is possible to attain metal heights of 5 microns (which we have successfully deposited) or taller.

This image shows the significant undercut, ~14μm, in the photoresist pattern that facilitates metal liftoff. We measure a photoresist height of ~7μm, suggesting that metal

156

grids 5μm or taller can be deposited and lifted off cleanly. We have been able to deposit ~5μm grids with no trouble using this process, and the added metal helps to significantly reduce R_{Grid} of the top cell.

Transition to a Lower Bandgap Top Cell

We have also explored a switch to lower bandgap top cells for three reasons. First, we observe from Figure 5.4 and Figure 5.9 that the 2.0eV AlGaInP cell has a much lower one-sun J_{SC}, ~10mA/cm^2, at 400°C than the filtered GaAs cell, which has a one-sun J_{SC} of ~14mA/cm^2 at 400°C. Moving to a lower bandgap top cell would help improve current matching. Second, reducing the aluminum composition of the top cell would help to reduce the W_{OC}, as is shown in Figure 4.19 [120]. Third, the mobility of 1.9eV GaInP is about 60% higher than the mobility of 2.0eV AlGaInP. For this reason, transitioning to a lower bandgap top cell will make it easier to attain a low R_{Sheet}, which is inversely proportional to the mobility.
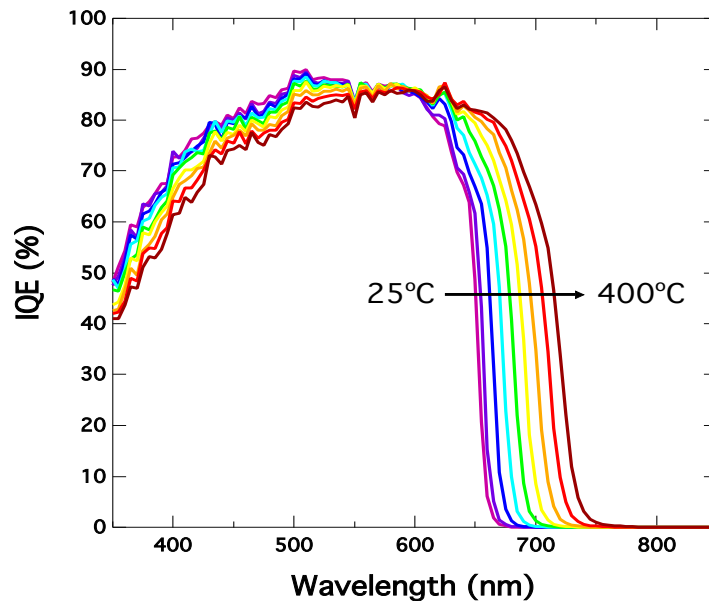
Figure 5.18: Temperature dependent IQE of the improved GaInP top cell showing no significant degradation to the peak IQE and a reduction in the bandgap of the AlInP window and the GaInP active layers as the temperature is increased.

157

We have fabricated ~1.9eV GaInP solar cells with 5μm-tall grids composed of Ti/Pt/Al/Ti (50/50/5000/50nm) to compare to ~2.0eV AlGaInP top cells. Figure 5.18 shows the temperature dependent IQE of this improved GaInP solar cell.

These curves look very similar to the IQE plots of the AlGaInP solar cell shown in Figure 5.3, and again we observe no significant degradation to the IQE and a reduction in the bandgap of the AlInP window and GaInP active layers as the temperature is increased. These two factors will drive an increase in the current density at high-temperatures. Figure 5.19 shows temperature dependent LIV measurements of the GaInP solar cell taken at 1000 W/m^2 (one-sun) under the AM1.5D spectrum.
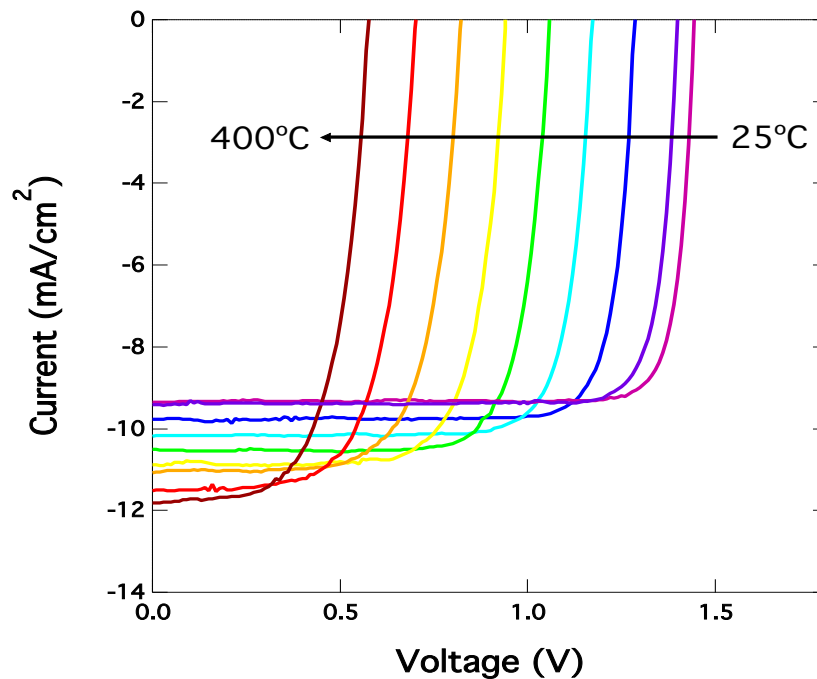
Figure 5.19: Temperature dependent LIV measurements of the improved GaInP top cell taken at a light intensity of one-sun under the AM1.5D spectrum. As the temperature is increased, we observe an increase in the J_{SC} and decrease in the V_{OC}.

The GaInP cell obtains a one-sun J_{SC} of ~12mA/cm^2 at 400°C (~2mA/cm^2 higher than the AlGaInP cell), and if we assume that it will remove ~2mA/cm^2 from the filtered GaAs

cell then both subcells will be very nearly current-matched. We also observe a considerable decrease in the V_{OC} as the temperature is increased, resulting from the exponentially increasing J_{01} and J_{02} dark currents.

Temperature dependent DIV measurements of the improved GaInP top cell are shown in Figure 5.20. The dashed lines on this plot indicate the slopes of ideal diodes with ideality factors of 1 and 2, at temperatures of 25°C and 400°C. Similar to what we observed for the AlGaInP cell, there are clear n=1 and n=2 regions at every temperature measured. This allows us to extract the temperature-dependent J_{01} and J_{02} dark currents from 25°C to 400°C.
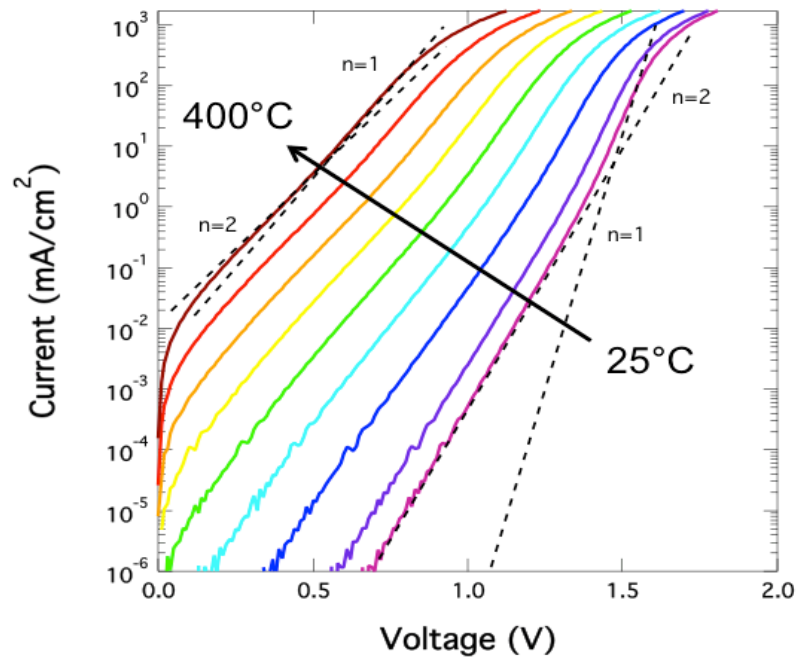
Figure 5.20: Temperature dependent DIV measurements of the improved GaInP top cell showing an increase in the J_{01} and J_{02} dark currents as the temperature is increased. The dashed lines indicate the slopes of ideal diodes with ideality factors of 1 and 2, at temperatures of 25°C and 400°C.

Figure 5.21 shows a comparison between the dark currents extracted from the DIV measurements of the GaInP solar cell shown in Figure 5.20 and the n_i-dominated temperature dependence of the dark currents calculated using Equation 5.2 and Equation 5.3

159

[39,111]. Again, we see excellent agreement between the extracted J_{01} & J_{02} dark currents and the dark currents calculated from the Hovel model. This again confirms that n_i is the dominant term impacting the temperature dependence of the dark currents.
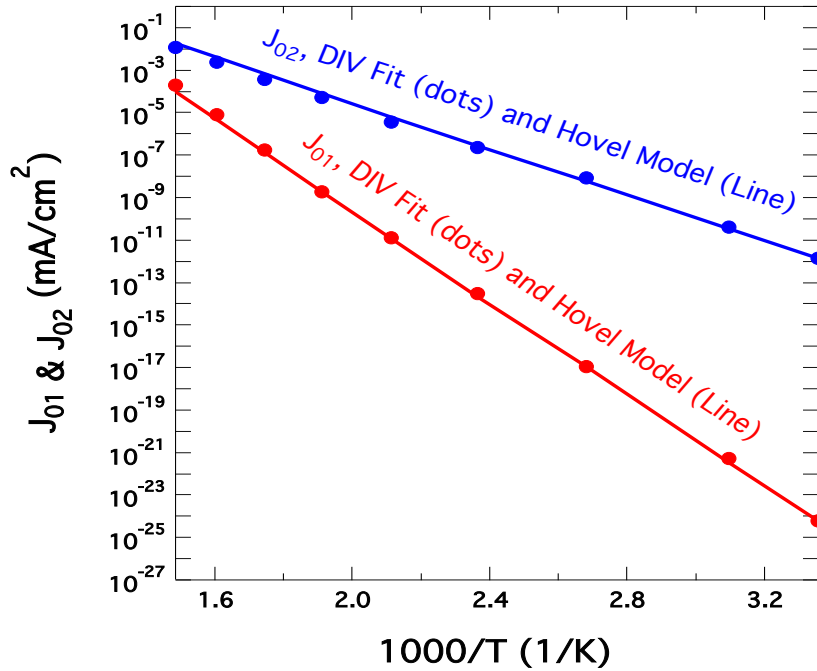
Figure 5.21 Comparison between the dark currents extracted from temperature dependent DIV measurements of the improved GaInP top cell and the n_i-dominated temperature dependence of the dark currents calculated using Equations 5.2 & 5.3.

Flash measurements of the improved GaInP top cell, taken using the HIPSS, are shown in Figure 5.22. This cell had a significantly lower R_s than the AlGaInP cell, as is evident from the high fill factor of the cell at all concentrations. For the flash measurements taken at 400°C, the fill factor only drops from ~70% at 40 suns to ~65% at 1000 suns. The reason for the improved fill factor is twofold. First, the 5μm-tall grids help to significantly reduce R_{Grid}. Second, the transition to a cell with a highly doped GaInP emitter helps to significantly reduce R_{Sheet}, which is inversely proportional to both the doping and the mobility of the emitter.
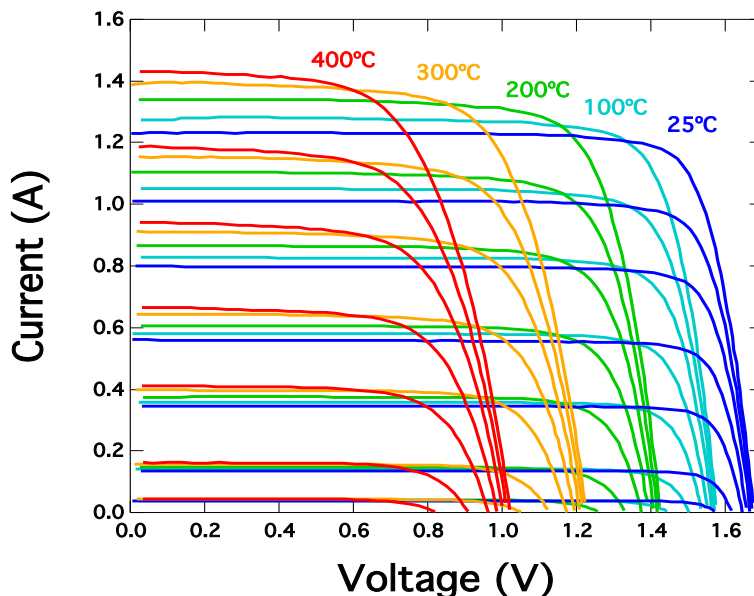
Figure 5.22: Flash measurements of the improved GaInP top cell taken using the HIPSS at seven different apertures. The light intensities range from less than 40 suns at the smallest aperture to over 1000 suns at the largest aperture. Concentration levels for each curve are shown in the next figure.

In addition to having a significantly improved fill factor, we found that this GaInP cell also had a notably higher V_{OC} (~1.01V) than the AlGaInP cell (~0.95V) at 400°C and 1000x. Upon investigation, we determined that the emitter doping concentration had a dramatic impact on cell voltage at 400°C. Figure 5.23 shows a plot of the V_{OC} as a function of both temperature and concentration for three GaInP cells where the emitter doping concentration is varied. The solid lines on this plot correspond to the cell shown in Figures 5.18-5.22.

This plot shows that the emitter doping concentration can drastically impact the V_{OC} at 400°C, with higher emitter doping leading to a higher V_{OC} at elevated temperatures. Additionally, increasing the emitter doping can help to improve the fill factor of the device by reducing R_{Sheet}. Interestingly, we did not observe a significant change in the room temperature V_{OC} for these three samples. Equation 4.3 suggests that this phenomenon could possibly be understood by exploring the temperature-dependence of the ratio of $D_p/(L_p*N_d)$, and this investigation is of great interest to this project [39,40,95].

161
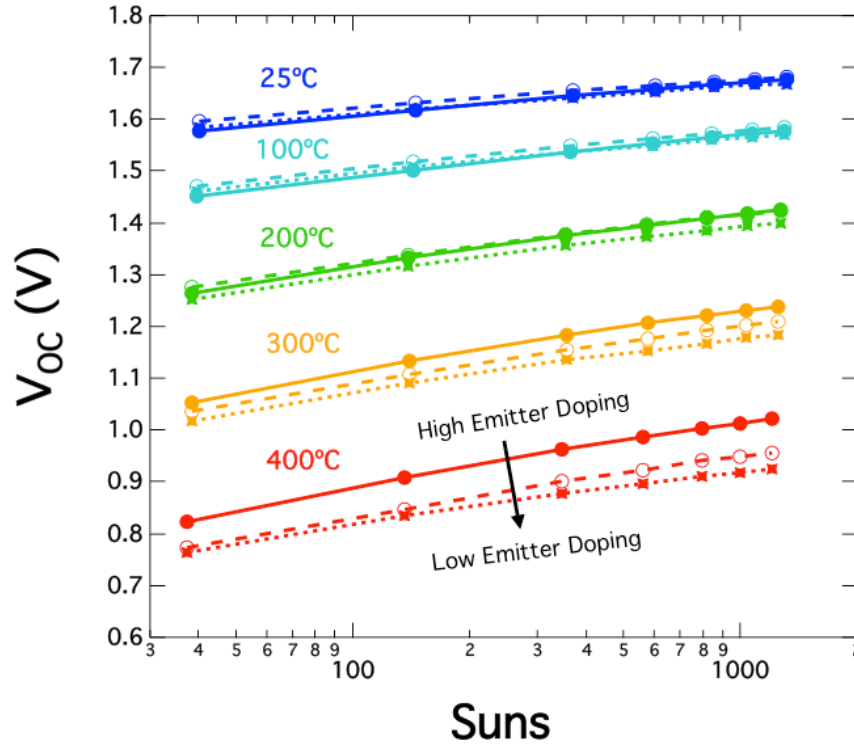
Figure 5.23: V_{OC} as a function of both temperature and concentration for three GaInP top cells. This plot shows the results for three devices where the emitter doping was varied. While there was very little difference between the measured V_{OC} for these three cells at room temperature, we observed a significant improvement to the high-temperature V_{OC} for the GaInP cell with high emitter doping.

We attained an efficiency of ~8% for the best GaInP cell at 400°C, with the peak efficiency occurring at a concentration of about 300 suns. It is important to note that this sample did not have an ARC, and we expect a real-world efficiency of ~18% at 400°C after combining the two subcells into a dual-junction device and depositing an ARC onto the front surface of the sample. Further improvements to the series resistance and top cell voltage should push this efficiency to well over 20%, and while 25% is a very ambitious goal, we think there is a realistic pathway to achieving this objective.

5.5 Chapter Summary

In this chapter, we characterized the temperature-dependent behavior of real-world solar cells. The chapter started by discussing our procedures for measuring the performance of

solar cells at temperatures up to 400°C using a temperature-controlled stage built by Linkam Scientific Instruments. This stage is portable and can be integrated into our existing quantum efficiency, current-voltage, and concentrator testing setups. We then discuss our temperature-dependent quantum efficiency, current-voltage, and concentrator results for AlGaInP and GaAs solar cells. As the operating temperature is increased, we observe a small increase in the J_{SC} of both cells resulting from a bandgap reduction in the semiconductor that can be predicted by the Varshni equations. We also observe a notable decrease to the open-circuit voltage at elevated temperatures that leads to a significant drop in cell efficiency. This V_{OC} drop can be attributed to an exponential increase in the J_{01} & J_{02} dark currents. By fitting DIV and concentrator measurements to a two-diode model, we are able to extract the temperature-dependent J_{01} & J_{02} dark currents. When we compare the extracted dark currents to the Hovel equations, we find that there is excellent agreement between our measurements and the model. This confirms that the intrinsic carrier concentration, n_i, is the dominant term that impacts the temperature dependence of the dark currents, open-circuit voltage, and cell efficiency as the temperature is varied. Finally, we discuss improvements that have been made to the top cell to improve the efficiency at high-temperatures. To minimize grid resistance, we developed a photolithographic process that enables us to deposit 5μm of metal onto the front surface of the solar cell. We also reduced the bandgap of the top cell in order to improve current matching, reduce the bandgap-voltage offset, and decrease the emitter sheet resistance. In addition to significantly improving the fill factor at high-temperatures and concentrations, we found that increasing the emitter doping also led to a significant increase in the high-temperature V_{OC} of the top cell. Interestingly, we did not observe any significant change in the room temperature V_{OC},

suggesting that the improved performance is related to the non-n_i terms in the Hovel equations. By combining the GaInP and GaAs subcells into a dual-junction device and depositing an ARC onto the front surface of the sample, we expect to achieve a real-world efficiency of ~18% at 400°C. Further improvements to the series resistance and top cell voltage should push this efficiency to well over 20%, and while 25% is a very ambitious goal, we think there is a realistic pathway to achieving this objective.

Chapter 6: Conclusions and Future Work

6.1 Conclusions

In this dissertation, we explored material science to advance the state of III-V multijunction solar cells for concentrator photovoltaic (CPV) and hybrid photovoltaic-thermal (PV-T) systems. We present on topics ranging from the design of high-performance optical coatings for record InGaN/GaN solar cells to the growth of AlGaInP solar cells with the lowest reported bandgap-voltage offset to the development of solar cells with the highest reported efficiencies at temperatures of 400°C. The common purpose of work is to improve the efficiency of systems that utilize high-efficiency multijunction solar cells.

In Chapter 2, we discussed the design of broadband optical coatings for multijunction solar cells. Optical design is essential to the development of high-efficiency solar cells. Without antireflection coatings, a photovoltaic device would lose more than a quarter of its efficiency from reflection losses. High-reflectivity mirrors have enabled world-record efficiencies for single-junction GaAs solar cells developed by Alta devices [56]. We provide an overview of thin-film optical coating design, first discussing the physics of ideal single-layer ARCs and multilayer DBRs. When designing broadband optical coatings for solar cells, we are constrained to using real-world materials. Since the highest performing coatings are often complex and difficult to analyze, it is best to optimize the layer thicknesses by minimizing a merit function that describes the quality of the design. Using these design principles, we develop broadband ARCs and dichroic mirrors (DMs) to enhance the efficiency of an InGaN/GaN photovoltaic device. A 6-layer ARC consisting of alternating layers of Ta_2O_5 and SiO_2 is deposited onto the front surface of the cell, and with the addition of this coating we measure a reduction in the average broadband (365-1771nm)

reflectance from 15.7% to 2.4%. To increase absorption of light in the InGaN/GaN multiple quantum well (MQW) structure, we developed a 14-layer Ta_2O_5/SiO_2 DM that achieved an average reflectance of 89.3% for short-wavelength photons (365-470nm) and 4.0% for long-wavelength photons (470-1771nm). The deposition of the ARC and DM resulted in a 56% relative increase in the peak EQE compared to the uncoated sample. This led to a notable improvement in the J_{SC} and an increase in the cell efficiency from 2.4% without optical coatings to 3.3% for the device with an ARC and DM. This represents the highest reported efficiency for any standalone InGaN solar cell to date.

In Chapter 3, we discussed the design of a hybrid optical coating that combines antireflective (AR) nanostructures with a thin-film ARC. We began by exploring the physics of AR nanostructures, and develop a model to describe the optical properties of these surfaces. While AR nanostructures can achieve near-zero reflectance over a broad range of wavelengths and angles, it is difficult to incorporate these structures into a solar cell without introducing additional loss mechanisms. Placing the nanostructures into a thickened $AlInP_2$ window layer will lead to a significant increase in absorption at short wavelengths. Etching nanostructures into a low-loss dielectric layer can minimize this absorption, but will introduce a large gap in the refractive index between the dielectric layer and the semiconductor, leading to a significant increase in reflection losses. To evaluate the performance of various standalone nanostructure configurations for use in multijunction solar cells, we modeled transmitted, absorbed, and reflected AM1.5D power as the nanostructure height was varied. We found that the highest transmission is possible when the nanostructures are composed of TiO_2, however no standalone nanostructure design was able to outperform an optimized thin-film ARC. We then describe the benefits of combining

AR nanostructures with thin-film optical coatings, and using this hybrid design we are able to increase transmitted power by 2.1% compared to a standalone nanostructure design, and 1.3% compared to an optimal multilayer ARC. For a multijunction solar cell, this should correspond to an increase of ~0.5-1% in absolute cell efficiency. We then describe the fabrication process that we developed for placing the hybrid design onto $AlInP_2$ and $GaInP_2$ epilayers, GaN and alumina substrates, and an upright GaAs single-junction active photovoltaic device. Measurements of the hybrid design for various samples are compared to our optical model, and we find that there is excellent agreement between the two. For hybrid designs placed on $AlInP_2$ and $GaInP_2$ epilayers, we are able to reduce the average broadband reflectance by ~2% absolute compared to an optimized multilayer ARC, and after the hybrid design is placed onto a GaAs photovoltaic device, we measure a 27% increase in the I_{SC}. For low-index materials, the hybrid approach can achieve near-perfect broadband and wide-angle antireflection, minimizing reflection losses to just 0.2% on sapphire and 0.6% on gallium nitride for 300-1800nm light.

In Chapter 4, we explored the development of solar cells for high-temperature applications. There are significant challenges associated with operating a solar cell at elevated temperatures. Raising the operating temperature will increase the J_{01} and J_{02} dark currents exponentially, leading to a significant reduction in the open-circuit voltage and efficiency of a solar cell. High-temperature operation could also accelerate material degradation, reduce long-term reliability, and necessitate the development of a stable metallization and cell encapsulant. These challenges need to be carefully explored and understood before any photovoltaic device can be viably integrated into a system that requires high-temperature operation. We begin the chapter by motivating the development

of high-temperature III-V solar cells for photovoltaic-thermal (PV-T) hybrid solar collectors. One of the biggest advantages of this type of system is that it enables the recovery of in-cell thermal losses, which can be transferred to a thermal collector, stored, and converted into usable energy on demand. We develop a solar cell model to predict the temperature-dependence of the J_{SC}, V_{OC}, fill factor, and cell efficiency for single-junction and dual-junction photovoltaic devices. While efficiencies greater than 20% at a temperature of 400°C appear to be possible with single-junction III-V solar cells, we determined that we would have to use dual-junction solar cells in order to reach our efficiency goal of 25% at 400°C. We found that we could reach an efficiency close to the global maximum using a lattice-matched dual-junction design with room-temperature bandgaps of 1.42eV (GaAs) and 2.0eV (AlGaInP). While many GaAs solar cells have been able to achieve a W_{OC} < 400mV, the best reported AlGaInP solar cell prior to this work had a W_{OC} of 485mV. We describe the growth conditions and cell design for a 2.0eV AlGaInP solar cells that attained the lowest W_{OC} (440mV) of any AlGaInP solar cell reported to date. Finally, we discussed some of the cell development challenges that we faced in this project, including the investigation of dopant diffusion in our devices, the deposition of an Al_2O_3 encapsulant to protect the semiconductor surface, and the development of a stable Ti/Pt/Al/Ti contact metallization. Even after annealing an AlGaInP solar cell at 400°C for 200 hours, we observed no measurable degradation to the EQE, J_{SC}, and V_{OC}. This result is a testament to the quality of these cell components and shows that it should be possible for III-V solar cells to achieve excellent reliability even when operated at temperatures up to 400°C.

In Chapter 5, we characterized the temperature-dependent behavior of AlGaInP and GaAs solar cells. To measure solar cell performance at temperatures ranging from 25°C-

400°C, we use a temperature-controlled stage built by Linkam Scientific Instruments. This stage is mobile and can be integrated into our existing quantum efficiency, current-voltage, and concentrator testing setups. As the cell temperature is increased, we measure a small increase in the J_{SC} resulting from a bandgap reduction of the semiconductor materials. We also observe a notable decrease to the open-circuit voltage at elevated temperatures, causing a significant drop in cell efficiency. It is possible to recover some of the lost voltage by operating the solar cell at high light intensities, and we find that concentration becomes more leveraging to cell performance at high temperatures due to the increasing kT/q arguments in the exponents of the diode equation. Unfortunately, high temperatures also lead to a fundamental increase in the semiconductor sheet resistance and the metal grid resistance, making it more difficult to achieve a high fill factor under concentrated sunlight. For this reason it is critically important to engineer a metal grid to minimize these resistive losses. By fitting DIV and concentrator measurements to a two-diode model, we can extract the temperature-dependent J_{01} & J_{02} dark currents. We find that the exponential increase in the dark currents can be well explained with the Hovel equations. Finally, we discuss improvements that have been made to the top cell to increase the efficiency at 400°C. To reduce grid resistance, we developed a photolithographic process that enables us to deposit 5μm of metal onto the front surface of the solar cell. We also lowered the bandgap of the top cell in order to improve current matching, reduce the bandgap-voltage offset, and decrease the emitter sheet resistance. If we were to combine the GaInP and GaAs subcells into a dual-junction device and deposit an ARC onto the front surface of the sample, we expect to achieve a real-world efficiency of ~18% at 400°C. Further improvements to the series

resistance and top cell voltage should push this efficiency to well over 20%, and while 25% is a very ambitious goal, we think there is a realistic pathway to achieving this objective.

6.2 Future Work

Improved Optical Design for InGaN/GaN MQW solar cells

For the InGaN/GaN solar cells presented in Chapter 2, there are two relatively simple improvements that could be made to the optical coatings that could further improve cell performance. First, we could replace the thin-film ARC with the hybrid AR design detailed in Chapter 3. Using the hybrid approach, we could in principle achieve near-perfect antireflection across a very large wavelength range (300-1800nm). Second, we could improve the quality of the dichroic mirror by increasing the number of layers in the thin-film stack or by using materials with a higher index contrast than Ta_2O_5/SiO_2. While a ~10% increase in the reflectivity of short-wavelength light is feasible, it is important to note that this will only lead to an incremental improvement in the efficiency of the device.

Perhaps the most significant challenge for any MQW solar cell is that these designs are fundamentally not well suited to absorb a significant fraction of incoming light. To ensure good minority carrier transport, all of the quantum wells must be placed inside the depletion region where there is a high electric field. However, the thickness of the depletion region is limited by the unintentional doping (UID) concentration in the solar cell. Furthermore, only a fraction of the depletion region will consist of the lower bandgap QW material, equal to $t_{qw}/(t_{qw}+t_{barrier})$ where t_{qw} is the QW thickness and $t_{barrier}$ is the barrier thickness. These constraints will limit the total thickness of the lower bandgap material to under 100nm in a typical MQW solar cell. In contrast, homojunction III-V solar cells are typically 1-3μm thick

(>10x thicker) to ensure that the device will absorb most of the above-bandgap light that strikes the solar cell.

While placing a good reflector on the backside of the sample can double the optical path length, this is not enough to ensure near-complete absorption. It is possible to increase this factor to a value approaching $4n^2$ (~25x for InGaN) with a well-designed scattering structure [154]. However, for the bonded InGaN/arsenide-phosphide five-junction design proposed in this work, it is also critical that longer wavelength light is transmitted to the lower subcells.

Our antireflective nanostructures offer one potentially intriguing solution. As was seen in Figure 3.21 (shown again here in Figure 6.1), the nanostructures diffract short-wavelength light ($\lambda<450$nm) while efficiently transmitting longer-wavelength light ($\lambda>450$nm).
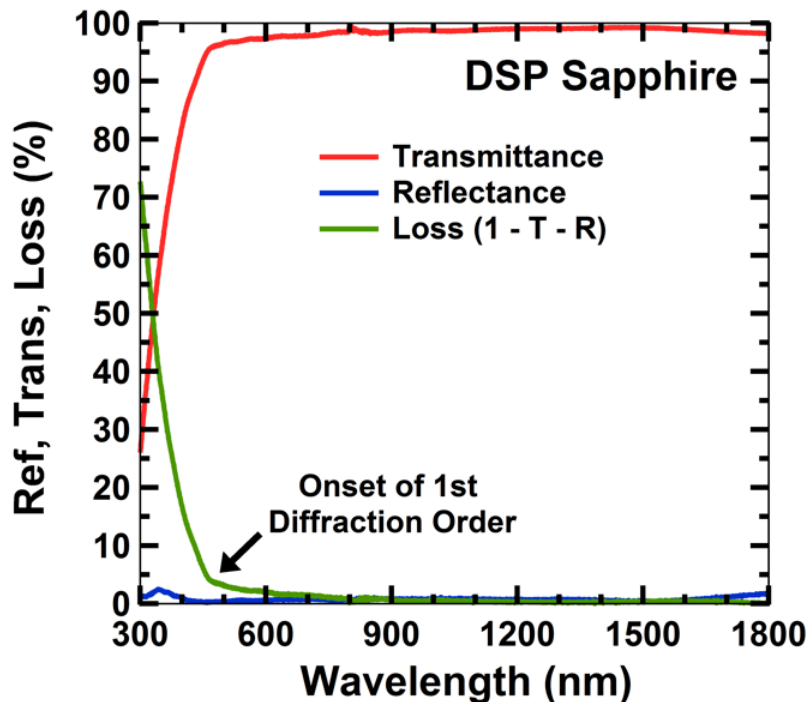
Figure 6.1: Plot showing reflectance, transmittance, and optical loss $(1 - T - R)$ for a hybrid AR design placed on both sides of a DSP sapphire sample. Optical losses can be attributed to absorption, scattering, & diffraction.

One interesting research direction for the hybrid InGaN/arsenide-phosphide five-junction solar cell involves the investigation of a surface texture that can selectively diffract high-energy light into the MQW solar cell to enhance the optical path length to a value approaching $4n^2$. If an ideal design were possible ($4n^2$ enhancement), then a MQW solar cell with <100nm of InGaN material could absorb nearly all of the above-bandgap light in the solar spectrum. It is also critical that this design selectively transmit long-wavelength light to the underlying quadruple-junction photovoltaic device with minimal optical losses. Figure 6.2 shows a diagram of an idealized optical design that could greatly improve absorption in an InGaN/GaN MQW solar cell while ensuring that long-wavelength light is transmitted to the underlying junctions.
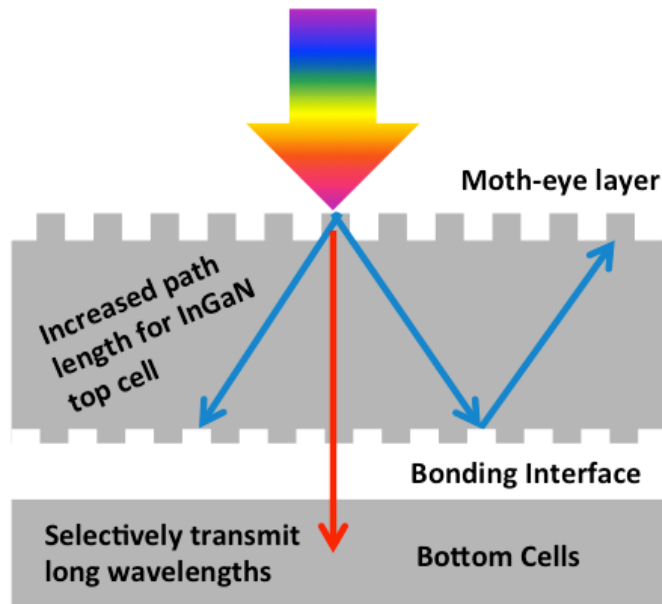
Figure 6.2: Diagram of one potential optical design that could greatly improve absorption in a MQW solar cell. The surface structure would need to selectively diffract high-energy light to increase the optical path length in the MQW cell while selectively transmitting low-energy light to the underlying junctions.

Designing a structure that meets these requirements would be quite complicated and the ideal design is almost certainly not possible. The physics is simplified for antireflective

nanostructures, where the lateral spacing of the nanostructures is smaller than the wavelength of light and only zeroth order diffraction is possible. Large surface structures can also be easily described using a ray optics model. However, it would be interesting to study the optical properties of various nanostructure designs when the lateral feature size is similar to the wavelength of light, or when $d_{lat} \approx \lambda_0/n$.

Study the Impact of Lateral Spacing on the Optical Properties of AR Nanostructures

When the AR nanostructures that we developed in this dissertation are placed into a layer of SiO_2, they diffract normally incident light with wavelengths shorter than 450nm, as is evident in Figure 6.1. We would like to suppress the onset of this diffraction for all wavelengths longer than 300nm in order to maximize transmission of light into a solar cell. As we discussed in Chapter 3, normally incident light will begin to diffract when $d_{lat} > \lambda_0/n$. This suggests that the pathway to increasing transmittance for high-energy light is to decrease the lateral spacing between features in our nanostructure design.

For this reason, it is important to first investigate the impact of lateral spacing on the optical properties of AR nanostructures before placing a hybrid AR design onto a multijunction solar cell. One relatively simple study could compare the transmittance of SiO_2 nanostructures with a lateral spacing ranging from 100-400nm. We would expect the onset of the 1st diffraction order, shown in Figure 6.1, to shift to shorter wavelengths as the lateral spacing is decreased.

It would also be interesting to study the diffractive properties of various nanostructure designs when the lateral feature size is similar to the wavelength of light, or when $d_{lat} \approx \lambda_0/n$. The shape, geometry, and height of the nanostructures will likely influence the diffraction efficiency, and these effects need to be investigated. For the design shown in Figure 6.2, we

173

would like the nanostructures to selectively diffract as much high-energy light as possible. At the same time, we need to make sure that diffraction is suppressed for longer-wavelength light. To accomplish this, we would like to better understand how to design the nanostructures to best meet these requirements. It would also be interesting to investigate whether a thin-film optical coating could help improve the performance of such a design.

Developing a process to fabricate increasingly small nanostructures will also be a challenge. Interference lithography represents one potential technique for varying the lateral spacing of AR nanostructures. However, achieving very small feature sizes on the order of 100nm will be challenging. Electron-beam lithography could be the best way to develop nanostructures with increasingly small feature sizes. While electron-beam lithography is expensive and is not commercially viable, it is important to remember that once an optimal design is developed, we can replicate the pattern using lower-cost nanoimprint lithography.

AlGaInP Solar Cell Development for Five-Junction Photovoltaic Devices

In Chapter 4, we discussed the design of high-bandgap AlGaInP solar cells with the lowest W_{OC} of any AlGaInP solar cell reported to date. While these cells were developed for use as the top junction in a high-temperature dual-junction photovoltaic device, AlGaInP is also an excellent candidate material for use as the top junction for five-junction photovoltaic devices. The work presented in this thesis is therefore highly pertinent to the design of an AlGaInP solar cell for a five-junction photovoltaic device. There are, however, a few important differences between the two designs that need to be investigated in more detail.

First, we grew the AlGaInP solar cells from Chapter 4 in an upright configuration, where the p-type BSF and base layers are grown prior to the n-type emitter and window layers. In contrast, both bonded and inverted metamorphic (IMM) five-junction designs require that

the top cells be grown in an inverted configuration, where the BSF, base, emitter, and window layers are grown in the reverse order. One of the biggest differences observed in prior work is related to a change in the dopant diffusion behavior for both zinc (p-type) and selenium (n-type) for the two configurations. Selenium is known to have a memory effect where the selenium dopant will remain in the MOCVD, and this will lead to a non-zero concentration of selenium in the p-type base for the inverted configuration but not the upright configuration. Additionally, it has been observed that growing n-type layers on top of zinc-doped p-type layers (upright growth) can cause an increase in zinc diffusion in a solar cell structure. These differences need to be studied in order to understand performance differences between upright and inverted AlGaInP solar cells.

Second, while we primarily studied 2.0eV AlGaInP solar cells in this dissertation, the ideal bandgap for a five-junction photovoltaic device is closer to 2.1eV. Figure 4.19 (shown again here in Figure 6.3) showed the IQE & LIV characteristics that we measured for upright AlGaInP solar cells with bandgaps ranging from ~1.9-2.2eV.
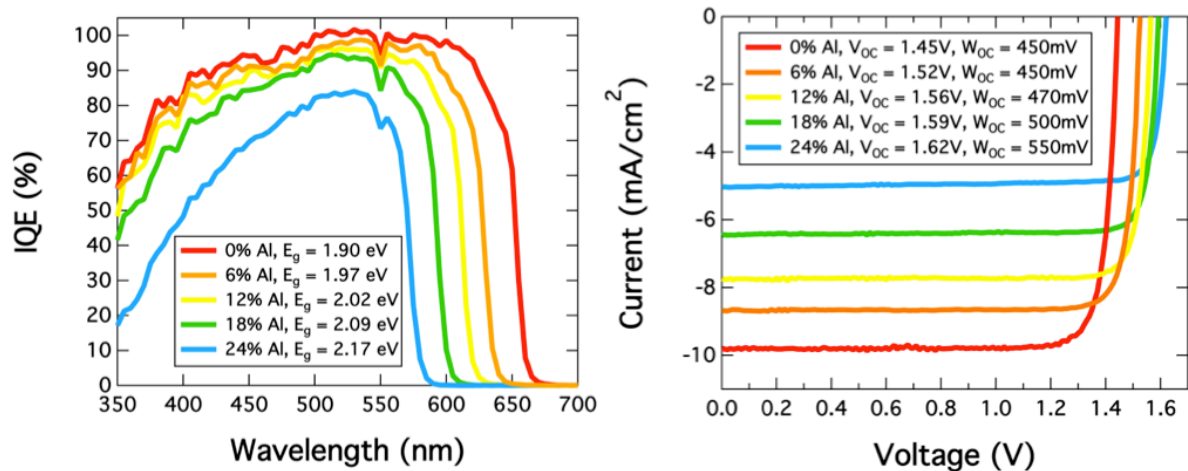
Figure 6.3: (Left) IQE and (right) LIV characteristics of AlGaInP solar cells grown with nominal aluminum compositions ranging from 0% to 24%.

When comparing upright 2.0eV and 2.1eV solar cells with the same growth conditions, we observe a notable decrease to the IQE and a ~30mV increase in the W_{OC} for the higher bandgap device. We also measured a significant decrease in the electron mobility for the higher bandgap device, indicating that attaining a low sheet resistance will be more difficult for a 2.1eV cell than it is for a 2.0eV cells. We only grew a single upright AlGaInP solar cell with a 2.1eV bandgap, so further investigation on the effect of aluminum composition on bandgap and cell performance is necessary.

Third, all of the AlGaInP solar cells detailed in this dissertation were grown on 6°A GaAs substrates to disorder the material and reduce oxygen incorporation. By growing more disordered AlGaInP, it is possible to achieve our target bandgap with a lower aluminum composition than if we were to grow more ordered AlGaInP, helping to minimize oxygen contamination in the AlGaInP layers. On the other hand, the most efficient IMM quadruple-junction devices have been grown on 2°B substrates, which help to facilitate order-mediated dislocation glide and can significantly improve performance of the bottom ~0.7eV junction. 2°B substrates also incorporate selenium more efficiently than 6°A substrates, which could lead to higher doping and a lower sheet resistance for the emitter of the AlGaInP solar cell. These design tradeoffs need to be carefully examined to determine whether 2°B or 6°A substrates will lead to higher efficiencies for a five-junction photovoltaic device.

Efficiency Improvements for High-Temperature Solar Cells

In Chapter 5, we discussed measurements and modeling of single-junction GaInP and GaAs solar cells at high temperatures up to 400°C. By combining these two subcells into a dual-junction device and depositing an ARC onto the front surface of the sample, we expect an efficiency of ~18% at 400°C. While this is significantly higher than what any solar cell

176

has been able to achieve at 400°C, it is still lower than our 25% efficiency goal. Figure 5.11 and Figure 5.22 showed concentrator measurements for GaInP and GaAs solar cell at temperatures ranging from 25-400°C, and using these curves we can figure out what is limiting our cell efficiency. Looking first at the GaAs solar cell results at 400°C, we measure an excellent IQE and a 1000x V_{OC} that is slightly higher than what we expect from the Hovel equations, suggesting that the GaAs cell is actually outperforming our model. While the 400°C performance (V_{OC}, J_{SC}, and FF) of the GaInP solar cell improved significantly compared to the AlGaInP cell, we still measure a V_{OC} at 1000x that is ~80mV lower than what we calculate using the Hovel equations. We also observe that the FF begins to degrade as the concentration increases above ~100x. These represent two of the biggest opportunities to improve the cell efficiency at 400°C. Figure 6.4 shows some of the cell improvements that are required to increase the 400°C cell efficiency from ~18% today to our goal of 25%.
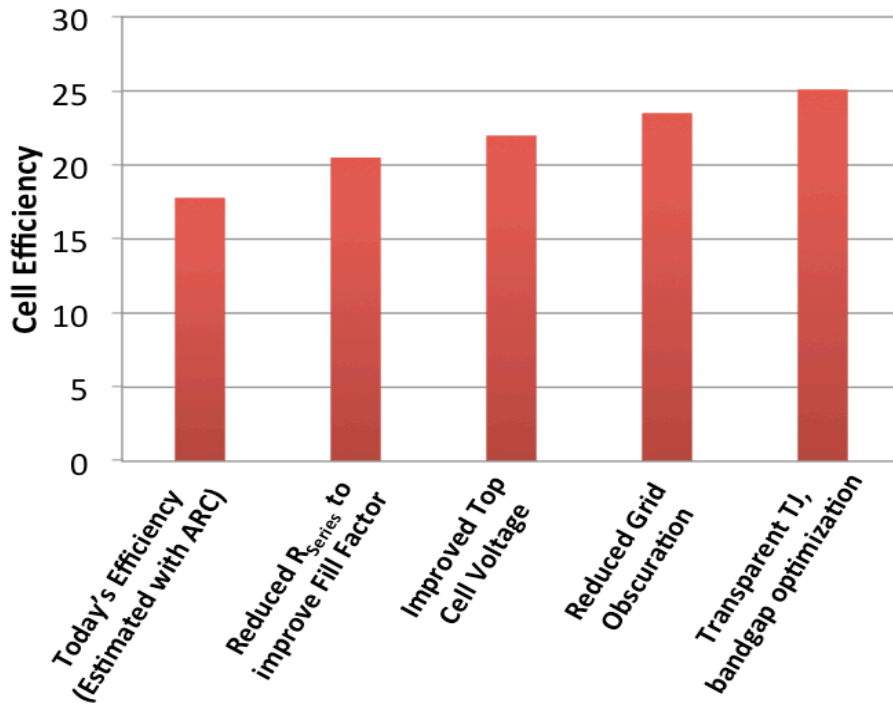
Figure 6.4: Bar chart showing some of the cell improvements that are required to increase the 400°C cell efficiency from ~18% today to our goal of 25%.

We have recently seen hints that the high-temperature (400°C) performance of the top junction can be significantly improved by increasing the emitter doping. Figure 5.23 (shown again here in Figure 6.5) showed that a ~100mV increase in the V_{OC} at 400°C is possible by increasing the emitter doping in the top GaInP top cell from to ~1x10^{17} to ~3x10^{18} cm^{-3}.
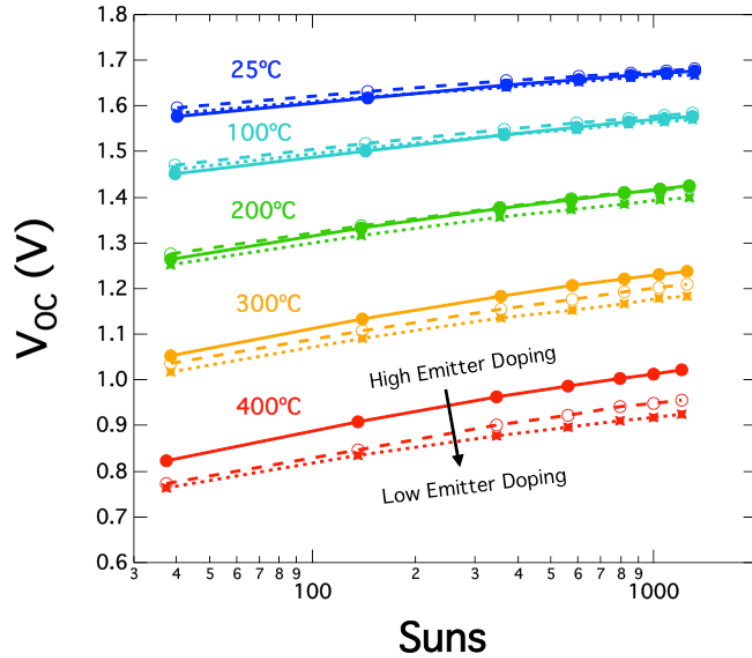
Figure 6.5: V_{OC} as a function of both temperature and concentration for three GaInP top cells. This plot shows the results for three devices where the emitter doping was varied. While there was very little difference between the measured V_{OC} for these three cells at room temperature, we observed a significant improvement to the high-temperature V_{OC} for the GaInP cell with high emitter doping.

Interestingly, we did not observe any significant change in the room temperature V_{OC} for these three cells, suggesting that the improved performance cannot be explained by the temperature-dependences that we derived from the Hovel equations (Equation 4.7 & Equation 4.8). One important study would further increase the emitter doping concentration to see if the voltage continues to improve. In addition to improving the V_{OC} at 1000x and 400°C, we would also expect increased emitter doping to help to reduce the series resistance of the cell and improve the *FF*. These improvements should push the cell efficiency to well

over 20% at 400°C. While 25% efficiency at 400°C is a very ambitious goal, we think there

is a realistic pathway to achieving this objective.

References

[1]   IEA "Key World Energy Statistics 2015," OECD/IEA, 2015.

[2]   J. Twidell and T. Weir, *Renewable Energy Resources* Routledge, 2015.

[3]   R. V. G. Menon, *Technology and Society*, (Pearson Education, 2010).

[4]   http://www.eia.gov/electricity/monthly/pdf/epm.pdf, Electric Power Monthly, June 2016.

[5]   http://pv.energytrend.com, PV Market Status, June 2016.

[6]   H. M. Branz, W. Regan, K. Gerst, J. B. Borak, and E. A. Santori, "Hybrid solar converters for maximum exergy and inexpensive dispachable energy", *Energy Environ. Sci.,* vol. 8, no. 11, pp. 3083-3091, 2015.

[7]   C. Philibert "Solar Photovoltaic Energy Technology Roadmap," International Energy Agency, 2014.

[8]   "Roadmap 2015," International Technology Roadmap for Photovoltaics, 2015.

[9]   A. Mills and R. Wiser "Changes in the Economic Value of Variable Generation at High Penetration Levels: A Pilot Case Study of California," LBNL report 5445E, 2012.

[10]   P. Denholm, R. Margolis, and J. Milford "Production cost modeling for high levels of photovoltaics penetration," National Renewable Energy Laboratory, 2008.

[11]   J. Khan and M. H. Arsalan, "Solar power technologies for sustainable electricity - A review", *Renewable and Sustainable Energy Reviews,* vol. 55, pp. 414-425, 2016.

[12]   K. Vignarooban, X. Xu, A. Arvay, K. Hsu, and A. M. Kannan, "Heat transfer fluids for concentrating solar power systems - a review", *Applied Energy,* vol. 146, pp. 383-396, 2015.

[13]   http://www.nrel.gov/ncpv/images/efficiency_chart.jpg, Research Cell Efficiency Records Chart.

[14]   M. A. Green, K. Emery, Y. Hishikawa, W. Warta, and E. D. Dunlop, "Solar cell efficiency tables (version 47)", *Prog. Photovolt.: Res Appl.,* vol. 24, no. 1, pp. 3-11, 2015.

[15]   "Photovoltaics Report," Fraunhofer Institute for Solar Energy Systems with support of PSE AG, 2016.

[16]   D. C. Jordan and S. Kurtz, "Photovoltaic degradation rates-an analytical review", *Prog. Photovolt.: Res Appl.,* vol. 21, no. 1, pp. 12-29, 2013.

[17]   A. Feltrin and A. Freundlich, *IEEE 4th World Conference on Photovoltaic Energy*; Waikoloa, HI, 2006, pp. 2469-2472.

[18]   F. Jia, H. Sun, and L. Koh, "Global solar photovoltaic industry: an overview and national competitiveness of Taiwan", *Journal of Cleaner Production,* vol. 126, no. 10, pp. 550-562, 2016.

[19]   P. Sharps, *33rd IEEE Photovoltaics Specialists Conference*; San Diego, CA, 2008, pp. 1-6.

[20]   S. P. Philipps and A. W. Bett "Current Status of Concentrator Photovoltaic (CPV) Technology," Fraunhofer Institute for Solar Energy Systems, 2016.

[21]   S. Kurtz "Opportunities and Challenges for Development of a Mature Concentrating Photovoltaic Power Industry," National Renewable Energy Laboratory, 2012.

[22]   D. J. Friedman, R. R. King, R. M. Swanson, J. McJannet, and D. Gwinner, "Toward 100 Gigawatts of Concentrator Photovoltaics by 2030", *IEEE J. Photovoltaics,* vol. 3, no. 4, pp. 1460-1463, 2013.

[23]   M. A. Green, M. J. Keevers, I. Thomas, J. B. Lasich, K. Emery, and R. R. King, "40% efficient sunlight to electricity conversion", *Prog. Photovolt.: Res Appl.,* vol. 23, no. 6, pp. 685-691, 2015.

[24]   A. Luque and S. Hegedus, *Handbook of Photovoltaic Science and Engineering* London: Wiley, 2003.

[25]   T. Markvart and L. Castaner, *Practical Handbook of Photovoltaics* Oxford, UK: Elsevier, 2003.

[26]   R. Sondergaard, M. Hosel, D. Angmo, T. T. Larsen-Olsen, and F. Krebs, "Roll-to-roll fabrication of polymer solar cells", *Materials Today,* vol. 15, no. 1-2, pp. 36-49, 2012.

[27]   R. Bormann and J. Nolting, "Stability limits of the perovskite structure in the Y-Ba-Cu-O system", *Appl. Phys. Lett.,* vol. 54, no. 21, pp. 2148-2150, 1989.

[28]   A. Mills and R. Wiser, "Changes in the economic value of photovoltaic generation at high penetration levels: a pilot case study of California", *IEEE J. Photovoltaics,* vol. 3, no. 4, pp. 1394-1402, 2013.

[29]   Y. Vorobiev, J. Gonzalez-Hernandez, P. Vorobiev, and L. Bulat, "Thermal photovoltaic solar hybrid system for efficient solar energy conversion", *Solar Energy,* vol. 80, no. 2, pp. 170-176, 2006.

[30]   T. T. Chow, "A review on photovoltaic/thermal hybrid solar technology", *Applied Energy,* vol. 87, no. 2, pp. 365-379, 2010.

[31]   C. Gueymard, "The sun's total and spectral irradiance for solar energy applications and solar radiation models", *Solar Energy,* vol. 76, no. 4, pp. 423-453, 2004.

[32]   C. Riordan and R. L. Hulstrom, "What is an air mass 1.5 spectrum?", in *21st IEEE Photovoltaic Specialists Conference*, 1990, pp. 1085-1088.

[33]   C. Gueymard, D. Myers, and K. Emery, "Proposed reference irradiance spectra for solar energy system testing", *Solar Energy,* vol. 73, no. 6, pp. 443-467, 2002.

[34]   http://rredc.nrel.gov/solar/spectra/am1.5/, Reference solar spectral irradiance: air mass 1.5.

[35]   http://www.microchemicals.com/products/photoresists/az_nlof_2070.html,

[36]   D. A. Lashof and D. R. Ahuja, "Relative contributions of greenhouse gas emissions to global warming", *Nature,* vol. 344, no. pp. 529-531, 1990.

[37]   M. A. Green, *Third generation photovoltaics* New York: Springer, 2006.

[38]   B. G. Streetman and S. Banerjee, *Solid state electronic devices* New Jersey: Prentice Hall, 2000, vol. 5.

[39]   H. J. Hovel, *Solar Cells*. R. K. Willardson and A. C. Beer, Eds., Semiconductors and Semimetals New York: Academic Press, 1975, vol. 11.

[40]   A. L. Fahrenbruch and R. H. Bube, *Fundamentals of Solar Cells* (Academic Press, New York, New York, 1983) pp. 69-104.

[41] R. Ciocan, Z. Li, D. Han, D. Assalone, F. Yang, T. Bilir, E. Ciocan, and K. Emery, *35th IEEE Photovoltaic Specialists Conference*; Honolulu, HI, 2010, pp. 1675-1677.

[42] T. Esram and P. L. Chapman, "Comparison of photovoltaic array maximum power point tracking techniques", *IEEE Transactions on Energy Conversion,* vol. 22, no. 2, pp. 439, 2007.

[43] W. Shockley and H. J. Queisser, "Detailed balance limit of efficiency of p-n junction solar cells", *J. Appl. Phys.,* vol. 32, no. 3, pp. 510-519, 1961.

[44] L. C. Hirst and N. J. Ekins-Daukes, "Fundamental losses in solar cells", *Progress Photovoltaics: Res. Appl.,* vol. 19, no. 3, pp. 286-293, 2011.

[45] D. J. Friedman, J. M. Olson, and S. R. Kurtz, *High-efficiency III-V multijunction solar cells, Handbook of Photovoltaic Science and Engineering, 2nd Ed.,* A. Luque and S. Hegedus, Ed. (Wiley, Chichester UK, 2011) pp. 314-364.

[46] S. P. Bremner, M. Y. Levy, and C. B. Honsberg, "Analysis of tandem solar cell efficiencies under AM1.5G spectrum using rapid flux calculation method", *Prog. Photovolt.: Res Appl.,* vol. 16, no. 3, pp. 225-233, 2007.

[47] R. R. King, A. Boca, W. Hong, X. Q. Liu, D. Bhusari, D. Larrabee, K. M. Edmondson, D. C. Law, C. M. Fetzer, S. Mesropian, and N. H. Karam, *24th European Photovoltaic Solar Energy Conference and Exhibition*; Hamburg, Germany, 2009.

[48] R. M. France, I. Garcia, W. E. McMahon, A. G. Norman, J. Simon, J. F. Geisz, D. J. Friedman, and M. J. Romero, "Lattice-Mismatched 0.7-eV GaInAs Solar Cells Grown on GaAs Using GaInP Compositionally Graded Buffers", *IEEE J. Photovoltaics,* vol. 4, no. 1, pp. 190-195, 2014.

[49] R. M. France, J. F. Geisz, M. A. Steiner, I. García, W. E. McMahon, and D. J. Friedman, "Quadruple junction inverted metamorphic concentrator devices", *IEEE J. Photovoltaics,* vol. 5, no. 1, pp. 432, 2015.

[50] P. T. Chiu, D. C. Law, R. L. Woo, S. B. Singer, D. Bhusari, W. D. Wong, A. Zakaria, J. Boisvert, S. Mesropian, R. R. King, and N. H. Karam, "Direct seminconductor bonded 5J cell for space and terrestrial applications", *IEEE J. Photovoltaics,* vol. 4, no. 1, pp. 493, 2014.

[51] F. Dimroth, M. Grave, P. Beutel, U. Fiedeler, C. Karcher, T. N. D. Tibbits, E. Oliva, G. Siefer, M. Schaechtner, A. Wekkeli, A. W. Bett, R. Krause, M. Piccin, N. Blanc, C. Drazek, E. Guiot, B. Ghyselen, T. Salvetat, A. Tauzin, T. Signamarcheix, A.

Dobrich, T. Hannappel, and K. Schwarzburg, "Wafer bonded four-junction GaInP/GaAs//GaInAsP/GaInAs concentrator solar cells with 44.7% efficiency", *Progress Photovoltaics, Res. Appl.,* vol. 22, no. 3, pp. 277-282, 2014.

[52]   S. Bhushan, "Silicon Nitride coatings for Si solar cells: control of optical reflection and surface/bulk passivation", in *Dielectrics in Emerging Technologies: Proceedings of the International Symposium*, 2003, pp. 186.

[53]   D. Aiken, "High performance anti-reflection coatings for broadband multi-junction solar cells", *Sol. Energy Mater, Sol. Cells,* vol. 64, no. 4, pp. 393-404, 2000.

[54]   C. G. Bernhard, "Structural and functional adaptation in a visual system", *Endeavor,* vol. 26, no. 98, pp. 79-84, 1967.

[55]   S. J. Wilson and M. C. Hutley, "The optical properties of moth eye antireflection surfaces", *J. Modern Opt.,* vol. 29, no. 7, pp. 993-1009, 1982.

[56]   V. Ganapati Thesis, UC Berkeley, 2015.

[57]   N. G. Young, E. E. Perl, R. M. Farrell, M. Iza, S. Keller, J. E. Bowers, S. Nakamura, S. P. DenBaars, and J. S. Speck, "High-performance broadband optical coatings on InGaN/GaN solar cells for multijunction device integration", *Appl. Phys. Lett.,* vol. 104, pp. 163902, 2014.

[58]   A. Polman and H. A. Atwater, "Photonic design principles for ultrahigh-efficiency photovoltaics", *Nature Materials,* vol. 11, no. pp. 174-177, 2012.

[59]   A. Thelen, *Design of optical interference coatings* McGraw-Hill Companies, 1989.

[60]   J. D. Rancourt, *Optical thin films: user handbook* SPIE Press, 1996.

[61]   H. A. Macleod, *Thin-film optical filters* CNC Press, 2001.

[62]   D. K. Cheng, *Field and wave electromagnetics* Pearson Education, 1989.

[63]   E. E. Perl, W. E. McMahon, J. E. Bowers, and D. J. Friedman, "Design of antireflective nanostructures and optical coatings for next-generation multijunction photovoltaic devices", *Opt Express,* vol. 22, no. S5, pp. A1243-A1256, 2014.

[64]   S. Wang, "Principles of distributed feedback and distributed Bragg-reflector lasers", *IEEE Journal of Quantum Electronics,* vol. 10, no. 4, pp. 413-427, 1974.

[65]   M. N. Polyanskiy, refractiveindex.info.

[66]   W. H. Southwell, "Coating design using very thin high- and low-index layers", *Appl. Opt.,* vol. 24, no. 4, pp. 457-460, 1985.

[67]   S. S. TFCalc Version 3.5.15, Inc., Portland, OR, USA, 2009, pp.

[68]   H. G. Tompkins and W. A. McGahan, *Spectroscopic ellipsometry and reflectometry: a user's guide* Wiley, 1999.

[69]   E. E. Perl, C. T. Lin, W. E. McMahon, D. J. Friedman, and J. E. Bowers, "Ultrabroadband and wide-angle hybrid antireflection coatings with nanostructures", *IEEE J. Photovoltaics,* vol. 4, no. 3, pp. 962-967, 2014.

[70]   W. E. McMahon, C.-T. Lin, J. S. Ward, J. F. Geisz, M. W. Wanlass, J. J. Carapella, W. Olavarria, M. Young, M. A. Steiner, R. M. France, A. E. Kibbler, A. Duda, J. M. Olson, E. E. Perl, D. J. Friedman, and J. E. Bowers, "Metal pillar interconnection topology for bonded two-terminal multijunction III-V solar cells", *IEEE J. Photovoltaics,* vol. 3, no. 2, pp. 868-872, 2013.

[71]   A. Tommila, A. Aho, A. Tukiainen, V. Polojarvi, J. Salmi, T. Niemi, and M. Guina, "Moth-eye antireflection coating fabricated by nanoimprint lithography on 1 eV dilute nitride solar cell", *Prog. Photovolt.: Res Appl.,* vol. 21, pp. 1558-1162, 2013.

[72]   D. Liang, Y. Kang, Y. Huo, Y. Chen, Y. Cui, and J. S. Harris, "High-efficiency nanostructured window GaAs solar cells", *Nano Letters,* vol. 13, no. 10, pp. 4850-4856, 2013.

[73]   A. Tommila, V. Polojarvi, A. Aho, A. Tukiainen, J. Viheriala, J. Salmi, A. Schramm, J. M. Kontio, A. Turtiainen, T. Niemi, and M. Guina, "Nanostructured broadband antireflection coatings on AlInP fabricated by nanoimprint lithography", *Sol. Energy Mater, Sol. Cells,* vol. 94, no. 10, pp. 1845-1848, 2010.

[74]   K.-H. Hung, T.-G. Chen, T.-T. Yang, P. Yu, C.-Y. Hong, Y.-R. Wu, and G.-C. Chi, *38th IEEE Photovoltaics Specialists Conference*; 2012, pp. 003322-003324.

[75]   P. Yu, M.-Y. Chiu, C.-H. Chang, C.-Y. Hong, Y.-L. Tsai, H.-V. Han, and Y.-R. Wu, "Towards high-efficiency multi-junction solar cells with biologically inspired nanosurfaces", *Prog. Photovolt.: Res Appl.,* vol. 22, no. 3, pp. 300-307, 2014.

[76]   E. E. Perl, W. E. McMahon, R. M. Farrell, S. P. DenBaars, J. S. Speck, and J. E. Bowers, "Surface structured optical coatings with near-perfect broadband and wide-angle antireflective properties", *Nano Letters,* vol. 14, no. 10, pp. 5960-5964, 2014.

185

[77] P. I. Stavroulakis, S. A. Boden, T. Hohnson, and D. M. Bagnall, "Suppression of backscattered diffraction from sub-wavelength 'moth-eye' arrays", *Opt Express,* vol. 21, no. 1, pp. 1-11, 2013.

[78] M. C. Hutley, *Diffraction Gratings in Techniques of Physics* London: Academic Press, 1982.

[79] D. G. Stavenga, S. Foletti, G. Palasantzas, and K. Arikawa, "Light on the moth-eye corneal nipple array of butterflies", *Proc. Biol. Sci.,* vol. 273, no. 1587, pp. 661-667, 2006.

[80] Y. M. Song, H. J. Choi, J. S. Yu, and Y. T. Lee, "Design of highly transparent glasses with broadband antireflective subwavelength structures", *Opt Express,* vol. 18, no. 12, pp. 13063-13071, 2010.

[81] G. C. Park, Y. M. Song, E. K. Kang, and Y. T. Lee, "Size-dependent optical behavior of disordered nanostructures on glass substrates", *Appl. Opt.,* vol. 51, no. 24, pp. 5890-5896, 2012.

[82] W. H. Southwell, "Gradient-index antireflection coatings", *Opt. Lett.,* vol. 8, no. 11, pp. 584-586, 1983.

[83] D. S. Hobbs, B. D. MacLeod, and J. R. Riccobono, "Update on the development of high performance anti-reflecting surface relief micro-structures", in *SPIE*, 2007, pp. 65450Y.

[84] D. A. G. Bruggeman, "Calculation of various physics constants in heterogeneous substances: Part I. Dielectric constants and conductivity of mixed bodies from isotropic substances", *Annalen der Physik,* vol. 24, no. 7, pp. 636-664, 1935.

[85] A. Garahan, L. Pilon, J. Yin, and I. Saxena, "Effective optical properties of absorbing nanoporous and nanocomposite thin films", *J. Appl. Phys.,* vol. 101, no. 1, pp. 014320, 2007.

[86] E. E. Perl, W. E. McMahon, J. E. Bowers, and D. J. Friedman, "Material selection and fabrication parameters for antireflective nanostructures integrated with multijunction photovoltaics", in *40th IEEE Photovoltaics Specialist Conference*, 2014, pp. 1174-1179.

[87] P. Herve and L. K. J. Vandamme, "General relation between refractive index and energy gap in semiconductors", *Infrared Pysics & Technology,* vol. 35, no. 4, pp. 609-615, 1994.

186

[88]   D. D. John, J. F. Bauters, J. Nedy, W. Li, R. Moreira, J. S. Barton, J. E. Bowers, and D. J. Blumenthal, *Optical Fiber Communication Conference*; 2011.

[89]   Y. YHirai, S. Yoshida, and N. Takagi, "Defect analysis in thermal nanoimprint lithography", *J Vac Sci Technol B,* vol. 21, no. 6, pp. 2765-2770, 2003.

[90]   S. Y. Chou, P. R. Krauss, and P. J. Renstrom, "Nanoimprint lithography", *J Vac Sci Technol B,* vol. 14, no. 6, pp. 4129-4133, 1996.

[91]   U. Plachetka, M. Bender, A. Fuchs, B. Vratzov, T. Glinsner, F. Lindner, and H. Kurz, "Wafer scale patterning by soft UV-nanoimprint lithography", *Microelectronics Engineering,* vol. 73, pp. 167-171, 2004.

[92]   J. Viheriala, T. Niemi, J. Kontio, and M. Pessa, *Nanoimprint lithography - next generation nanoimprinting methods for nanophotonics fabrication, Recent Optical and Photonic Technologies, Chapter 14,* 2010).

[93]   P. Singh and N. M. Ravindra, "Temperature dependence of solar cell performance-an analysis", *Solar Energy Materials & Solar Cells,* vol. 101, no. pp. 36-45, 2012.

[94]   D. Meneses-Rodriguez, P. P. Horley, J. Gonzalez-Hernandez, Y. Vorobiev, and P. N. Gorley, "Photovoltaic solar cells performance at elevated temperatures", *Solar Cells,* vol. 78, no. 2, pp. 243-250, 2005.

[95]   S. R. Kurtz, J. M. Olson, D. J. Friedman, J. F. Geisz, A. E. Kibbler, and K. A. Bertness, *MRS Spring Meeting*; San Francisco, CA, 1999.

[96]   J. C. C. Fan, "Theoretical temperature dependence of solar cell parameters", *Solar Cells,* vol. 17, no. 2-3, pp. 309-315, 1986.

[97]   O. V. Sulima, P. E. Sims, J. A. Cox, M. G. Mauk, R. L. Mueller, R. C. R. Jr., A. M. Khammadov, P. D. Paulson, and G. A. Landis, "High-temperature AlGaP/GaP solar cells for NASA space missions", in *3rd World Conference on Photovoltaic Energy Conversion*, 2003, pp. 737-740.

[98]   G. A. Landis, D. Merritt, R. Raffaelle, and D. Scheiman, "High-temperature solar cell development", in *Proc. 18th Space Photovoltaic Research and Technology Conference*, 2005, pp. 241-247.

[99]   D. Feldman, G. Barbose, R. Margolis, T. James, S. Weaver, N. Darghouth, R. Fu, C. Davidson, S. Booth, and R. Wiser "Photovoltaic system pricing trends: historical, recent, and near-term projections, 2014 edition," National Renewable Energy Laboratory, 2014.

[100] H2 2014 Global LCOE Outlook, *Bloomberg New Energy Finance*, 2014.

[101] J. Appen, M. Braun, T. Stetz, K. Diwold, and D. Geibel, "Time in the sun: the challenge of high PV penetration in the German electric grid", *IEEE Power and Energy Magazine,* vol. 11, no. 2, pp. 55-64, 2013.

[102] A. Adelfio Thesis, Duke University, 2014.

[103] U. Eberle, B. Muller, and R. von Helmolt, "Fuel cell electric vehicles and hydrogen infrastructure: status 2012", *Energy and Environmental Science,* vol. 5, pp. 8780-8798, 2012.

[104] "Flexibility demands of a variable RE based electricity supply," IRENA International Energy Storage Policy and Regulation Workshop, 2014.

[105] A. A. Akhil, G. Huff, A. B. Currier, B. C. Kaun, D. M. Rastler, S. B. Chen, A. L. Cotter, D. T. Bradshaw, and W. D. Gauntlett Sandia National Laboratories, 2013.

[106] I. Hadjipaschalis, A. Poullikkas, and V. Efthimiou, "Overview of current and future energy energy storage technologies for electric power applications", *Renewable and Sustainable Energy Reviews,* vol. 13, no. 6, pp. 1513-1522, 2009.

[107] Z. Yang, J. Zhang, M. C. Kintner-Meyer, X. Lu, D. Choi, J. P. Lemmon, and J. Liu, "Electrochemical energy storage for green grid", *Chemical reviews,* vol. 111, no. 5, pp. 3577-3613, 2011.

[108] S. Kuravi, J. Trahan, D. Y. Goswami, M. M. Rahman, and E. K. Stefanakos, "Thermal energy storage technologies and systems for concentrating solar power plants", *Progress in Energy and Combustion Science,* vol. 39, no. 4, pp. 285-319, 2013.

[109] A. Mojiri, R. Taylor, E. Thomsen, and G. Rosengarten, "Spectral beam splitting for efficient conversion of solar energy-a review", *Renewable and Sustainable Energy Reviews,* vol. 28, no. pp. 654-663, 2013.

[110] A. Luque and A. Marti, "Limiting efficiency of coupled thermal and photovoltaic converters", *Solar Energy Materials and Solar Cells,* vol. 58, no. 2, pp. 147-165, 1999.

[111] E. E. Perl, J. Simon, J. F. Geisz, M. L. Lee, D. J. Friedman, and M. A. Steiner, "Measurements and modeling of III-V solar cells at high temperatures up to 400°C", *J. Photovoltaics,* DOI: 10.1109/JPHOTOV.2016.2582398, 2016.

[112] E. F. Fernandez, P. Perez-Higueras, A. J. Garcia Loureiro, and P. G. Vidal, "Outdoor evaluation of concentrator photovoltaic systems modules from different manufacturers: first results and steps", *Prog. Photovolt.: Res Appl.,* vol. 21, no. 4, pp. 693-701, 2013.

[113] M. Steiner, G. Siefer, T. Schmidt, M. Wiesenfarth, F. Dimroth, and A. W. Bett, "43% sunlight to electricity conversion efficiency using CPV", *IEEE J. Photovoltaics,* vol. 6, no. 4, pp. 1020-1024, 2016.

[114] Y. P. Varshni, "Temperature dependence of the energy gap in semiconductors", *Physica E: Low-dimensional Systems and Nanostructures,* vol. 34, no. 1, pp. 149-154, 1967.

[115] J. S. Blakemore, "Semiconducting and other major properties of gallium arsenide", *J. Appl. Phys.,* vol. 53, no. 10, pp. R123, 1982.

[116] S. C. Lu, M. C. Wu, C. Y. Lee, and Y. C. Yang, "Temperature dependence of photoluminescence from Mg-doped In0.5Ga0.5P grown by liquid-phase epitaxy", *J. Appl. Phys.,* vol. 70, no. 4, pp. 2309-2312, 1991.

[117] P. Patel, D. Aiken, D. Chumney, A. Cornfeld, Y. Lin, C. Mackos, J. McCarty, N. Miller, P. Sharps, and M. Stan, "Initial results of the monolithically grown six-junction inverted metamorphic multi-junction solar cell", in *Proc 38th IEEE Photovoltaic Spec. Conf.*, 2012, pp. 1-4.

[118] J. F. Geisz, M. A. Steiner, I. Garcia, S. R. Kurtz, and D. J. Friedman, "Enhanced external radiative efficiency for 20.8% efficient single-junction GaInP solar cells", *Appl. Phys. Lett.,* vol. 103, no. 4, pp. 041118, 2013.

[119] E. E. Perl, J. Simon, J. F. Geisz, W. Olavarria, M. Young, A. Duda, P. Dippo, D. J. Friedman, and M. A. Steiner, "Development of a 2.0 eV AlGaInP solar cell grown by OMVPE", in *Proc 42nd IEEE Photovoltaic Spec. Conf.*, 2015, pp. 1-6.

[120] E. E. Perl, J. Simon, J. F. Geisz, W. Olavarria, M. Young, A. Duda, D. J. Friedman, and M. A. Steiner, "Development of high-bandgap AlGaInP solar cells grown by organometallic vapor-phase epitaxy", *IEEE J. Photovoltaics,* vol. 6, no. 3, pp. 770-776, 2016.

[121] G. B. Stringfellow, *Organometallic vapor-phase epitaxy: theory and practice*, (Academic Press, 1999) pp. 92, 427-433.

[122] *Spontaneous ordering in Semiconductor Alloys,* A. Mascarenhas, ed., Ed. (Kluwer Academic/Plenum Publishers, 2002) pp. 8-20.

[123]   *High brightness light emitting diodes, Semiconductors and semimetals,* G. B. Stringfellow and M. G. Craford, Ed. (Academic Press, 1997), vol. 48, pp. 97-148.

[124]   M. Kondo, N. Okada, K. Domen, K. Sugiura, C. Anayama, and T. Tanahashi, "Origin of Nonradiative Recombination Centers in AlGaInP Grown by Metalorganic Vapor Phase Epitaxy", *J. Electron. Mater.,* vol. 23, no. 3, pp. 355-358, 1994.

[125]   M. Kondo, C. Anayama, N. Okada, H. Sekiguchi, K. Domen, and T. Tanahashi, "Crystallographic Orientation Dependence of Impurity Incorporation into III-V Compound Semiconductors Grown by Metalorganic Vapor Phase Epitaxy", *J. Appl. Phys.,* vol. 76, no. 2, pp. 914-927, 1994.

[126]   S. Nojima, H. Tanaka, and H. Asahi, "Deep Electron Trapping Center in Si-doped InGaAlP Grown by Molecular-Beam Epitaxy", *J. Appl. Phys.,* vol. 59, no. 10, pp. 3489-3494, 1986.

[127]   S. Heckelmann, D. Lackner, C. Karcher, F. Dimroth, and A. W. Bett, "Investigations on AlGaAs solar cells grown by MOVPE", *IEEE J. Photovoltaics,* vol. 5, no. 1, pp. 446-453, 2014.

[128]   M. W. Wanlass, S. P. Ahrenkiel, J. J. Carapella, D. J. Friedman, C. R. Osterwald, and M. Romero, "Progress toward an advanced four-subcell inverted metamorphic multi-junction (IMM) solar cell", *Progress Photovoltaics, Res. Appl.,* 2015.

[129]   T. Masuda, S. Tomasulo, J. R. Lang, and M. L. Lee, "Comparison of single junction AlGaInP and GaInP solar cells grown by molecular beam epitaxy", *J. Appl. Phys.,* vol. 117, no. 9, pp. 094504, 2015.

[130]   L. Hongbo, L. Xinyi, Z. Wei, Z. Dayong, S. Mengqui, S. Lijie, and C. Kaijian, "A 2.05 eV AlGaInP sub-cell used in next generation solar cells", *J. Semicond.,* vol. 35, no. 9, pp. 094010, 2014.

[131]   A. B. Cornfeld, P. Patel, J. Spann, D. Aiken, and J. McCarty, "Evolution of a 2.05 eV AlGaInP top sub-cell for 5 and 6J-IMM applications", in *Proc 38th IEEE Photovoltaic Spec. Conf.*, 2012, pp. 002788-002791.

[132]   M. A. Steiner, I. Garcìa, D. J. Friedman, A. Duda, W. J. Olavarria, M. Young, D. Kuciauskas, and S. Kurtz, "Effects of internal luminescence and internal optics on Voc and Jsc of III-V solar cells", *IEEE J. Photovoltaics,* vol. 3, no. 4, 2013.

[133]   J. I. Pankove, *Optical Processes in Semiconductors* Courier Corporation, 2012.

[134] L. C. Su, I. H. Ho, and G. B. Stringfellow, "Effects of Substrate Misorientation and Growth Rate on Ordering in GaInP", *J. Appl. Phys.,* vol. 75, no. 10, pp. 5135-5141, 1994.

[135] A. Le Donne, M. Acciarri, G. Gori, R. Colletto, R. Campesato, and S. Binetti, "Optical and electrical characterization of AlGaInP solar cells", *Solar Energy Materials and Solar Cells,* vol. 94, no. 12, pp. 2002-2006, 2010.

[136] S. A. Stockman, J.-W. Huang, T. D. Ostentowski, H. C. Chui, M. J. Peanasky, S. A. Maranowski, P. N. Grillot, A. J. Moll, C. H. Chen, C. P. Kuo, and B. W. Liang, "Oxygen incorporation in AlInP, and its effect on p-type doping with magnesium", *J. Electron. Mater.,* vol. 28, no. 7, pp. 916-925, 1999.

[137] G. B. Lush, H. F. MacMillan, B. M. Keyes, D. H. Levi, M. R. Melloch, R. K. Ahrenkeil, and M. S. Lundstrom, "A study of minority carrier lifetime versus doping concentration in n-type GaAs grown by metalorganic chemical vapor deposition", *J. Appl. Phys.,* vol. 72, no. 4, pp. 1436-1442, 1992.

[138] M. P. Lumb, M. A. Steiner, J. F. Geisz, and R. J. Walters, "Incorporating photon recycling into the analytical drift-diffusion model of high efficiency solar cells", *J Appl Phys,* vol. 116, no. 19, pp. 194504, 2014.

[139] Y.-G. Zhan and Y. Gu, *Al(Ga)InP-GaAs photodiodes tailored for specific wavelength range, Photodiodes - From Fundamentals to Applications,* I. Yun, Ed. (INTECH Open Access Publisher, 2012).

[140] M. A. Steiner, J. F. Geisz, D. J. Friedman, W. J. Olavarria, A. Duda, and T. Moriarty, "Temperature-dependent measurements of an inverted metamorphic multijunction (IMM) solar cell", in *37th IEEE Photovoltaics Specialist Conference*, 2011, pp. 002527-002532.

[141] H. Helmers, M. Schachtner, and A. W. Bett, "Influence of temperature and irradiance on triple-junction solar subcells", *Sol. Energy Mater, Sol. Cells,* vol. 116, pp. 144-152, 2013.

[142] S. P. Philips, R. Hoheisel, T. Gandy, D. Stetter, M. Hermle, F. Dimroth, and A. W. Bett, "An experimental and theoretical study on the temperature dependence of GaAs solar cells", in *37th IEEE Photovoltaics Specialist Conference*, 2011, pp. 001610-001614.

[143] K. Nikhioka, T. Takamoto, T. Agui, M. Kaneiwa, Y. Uraoka, and T. Fuyuki, "Evaluation of temperature characteristics of high-efficiency InGaP/InGaAs/Ge triple-junction solar cells under concentration", *Sol. Energy Mater, Sol. Cells,* vol. 85, pp. 429-436, 2005.

[144] B. Goldstein, "Diffusion in compound semiconductors", *Physical Review,* vol. 121, no. 5, pp. 1305, 1961.

[145] M. Yamaguchi, "III-V compound multi-junction solar cells: present and future", *Sol. Energy Mater, Sol. Cells,* vol. 75, no. 1, pp. 261-269, 2003.

[146] A. Benninghoven, "Surface investigation of solids by the statistical method of secondary ion mass spectroscopy (SIMS)", *Surface Science,* vol. 35, pp. 427-457, 1973.

[147] R. P. Elliott and F. A. Shunk, "The Au-Ga (gold-gallium) system", *Bulletin of Alloy Phase Diagrams,* vol. 2, no. 3, pp. 356-358, 1981.

[148] C. Uchibori, Y. Ohtani, T. Oku, N. Ono, and M. Murakami, "InGaAs ohmic contacts to n-type GaAs with a tungsten nitride barrier", *Journal of Electronic Materials,* vol. 26, pp. 410-414, 1997.

[149] M. A. Nicolet, "Diffusion barriers in thin films", *Thin Solid Films,* vol. 52, no. 3, pp. 415-443, 1978.

[150] R. Kishore, "Electrical conductivity of metals", *Physica Status Solidi B,* vol. 26, no. 1, pp. 133-138, 1968.

[151] N. Kobayashi and Y. Kobayashi, "As and P desorption from II-V semiconductor surface in metalorganic chemical vapor deposition studied by surface photo-absorption", *Jap. J. Appl. Phys.,* vol. 30, no. 10A, pp. L1699, 1991.

[152] D. J. Friedman, "Modeling of tandem cell temperature coefficients", in *25th IEEE Photovoltaic Specialists Conference*, 1996, pp. 89-92.

[153] A. R. Moore, "An optimized grid design for a sun-concentrator solar cell", *RCA Review,* vol. 40, pp. 140-152, 1979.

[154] E. Yablonovitch, "Statistical ray optics," J. Opt. Soc. Am., vol. 72, no. 7, pp. 899-907, 1982.

Appendix A: Process Followers

InP/GaAs Solar Cell Bonding Process

Step	Title	Description
1	Back Contact Dep	Start with InP sample
		3 min ultrasonic clean in Ace, ISO, and DI followed by N2 dry, make sure to clean both sides
		Dehydration Bake at 110°C for ~1 min, clean spinner chuck so no blue tape necessary
		Protect Frontside of sample using 1 or 2 layers of SPR 220-3
		Dispense **HMDS** in puddle, wait 15 sec, then spin at **3000 rpm** for **30 sec** (**spin recipe 5**)
		Dispense **SPR 220-3**, then spin at **3000 rpm** for **30 sec** (**spin recipe 5**) for > 3μm photoresist
		Bake at **115°C** for at least **1 min 30 sec** to harden photoresist
		InP **Etch** in **HCl** for **~2+ min** to clean off back of sample. Look for dark ring to disappear
		Load sample into e-beam #3 backside up, place on smooth side of aluminum foil
		Deposit **Ti/Au** with thickness **10/2000Å**
		Load sample into thermal evap #1, place on Al foil, change gold XTAL
		Load Zn into closed boat in slot 1, Au into slot 3 (44 need XTAL to detect Zn evaporation) 77
		Deposit Zn/Au with thickness **2000/2000Å**, turn dial to ~40 to start deposition
		Deposit ~2 microns of Au using electroplating bench
		Remove Photoresist and Solvent Clean Sample
2	Edge Mesa Etch	Cleave 2 InP samples into 1.2" x 1.2" pieces
		Cleave 2 GaAs samples into 1" x 1" pieces
		Anneal InP samples (back contact down) at 390° C for 1 minute
		3 min ultrasonic clean in Ace, ISO, and DI followed by N2 dry
		Dehydration Bake at 110°C for ~1 min, clean spinner chuck so no blue tape necessary
		Dispense **HMDS** in puddle, wait 15 sec, then spin at **3000 rpm** for **30 sec** (**spin recipe 5**)
		Dispense **SPR 220-3**, then spin at **3000 rpm** for **30 sec** (**spin recipe 5**) for > 3μm photoresist
		Clean Backside of Samle & Edge Bead removal with EBR-100 on cleanroom Q-tip
		Bake at **115°C** for **1 min 30 sec**
		Expose "Edge Mesa" mask with **no filter** for **1 min**, raise stage for light contact for InP
		Develop in **MIF-300** for **1 min**
		InP Contact Layer **Etch** in **HCl** for **7-10 sec**, should stop bubbling
		Remove Photoresist and Solvent Clean Sample
3	Inteface Metal 1	GaAs based sample
		3 min ultrasonic clean in Ace, ISO, and DI followed by N2 dry
		Dehydration Bake at 110°C for ~1 min, clean spinner chuck so no blue tape necessary
		Dispense **HMDS** in puddle, wait 15 sec, then spin at **3000 rpm** for **30 sec** (**spin recipe 5**)
		Dispense **nLOF2020**, then spin at **3000 rpm** for **30 sec** (**spin recipe 5**) for > 2μm photoresist
		Clean Backside of Samle & Edge Bead removal with EBR-100 on cleanroom Q-tip
		Soft-Bake at **110°C** for **1 min 35 sec**
		Expose "Interface Metal" Mask with **i-line filter** for **10 sec**
		Post-Bake at **110°C** for **1 min 15 sec**
		Develop in **MIF-300** for **1 min**
		O2 Plasma Clean at 100W, 300mTorr, **10 sec**
		OCL Etch (~1 μm InGaP/AlGaAs/InGaP, can be thinner depending on epi variation)
		HCl for **3 sec**, H3PO4:H2O2:H2O 3:4:1 for **17 sec**, **HCl** for **3 sec**
		Use E-Beam #3 to deposit **Ti/Pt/Au** with thickness **300/500/4200Å** & max rate **2/1/3 Å/s**
		Do multiple deps to calibrate rate and make sure the thickness is very close to 5000Å
		Liftoff Metal with **heated 1165 at 80°C**
		Solvent Clean Sample
		Measure height of the metal using Dektak or Laser Confocal Microscope

3	Inteface Metal 2	InP based sample
		3 min ultrasonic clean in Ace, ISO, and DI followed by N2 dry
		Dehydration Bake at 110°C for ~1 min, clean spinner chuck so no blue tape necessary
		Dispense **HMDS** in puddle, wait 15 sec, then spin at **3000 rpm** for **30 sec** (**spin recipe 5**)
		Dispense **nLOF2020**, then spin at **3000 rpm** for **30 sec** (**spin recipe 5**) for > 2μm photoresist
		Clean Backside of Samle & Edge Bead removal with EBR-100 on cleanroom Q-tip
		Soft-Bake at **110°C** for **1 min 35 sec**
		Expose "Interface Metal" Mask with **i-line filter** for **10 sec**
		Post-Bake at **110°C** for **1 min 15 sec**
		Develop in **MIF-300** for **1 min**
		O2 Plasma Clean at 100W, 300mTorr, **10 sec**
		Native Oxide Removal, NH4OH (39%) for **1 min,** or **BHF** for **1 min**
		Use E-Beam #3 to deposit **Ti/Pt/Au** with thickness **300/500/(fill gap + 300-1000)Å**
		Do multiple deps to calibrate rate and make sure the thickness is correct
		Liftoff Metal with **heated 1165 at 80°C**
		Solvent Clean Sample
		Measure height of the metal using Dektak or Laser Confocal Microscope
4	Bonding	**Wear mask**, metal bar on top with larger glasses to avoid fogging up
		Always transfer samples with **clean glass container** & **clean tweezers**
		Prep **POLOS Spinner** in **bay 5**, set to **recipe 17 (300RPM, 120 sec, 1000RPM/sec)**
		Put on cover with small tube sticking up in center for vacuum
		Fill Ace, Iso, DI bottles, along with **Tergitol bottle** with **10 drops Tergitol** then **fill with DI**
		For each sample (top & bottom subcells) spin **Tergitol (x2), DI-Iso-Ace(x2), Iso (x2), DI + dry**
		Dehydration bake at **130°C** while in glass container on hotplate, use **Al foil** on bottom
		UV Ozone for **20 min,** wipe off bottom sheet & keep samples in glass
		Set up flip chip bonder, **zero offset plate**, **10x10x1mm collar**, **shim + top substrate = 1mm**
		Remove collar (offset plate if necessary), put in new shims (washers) **0.65mm for GaAs**
		When replacing collar, make sure the crosshatch lines up with the lines in the program
		Right before bonding each set of samples, **O2 Plasma Clean** at 100W, 300mTorr, 60 sec
		Focus camera, then pick up GaAs sample which is face down using "pick & place"
		Make sure sample is centered on collar, redo "pick & place" until it is centered
		Use Z focus on left side of tool to focus the GaAs sample
		Place InP sample face up on the stage, vacuum, focus, then align with fine rotation & x,y
		When aligned, run Tony's "Au-Au Thermo 400C" program, **320°C** with **24 Newtons of force**
		Repeat for 2nd sample set, switch back to "Pick & Place" to cool down stage, close program
		Get bonding fixtures from large "Bowers Wafer" box
		Open up bonding fixture, place sample on bottom, cube on top of sample
		Close bonding fixture, tighten to **0.5-1 lb-ft** of **torque** using NIST calibrated wrench
		Place fixtures in **oven** using holder, **300°C for 1 hour**, let cool then remove samples
		Melt (**T > 120°C**) Tony's special "acid resistant" **wax** onto **2 small glass slides**
		Place samples on wax face up
		Use q-tips to **push wax onto the sample sides** (none on top) to protect bonding interface
		Mount both glass slides onto 2 q-tips using yellow tape
		Substrate removal to remove GaAs with **NH4OH:H2O2 1:1**, use **magnetic spinner** to **mix**
		Take up to 30 min break, then watch samples near end (**1-2 hours**). Look for shiny surface
		Etch stop removal (GaInP), **HCl** for **~10 sec**
		Unmount samples from wax, solvent clean

5	Top Grid	3 min ultrasonic clean in Ace, ISO, and DI followed by N2 dry
		Dehydration Bake at 110°C for ~1 min, clean spinner chuck so no blue tape necessary
		Dispense **HMDS** in puddle, wait 15 sec, then spin at **3000 rpm** for **30 sec** (**spin recipe 5**)
		Dispense **nLOF2020**, then spin at **3000 rpm** for **30 sec** (**spin recipe 5**) for > 2µm photoresist
		Clean Backside of Samle & Edge Bead removal with EBR-100 on cleanroom Q-tip
		Soft-Bake at **110°C** for **1 min 35 sec**
		Expose "Top Grid" Mask with **i-line filter** for **10 sec** using IR Aligner
		Post-Bake at **110°C** for **1 min 15 sec**
		Develop in **MIF-300** for **1 min**
		O2 Plasma Clean at 100W, 300mTorr, **10 sec**
		Native Oxide Removal, HCl for **30 sec**
		Use E-Beam #3 to deposit **Ti/Au** with thickness **50/5000Å**
		Liftoff Metal with **heated 1165 at 80°C**
		Solvent Clean Sample
6	Top Mesa	**Wear mask**, metal bar on top with larger glasses to avoid fogging up
		Always transfer samples with **clean glass container** & **clean tweezers**
		Prep **POLOS Spinner** in **bay 5**, set to **recipe 17 (300RPM, 120 sec, 1000RPM/sec)**
		Put on cover with small tube sticking up in center for vacuum
		Fill Ace, Iso, DI bottles, along with **Tergitol bottle** with **10 drops Tergitol** then **fill with DI**
		For each sample (top & bottom subcells) spin **Tergitol (x2), DI-Iso-Ace(x2), Iso (x2), DI + dry**
		Dehydration bake at **130°C** while in glass container on hotplate, use **Al foil** on bottom
		UV Ozone for **20 min,** wipe off bottom sheet & keep samples in glass
		Set up flip chip bonder, **zero offset plate**, **10x10x1mm collar**, **shim + top substrate = 1mm**
		Remove collar (offset plate if necessary), put in new shims (washers) **0.65mm for GaAs**
		When replacing collar, make sure the crosshatch lines up with the lines in the program
		Right before bonding each set of samples, **O2 Plasma Clean** at 100W, 300mTorr, 60 sec
		Focus camera, then pick up GaAs sample which is face down using "pick & place"
7	Bottom Mesa	Make sure sample is centered on collar, redo "pick & place" until it is centered
		Use Z focus on left side of tool to focus the GaAs sample
		Place InP sample face up on the stage, vacuum, focus, then align with fine rotation & x,y
		When aligned, run Tony's "Au-Au Thermo 400C" program, **320°C** with **24 Newtons of force**
		Repeat for 2nd sample set, switch back to "Pick & Place" to cool down stage, close program
		Get bonding fixtures from large "Bowers Wafer" box
		Open up bonding fixture, place sample on bottom, cube on top of sample
		Close bonding fixture, tighten to **0.5-1 lb-ft** of **torque** using NIST calibrated wrench
		Place fixtures in **oven** using holder, **300°C for 1 hour**, let cool then remove samples
		Melt (**T > 120°C**) Tony's special "acid resistant" **wax** onto **2 small glass slides**
		Place samples on wax face up
		Use q-tips to **push wax onto the sample sides** (none on top) to protect bonding interface
		Mount both glass slides onto 2 q-tips using yellow tape
		Substrate removal to remove GaAs with **NH4OH:H2O2 1:1**, use **magnetic spinner** to **mix**
		Take up to 30 min break, then watch samples near end (**1-2 hours**). Look for shiny surface
		Etch stop removal (GaInP), **HCl** for **~10 sec**
		Unmount samples from wax, solvent clean

Thermal Imprinting Process

Step	Title	Description
1	Cleave Sample	Cleave sample, ideally so that it is larger than imprint stamp so no EBR is needed
2	Solvent Clean	3 min ultrasonic clean in Acetone, ISO, and DI followed by N2 dry
		5 min dehydration bake at **140C**
3	MR-I 7020E	Cool down for 1 min and secure sample on blue tape
		Dispense **HMDS** in puddle wait 15 sec then spin at 3000 rpm for 30 sec (**recipe 5**)
		Dispense **mr-I 7020E**, then spin at 2000 rpm for 45 sec (**recipe 3**)
		Optional: Edge bead removal with EBR-100 if sample is smaller than imprinting stamp
		Bake at 140C for 2 min
4	Imprint	Center and place imprint stamp on top of sample
		Login to Nanonex NX-2000 with signupmonkey login
		Open system, place 2 plastic films in correct place with magnets holding down top film
		Place sample on carrier wafer, place between the two plastic sheets
		Close system, edit recipe for imprinting conditions
		Imprint at 140C, 450psi, for 3 min
		Demould and clean stamp, imprinted sample ready for etch
5	ICP etch	On **ICP2**, check that **mode** is **auto**, **process** is **slice**, and **start button** is **not highlighted**
		Make sure gas switches are **CF4, CHF3, N2** (all up), if not, do gas change
		Run **10 min O2 clean, recipe 103** change time to **10 min**, put in **cleaning wafer**, hit **start**
		Mount sample on carrier wafer using vacuum grease, place wafer in chamber after clean
		Etch Sample using **recipe 126**, change **time** in **step 3** to **156 sec** (400 nm PR etched), bias from **50W to 300W**, **CHF3/CF4** from **10/30 to 40/0**
		Run **minimum 5 min O2 clean**, **recipe 103**
		Change **recipe 126** back to **50W bias** and **10/30 CHF3/CF4**
6	Clean Sample	Clean sample for **3 min** in **Acetone/ISO/DI** no ulrasonic clean
		Sample Complete!

Fabrication of Flexible PDMS Stamp

Step	Title	Description
1	PDMS Soft Stamp	Mix PDMS and curing agent in weighing dish at 1:10 ratio, stir thouroughly
		To remove air bubbles, place sample in Vacuum Oven for about 1 hour
		Heat to 100-130°C for ~1hr to cure PDMS (hotter cures PDMS faster)
	I prefer using Silicone membranes since they are easier to work with, http://www.sspinc.com/ssp_store/	
2	Substrate Prep	Solvent Clean PDMS
		10" O2 Plasma Treatment of Surface
		Spin on OrmoPrime08 at 4000 rpm for 60 sec with 1000 rpm/sec acceleration
		Hardbake at 150°C for 5 min (Note: high temperatures can be troublesome for PDMS)
3	Master Prep	Solvent Clean + Dehydration Bake Master
		Make sure the master has a fresh Anti-Stick treatment
4	Ormostamp Layer	Pipet a small amount of Ormostamp (1-2 drops for 1cm x 1cm area) directly onto Master
		Carefully place PDMS sheet onto the Master coated with Ormostamp
		Wait until pressure from the PDMS sheet causes the Ormostamp to spread over the master
		Make Sure there are no Air Pockets, Gently Press the substrate to help spread Ormostamp
		Flood Expose Ormostamp with UV Light to Cure (10 min DUV flood exposure works well)
		Demould the PDMS, pattern should be successfully transferred into Ormostamp Layer
		Flood Expose for an additional 5 min to harden Ormostamp Layer
		Hardbake PDMS Stamp at 130°C for 30 min
		Apply FDTS Anti-Stick Treatment with MVD

Soft UV Imprinting Process

Step	Title	Description
1	Substrate Prep	Solvent Clean + Dehydration Bake
		Spin **Omnicoat** on sample at 3000 rpm for 30 sec with an acceleration of 300rpm/s
		Bake at **200°C** for **1 min**
		Spin on MR-UVCur21 at **3000rpm for 60 sec** (300nm thickness)
		Softbake at **80°C** for **1 min**
		Edge Bead Removal recommended, not necessary for flexible PDMS stamps
2	Imprint	Place transparent stamp on top of sample
		Imprint at 25C, 5psi, for 2 min with **20 sec UV exposure**
		Demould and clean stamp

Upright AlGaInP Solar Cell Processing

Step	Title	Description
1	Back Contact	Protect Frontside of sample by painting on photoresist
		Bake at 100°C for 10 min to harden photoresist
		GaAs Etch in NH4OH:H2O2:H2O 2:1:2 for ~60 sec after removing orange peel to prepare surface
		Turn on Autolab, pour in back contact solution into back contact beaker, heat above 55°C (preset 2)
		Start Computer. Choose NREL generic recipe. Change Input time to 4 min, current to 4mA for 20x20
		Mount sample on tweezer. Clip black clip on tweezer, red clip on source. Lower sample into solution
		Start Deposition
		Remove Photoresist and Solvent Clean Sample
2	Top Contact	Spin on SPR220 at 4500 rpm for 30 sec
		Bake at 110°C for 90 sec
		Roughly align to the edge of the sample and expose for 8.5 sec
		Bake at 110°C for 90 sec
		Develop in MF-CD+26 for 75 sec
		Open up a corner of the sample using acetone so the tweezer can make contact to the sample
		Protect Backside of sample by painting on photoresist
		Turn on Autolab, pour in front contact solution into front contact beaker, heat above 55°C (preset 2)
		Start Computer. Choose CNC4 recipe.
		Mount sample on tweezer. Clip black clip on tweezer, red clip on source. Lower sample into solution
		Start Deposition
		Remove Photoresist and Solvent Clean Sample
3	Mesa Etch	Spin on 1818 at 4000 rpm for 30 sec
		Bake at 100°C for 5 min
		Let sample rest for 5 min prior to exposing sample
		Align mesa pattern to grid pattern and expose for 3 sec
		Develop in MF-CD+26 for 45 sec
		GaAs Contact Layer Etch in H3PO4:H2O2:H2O 3:4:1 for about 2 sec until surface clears
		Phosphide etch in HCl for ~15 sec per micron, sample should be specular and stop bubbling when complete
		Remove Photoresist and Solvent Clean Sample

NLof2070 Liftoff Process for 5 Microns Metal Deposition

Step	Title	Description
1	Litho for metal liftoff	Spin on nLof2070 at 2500 rpm for 30 sec, pour photoresist directly from bottle
		Softbake at 110°C for 60 sec
		Cool sample to room temperature
		Align sample to CNC12 negative 10 micron grid mask & expose for 3-4 seconds
		Wait ~60 sec after exposure
		Post exposure bake at 110°C for 60 sec
		Develop sample ~90 sec using AZ 300 MIF
		Native Oxide Removal in NH4OH:H2O 1:10
2	High temp metal	Deposit Ti/Pt/Al/Ti, up to ~5 microns
3	Liftoff	Liftoff in technistrip, heat to 65-75°C if you can babysit the sample